



HAL
open science

Study of the thermo-mechanical and fracture behaviour of iron oxide scales at room temperature and at high temperature

Victor Claverie

► **To cite this version:**

Victor Claverie. Study of the thermo-mechanical and fracture behaviour of iron oxide scales at room temperature and at high temperature. Mechanics of materials [physics.class-ph]. Université Paris sciences et lettres, 2023. English. NNT : 2023UPSLM082 . tel-04615324

HAL Id: tel-04615324

<https://pastel.hal.science/tel-04615324>

Submitted on 18 Jun 2024

HAL is a multi-disciplinary open access archive for the deposit and dissemination of scientific research documents, whether they are published or not. The documents may come from teaching and research institutions in France or abroad, or from public or private research centers.

L'archive ouverte pluridisciplinaire **HAL**, est destinée au dépôt et à la diffusion de documents scientifiques de niveau recherche, publiés ou non, émanant des établissements d'enseignement et de recherche français ou étrangers, des laboratoires publics ou privés.



THÈSE DE DOCTORAT
DE L'UNIVERSITÉ PSL

Préparée à Mines Paris-PSL

Study of the thermo-mechanical and fracture behaviour of iron oxide scales at room temperature and at high temperature.

Etude du comportement thermo-mécanique et de fissuration d'oxydes de fer à température ambiante et à haute température

Soutenue par

Victor

CLAVERIE-BURGUE

Le 17/10/2023

Ecole doctorale n° 364

**Sciences Fondamentales
et Appliquées**

Spécialité

**Mécanique Numérique
et Matériaux**

Composition du jury :

Salima BOUVIER

Professeure, UT Compiègne, Roberval
Présidente

Muriel Braccini

Chargé de Recherche HDR, CNRS, SIMAP
Rapporteuse

Henri BUSCAIL

Professeur, Université Clermont Auvergne, LVEEM
Rapporteur

Laurent LANGLOIS

Maître de conférence HDR, Arts & Métiers Metz, LCFC
Examineur

Karim INAL

Professeur, MINES Paris, CEMEF
Co-Directeur de thèse

Pierre MONTMITONNET

Directeur de Recherche, CNRS, CEMEF
Directeur de thèse

Remerciements

Je tiens à exprimer ma profonde gratitude envers toutes les personnes qui ont contribué, de près ou de loin, à la réalisation de cette thèse. Ce travail a été long et exigeant, mais il n'aurait pas été possible sans le soutien, l'encouragement et la collaboration de nombreuses personnes exceptionnelles. Je suis reconnaissant envers chacune d'entre elles. Merci d'avoir été à mes côtés tout au long de cette aventure passionnante.

Je souhaite exprimer mes remerciements aux membres du jury, composé de Muriel Braccini de l'Université Grenoble Alpes, Henri Buscail de l'Université Clermont Auvergne, Salima Bouvier de l'Université de Technologie de Compiègne, ainsi que Laurent Langlois de l'École Nationale Supérieure d'Arts et Métiers, d'avoir accepté de consacrer leur temps et leur expertise à l'évaluation de ce travail. Leurs commentaires constructifs et la discussion lors de la soutenance ont permis d'enrichir cette thèse.

Ce travail de thèse a été mené à bien à la fois au laboratoire du Centre de Mise en Forme des Matériaux de l'École des Mines de Paris et au centre de Recherche d'ArcelorMittal Maizières. À cet égard, je tiens à exprimer ma gratitude envers Elisabeth Massoni, directrice du CEMEF, José Barros Lorenzo, qui dirige le centre Process Engineering (PE), Pascal Gardin, responsable de la recherche au sein de PE, ainsi que Valentine Weber et Benjamin Riveaux, manager de l'Équipe PCS puis PCR. Leur accueil chaleureux dans leurs centres et laboratoires respectifs a grandement facilité mon travail.

Je tiens, ensuite, à exprimer ma profonde gratitude envers mon directeur de thèse, Pierre Montmitonnet, pour son expertise, sa patience, sa disponibilité et sa confiance en moi tout au long de cette aventure. Ses conseils éclairés et sa passion pour la recherche ont été une source d'inspiration inestimable. Un grand merci également pour ses nombreuses relectures du manuscrit, qui ont contribué à bien structurer celui-ci. Je lui suis tout particulièrement reconnaissant pour la marge importante d'initiative et de liberté qu'il m'a accordée.

Je suis également reconnaissant envers, Karim Inal pour sa précieuse contribution à ce travail, notamment sur la partie sur la diffraction. Les nombreuses configurations testées ensemble ont permis d'optimiser, dans la mesure des moyens disponibles les analyses de diffraction. Merci à aussi Alain Burr.

Mes encadrants industriels, Michel Picard et Amico Settefrati méritent également ma plus profonde reconnaissance. Leur expérience du monde professionnel, leur expertise et leur confiance m'ont offert une perspective précieuse et ont enrichi ma recherche. Malgré mes visites peu fréquentes durant ces 3 années à Maizières-Lès-Metz, leurs conseils ont permis de m'orienter dans ce travail, et cela a été un réel plaisir de collaborer avec eux.

Un travail de thèse, comme tout travail, ne se fait pas seul, mais aussi avec la contribution de nombreuses autres personnes. Je tiens à remercier Patrice Alexandre et Patrice Boileau pour la formation sur le four Orion, Nadine Marcot pour son aide lors de la préparation des échantillons, Jeremy Jactard pour son implication lors des essais dans le four de Trempe, Laura Turri pour la réalisation des essais thermo-balance, et Jean-Luc Borean pour l'analyse des essais sur le pilote de décalaminage Neptune.

Je tiens aussi à exprimer ma gratitude à Alexis Nicolai pour les nombreuses coupes FIB, Cyrille Colin de son aide pour la préparation de surface des échantillons, Suzanne Jacomet pour la

formation sur les MEB, Imène Lahouij pour la réalisation des essais de dureté dans le MEB, Christophe Pradille pour la calibration des thermocouples, Gabriel Monge pour son travail sur la diffraction, Francis Fournier et Arnaud Pignolet pour le temps passé pour la réparation du μ -durochaud (bien que celle-ci n'a jamais aboutie), Pierre-Olivier Bouchard et Daniel Pino-Munoz pour les discussions sur les simulations numériques ainsi que toute l'équipe administrative : Florence Morcamp, Coralie Fischer, Sylvie Massol et Marie-Francois Guenegan.

Un grand merci à Renato Pero pour le séjour à Thun et la réalisation des essais d'indentation à chaud. Looking forward to meeting you again.

Je tiens à remercier tous mes amis : les improvisateurs du Théâtre Antibéa, les copains avec qui j'ai pu courir quelques kilomètres, mes amis d'enfance du Pays Basque, mes amis de Seatech, et tout ceux que j'ai pu rencontrer pendant ces trois ans de thèse... Vous avez été une source constante de soutien, d'encouragement, et de distractions bienvenues pour décompresser de la thèse. Votre amitié a été un pilier sur lequel je pouvais compter.

Mention spéciale à tous les doctorants que j'ai pu rencontrer, de la Promo 2017 à 2022, vous avez tous été des personnes incroyables et cela a été un honneur de partager cette aventure avec vous. Merci pour les nombreux échanges que j'ai pu avoir, les cafés, les week-ends évasions, les randonnées, les repas partagés ...

À mes parents, je suis infiniment reconnaissant de leur amour inconditionnel, leur soutien constant et leurs encouragements à poursuivre mes études. Pendant ces trois années, leurs séjours dans mon appartement de Juan-les-Pins et nos voyages m'ont rempli de joie. Merci aussi d'avoir organisé superbement mon pot de thèse pour conclure ce chapitre de ma vie.

Merci à ma sœur et mon beau-frère de leur soutien et des vacances partagées, nécessaires pour me ressourcer

Merci à ma grand-mère d'avoir traversé la France et d'être venue assister à ma soutenance : « ça y est Grand-mère, il y a un Docteur dans la famille ! ».

Merci à mes oncles et tantes d'avoir fait le déplacement en très grand nombre pour m'encourager pour la soutenance.

Merci aussi à ma tante pour ses séances de sophrologie me mettant en bonnes conditions pour mon oral.

Merci à ma belle famille de m'avoir accueilli, notamment pendant les confinements ce qui m'a permis de continuer à travailler agréablement.

Ma copine mérite une mention très spéciale. Son amour, sa patience, et son soutien indéfectible a été essentiel pour mener à bien ma thèse. Son rôle dans cette aventure a été inestimable. Malgré les nombreuses difficultés rencontrées lors de la thèse, elle a toujours été là pour m'épauler. Maite zaitut, Moggy eta Socky ere.

Comme l'a dit un de mes encadrants, une bonne thèse n'est jamais linéaire. Pour ma part, cela s'est bien vérifié. C'est avec une grande fierté que je clôture ce « marathon-haies », pour reprendre l'expression de mon directeur de thèse.

Table of contents

INTRODUCTION.....	5
CHAPTER 1: FOR A BETTER UNDERSTANDING OF DESCALING	9
1.1 INDUSTRIAL CONTEXT	11
1.1.1 <i>Production of steel</i>	11
1.2 HOT STRIP MILL (HSM)	12
1.3 OXIDATION AT THE SURFACE OF SLABS DURING HSM.....	13
1.3.1 <i>Primary scale</i>	14
1.3.2 <i>Secondary scale</i>	14
1.3.3 <i>Tertiary scale</i>	14
1.4 OXIDE BEHAVIOUR IN HSM	16
1.4.1 <i>Temperature evolution during HSM</i>	16
1.4.2 <i>Evolution of stresses in the mill</i>	16
1.4.3 <i>Surface defect during HSM : rolled-in scale defect</i>	17
1.5 DESCALING TO LIMIT SURFACE DEFECT	20
1.5.1 <i>Description of the process</i>	20
1.5.2 <i>Descaling is an important source of costs</i>	21
1.5.3 <i>Difference between primary and secondary descaling</i>	21
1.5.4 <i>Descaling as a thermo-mechanical process</i>	22
1.6 EXPERIMENTAL STUDY OF DESCALING.....	24
1.6.1 <i>Influence of descaling parameters</i>	24
1.6.2 <i>Rolling parameter</i>	24
1.6.3 <i>Oxide properties</i>	25
1.7 NUMERICAL STUDY OF THE DESCALING	28
1.7.1 <i>Finite element simulation (FEM) of thermo-elastic fracture</i>	28
1.7.2 <i>Analytical model of oxide fracture</i>	29
1.8 SUMMARY OF MECHANISMS PROPOSED FOR HIGH PRESSURE DESCALING.....	31
1.9 CONCLUSION	33
CHAPTER 2: A REVIEW OF OXIDE PROPERTIES	35
2.1 OXIDATION OF STEEL	37
2.1.1 <i>Oxidation mechanism</i>	37
2.1.2 <i>Oxidation kinetics</i>	38
2.1.3 <i>Multiscale oxidation</i>	40
2.2 INFLUENCE OF ALLOYING ELEMENTS ON THE SCALE STRUCTURE	46
2.2.1 <i>Elements less oxidizable than iron</i>	47
2.2.2 <i>Elements more oxidizable than iron</i>	47
2.3 INTERNAL STRESSES.....	48
2.3.1 <i>Growth stresses during oxidation</i>	48
2.3.2 <i>Thermal stresses during temperature change</i>	50
2.3.3 <i>Other internal stresses</i>	51
2.3.4 <i>Relaxation by creep, fracture, spallation</i>	52
2.4 FRACTURE OF THIN FILM	54
2.4.1 <i>Failure under tension</i>	54
2.4.2 <i>Failure in compression : spallation</i>	56
2.4.3 <i>Blistering</i>	58
2.5 MECHANICAL PROPERTIES	61
2.5.1 <i>Oxide behaviour</i>	62
2.5.2 <i>Hardness</i>	68
2.5.3 <i>Ductile-brittle transition behaviour of oxide</i>	71

2.5.4	<i>Measurement of fracture toughness</i>	73
2.5.5	<i>Critical fracture stress</i>	74
2.5.6	<i>Adhesion</i>	76
2.6	CONCLUSION	84
CHAPTER 3: X-RAY DIFFRACTION CHARACTERISATION OF OXIDE: FROM THE IN-SITU-OXIDATION TO THE POST-MORTEM OBSERVATIONS		87
3.1	INTRODUCTION	89
3.2	OXIDATION EXPERIMENTS	90
3.2.1	<i>Steel composition</i>	90
3.2.2	<i>Oxidation of low carbon steel</i>	90
3.2.3	<i>Observation of oxidized cross-sections</i>	91
3.3	A DESCRIPTION OF THE DIFFRACTION: PHASE AND STRESS ANALYSIS	94
3.3.1	<i>Diffraction principle</i>	94
3.3.2	<i>Theory for stress analysis : $\sin^2 \psi$ law</i>	95
3.3.3	<i>Others methods to evaluate internal stresses</i>	99
3.3.4	<i>Literature review for diffraction of iron oxides</i>	99
3.4	METHODOLOGY USED IN THIS WORK	102
3.4.1	<i>CEMEF diffraction set-up</i>	102
3.4.2	<i>Fluorescence</i>	103
3.4.3	<i>Penetration depth evaluation</i>	103
3.5	ROOM TEMPERATURE: XRD RESULTS OF A SPECIMEN PRE-OXIDIZED IN THE ORION FURNACE	106
3.5.1	<i>Phase analysis</i>	106
3.5.2	<i>Crystallographic texture</i>	110
3.5.3	<i>Stress analyses</i>	113
3.6	HIGH TEMPERATURE X-RAY DIFFRACTION (HTXRD) FOR IN SITU ANALYSIS OF STRESS EVOLUTION	119
3.6.1	<i>Description of the equipment</i>	119
3.6.2	<i>Determination of the coefficient of thermal expansion (CTE)</i>	121
3.6.3	<i>Long Cycle stress analysis at high temperature: evaluation of thermal stresses and relaxation</i>	122
3.6.4	<i>Short Cycle analysis: to evaluate relaxation with a better time resolution</i>	126
3.7	CONCLUSION	130
CHAPTER 4: INDENTATION TO EVALUATE PROPERTIES OF OXIDE (AT ROOM TEMPERATURE AND HIGH TEMPERATURE)		133
4.1	INTRODUCTION	135
4.2	A REVIEW OF INDENTATION FRACTURE IN LITERATURE	136
4.2.1	<i>Fracture of material due to indentation: bulk material</i>	136
4.2.2	<i>Fracture of a thin film</i>	140
4.2.3	<i>Thin hard film on a soft substrate</i>	140
4.3	METHODOLOGY USED IN THIS WORK	146
4.4	ROOM TEMPERATURE INDENTATION	148
4.4.1	<i>Indentation on cross-sections to evaluate hardness</i>	148
4.4.2	<i>Fracture of oxide at room temperature: brittle behaviour</i>	149
4.5	HIGH TEMPERATURE INDENTATION	160
4.5.1	<i>Difficulties inherent to high temperature indentation</i>	160
4.5.2	<i>Micro-indentation up to $30 \mu\text{m}\cdot\text{s}^{-1}$ at 800°C</i>	162
4.6	CONCLUSION	170
CHAPTER 5: NUMERICAL STUDY OF THE INDENTATION PROCESS TO UNDERSTAND FRACTURE AND DELAMINATION OF OXIDE		173
5.1	INTRODUCTION	175
5.2	A REVIEW OF NUMERICAL SIMULATIONS OF INDENTATION OF THIN & HARD FILMS	176
5.2.1	<i>Cohesive zone model (CZM) for thin film</i>	176
5.2.2	<i>eXtended-Finite Element Method (XFEM) models to evaluate cracking</i>	179
5.3	SIMULATION OF INDENTATION WITH A CONTINUUM APPROACH	183
5.3.1	<i>Description of the model</i>	183

5.3.2	<i>Influence of the residual/internal stresses during indentation</i>	190
5.4	MODELLING THE DELAMINATION OF OXIDE WITH CZM ELEMENTS	193
5.4.1	<i>Numerical reproduction of the delamination</i>	193
5.4.2	<i>Influence of CZM parameters</i>	196
5.5	OXIDE FRACTURE MODELLING WITH XFEM : CIRCULAR CRACKS	203
5.5.1	<i>Description of the model</i>	203
5.5.2	<i>Single crack initiated with a defect in surface (pre-crack)</i>	204
5.5.3	<i>Multiple fracture without pre-crack</i>	210
5.6	XFEM FOR "NORMAL" CRACKS (NORMAL TO THE INTERFACE)	213
5.6.1	<i>Description of the model</i>	213
5.6.2	<i>Conclusion on the room temperature indentation</i>	216
5.7	TRANSPOSITION TO HIGH TEMPERATURE	217
5.7.1	<i>Description of the model for high temperature indentation</i>	217
5.7.2	<i>Delamination for adhesion</i>	222
5.8	CONCLUSION	224
CONCLUSION		227
APPENDICES		235
BIBLIOGRAPHY		249

Introduction

The present research is proposed by the ARCELOR group. ARCELOR is a multinational group that mobilises its technical, industrial, and commercial skills to become a global leader. ArcelorMittal is one of the world's leading integrated steel and mining companies. ArcelorMittal is the largest steel producer in Europe and among the largest in the Americas, second largest in Africa and the sixth largest steel producer in the CIS (Commonwealth of Independent States) region and has a smaller but growing presence in Asia. ArcelorMittal's steel-making operations have a high degree of geographic diversification. In 2022, approximately 34% of its crude steel was produced in the Americas, approximately 54% was produced in Europe and approximately 12% was produced in other countries, such as Kazakhstan, South Africa and Ukraine.

The hot rolling process is a crucial step in the production of high-quality finished steel products. During this step, the slabs of steel are heated at high temperature (1200°C) to be softer (reduction of the roll load), more deformable and to transform the improper cast microstructure. Due to the high affinity of iron with oxygen, an oxide film called scale inevitably forms on the steel surfaces during heating and rolling operations in the hot strip mill (HSM). This oxidation is unwelcome since it represents a loss of metal and usually has to be removed at the end of the operation. Oxide scale plays an important role in determining friction and heat transfer during thermomechanical processing, as well as quality of the formed product, due to its position on the interface between tool and workpiece.

Formation of scale in HSM can lead to surface defects, sources of important costs in terms of downgrading, litigations and repairs. These defects are more present when the thickness of oxide is important (above 20 µm at the entry of the finishing mill). Below the rolls, stresses imposed on the scale, joined to the degradation of the rolls, may cause delamination, cracks perpendicular to the direction of rolling and embedding in the strip metal (rolled-in scale defects). The appearance of the strip surface is a critical factor that affects the costs of high-speed milling operations and can limit productivity.

Nowadays, programming rules have been empirically established to reduce the apparition of surface defects. However, these rules are important constraints that penalise productivity and such consistency is difficult to achieve with new operations, where the alloy or forming operation has not been tested.

The descaling operation is an important factor for obtaining steel strips with a high surface quality. It consists in adding descaling boxes in the production line to remove this scale by sending pressurised water on the scale. It is a thermo-mechanical process that is poorly understood. The descaling process has two components: the mechanical effect of the water jets and also a thermal stresses generated by the fast cooling of the oxide in surface.

However, the interrelations for scale formation and scale properties during descaling are not known properly and the efficiency of descaling process cannot be verified, because of the speed of the process (slab speeds of 2m/s below the water jets and it lasts less than 10⁻²s). Indeed, investigation of the descaling process is fraught with difficulties even under laboratory conditions (long and complicated tests and hard to interpret). In an industrial context, the descaling configuration of HSM mills are different and no design rules or clear comprehensive parameters to compare them are available. Regrettably, in reality some steel grades have difficulty to be descaled, some solutions have to be implemented (modification of descaling parameters (pressure...), rolling parameters (speed, temperature...)), it takes time to solve these issues.

The idea is to identify which parameters affect the descability of slabs. These mostly concern the parameters determining adherence and fracture of the oxide scale in the high-temperature range. Among the key oxide scale properties are scale thickness and uniformity, composition, mechanical properties, thermal properties, scale structure, adherence and cohesion, steel-oxide scale interface morphology and influence of alloying elements.

Introduction

Understanding of the scale removal mechanism is important for optimization of industrial descaling conditions. Thus, the characterisation of these properties at the temperature involved in the HSM as well as the understanding of the relations between these properties and the descaling efficiency are fundamental prerequisites for enabling, in the future, a better estimation of the descalability of a steel grade and for optimising the descaling process.

The core of the PhD consists in designing and carrying out experiments at high temperature to understand the behaviour of this scale and determine a stress-based fracture criterion relevant for the computation of descaling - although the latter is not part of this PhD work. The final descaling modelling should highlight the mechanisms of descaling to better understand the behaviour of the oxide.

The manuscript is divided in five chapters. In the first chapter, successive steps of the complex hot rolling process are described. A global description of the descaling process is realised, several possible mechanisms are presented. After the presentation of the industrial process and the context of the study, the second chapter highlights the physical properties of the oxide scale in the finishing mill (oxidation mechanism, internal stresses, alloying elements...) as well as its mechanical properties. The third chapter introduces an *in situ* X-Ray diffraction methodology to evaluate the phases and internal stresses of oxide at room temperature and at high temperature. The fourth chapter is devoted to the mechanical test selected to evaluate the properties of the oxide and its interface : indentation. The tests are carried first at room temperature for a preliminary study and at temperature encountered during the descaling (up to 800°C). In the fifth chapter, a numerical study is performed to model the indentation tests on the Abaqus finite element software. The idea is to simulate the different kinds of oxide damage (crack, delamination) observed experimentally to evaluate properties of oxide. The study is then articulated around two extremely linked parts: numerics and experiments.

Résumé

Cette thèse est proposée par le groupe ArcelorMittal. C'est un groupe multinational qui utilise ses compétences techniques pour être le leader mondial de l'industrie sidérurgique. ArcelorMittal est le plus grand producteur d'acier en Europe et l'un des plus grands en Amérique, le deuxième en Afrique et le sixième dans la région de la CEI (Communauté des États indépendants), avec une présence plus modeste mais croissante en Asie. Les activités sidérurgiques d'ArcelorMittal sont très diversifiées sur le plan géographique. En 2022, environ 34 % de l'acier brut a été produit dans les Amériques, environ 54 % en Europe et environ 12 % dans d'autres pays, tels que le Kazakhstan, l'Afrique du Sud et l'Ukraine.

Le processus de laminage à chaud est une étape cruciale dans la production de produits finis d'acier. Au cours de cette étape, les brames d'acier sont chauffées à haute température (1200°) pour être plus déformables (réduction de la charge du laminoir), et pour transformer la microstructure de la coulée continue. En raison de la forte affinité du fer avec l'oxygène, une couche d'oxyde appelé calamine se forme inévitablement à la surface de l'acier pendant les opérations de chauffage et de laminage. Cette oxydation est indésirable car elle représente une perte de métal et doit généralement être éliminée. La calamine joue aussi un rôle important d'un point de vue du frottement et du transfert de chaleur, en raison de sa position centrale sur l'interface entre le cylindre et la pièce déformée.

La formation de calamine dans le laminoir peut entraîner des défauts de surface, générant des coûts importants en termes de déclassement et de réparations. Ces défauts sont d'autant plus présents que l'épaisseur d'oxyde est importante (supérieure à 20 µm à l'entrée du laminoir de finition). Sous les cylindres, les contraintes imposées à la calamine, jointes à la dégradation des cylindres, peuvent provoquer des décollements, des fissures perpendiculaires à la direction du laminage et des incrustations dans le métal (défauts de calamine incrustée).

De nos jours, des règles de programmation ont été établies empiriquement pour réduire l'apparition des défauts de surface. Cependant, ces règles sont des contraintes importantes qui pénalisent la productivité, et elles sont difficiles à mettre en place.

Le décalaminage est donc nécessaire pour obtenir des bandes d'acier avec une haute qualité de surface. Elle consiste à ajouter des boîtes de décalaminage dans la ligne de production pour éliminer cette calamine en envoyant de l'eau sous pression sur la calamine. Il s'agit d'un processus thermo-mécanique encore mal compris. Le processus de décalaminage a deux composantes : un effet mécanique des jets d'eau et aussi une contrainte thermique générée par le refroidissement rapide de l'oxyde en surface.

La formation de calamine et ses propriétés pendant le décalaminage ne sont pas bien connues et l'efficacité du processus de décalaminage ne peut pas être vérifiée, en raison de la vitesse du processus (vitesse des brames de 2m/s sous les jets d'eau et durée inférieure à 10⁻²s). En effet, l'étude du décalaminage présente de nombreuses difficultés, même dans des conditions de laboratoire (tests longs et compliqués et difficiles à interpréter). Dans un contexte industriel, les configurations de décalaminage dans les nombreux laminoirs du groupe ArcelorMittal sont différentes et il n'existe pas de règles ni de paramètres clairs et exhaustifs pour les comparer. Malheureusement, dans la réalité, certaines nuances d'acier ont des difficultés à être décalaminées, certaines solutions doivent être mises en œuvre (modification des paramètres de décalaminage (pression...), des paramètres de laminage (vitesse, température...)), et cela demande du temps pour résoudre ces problèmes.

L'idée est donc d'identifier les paramètres qui affectent le décalaminage des brames. Il s'agit principalement des paramètres qui déterminent l'adhérence et la rupture de la couche d'oxyde hautes températures. Parmi les principales propriétés de la calamine, on peut citer l'épaisseur et l'uniformité de la calamine, sa composition, ses propriétés mécaniques, ses propriétés thermiques, sa structure, son adhérence et sa cohésion, la morphologie de l'interface acier-calamine et l'influence des éléments d'alliage.

La compréhension du décalaminage est nécessaire pour l'optimisation du procédé industriel. Ainsi, la caractérisation de ces propriétés à la température impliquée lors du décalaminage va permettre, à l'avenir, d'estimer la décalaminabilité d'une nuance d'acier et d'optimiser le processus de décalaminage.

Introduction

Le cœur de la thèse consiste à concevoir et à réaliser des essais à haute température pour comprendre le comportement de la calamine et déterminer un critère de rupture pour la simulation du décalaminage - bien que ce dernier ne fasse pas partie de ce travail de thèse. La modélisation finale du décalaminage devrait mettre en évidence les mécanismes du décalaminage et permettre de mieux comprendre le comportement de l'oxyde.

Le manuscrit est divisé en cinq chapitres. Dans le premier chapitre, une description globale du processus de décalaminage est réalisée, plusieurs mécanismes possibles sont présentés. Après la présentation du procédé industriel et du contexte de l'étude, le deuxième chapitre met en évidence les propriétés physiques de la calamine dans le laminoir de finition (mécanisme d'oxydation, contraintes internes, éléments d'alliage...) ainsi que ses propriétés mécaniques. Le troisième chapitre présente une méthodologie de diffraction des rayons X pour évaluer les phases et les contraintes internes de l'oxyde à température ambiante et à haute température. Le quatrième chapitre est consacré à l'essai mécanique choisi pour évaluer les propriétés de l'oxyde et de son interface : l'essai d'indentation. Les essais sont réalisés d'abord à température ambiante pour une étude préliminaire et à une température similaire rencontrée lors du décalaminage (jusqu'à 800°C). Dans le cinquième chapitre, une étude numérique est réalisée pour modéliser les essais d'indentation sur le logiciel d'éléments finis Abaqus. L'idée est de simuler les différents types d'endommagement de l'oxyde (fissure, délamination) observés expérimentalement afin d'évaluer les propriétés de l'oxyde. L'étude s'articule donc autour de deux parties extrêmement liées : la partie numérique et la partie expérimentale.

Chapter 1: For a better understanding of descaling

Chapter 1: For a better understanding of descaling

This chapter is focused on a complete description of the high-pressure water jet descaling. First, the industrial context of the thesis is presented. The oxide and its behaviour in the HSM (Hot Strip Mill) are then evoked. The descaling process is described in detail. In order to understand this complex process, experimental and numerical studies of the descaling are reported to denote the influence of parameters. Finally, some possible descaling mechanisms are discussed.

1.1 Industrial context

The production of steel is one of the most important industries. Steel is used in lots of different fields, from the automobile to the packaging and the construction industry.

1.1.1 Production of steel

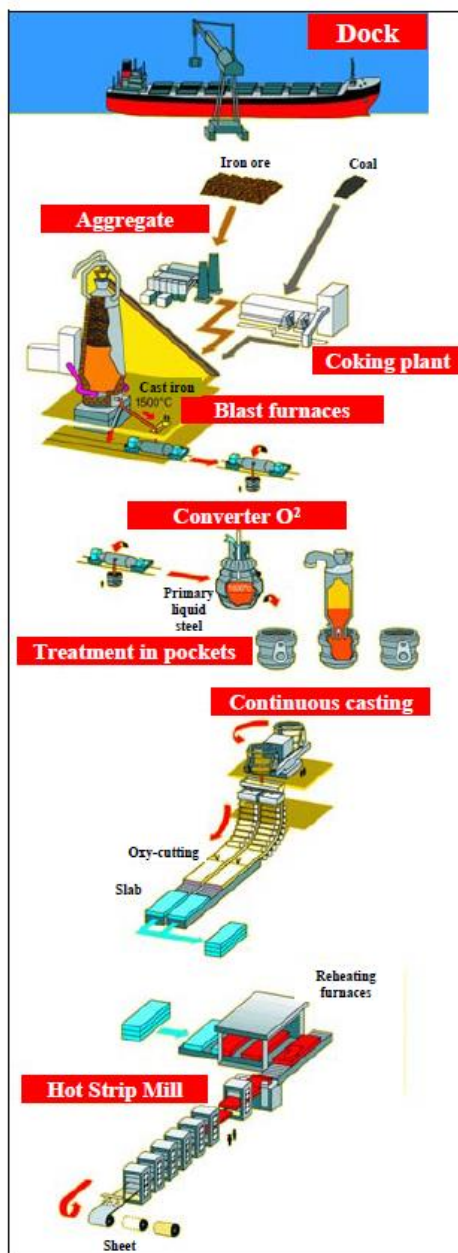


Figure 1.1: Schematic representation of the production of steel (Fos-Sur-Mer plant) (document ArcelorMittal)

The production of steel sheet involves several stages, from the mines to the semi-finished product: iron-making, steel-work and finally rolling (Figure 1.1) [1].

First, it requires extraction of iron ore, coal, and other minerals from mines around the world [1]. Iron ore mining operations use the ‘open pit’ method, where miners drill into the rock and blast the ore-bearing material loose with explosives. To mine metallurgical coal, vertical mine shafts are sunk to access coal which is deposited in layers underground. Before the transport with large ocean-going ships to the factory, the material is transformed into usable raw material by crushing and concentrating it (by milling for example). Once arrived into the coking plant, coal is turned into coke during 17 hours heating in a non-oxygen atmosphere to remove any impurities. In the same time, the iron ore is burned with fluxes to have a consistent substance: the sinter which is crushed. The blast furnace is the place for the reaction between coke and the sinter with injected hot air. The coke provides the heat needed to melt the ore and it “steals” the oxygen from the iron ore to leave pure iron. The liquid iron is then transported to the basic oxygen furnace. Here, percentage of carbon is still important (4%), so oxygen is blown to reduce it below <0.5%. Then, poured in pockets, ferro-alloys are added to have the proper composition of each grade. In the continuous caster, liquid steel is brought in a ladle. The liquid steel passes through a vertical mould, and the deflection to the horizontal is done between series of rollers, as it cools. The continuous slab of steel is cut out by blowtorches to length into semi-finished products [1]. The next step is the HSM, it can be done in the same factory or transported to another one.

As an alternative to the traditional blast furnace method, Electric Arc Furnaces (EAF) are now used to reduce greenhouse gas emissions to achieve carbon neutrality by 2050 (Figure 1.2). The blast furnace step (and the use of coal), which is particularly polluting, is not used. It uses thermal energy of the electric arc established between electrodes and the metal to obtain a temperature sufficient to melt it (above 1520°C). After the continuous caster, the traditional HSM is used. Upstream of the production chain, the extraction of minerals is also greatly reduced as scrap metal is recycled. The risk of unwanted impurities can be controlled by the steelmaker because the choice of scrap allows the elimination of suspect scrap. For example, offcuts from rolling mills can be used (because the history of material is known). Anyway, anomalies can be detected after the first analyses carried out during melting.

In 2021, ArcelorMittal launched two solutions under the XCarb™ brand: XCarb™ green steel certificates and XCarb™ recycled and renewable produced, which was well received in industry and automotive markets. The first XCarb® recycled and renewable produced steels have been successfully launched. Hot Rolled steels are already available in Europe, exhibiting strongly reduced global warming potential

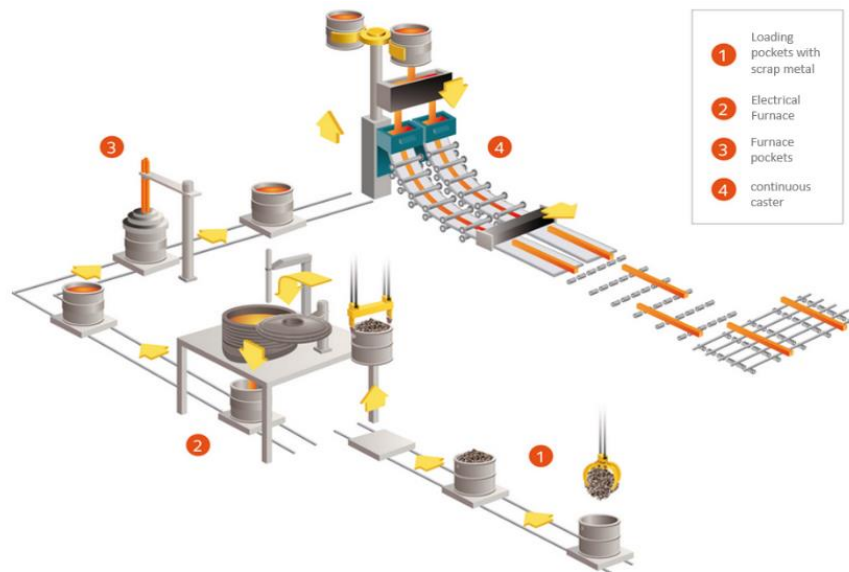


Figure 1.2 : Electric Arc Furnace (EAF) method [2]

1.2 Hot Strip Mill (HSM)

The aim of HSM is to change the thickness of slabs from 250 mm to 2-5 mm (Figure 1.3). (on the other hand, the length of the slab will range from a few metres to several hundred metres for the hot-rolled product before the coiling).

Slabs are re-heated at 1250°C in furnaces before the HSM to make them easier to deform. The heating takes approximately 3 hours. Red-hot slabs move on a conveyor to automated roughing and finishing mills. In the presence of oxygen for hours, a thick oxide scale forms at the surface of slabs (“primary scale”). At this stage (1200/1250°C), oxide is ductile and porous. This primary scale (several hundreds of μm to 1-2 mm in thickness) is removed by the descaling box. Nozzles project water under-pressure (150 bars) on the products. A combination of thermal and mechanical effects removes the thick primary scale.

Slab then enters the roughing mill and passes through stands comprising two work-rolls, with two back-up rolls to limit their deformation under load. Here, a pressure above the yield stress of steel is applied to reduce its thickness. Roughing mill can be constituted of several stands, or a reversible stand to reduce the length of the production line. Edging stands with vertical axis, grooved rolls are added to control the width of the slab.

At the end of this step, the temperature is about 1100°C and the slab thickness has been reduced to 30-40mm. As the slabs are still at high temperature, oxide has re-grown through the roughing mill (“secondary scale”), so that a descaling box is added to remove the oxide (which is here below 100 μm in thickness). The idea is to remove the oxide thickness in excess in order to limit surface defects ;

indeed, it is estimated that an oxide with a thickness above 20 μm entering the finishing mill may increase the risk of defects. In the finishing mill, strip thickness is reduced from 30-40 mm to 2-5 mm. Finally, the steel strips are coiled for cooling and storage. During finishing rolling (1100-850°C), during cooling on the run-out table (750°-700°C) and during the coiling (650°C), the temperature is still high (600°C) and thus a thin oxide scale forms again (“tertiary scale”).

After days of cooling, cold rolling is a process whereby metal strip is re-rolled at room temperature (well below recrystallisation temperature) down to 0.1 – 1 mm thickness. An advantage is the increase of the conventional yield strength and hardness of the metal. Before cold rolling, the steel has to be ‘pickled’ in heated hydrochloric acid to remove the tertiary scale. Most of the time, a heat treatment is carried out at the annealing line after cold rolling, a coating may be applied and the skin pass finally gives the desired elongation, roughness and flatness. This last heat treatment is performed under a reducing atmosphere, so that oxide does not form again.

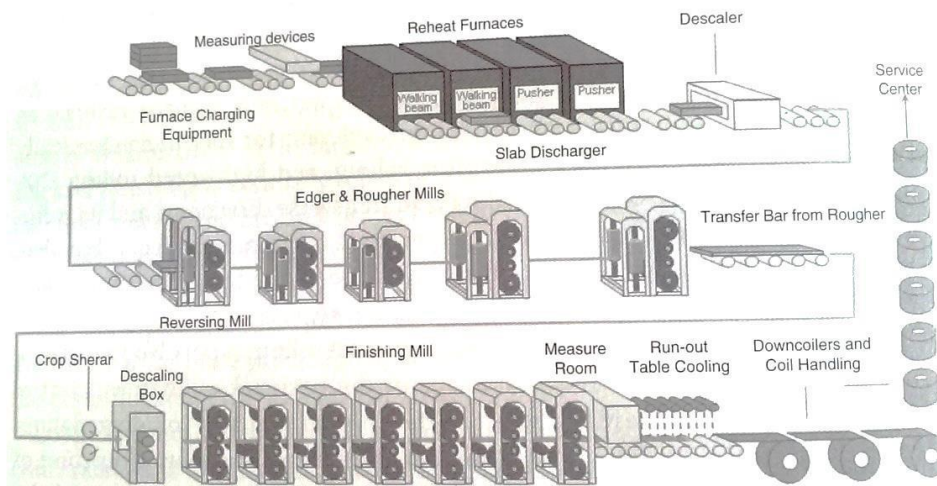


Figure 1.3: Typical hot strip mill layout [3]

The HSM is a complex process, the next part is a description of the oxide scale that is present from the reheating furnace to the end of the coiling.

1.3 Oxidation at the surface of slabs during HSM

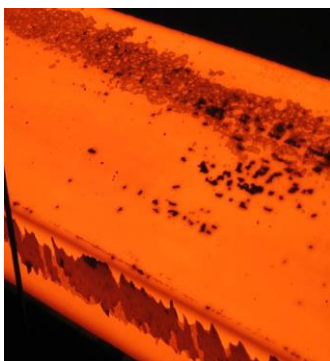


Figure 1.4 : Presence of oxide on a slab during HSM (document ArcelorMittal)

As described before, the production and forming of steel is a very long process. In this work, we are interested in the hot strip mill and more precisely the descaling process. In addition to the right geometry (width, thickness, flatness), the surface quality at the end is a key parameter for the factory. It requires mastering the oxidation from the re-heating furnace to the coiling. The oxide is present all along the hot strip mill (Figure 1.4). However, the morphology of oxide is different depending on the location (Figure 1.5). From the reheating furnace to the furnace scale breaker, there is the primary scale. From the roughing mill to the finishing scale breaker, it is the secondary scale. Finally, until the cooling to room temperature, the tertiary scale forms of the surface.

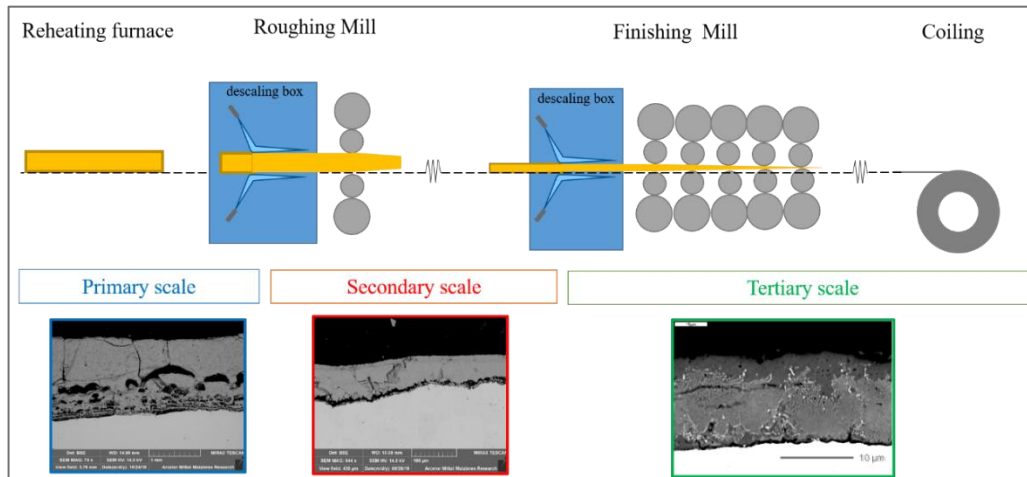


Figure 1.5 : Schematic representation of the presence of oxide during HSM

1.3.1 Primary scale

First, during more than 3 hours, the primary scale grows in the reheating furnace. It is a very thick (up to 2 mm) and porous scale. This porosity can be observed in Figure 1.5, making oxide multi-layered: Hematite ($\alpha\text{-Fe}_2\text{O}_3$) in surface, Magnetite Fe_3O_4 and Wüstite Fe_{1-x}O closest to the steel (but mainly composed of Wüstite 95 to 99%). At the interface, some alloying elements are enriched and the metal is denatured by various mechanisms such as decarburization or internal oxidation.

This scale is partly removed by primary descaling, before any rolling. At high temperature, the remaining oxide is ductile and is co-deformed with the steel, forming the substrate of the secondary scale.

1.3.2 Secondary scale

The secondary scale grows with time from primary descaling till the entry of the finishing mill. Secondary scale is a single layer (Wüstite 99%) more compact than primary scale due to the deformation below rolls (roughing mill). The pores are closed, and the interface is rough. Depending on the temperature, the oxide can be brittle, the multiple deformation can also induce cracks inside the layer. The maximum thickness can be up to 100 μm on the transfer table, so a descaling box is added before the finishing mill, the purpose being to maintain the final thickness below 20 μm.

1.3.3 Tertiary scale

From the 10-20 μm remaining from the secondary scale after finishing descaling, tertiary oxide grows throughout the finishing stands, the run-out table and coiling; the scale thickness decreases however, due to plastic thinning in the rolling passes.

On the coil after cooling down, the tertiary scale has transformed depending on the cooling rate. Wüstite is no more stable below 570°C, it decomposes into pure iron and Magnetite with an eutectic structure (Figure 1.5). Intergranular oxidation is also possible. As the coil takes several days to cool, a thin layer of Magnetite may also be present on the surface.

Due to these different mechanisms, the steel-oxide interface may be rough. At pickling, the previous thin oxide particles embedded disappear and leave a rough surface, sheet surface presents cavities (Figure 1.6). In some cases, particles are not removed and remain on the sheet, degrading the final quality.

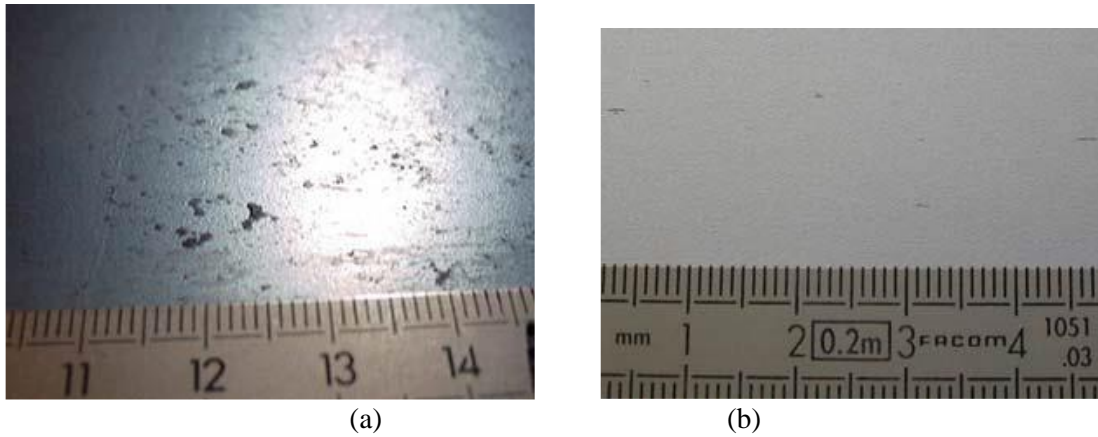


Figure 1.6: ArcelorMittal HSM observations: Consequences of rolled-in scale defects on (a) hot rolled coils (b) on the cold rolled sheet [4])

Indeed, oxidation is responsible for lots of surface defects when oxide is thick. It degrades the final quality of slabs and can lead to losses. It is also at the origin of metal losses (reaction of Fe with O). The heterogeneity of scale degrades rolls, and thus reduces the mount time, accelerating the cylinder change, which stops the production. In brief, this scale is an important source of costs. It is also important to remind that, without the oxide, rolling is not possible, as the slabs and the work roll would be sticking together : oxide acts as a lubricant, at least an anti-seizure agent. Oxide scale is also useful as a thermal barrier between hot strips and cold work-rolls.

This study is focused on the secondary scale that is present from the end of the roughing mill to the entry of the finishing mill.

1.4 Oxide behaviour in HSM

1.4.1 Temperature evolution during HSM

In the HSM, the temperature of oxide is changing. From the re-heating furnace to the coiling, temperature is decreasing from 1250°C to 600°C. The oxide thickness and its temperature can be predicted accurately by models. In the simulation of a finishing mill, the curves in blue and green refer to the temperature, and the red and grey are the thickness of oxide (Figure 1.7). The descaling induces a fast cooling in surface and a re-heating by conduction with the heat from the centre of the slab. The temperature drops in each stand because the rolls are not heated. The oxide therefore undergoes thermal cycling all along the finishing mill. It can be noted that the temperatures at the surface and in the centre are different, but tends to be more uniform when the thickness is reduced. This difference in temperature is the source of thermal stresses in oxide. In terms of scale, a thin layer of scale is left after the descaling box. The oxide re-grows until the first stand. In the stand, the oxide is plastically deformed, and its thickness is reduced. At the end of the finishing mill, the oxide is thinner, usually in the range 7-15 µm.

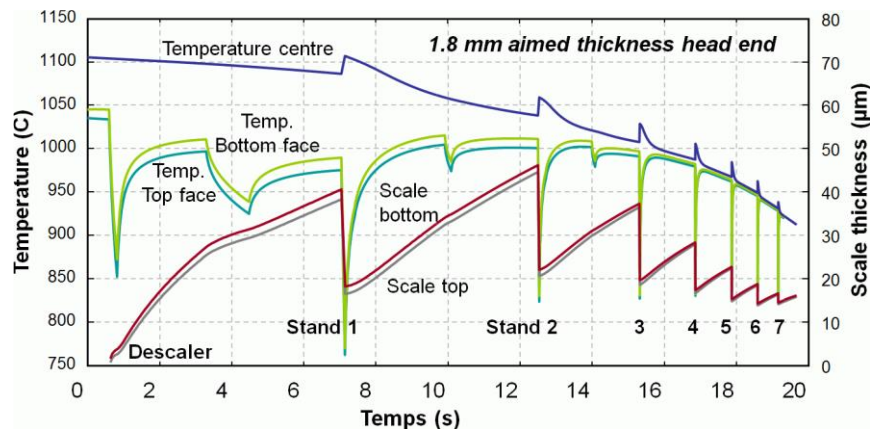


Figure 1.7: Scale thickness (red and grey) and temperature (blue and green) calculations in the finishing mill (ArcelorMittal) [5]

1.4.2 Evolution of stresses in the mill

All along the production line, oxide undergoes different stresses (detailed in Figure 1.8). Between the stands (1) internal stresses are generated. At the entry of the rolls (2), oxide is in tension. Below the rolls, oxide is in compression (3). The scale is thus subject to cyclic sollicitation.

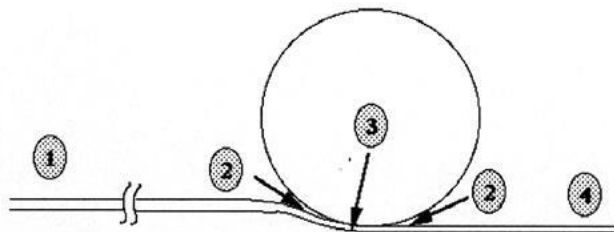


Figure 1.8 : (1) and (4): internal stresses (thermal and growth) ; (2): thermo-mechanical stresses before and after the rolling bite; (3): thermo-mechanical stresses under rolls [4]

Internal stresses

A more detailed description of the internal stresses will be done in section 2.3. During the hot rolling process, mainly compressive growth and thermal stresses are present. The growth stresses are generated during the oxidation [6] from the furnace to the run-out table, as long as the temperature of the slab is high. Thermal stresses are generated during the cooling due to the coefficient of thermal expansion (CTE) mismatch between the metal and the oxide [6]. CTE is smaller for the oxide, and thus

the retraction of the oxide is smaller. Therefore, the substrate is in tension and the oxide undergoes compressive strain during cooling. The relaxation of thermal stresses is directly impacted by the cooling rate. The growth stresses are mostly relaxed due to the long oxidation process and insignificant in comparison to thermal stresses.

Stresses induced by rolling

The behaviour of oxide has been widely described in the finishing mill. The combination between finite element simulations and experimental work has been done by Krzyzanowski et al. [7]. The mathematical model used for the analysis is composed of macro and micro parts, which allow for simulation of metal/scale flow, heat transfer, cracking of the oxide scale, as well as sliding along the oxide/metal interface and spallation of the scale from the metal surface. In this study, the oxide is composed of fragments of scale which are joined along the metal surface to have a continuum scale layer. In Figure 1.9, a 100 μm oxide is modelled at the entry of the roll for an initial temperature of 800°C. The roll is moving faster than the slab. As the oxide gets closer to the entrance, tensile strain is increasing until the critical value to initiate through thickness crack (Figure 1.9). If $\sigma > \sigma_{\text{crit}}$, oxide cracks and stresses are relaxed. Once the critical stress is reached again, a new crack initiates. This multi-cracking behaviour is detrimental for the surface quality. Moreover, tensile stresses are also high at the exit of the roll bite (the strip is faster than the rolls). Under the rolls, compression and shearing stresses cause the scale failure and the embedding of oxide part.

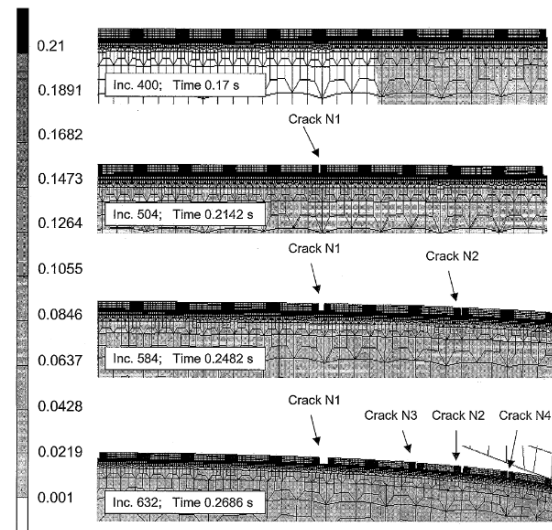


Figure 1.9 : Distribution of strain component for different moment of scale entering the roll gap at 800°C [7]

Oxide undergoes internal and external stresses all along the HSM. These stresses are changing rapidly, from tension to compression. At these speeds and for low temperatures, relaxation by creep is not possible and when stresses exceed a critical value, fracture of oxide occurs [8]. These degradations can be localised within oxide (microcrack or through-crack), or at the interface between oxide and steel inducing delamination or spalling of oxide. We will see later that the descaling process also induces large stresses within oxide, above the critical stress from oxide, to make it crack. The process is extremely rapid and relaxation is not possible. The stresses are thermo-mechanical. From a thermal point of view, descaling consists in a fast cooling of oxide which puts oxide in traction and then in compression [9]. These main cracking mechanisms of oxide will be detailed in the next chapter.

1.4.3 Surface defect during HSM : rolled-in scale defect

High thermo-mechanical stresses are generated in the scale, the oxide is cracking and surface defects are initiated. One of the most important defects is the rolled-in scale defect. Remember that before cold rolling, the steel is 'pickled' in acid to remove the residual scale. The surface quality is thus degraded by a rough metal-oxide interface Figure 1.10.

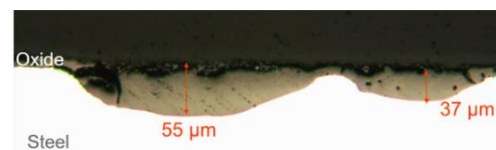


Figure 1.10: Rolled-in scale defect (embedded oxide) (document ArcelorMittal)

The occurrence of rolled-in scale during rolling is described by Picqué [4]. The author models the scale during hot rolling process. Figure 1.11 corresponds to the 2nd stand of the finishing mill. The initial thickness of oxide is 20 µm and the reduction is 35%. In this case, the temperature of the slab is 900°C. Transverse cracks initiate in a quasi-periodic manner. In this model, the mesh is modified to open the crack where the critical stress is reached, then cracks propagate to the interface. This study confirms the presence of the crack evoked by Krzyzanowski et al. for thicker oxide (100 µm) [7]. In the vicinity of the crack, the stresses are relaxed, until the critical stress is reached again to form a new crack. In the bite, cracks widely open and fresh metal is micro-extruded. With a thicker oxide, larger free spaces are present between oxide fragments, and the metal is more easily extruded. The temperature of the hot extruded metal is higher than the temperature of the oxide, which also damages the rolls.

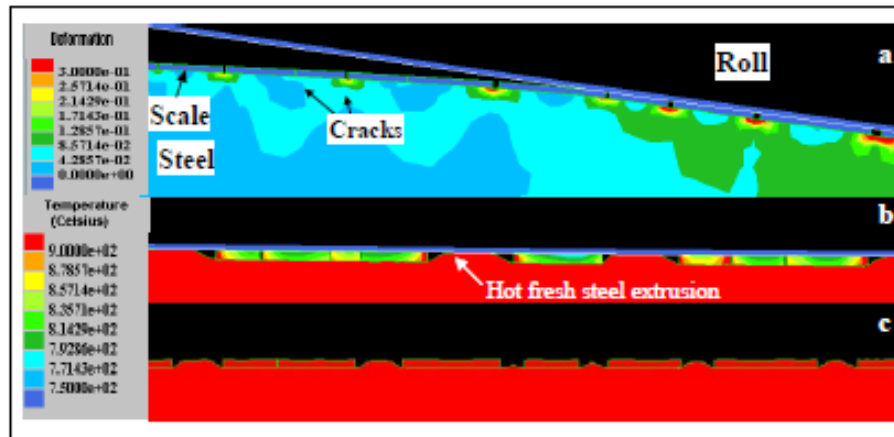


Figure 1.11: Fracture of the oxide before the roll bite for an initial temperature of 900°C and a reduction of 35% [4]

The severity of this defect depends on lots of parameters, temperature, thickness of oxide, oxide properties and rolling parameters. Indeed, when rolls are degraded, printing defects are observed, and the steel-oxide interface is irregular. This roll degradation increases friction and thus leads to higher stresses in the oxide scale, initiating cracks at the entry of the roll gap. This kind of defect can be reduced by changing the rolls regularly. The presence of heterogeneity of oxide thickness can be also detrimental for the surface quality. It can be due to bad descaling efficiency or irregular growth of oxide (due to brutal temperature change). All along the finishing mill, the source of cracking is multiple, they are summarised in the Table 1-1.

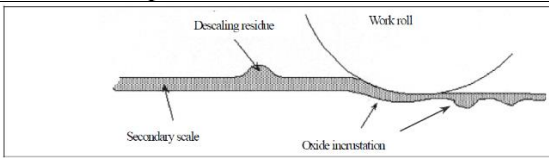
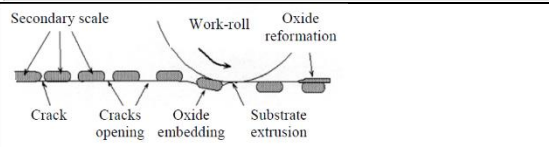
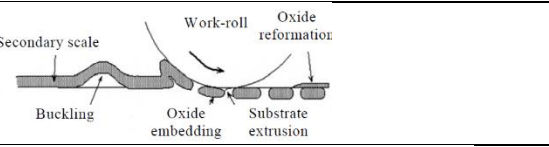
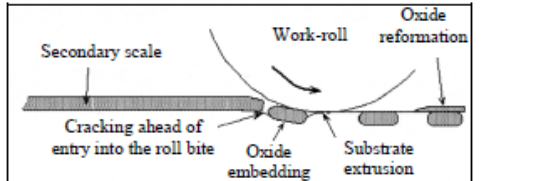
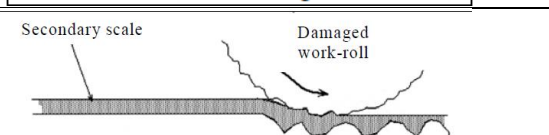
The main sources of defects appear randomly and are difficult to predict. However, some critical conditions are decreasing the probability to observe defects (Figure 1.12): the idea is to reduce the thickness of oxide and the stresses in the scale.

- Picqué highlights that thickness is critical for the formation of defects [4], it has to be below a critical thickness (20 µm) at the entry of the finishing mill.

- The temperature is also a key parameter to control the surface quality. On the one hand, higher temperature causes lower stresses at the entry of the roll gap, and ductility of oxide. On the other hand, higher strip temperature means more roll heating, as well as a thicker oxide scale, which may generate more severe rolled-in scale defects.

- An optimal control of the rolling parameters also reduces the occurrence of defects. For example, reducing the friction coefficient by adapting the roll grade (notably High Speed Steel) and increasing the efficiency of lubrication is another option to improve surface quality. Both of them improve the work roll wear and fatigue during the rolling of electrical steel [10].

Table 1-1: Summary of the cause and mechanism of rolled-in scale defect in HSM – [4]

Cause	Mechanism	Schematic representation of the defect
Scale residue due to bad descaling efficiency	Embedding of descaling residues	
Compressive internal stresses (adherent oxide → wedging)	Embedding to the cracking of oxide	
Compressive internal stresses (poor adherent oxide → buckling)	Embedding due to the buckling before roll bite	
Rolling conditions	Embedding to the cracking at the entry of the roll bite	
Roll degradation	Printing effect due to degraded rolls.	

To reduce oxide thickness, descaling boxes are added in the production line. By optimising this process, the surface quality can be significantly improved.

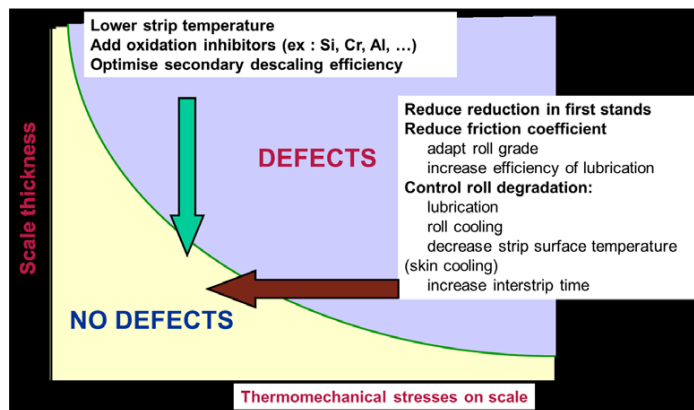


Figure 1.12: Two types of actuators can help decrease rolled-in-scale defects: actuators decreasing scale thickness and actuators decreasing the thermo-mechanical stress applied on the scale layer during rolling [5]

The oxidation in the HSM is detrimental for the surface quality. To limit the growth of oxide, descaling boxes are introduced in the production line. The descaling is described in the next part.

1.5 Descaling to limit surface defect

1.5.1 Description of the process

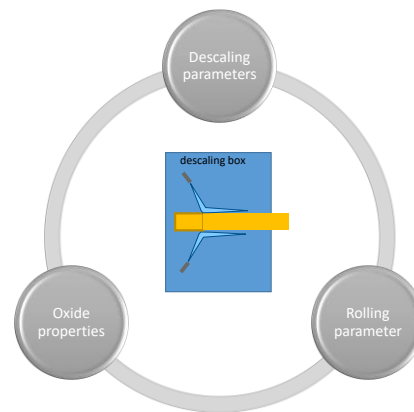
Descaling involves spraying the surface with cold water at high pressure. Descaling boxes are added before the roughing mill and the finishing mill to reduce oxide thickness (Figure 1.3 (a)). High pressure water descaling operations have an influence on surface temperature, and on the nature of the oxide scale prior to rolling. The idea is to control the surface quality without penalizing productivity. For new grades and new rolling parameters, it is difficult to optimise the descaling. One of the reasons is that the behaviour of scale during descaling is poorly known. The investigation of descaling is fraught with difficulties even under laboratory conditions. Understanding the scale removal is thus important for optimization of industrial descaling conditions.

The descaling box is not just about nozzles spraying water at high pressure. It also includes: pinch rollers to keep the distance between the nozzles and the surface of the metal, and a system for recovering the sprayed water to prevent parasitic cooling before descaling.

To simplify the understanding of the complex descaling process, it can be seen as a combination of 3 different main factors (Figure 1.13 (b)). To have an efficient descaling, it is necessary to understand the influence of these parameters. Working only on one parameter without looking at the others will not be effective, as they strongly interact with each other.



(a)



(b)

Figure 1.13 : (a) High pressure water jet in the descaling pilot at the research centre (b) Main characteristics of secondary descaling of Hot Strip Mill

(i) The descaling parameters represent the nozzle geometry and the set-up of descaling (flow rate, stand-off distance, pressure of the jet). A descaling ramp is defined by the main parameters illustrated below (Figure 1.14) where H is the height (distance between nozzle and product), L the width of the jet (in the rolling direction), R the overlap, E the nozzle spacing, α the jet opening angle, β the lead angle of inclination of the jet and δ the angle of rotation.

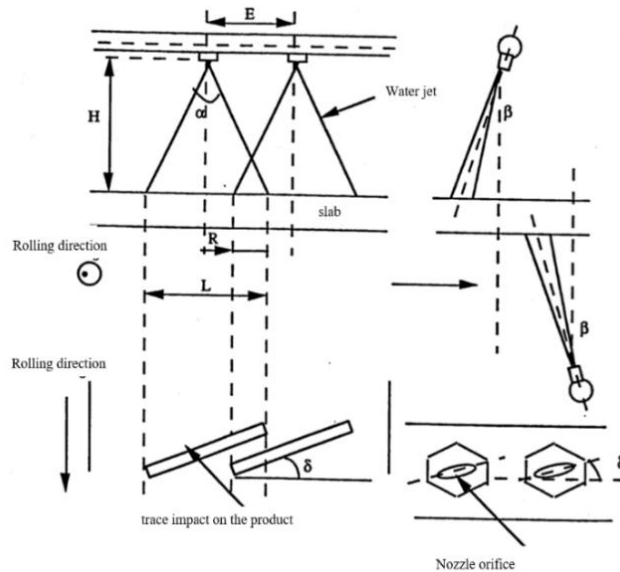


Figure 1.14: Schematic representation of a descaling jet [11]

(ii) The oxide properties are related to intrinsic behaviour of the scale. It refers to the adhesion and the fracture of oxide at high temperature. In this approach, the thickness, uniformity of the scale, the phase (Fe_xO_y), the porosity, mechanical and thermal behaviour, the interface between steel and oxide and the alloying elements are crucial.

(iii) The rolling parameters are the temperature of oxide, the speed of slabs. It represents all the history of the scale before the descaling. For the primary scale, it is directly linked to the re-heating furnace. For the secondary scale, it considers all the deformation induced during the roughing mill. The main parameters are the temperature, the speed of slabs (and the time under the spray), and the transfer time.

1.5.2 Descaling is an important source of costs

The consumption of energy in descaling represents 15% of the total energy consumption of the HSM (more than 3 millions euros per year for a HSM) [12]. It represents 1.05 Euro per tonne of hot rolled coil RC spent by the operators of a hot strip mill on energy for descaling alone. The cost estimation considers cost of energy, water, variable line speed, pump type and power and descaling time. It also accounts for wear rate of nozzle, pipes, valves, high pressure tank [13]. Optimising the descaling is thus an essential step to reduce costs. For each grade, the correct set of parameters is chosen to minimise the energy and ensure a limitation of surface defects (via a sufficiently low oxide thickness).

In the last decades, the tendency for the nozzle producer is to maximise impact pressure and at the same time reduce the flow rate from each nozzle as much as possible. The energy consumption is directly linked to the pressure and the flow of water.

1.5.3 Difference between primary and secondary descaling

As mentioned before, the secondary scale and the primary scale are different. The primary scale is thick and porous (due to the CO_2 and humidity in furnace atmosphere), the interface with steel is also composed of a mixed zone where FeO can react with oxides of alloying elements. The secondary scale has been deformed in the roll bites and is thinner ($<100 \mu\text{m}$) and denser. Thus, the behaviour during descaling for the primary and secondary scale is different. After the primary descaling, due to the porous scale, there is a thin and porous layer remaining depending on the grades [14]. The oxide is ductile at these temperatures, it will co-deform in the roughing mill. More than the thickness, a homogeneous scale is essential at the entry of the roughing mill.

The objective of the secondary descaling is not to remove all the scale from the strip but to limit thickness at the entry of the finishing mill. Before descaling, thickness is about $60\text{--}80 \mu\text{m}$ and it is to be reduced to a thin oxide scale (in general, the critical thickness is about $20 \mu\text{m}$) after the secondary

descaling. Industrially, just after the descaling, the re-oxidation is still present because surface temperature is high. The critical thickness at the entry of the finishing mill is linked to the efficiency of the descaling, but also the re-oxidation down to the entry of the finishing mill (3-4 μm per second at 1000°C). The highest thickness is at the entry of the finishing mill (see Figure 1.7), it has to be lower than 20/25 μm to avoid surface defects. As a reminder, the oxide has also a role for the lubrication and limits the wear of rolls.

The behaviour of each grade is different depending on the descaling. For example, the high-alloyed grades, particularly those likely to form liquid phases (silicon, copper grades, etc.) are generally a source of difficulty in primary descaling, but not for the secondary descaling. It is complicated to apply conclusions on primary scale to the secondary.

1.5.4 Descaling as a thermo-mechanical process

There are still two main points of view: the one that explains the descaling of the oxide by the stopping pressure of the water jet or the impact force of the water drops, a pure mechanical shock effect; and the one, which we follow, that leans towards a thermo-mechanical effect: the very sudden and very superficial cooling (the passage under the water jet, at a speed $\approx 2\text{m/s}$, lasts less than 10^{-2}s) generates thermoelastic stresses that break and spall the oxide

1.5.4.1 Mechanical impact of the jet

The mechanical impact of the high pressure water jet can be evaluated by observing the pressure distribution of jet, it is measured by spraying water on a moving plate equipped with a pressure sensor [15]. The results consist in the distribution of the impact force measured as a function of the width of the jet. The pressure in the Figure 1.15 is obtained for a spray height of 150 mm, feeding pressure 20 MPa (200 bars) and flow rate of 120 L/min. This nozzle produces a narrow footprint approximately 6 mm wide and 70 mm long, and a maximum pressure of 2,7 N/mm² – (MPa).

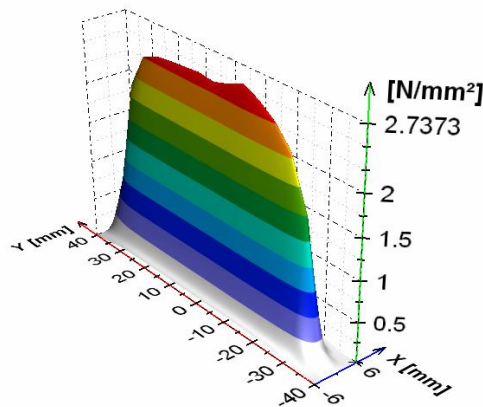


Figure 1.15: Example of impact pressure distribution for a spray height of 150 mm, feeding pressure 20MPa and flow-rate of 2L/s [15]

The erosion of Al plates is also representative of the degradation induced by the water jets [16]. This technique consists in spraying a High-Pressure Water Jet onto a plate of soft material for a set amount of time, and weighing the plate before and after to determine the amount of material removed. In the context of the HSM, this erosion test is used to control the homogeneity of water jets. In the Figure 1.16, the influence of the offset angle is highlighted.

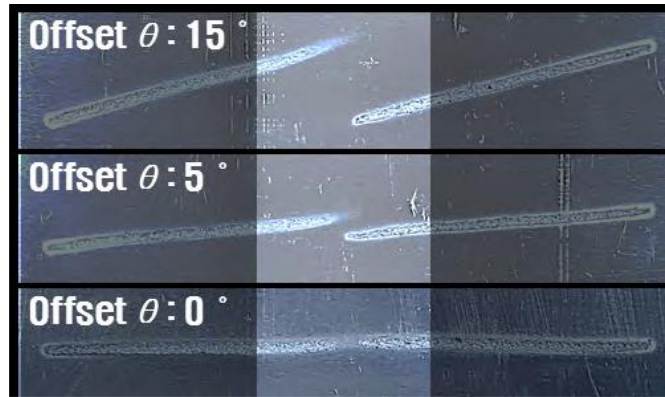


Figure 1.16 : Overlap difference by offset angle during erosion test on Al plate [16]

The mechanical aspect is the main aspect studied by other European research centres. We are not opposed to the conclusion that nozzle performance improves descaling, but this conclusion masks other phenomena that we want to study in this work.

1.5.4.2 Thermal impact of the jet

All the data concerning the thermal history of steel and oxide has been the subject of numerous studies during the descaling and rolling process. As an example, Choi and Choi estimate the influence of the impact pressure on the heat transfer coefficients during the descaling [17]. These coefficients are obtained from the experimental tests and calculated by inverse numerical analysis. As the impact pressure of jet increases, the coefficient increases linearly, and thus the scale is cooled more. According to the author, the value is up to 420 000 W/m²°C for a 8 bar impact pressure (the initial spray pressure is varying from 160 to 300 bar and spray height from 100 to 180 mm height) (Figure 1.17). Other authors have made a similar study [18] by measuring the temperature of a plate below descaling nozzles. The drop of temperature is measured at 1 mm of depth. Using an inverse analysis, the heat transfer coefficient (HTC) is calculated for pressure of water from 50 bar to 450 bar and spray height of 150 mm, it shows that the HTC is varying respectively from 3000 to 5000 W/m²°C, which is much lower than the results of Choi and Choi . The difference is probably due to the initial temperature of the plate (more than 1050°C for Choi and Choi and 880°C for Horský et al.), and the inverse method to calculate the HTC from the measured temperatures is specific to each author.

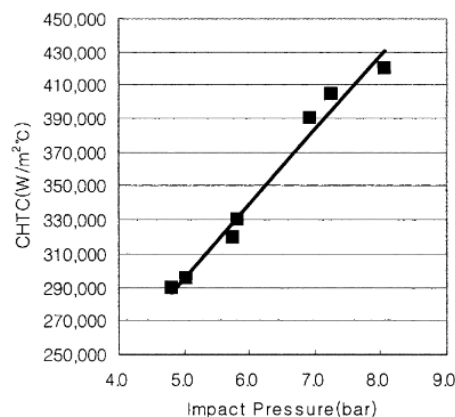


Figure 1.17 : Evolution of the heat transfer coefficient with the descaling impact pressure [17]

After the description of the process, the experimental study of the descaling is done. The idea is to determine which parameters influence descaling.

1.6 Experimental study of descaling

1.6.1 Influence of descaling parameters

Some descaling experiments have been made on steel plates with different pressures of water by Matsuno [19]. Here, the pressure was much lower (1, 4 and 15 bars) than in industrial descaling (100-250 kg/cm²). After oxidation at high temperature for various periods from 5 sec to 35 s, a jet of water was sent to the specimen and the extent of descaling was assessed visually. The plate temperature was between 800°C (secondary descaling) and 1200°C (primary descaling). It shows that the removal of scale layer is dependent on the water pressure, and it tends to be better as the pressure decreases (Figure 1.18). Above 900°C, oxide is easily removed with low pressure jet. It is not the case for larger pressures. The authors explain that with a lower pressure, the size of the water drops is larger, the cooling induced by the jet is more important. Of course, the conditions, in particular the pressure conditions, are far from industrial cases. Nevertheless, they show that descaling is a thermal process with a thermal shock and they conclude that a low-pressure jet can be more efficient than high pressure. Moreover, for a given jet pressure, the oxide thickness and the temperature influence the descaling. These parameters will be discussed later.

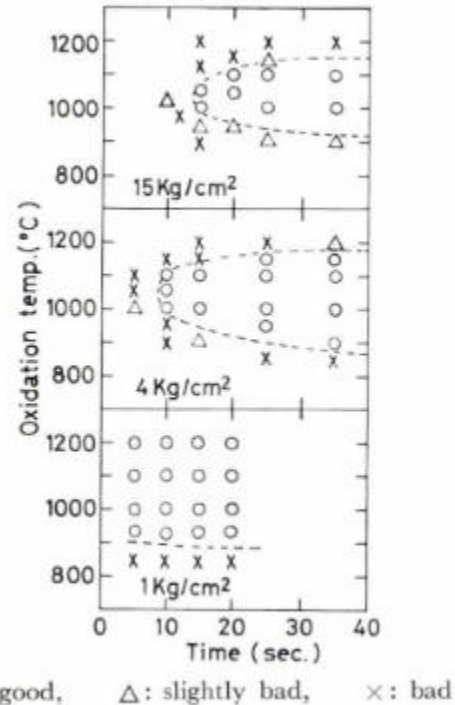


Figure 1.18 : Results of hydraulic removal of scale by water jet with water pressure of 15, 4 and 1 bar (1 Kg/cm² = 1 bar) [19]

The influence of nozzle parameters is discussed by Farrugia et al. [20]. A good descability requires a good overlap defined at 8 to 15% of spray width. This overlap may compensate for any pressure drop near the edge of a jet. It has to be controlled to avoid a washout regime or spray interference, which disturbs descaling and causes overcooling. The spray width has to be regular and the thickness small. The spray angle is ideally equal to 30° and finally the standoff distance has to be small to ensure perfect laminar flow and maximum impact. As standoff distance increases, the spray tends to break from a continuous jet. However, a good control of overlap/wash needs to be implemented.

According to Robb [21], the lead angle is found to have a significant effect on impact. Lead angle splits the overall impact into two forces, a horizontal and a vertical component. The vertical force is present to break the oxide, and the horizontal to pick up and remove oxide. By increasing the lead angle, the impact force is reduced (10% of loss for a variation of angle from 0° to 30°). Indeed, the impingement area increases with increasing lead angle and the specific impact pressure decreases. However, a minimum lead angle is needed to wash away the oxide during the descaling.

1.6.2 Rolling parameter

A key to control the secondary descaling is the temperature of oxide. We have seen previously that surface scale temperature evolves in a cyclic manner in HSM (Figure 1.7). Indeed, descaling consists in a fast cooling of the surface. Some thermal calculations show that the temperature drops

sharply within milliseconds. Obviously, the descaling parameters have an influence on the cooling effect. But how to do this is unclear. As described above by Matsuno [19], this thermal effect is enhanced by decreasing the pressure of the jet. In an opposite way, Choi and Choi estimate the influence of the impact pressure on the heat transfer coefficient during the descaling [17] (Figure 1.17) : by increasing the impact pressure, the heat transfer coefficient is also increasing.

The influence of steel surface temperature is studied by Mickler et al., [11]. They show the post-descaling remaining thicknesses as a function of the temperature after descaling, for two steel grades. The same pressure and flow are used. Three main areas of descability emerge for low carbon grade:

- below 930°C, the descaling is efficient (residual thickness always less than 20 μm), and the lower the temperature, the better the descaling,
- between 930°C and 975°C: transitional area where results are random (the residual thickness can be less or more than 20 μm)
- above 975°C: better descaling is achieved (residual thickness less than 20 μm). However, the residual thicknesses are higher than those corresponding to low temperatures, and at these temperatures level, re-oxidation will play a determining role.

In conclusion, according to Mickler et al. [11], decreasing temperature globally increases the efficiency of the secondary descaling.

The speed of slabs has also an influence: reducing the speed tends to increase the efficiency of descaling. It has been proved by Horský et al. [18]. Here, the lowest remaining thickness is obtained with a low speed, 1m/s (for a constant impact pressure) (Figure 1.19). When product speed is decreased, the time below the jet is increased, the surface is more cooled, and thus descaling efficiency is improved. In a similar way, this study also shows that the impact pressure of the jet is also important, here by increasing it to 10 MPa, the remaining thickness is also reduced (for a constant velocity motion).

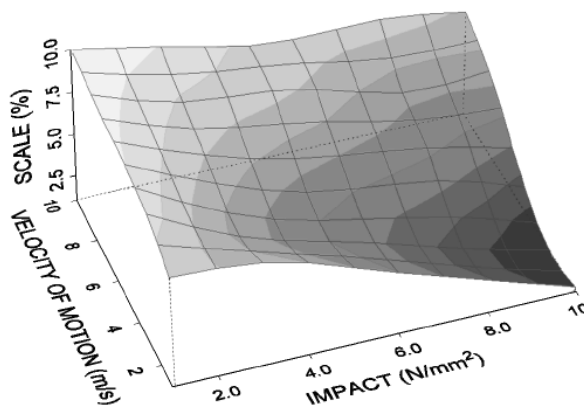


Figure 1.19: 3D-diagram of the dependence of the remaining scale on the velocity of steel and on impact pressure [18]. Here the percentage of the scale represents the remaining scale thickness compared to thickness before descaling

1.6.3 Oxide properties

The efficiency of the descaling is related to the intrinsic behaviour of the oxide and its properties. The mechanical properties of oxide are dependent on the temperature (hardness, tensile strength...). For example, Wüstite undergoes a ductile-brittle transition above 700°C, thus the temperature modifies the efficiency of the descaling. These properties will be described precisely in the next chapter. The influence of thickness, alloying elements and the oxide scale morphology are discussed in this part.

To evaluate the behaviour of oxide, the reproduction of water jets in laboratory on oxidized sample allows understanding localisation of fracture. The experimental study of descaling makes clear the degradation of scale. Basabe and Szpunar [14] studies the primary descaling using high pressure water jets (11.4 MPa and flow rate 6.8L/min). Low carbon steel samples are oxidized over the temperature range 1050-1250°C with a $\text{O}_2\text{-CO}_2\text{-H}_2\text{O-N}_2$ atmosphere. Here, the idea is to reproduce the

atmosphere of re-heating furnaces. Two mechanisms of degradation are identified depending on the scale morphology (Figure 1.20). For the first mode, the degradation is localised at the interface between the dense scale and the inner porous layer. The residual thickness is directly linked to the proportion of porous scale. For the mode II, the horizontal undercutting occurs at the first plane of large pores relative to the scale/steel interface. This morphology depends on the phase composition, the atmosphere, the time and temperature of oxidation. Indeed, the pores are created during the growth of oxide. The authors suggest that reducing the concentration of free oxygen in the tunnel furnace atmosphere is important for increasing primary scale removability.

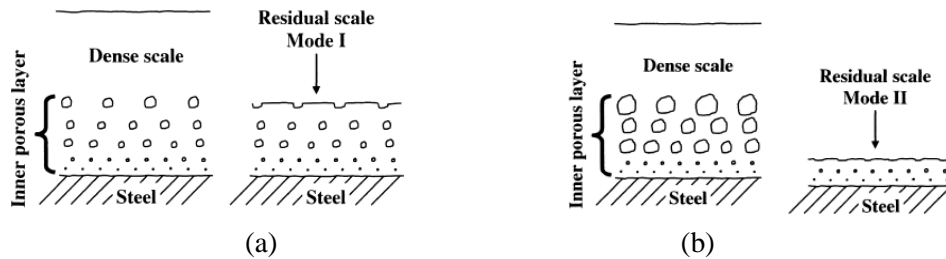


Figure 1.20 :Schematic diagram of a residual scale after primary descaling (a) mode I : undercutting at the boundary between the inner porous layer and dense scale (b) mode II [14]

Steel grade is known to have an effect on descaling efficiency and sensitivity to rolled-in scale. The effect of the grade on the scale adherence might be linked to the nature of oxides formed but this effect is not clearly understood today. The effect of the grade can be observed on the remaining thickness after descaling, which is not the same for all grades: it is lowest for DP grades, a bit higher for low carbon grades and highest for HSLA grade. The additional elements have an important impact on the behaviour of oxide and its adherence. Indeed, the effect of alloying elements has been widely described for the primary descaling, specifically for Ni and Si [22,23] (Figure 1.21) :

- For Si-rich alloy, the formation of a liquid phase (fayalite Fe_2SiO_4) above $1177^\circ C$ is detrimental because it penetrates at the interface with steel and acts as a mechanical anchor. When the temperature is decreasing, FeO/Fe_2SiO_4 solidifies and shrinks, forming pores at the interface.
- Ni is not oxidized and remains in the metallic phase with an enrichment at the interface. It becomes surrounded by iron oxides. An entangled layer of oxide and metal is formed. This interface is not removed by hydraulic descaler.
- The combination of Ni+Si is detrimental because it creates and combines entangled layers with oxide pegs. According to these authors, in order to maximise the descaling, this entanglement has to be minimised. Thus, controlling the temperature below $1300^\circ C$ is required to limit these interactions.

With only Si	With only Ni	With Ni and Si
Oxidation at $T > 1177^\circ C$		
Cooling down to room temperature		

Figure 1.21: Mechanism of occurrence of entanglement due to nickel and silicon by high temperature oxidation [22]

Here, the analysis and the quantification of the interface is a method to interpret the descability of oxide.

Kizu et al. [24] also clarify the effect of alloying elements by observing the blistering of oxide. In this study, specimens are oxidized at high temperature (900°C to 1150°C) and blistering is observed. Scale blistering is the balance between compressive stresses in growing oxide and adhesive forces between steel and oxide. For a fixed oxidation time, blistering tends to decrease for oxidation at $T > 800^\circ\text{C}$, when the percentage of Mn is higher than 0.2. At 800°C, for %wt C > 0.02, the same tendency is observed. Thus, high C and Mn content tends to promote blistering, and decrease adhesion of oxide.

Osei et al. [25] show that Cu at different levels significantly modifies scale structure, particularly the internal scale layers (Cu is varied from 0.2 to 0.8 wt%). This study is contextualised in the case where recovered scrap is used in Electric Arc Furnace, there are degrees of impurities that can be quite important. Indeed, the scale removability is impacted by the amount of Cu. Steel samples (with 0.3 wt% of Si and Mn) were first oxidized during 90 minutes at 1200°C, then descaled on a pilot descaler. The low Cu steel exhibits the lowest efficiency (70% of the surface sample is judged correctly descaled, in other cases, the complex subsurface is not totally removed) (Figure 1.22).

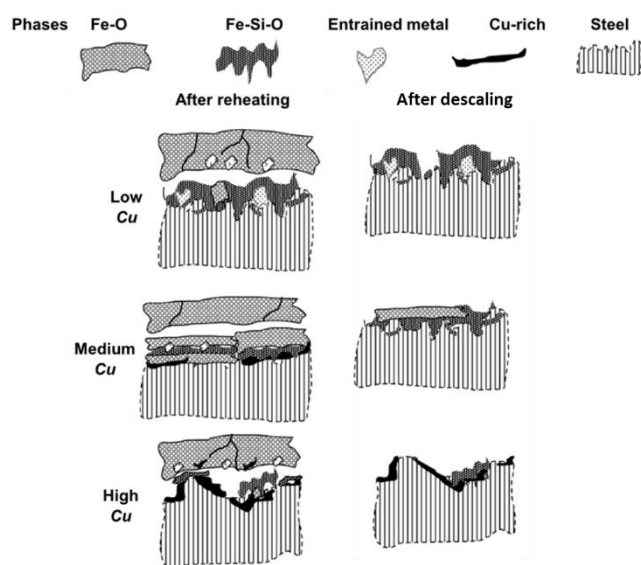


Figure 1.22: Schematic representation of scale structure of different Cu additions before and after primary descaling (impact pressure 1 MPa)

The residual scale is composed of Fe entrainment into a complex subsurface that is strongly adherent to the metal substrate. The medium and high Cu steels exhibit improved descaling efficiency (above 90%) with less retained scale due to fewer complexities. Indeed, the formation of a Cu-rich liquid phase above 1085°C, tends to limit the formation of complex interface. For the primary descaling, this phase is still liquid and thus the separation of oxide is easy. For these authors, increasing Cu additions (in a small range up to 0,8 wt%) decreased the complexity of the subsurface scale formed in low carbon steels, which is critical for efficient descaling.

This paragraph shows the complexity of the descaling process. It depends on many interacting parameters. A majority of the tests are focused on the study of primary descaling. The observation of the fracture mechanism during the descaling is not possible, and the oxide is observed post-mortem. To go further, the idea is to use models to describe descaling.

1.7 Numerical study of the descaling

1.7.1 Finite element simulation (FEM) of thermo-elastic fracture

This paragraph details work carried out in 2011 which summarises the state of knowledge at ArcelorMittal and Cemef at the start of this thesis.

The finite element method has been used in order to assess the contribution of the mechanical and thermal effects during descaling. The descaling process is described by Zhang et al. in a 2D FEM model [9]. A piece of an oxidized metal (80 μm of oxide on 2 mm of metal) is used and moved at velocity $1 \text{ m}\cdot\text{s}^{-1}$. At the surface, spatial distributions of hydraulic pressure of water and Heat Transfer Coefficient (HTC) are introduced in the model as boundary conditions. Virtual sensors are implemented through metal and oxide to observe evolution of temperature and stress (Figure 1.23 a)). This study emphasises the fact that high thermal tensile stresses generated overcome the stresses directly created by the impact pressure. This purely numerical model supports the hypothesis that descaling is primarily a thermal process.

The oxide surface is first cooled down by several hundreds of degrees while the underlying steel remains at higher temperature (Figure 1.23 (b)). The oxide tends to contract but is prevented to do so by the hot metal. Thus, the scale is in tension (150 MPa), and whenever a critical stress is reached at a surface point, a crack is created and instantaneously propagated vertically through the oxide (Figure 1.23(c) and (d)). In the oxide bulk, a gradient of stress in the direction normal to the strip is present and tends to bend it, opening interfacial cracks as soon as transverse cracking occurs. Cohesive Zone Model (CZM) is used at the interface to take care of oxide peeling off: numerically speaking, delamination is possible, but only at the interface (Figure 1.23(e)), contrary to experimental findings. Then, the oxide is re-heated by the metal and oxide stress turns compressive. If the oxide does not flake off, cracks are closed by the compressive stresses but elimination is then possible by buckling (not modelled).

This work has allowed studying numerically the impact of the process parameters on the descaling efficiency (influence of heat flux, scale thickness, strip speed) and particularly the ability of the scale to fracture.

This thermal effect in descaling is confirmed by Horsky et al. [15] using a 100 μm thick scale at 1100°C . Here the thermal contribution and the mechanical aspects are considered (water pressure jets also measured). The Heat Transfer Coefficient (HTC) has been previously calculated by an inverse method using experimentally measured temperature evolutions. The tensile stress in the scale layer is calculated. The main conclusion of the study is that the contribution of the impact is insignificant in comparison to the thermally induced one, in case of fast cooling.

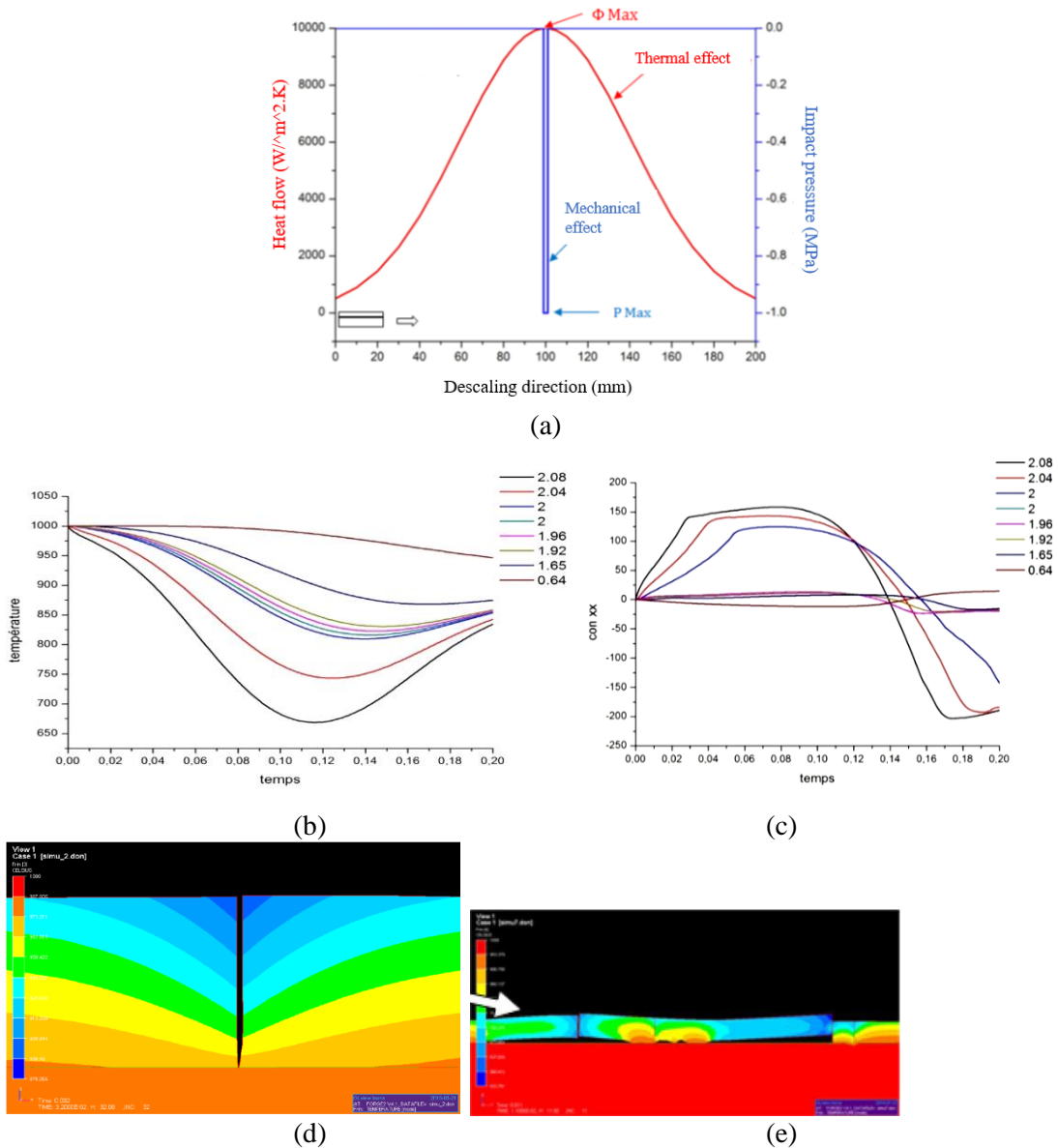


Figure 1.23: (a) description of the thermal and mechanical boundary conditions during descaling (b) Temperature and (c) stress fields in the oxide layer and the underlying metal (altitude 2.08 mm is the surface of oxide and 2.0 mm is the interface) (d) Through-thickness crack in oxide due to the fast cooling of oxide (e) interfacial cracks at the interface (cohesive elements) due to the gradient of stress within oxide [9]

This study and the corresponding assumptions are made on 2011 knowledge. Here, only the transverse cracking is considered, there is no modelling of the development of cracks (direct propagation through the entire thickness of the scale), there is a poor consideration of delamination, and the fracture properties are chosen arbitrarily.

1.7.2 Analytical model of oxide fracture

Another way to understand the descaling is to use analytical models, as described by Farrugia et al. [20]. Here, the calculation is directly made by using the impact pressure (IP) of the jet. The compressive stress induces spallation of the oxide. To simplify, the pressure exerted by the jet is considered uniform over its entire area of impact. The following criterion for fracture of oxide can be written:

$$\frac{IP}{E} \cos \beta > \varepsilon_c \quad (1-1)$$

ε_c being the critical strain for fracturing, E the Young's modulus of oxide scale and β the lead angle. The critical strain is calculated as follows from the elastic theory of Robertson and Manning [26]:

$$\varepsilon_c < \left(\frac{2.8\gamma}{tE} \right)^{0.5} \quad (1-2)$$

with γ the surface energy for a smooth surface, t the thickness of scale. The interfacial roughness can act to increase the adhesion of the oxide. It is taken into account in this model.

In Figure 1.24, the effect of several parameters is described for the impact pressure and the descaling energy theory. For both of them, the flow rate has a positive effect (blue colour). The red colour means a detrimental effect.

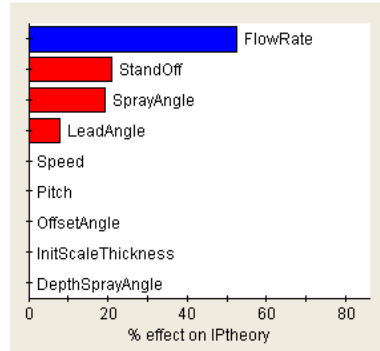


Figure 1.24 : Pareto effects of different parameters for the Impact Pressure Theory (blue = positive effect, red = negative correlation) [20]

This model is enriched by considering the thermal effect ; the thermal elastic strain is generated by the differential thermal contraction of both oxide and steel. The results show that thermal stresses generated due to thermal strain and temperature drop is between 12 to 236 MPa, the same order of magnitude as in the study of Zhang et al. [9]. In the case of fracture, the tensile stresses in the scale will introduce a shear stress which can be estimated. According to these authors, for primary scale, this thermal effect will only affect maximum 20% of the scale thickness and therefore it cannot be the only contributor for descalability. Nevertheless, this model is based on a decoupled effect of thermal transfer and mechanic which in real practice does not seem realistic.

1.8 Summary of mechanisms proposed for high pressure descaling

The mechanism of descaling is complex and is still not fully understood. The main proposed mechanisms are detailed in Figure 1.25. The most crucial factors that affect the process can be divided into mechanical effects and thermal effects.

The mechanical effect considers the jet as a “chisel effect” or “water hammer”. The nozzles produce a water jet with high impact force, which crushes the scale (Figure 1.25 (a)). In this theory, according to Raudensky et al. [27], the jet consists of aggregates of droplets projected at high speed. The level of the impact pressure peaks of several hundred MPa and a duration of a few milliseconds per peak, causing high pulses in the impact area. This phenomenon is confirmed by analytical models, finite element simulations and experiments. Other interpretations of the descaling mechanisms were, on the contrary, based on a pressure of a few MPa [9,15].

Once the oxide is fractured, there is a mechanical effect of the jet (due to the lead angle). The force of the jet shears the metal/scale interface with hundreds of MPa, causing detachment (Figure 1.25 (c)). The oxide is peeled off and washed away by water flow. But it needs a clean surface to initiate the phenomena. Here, a sufficiently high pressure is needed to flush out debris and prevent them from settling on the surface

For Zhang et al. [9], the fragmentation and flaking of the oxide is possible by the thermo-elastic stresses built up by fast superficial cooling. Indeed, there is a difference of several hundred degrees between the water jets and the surface of slabs. The oxide is therefore cooled down by several hundred degrees and undergoes high tensile stresses, leading it to fracture. Due to the thermal difference within the oxide, a gradient of stress is present, the oxide bends and interfacial cracks open (Figure 1.25 (b)). In a second time, the oxide is re-heated by the metal, and thus compressive stress appears in oxide. In this case, if delamination has not taken place previously, these compressive stresses may induce buckling. Note that Zhang et al. conducted a purely numerical study with hypothetical physical parameters, but this general scheme seems to be supported by Matsuno in the case of cooling by spraying Argon cold gas [19], without any mechanical impact: blistering is present instantly due to thermal stresses, so that stresses generated at the time of cooling are sufficient to explain descaling. After blistering, oxide is broken readily by water jets and the scale chips produced are subsequently washed away by the flow of water.

According to some authors [27], water penetrates into the cracks and its phase transition from liquid to vapour occurs due to the high temperature. It generates a volumetric expansion and a high pressure that opens the crack. The oxide is broken through both a tensile and a shearing component (Figure 1.25 (d)). This mechanism is dependent on the fact that an initial fracture has to be present at the surface of oxide. This initial fracture can be due to the above-mentioned thermal and mechanical concepts. In the case of an initial fracture that has stopped before reaching the interface, this mechanism can explain why the scale is not removed continuously, not starting from the surface, but in layers, and its initialisation is at a depth within the scale layer. This process is difficult to study experimentally since the cracking of scale occurs within milliseconds and the duration of high-pressure peaks due to water hammer effect lasts microseconds.

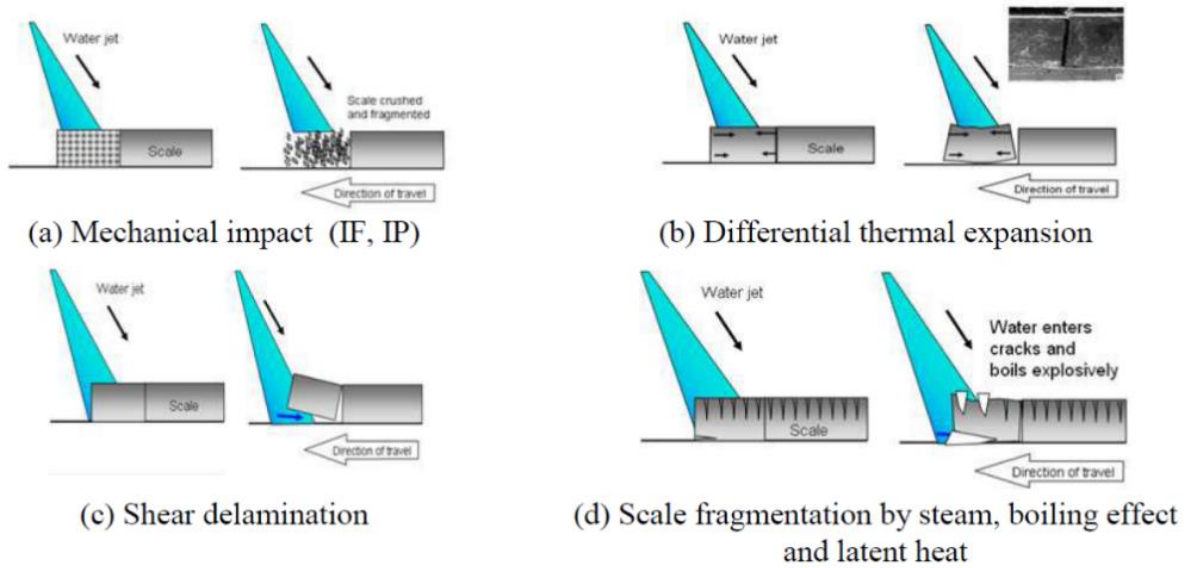


Figure 1.25 : some of the main mechanisms proposed for High Pressure Water Jet descaling: (a) mechanical impact of the jet by the hammer effect; (b) differential thermal expansion due to the gradient of cooling in oxide; (c) water shear delamination; (d) scale fragmentation by steam and boiling effect [20]

In reality, global descaling may be a combination of all these mechanisms. It depends on the impact pressure, the quantity of applied water per unit area and the total stress produced by the cooling action of water jets. First, the scale undergoes stresses (tensile or compressive), the values of which have to reach a threshold for fracture to occur. Increasing the cooling efficiency is a clue to improve the secondary descaling: decreasing the temperature of oxide brings it into its brittle range : the optimisation of descaling set-up (nozzle configuration, supply pressure) has to maximise the cooling. Secondly, it needs the propagation of an interfacial crack. The oxide fragments are thus detached and flushed away by the water. The interfacial properties (adhesion for exemple) is highly dependent on the roughness of the interface. For the secondary descaling, this roughness is impacted by the flow irregularities of steel, the internal oxide, metallic inclusion and liquid phase formation at high temperature.

In all the models described, it is considered that the whole thickness of oxide is removed. Studies under quasi-industrial conditions show that it is not really the case. Indeed, closer to the surface, the difference in temperature between steel and oxide is higher, and it is all the more likely that the critical fracture stress of the scale is reached. On the contrary, at the interface, the temperature difference with the steel is lower, and thus it is likely that below a certain initial scale thickness, the temperature gradient created at the bottom of the scale is not sufficient to induce the critical stresses. In addition, the gradient in temperature may induce gradients in oxide properties: the surface oxide (Magnetite) is more brittle, the deep oxide (wüstite) more ductile.

The determination of oxide properties as a function of temperature is therefore essential to have a better understanding of the descaling process.

Different descaling mechanisms have been described. To have a better understanding of the descaling, the idea is to reproduce the water jets (similar of HSM) in a laboratory.

1.9 Conclusion

The main conclusion of this chapter is that water jet descaling is a complex process. The idea is to reduce the thickness of oxide to limit surface defects formation in the finishing mill. The oxide is composed of 3 phases and undergoes several sources of stress. The descaling is a combination of thermal and a mechanical contributions. Several mechanisms are described in literature. It is still difficult to conclude to select a single mechanism. The primary and secondary descaling are different, and thus the mechanism may also be different:

- In the first case, the scale is thicker (up to 1-2 mm) and porous. The cooling probably does not impact the whole layer. Thus, the thermo-mechanical impact force coupled to the porous structure of oxide may be the main descaling mechanism.
- The secondary descaling is done at a lower temperature on an already deformed scale. The oxide is thinner and is cooled down throughout its thickness, the thermal effect may become predominant for the secondary descaling. The efficiency is depending on the water jet parameters, the rolling conditions (strip speed and surface temperature) and the properties of oxide. The temperature of the scale is a key parameter to remove efficiently the scale.

Résumé

Ce chapitre démontre la complexité du décalaminage lors du laminage à chaud. L'idée est de réduire l'épaisseur de l'oxyde pour limiter la formation de défauts de surface dans le laminoir de finition. L'oxyde est composé de 3 phases : la Wüstite, la Magnétite et l'Hématite et va subir plusieurs sources de contrainte (contrainte de croissance, contrainte thermique, contrainte liée à la déformation sous les cylindres, contraintes liée au décalaminage). Le décalaminage a deux composantes : thermiques et mécaniques. Plusieurs mécanismes sont décrits dans la littérature pour expliquer le décalaminage. Il est encore difficile de conclure à la sélection d'un mécanisme unique. Le décalaminage primaire et secondaire sont différents, et donc le mécanisme peut également être différent :

- Dans le premier cas, la calamine est plus épaisse (jusqu'à 1-2mm) et poreuse. Le refroidissement n'a probablement pas d'impact sur l'ensemble de la couche. Ainsi, la force d'impact thermomécanique couplée à la structure poreuse de l'oxyde peut être le principal mécanisme de décalaminage.

- Le décalaminage secondaire se fait à une température plus basse sur une couche déjà déformée (contraintes de compression sous le cylindre et contraintes de traction à l'entrée du cylindre). L'oxyde étant plus fin et refroidi sur toute son épaisseur, l'effet thermique peut devenir prédominant pour le décalaminage secondaire. L'effet thermique prépondérant a d'ailleurs été mis en lumière par une simulation aux éléments finis. L'efficacité du décalaminage secondaire dépend des paramètres du jet d'eau, des conditions de laminage (vitesse de la bande et température de surface) et des propriétés de l'oxyde. La température de la calamine est un paramètre clé pour éliminer efficacement la calamine.

Chapter 2: A review of oxide properties

This chapter is focused on a general description of steel oxides from the oxidation mechanism to the oxide properties. First, the hot oxidation of low carbon steel is explained. The effect of alloying elements is described. The internal stresses generated within oxides and the behaviour of oxides are stated. The last part is devoted to the mechanical properties of the oxides through different mechanical tests, to evaluate: elasticity, plasticity, hardness, toughness and adhesion.

2.1 Oxidation of steel

The present section is a description of the hot oxidation of steel, scale morphology and growth mechanisms in the conditions encountered by steels in industrial practice. At high temperature, the external oxidation leads to the formation of a thin scale at the surface of steel. This layer is complex due to the formation of different phases, porosity, gradient of composition... Within the steel, selective (internal) oxidation is also possible by precipitation in the Fe matrix of oxides from alloying elements more oxidizable than Fe (Si, Mn, Cr, Al, ...). This internal oxidation can be localised at the grain boundaries via short-circuit diffusion of oxygen.

2.1.1 Oxidation mechanism

Steel is mainly composed of iron which is a metal having 26 electrons. In the stable state, the external shell contains a single pair of electrons. But iron is a transition metal with three valences in classical oxidizing conditions (Fe^0 , Fe^{2+} , Fe^{3+}). Iron (0) is called metallic, while iron (II) compounds are called ferrous, and iron (III) compounds ferric.

The oxidation process in metals can be defined as the interaction of metal atoms with oxygen, with several determining factors including time, temperature, environment, partial pressure of oxygen and chemical composition. As described in the first chapter, in the presence of oxygen, an oxide scale grows at the surface of slabs all along the HSM. The oxidation is a spontaneous chemical reaction involving an exchange of electrons. The “oxidizer” is receiving electrons from a “reducer”. For the hot oxidation of iron, the oxidizer is mainly oxygen (and sometimes H_2O) and the reducer is the metal (iron) but also other alloying elements. This reaction occurs because the Gibbs free energy is lower for the reaction products than for initial reactants.

At the beginning of the oxidation, iron atomic bonds are not saturated. Surfaces are therefore thermodynamically unstable, and present a high reactivity with external environment. Metal surfaces thus create electrovalence in particular with oxygen and chemical adsorption of the oxygen occurs on the metal (Figure 2.1). Once the surface is saturated, an oxide nucleus appears and grows laterally (Figure 2.1). There is then an enlargement of nuclei, until they cover the metal surface. This first step is very fast (some seconds). It is controlled first by the oxygen flux through the surface boundary layer, and secondly the physico-chemical surface reaction. At high temperature and low alloying content, oxygen diffusion through the boundary layer is the limiting factor. In the HSM, the rate of oxidation is highly dependant on the renewal of oxygen at the surface. The surface reactivity strongly depends on the crystalline orientation of the metal and the presence of alloying elements at the interface.

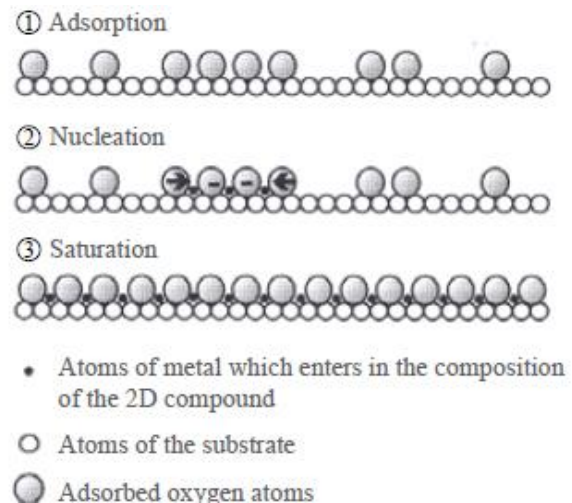


Figure 2.1: Mechanism of saturation at the surface of steel [28]

Once the surface is totally covered, growth continues perpendicularly at the expense of the substrate thickness. A double diffusion phenomenon of anions (oxygen ions) and cations (metallic ions) governs the oxide growth. Both of them migrate through the interstitial sites and gaps, from the metal-oxide interface to the surface for cations and in the opposite way for anions. In the same way, other defects such as dislocations, porosity and cracks can enhance diffusion of ions. Oxides are polycrystalline, and grain boundaries represent preferential diffusion paths.

2.1.2 Oxidation kinetics

A model of oxide scale growth (limited to the formation of FeO) is summarised by Lanteri [29]. The isothermal oxidation of the extra-low carbon steels in N₂+O₂ atmospheres comprises two stages (Figure 2.2 (a)):

1°) The first step is governed by the oxygen diffusion in the gaseous boundary layer, and thus the reaction at the steel surface. The oxidation kinetics has a linear time variation and the oxidation constant depends on the partial oxygen pressure P_{O_2} . The higher the temperature of treatment is, the longer this stage is.

$$X = k_l \cdot t \quad \text{and} \quad k_l = k_{l0} \cdot P_{O_2} \cdot \exp\left(-\frac{Q}{RT}\right) \quad (2-1)$$

with X is the thickness of oxidized metal, k_l and k_{l0} the kinetics constant (cm.s⁻¹) and the pre-exponential constant (cm.s⁻¹) of linear mode, t the time (s), Q the activation energy of the reaction (J.mol⁻¹), R the perfect gas constant (J.mol⁻¹.K⁻¹) and T the temperature (K).

2°) After this initial stage, as soon as the oxide layer becomes sufficiently thick, the kinetics follows a parabolic law as a function of time. The Wagner theory is based on the fact that the kinetics of oxidation depends on the diffusion of ions [30]. A transport process (Fe²⁺ ions diffusion) represents the limiting stage of the oxidation reaction. In most cases, this stage governs the major part of the oxidation time.

$$X^2 = k_p \cdot t \quad \text{and} \quad k_p = k_{p0} \cdot P_{O_2}^{\frac{1}{2}} \cdot \exp\left(-\frac{Q}{RT}\right) \quad (2-2)$$

with k_p and k_{p0} the kinetic constant (cm².s⁻¹) and the pre-exponential constant (cm².s⁻¹) of the parabolic mode. The parameters of these laws are determined by thermo-gravimetry tests. Thus, all previous growth parameters are more often expressed in terms of mass increase per unit surface ($\Delta m/S$), instead of X the thickness of oxidized metal.

The transition from the linear to the parabolic mode is a complex function of the temperature, time, steel grade, gas flow and oxygen partial pressure. In the case of HSM, the oxidation time is short, thus the linear growth stage cannot be neglected. Mathematically, the linear and parabolic curves can be connected with a continuous tangent (Figure 2.2(b)). For a steel at 900°C, the transition is estimated between 3 or 4 seconds. This model is correct when steel and scale are well in contact. Porosity, cracks or accumulation of additional elements at the interface modify this ideal law.

For pure iron, parameters of this law are determined by Paidassi between 700°C to 1200°C (Figure 2.2 (c)). For steel, the oxidation is more complex. Their oxide scales are mainly constituted of iron oxide but their structures change with the presence of additional elements, which can be oxidized too. Indeed, some elements are easier to oxidise than iron (P, Mn, Cr, Si and Al) and form solid solutions (MnO) or mixed oxides (FeAl₂O₄ or Fe₂SiO₄). They are localised at the interface and influence the oxidation, acting as a barrier for the diffusion of Fe ions.

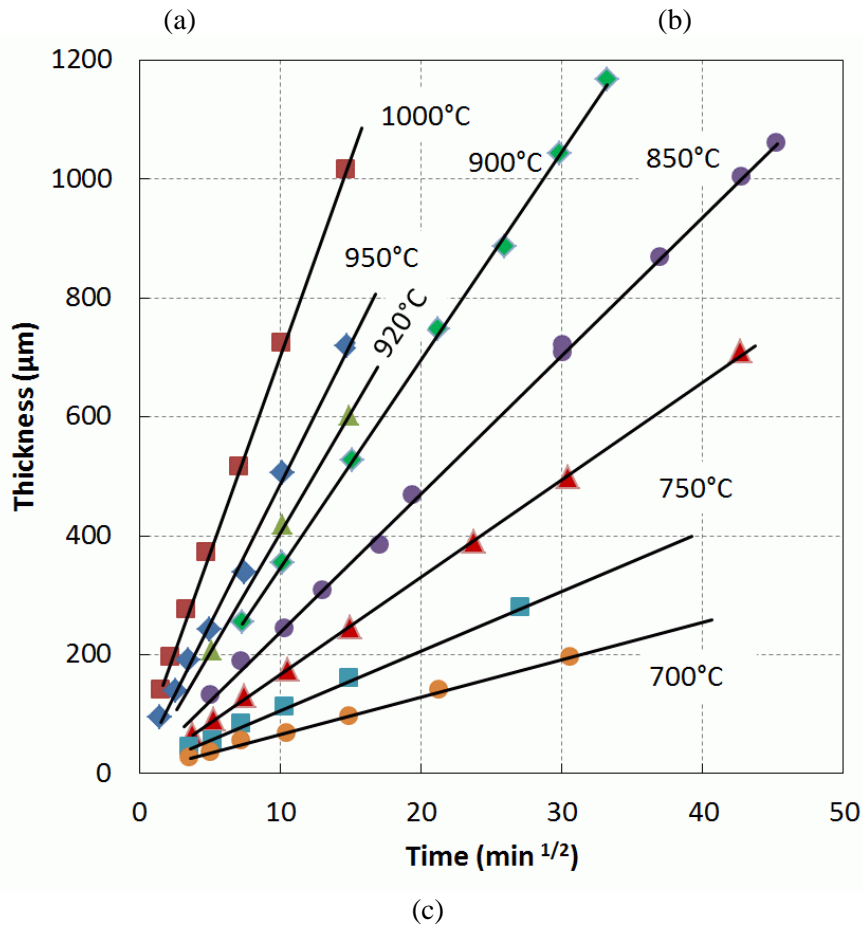
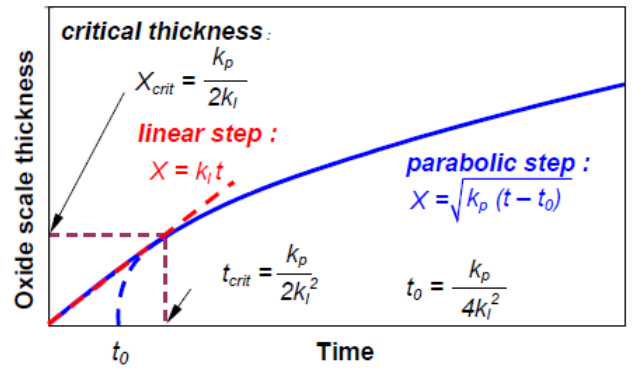
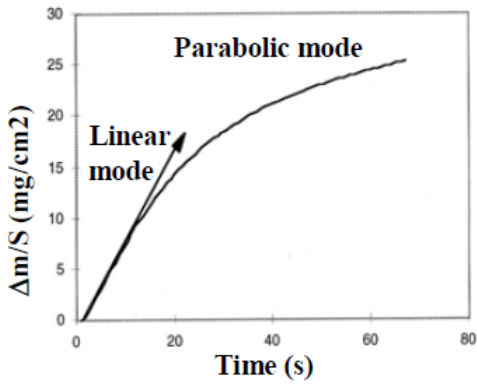


Figure 2.2 : (a) Evolution of oxidation (here the mass increase) for a steel oxidized at 900°C in a N₂-20%O₂-15%H₂O [4] (b) Mathematical representation of the transition between the linear and the parabolic step [4] (c) Variation of the scale thickness for temperatures from 700 to 1200°C for iron [31]

2.1.3 Multiscale oxidation

2.1.3.1 Above 570°C

According to Païdaissi, for the isothermal oxidation at high temperature of steel (above 570°C), three phases are present: Wüstite (FeO), Magnetite (Fe₃O₄) and Hematite (Fe₂O₃) [31]. There is a superposition, from the surface to the substrate, of Hematite (1% of the scale thickness), Magnetite (4%) and Wüstite (95%). For sure, the three phase repartition is highly dependent on the environment (temperature, partial pressure of O₂, humidity...), the Fe-O diagram gives an idea of each phase stability (Figure 2.3). Globally, iron oxides are composed of O²⁻ anion lattice with iron cations in octahedral and tetrahedral interstitial sites.

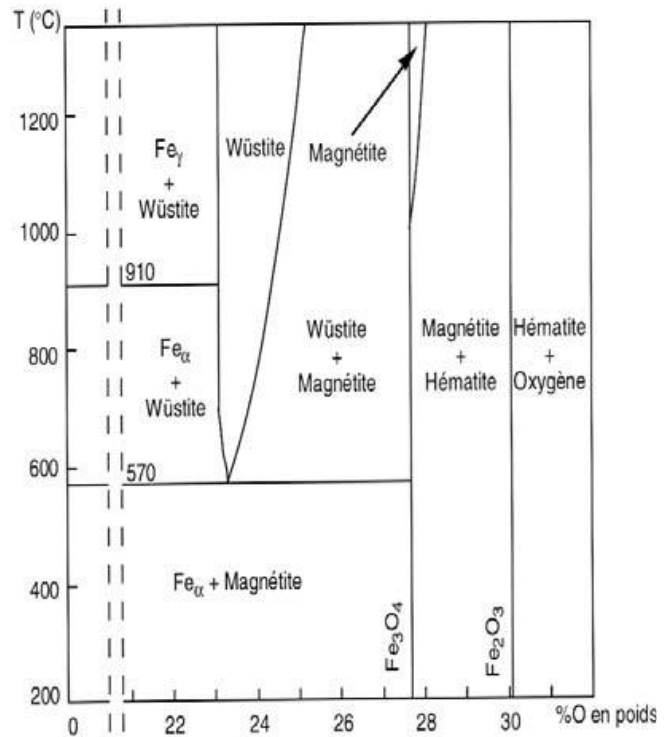


Figure 2.3: Equilibrium Fe-O diagram [4]

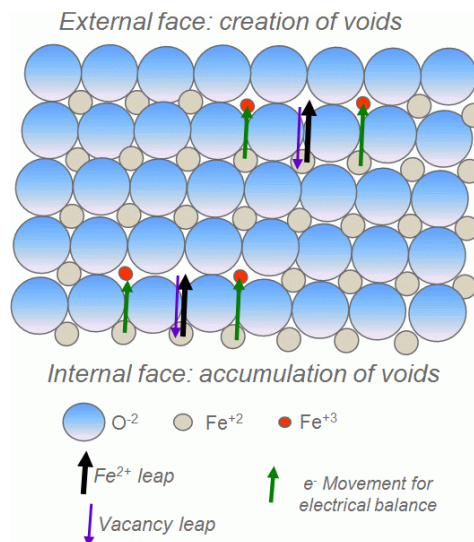


Figure 2.4: Schematic representation of Fe diffusion through vacancies [5]

Wüstite has a Face-Centered Cubic (FCC) structure with Fe²⁺ cations in octahedral sites. In the [111] direction, the material is composed of alternating planes of FCC O²⁻ anions and metal cations (see Figure 2.4). It is a non-stoichiometric oxide noted Fe_{1-x}O due to its iron deficiency (vacancy) in its crystalline structure. (1-x) varies from 0.83 to 0.95 and tends to decrease with the substrate/oxide interface distance. Indeed, to compensate for the lack of iron atoms, some Fe³⁺ and vacancies are present

in the structure [32]. Fe^{3+} cations are localised on tetrahedral sites linked to four Fe^{2+} vacancies. These vacancies help the diffusion of Fe^{2+} through the Wüstite layer. The ion jumps only to the neighbouring vacancies and another ion takes its place. Here, the driving force of the diffusion is the variation of iron vacancies concentration (5% at the interface with steel and 12% at the interface between Magnetite).

Magnetite has an “inverse” spinel structure [33]. The spinel structure has the general formula AB_2O_4 , where A (Fe^{2+}) and B (Fe^{3+}) designate the different cation species. The “inverse” structure is due to the stabilisation energy of Fe^{2+} [34]. The inverse spinel structure is based on the FCC arrangement of O^{2-} anion lattice, in which Fe^{3+} cations occupy 1/2 of the tetrahedral interstices, and a 50:50 mix of Fe^{3+} and Fe^{2+} cations occupy 1/8 of the octahedral sites

At lower temperature (below 570°C), Magnetite is directly formed from the iron oxidation. At higher temperatures, Magnetite is formed indirectly from the oxidation of Wüstite.

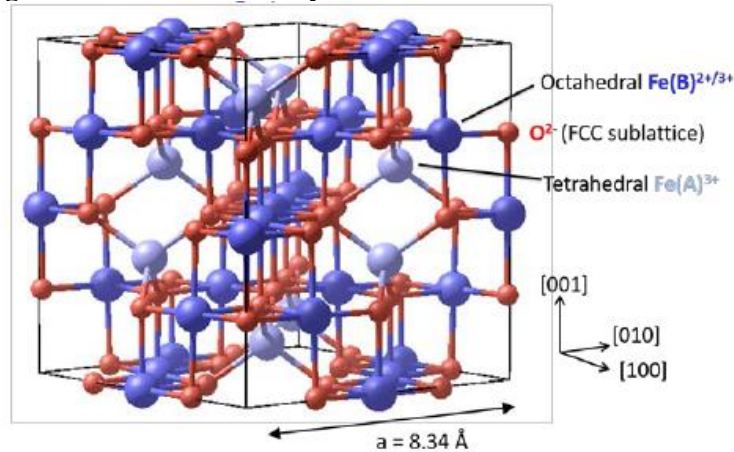


Figure 2.5: The inverse structure of Magnetite (FCC structure of O^{2-} arrangement where Fe cations occupy the tetrahedral and octahedral sites [33])

Hematite exists in two forms, a stable one $\alpha\text{-Fe}_2\text{O}_3$ and a metastable one $\gamma\text{-Fe}_2\text{O}_3$. $\alpha\text{-Fe}_2\text{O}_3$ has a corundum structure [35]. The unit cell is hexagonal, with $a = 0.5034\text{ nm}$ and $c = 1.375\text{ nm}$, and contains 6 units of Fe_2O_3 [33]. In other words, the structure is most easily seen as a slightly distorted Hexagonal Close Packed (HCP) stacking of O^{2-} anions in the c direction (2.29 \AA between the planes), with Fe^{3+} cations in two thirds of the octahedral interstices (Figure 2.6). $\gamma\text{-Fe}_2\text{O}_3$ is formed by oxidation of Magnetite at the surface.

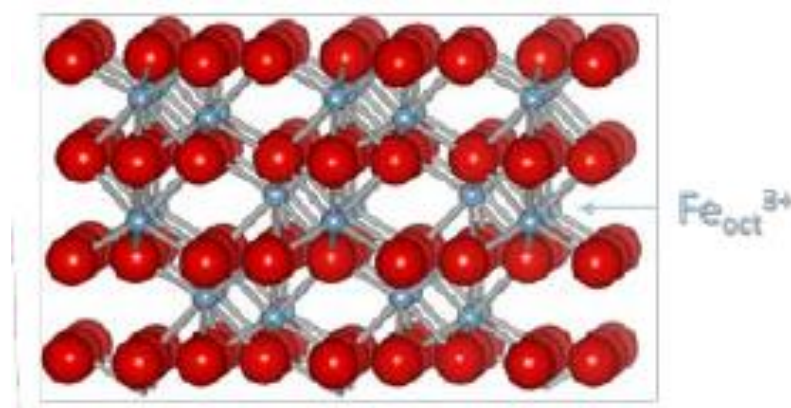


Figure 2.6: Hexagonal structure of Hematite, O^{2-} in red and Fe^{3+} in blue. Fe^{3+} occupies two thirds of octahedral interstitial sites [33]

According to the phase, the ions diffusion is changing (Figure 2.7). Either metallic ions diffuse through the layer or an oxygen ion diffuses the opposite way. The controlling process in FeO is Fe^{2+} diffusion via cation vacancies whereas, in Fe_3O_4 , both Fe^{2+} and Fe^{3+} are involved. On the contrary, growth of the Fe_2O_3 layer is done by diffusion of oxygen anions. The FeO layer adherence and

compactness obviously plays a decisive role on diffusion rate. If the oxide is no longer in contact with the metal, Fe^{2+} will no longer diffuse through this layer and so the vacancy concentration gradient will disappear. Indeed, oxidation may continue by direct access of oxygen to the metal surface. In addition to these main streams, interstitial diffusion of Fe^{3+} probably also occurs in Fe_2O_3 , while the contribution of oxygen transport by pipe diffusion (along dislocations, grain boundaries and micro-cracks) is probable in both Fe_2O_3 and Fe_3O_4 .

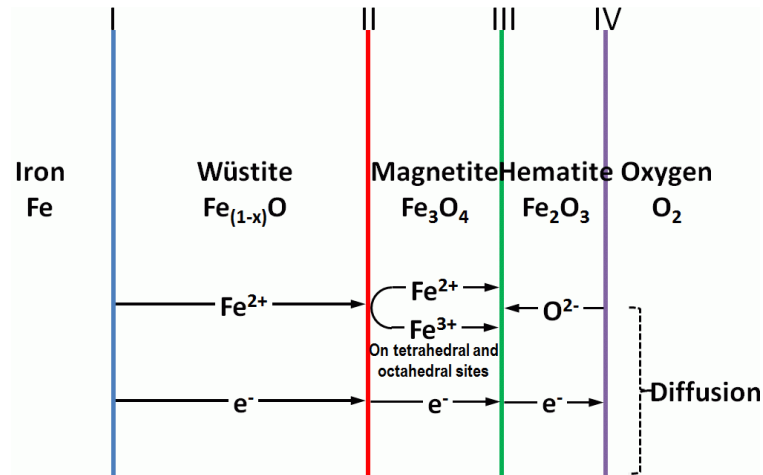


Figure 2.7 - Diffusion mechanisms in the oxidation of iron and elementary reactions occurring during iron oxidation [5]

Basabe and Szpunar study the repartition of oxides and its evolution in time for low carbon steel [36] (Figure 2.8). Secondary and tertiary scales grow in the roughing and finishing mill operations in less than 100 seconds. Therefore, it is extremely important to determine the phase composition of the iron oxide scales for quick oxidation (30 and 120 seconds). In this study, after the oxidation, samples are quenched to stop the transformation of phases. After 30 seconds, the main phase is Wüstite over the range of temperature 800-1200°C, in broad agreement with Païdassi's study. For a longer oxidation time and for a temperature between 800°C to 1000°C, Wüstite is still the main phase. Outside this range, the percentage of Wüstite decreases, while percentages of Magnetite and Hematite increase.

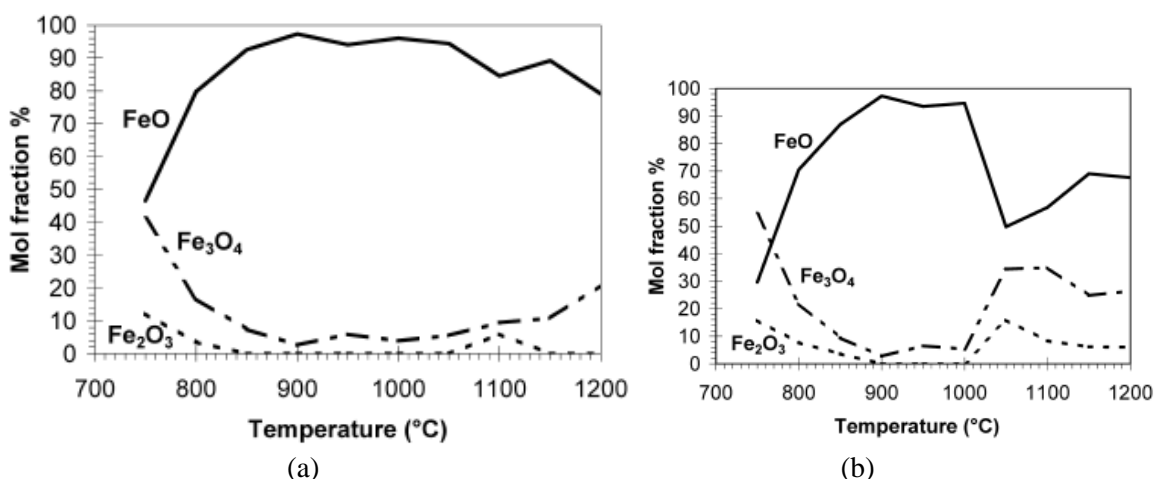
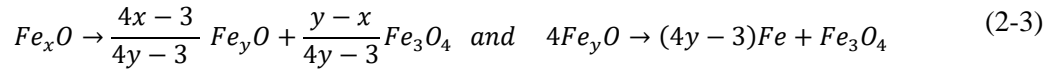


Figure 2.8: Low carbon oxide composition as a function of temperature and the oxidation time : (a) 30 s and (b) 120 s [36]

2.1.3.2 Below 570°C : Wüstite decomposition

The Fe-O diagram (Figure 2.3) shows that below 570°C, Wüstite is thermodynamically unstable and only Fe₂O₃ and Fe₃O₄ exist. Wüstite dissociates into magnetite and iron. According to Broussard, Wüstite is decomposed in two steps [37]:



First, there is a re-arrangement of the cations within Wüstite. Magnetite is produced using Fe³⁺ cations already present in the Fe_xO. Due to the diminution of these cations, an intermediate Wüstite is produced. The second step is the real decomposition of this new Wüstite into Fe₃O₄ and iron. The amount of the intermediate FeO is thus decreasing. This precipitation has been observed by Schmid et al. using in situ high temperature oxidation and cooling of iron by ESEM (Environmental Scanning Electron Microscope) [38]. This germination is first localised at the external part of the Wüstite, where the Fe³⁺ are more present.

This transformation is quick for temperatures ranging from 300 to 570 °C. Below, it becomes extremely slow. So Wüstite can easily be kept in dry conditions over 3 years in a laboratory (and even for longer periods).

The influence of the cooling rate on the decomposition of Wüstite is studied by Chen and Yuen [39]. During cooling, the temperature is still high, and cooling takes several hours. Three types of scales are described by the authors (Figure 2.9 (a)) :

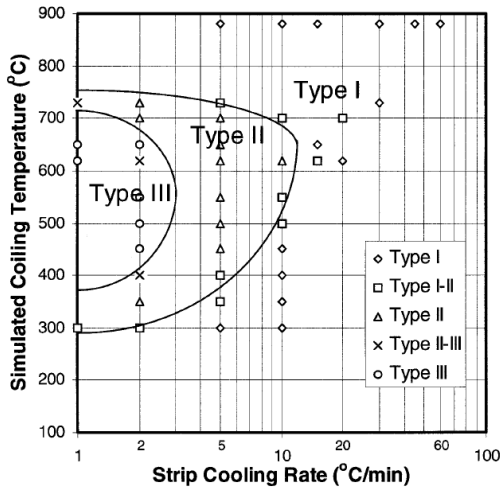
- Type I : for high cooling rate, Wüstite is retained (and some precipitation of Magnetite is present)

- Type II : for intermediate cooling speed rate, a continuous Magnetite layer is formed immediately over the steel substrate while the majority of the Wüstite layer is retained. Magnetite precipitates also form inside the Wüstite layer.

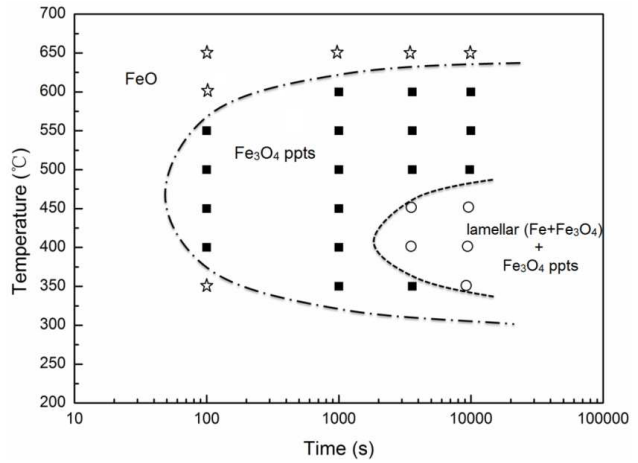
- Type III : for usual cooling temperature and cooling speed rate, most of the Wüstite layer is found to transform into an eutectoid mixture of mostly Magnetite and iron. A certain amount of precipitated Magnetite is present, both inside the original wüstite layer and at the scale–steel interface, with a small amount of retained Wüstite.

The isothermal transformation of FeO in the range of 650~350°C is studied by Liu et al. [40]. After a 20 seconds oxidation at 880°C, the oxide is annealed with argon for a long period. The same reactions are observed, first a precipitation into Magnetite and then the lamellar eutectoid transformation. These reactions have a C-curve trend on an isothermal transformation diagram (Figure 2.9 (b)). It confirms the decomposition into Wüstite in two steps.

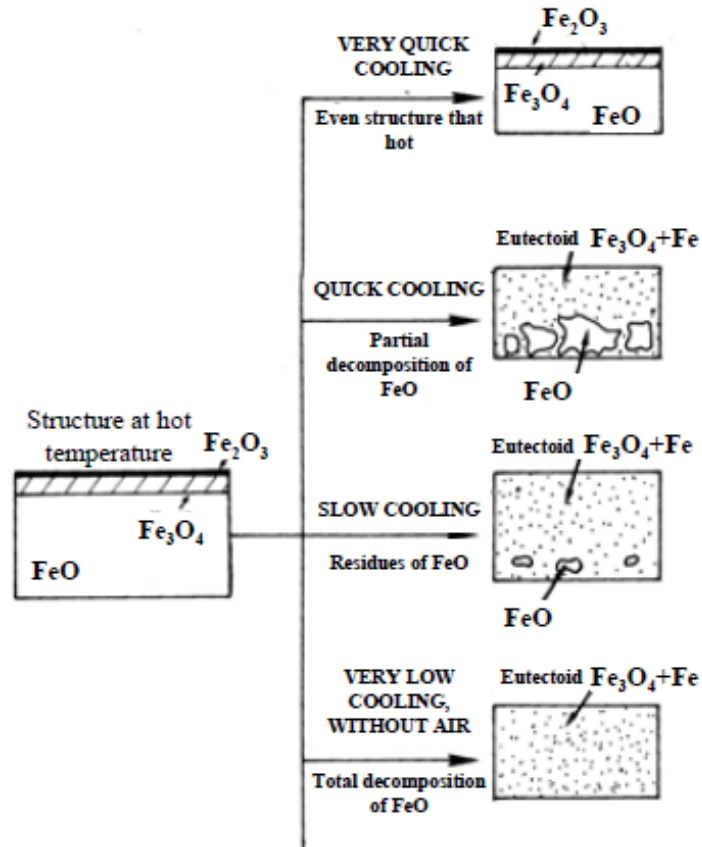
The Figure 2.9c shows the schematic evolution of Wüstite decomposition during cooling. For a rapid cooling, the oxide proportion is not changing, as is the case during quenching. By increasing the cooling time, decomposition increases and may become complete. Note that in the presence of air, only Magnetite and Hematite are present. Thus, direct observations of industrial oxide layers are impossible. Indeed, for the rare available pictures or micrographs taken after an accidental stop of the FM, strips are covered by oxide scales, however, it is complicated to interpret these images, due to modification of scale structures and compositions during the cooling.



(a)



(b)



(c)

Figure 2.9: Oxide decomposition depending on the cooling conditions (a) TTT-like diagram based on cooling rate (b) IT based on time of cooling (c) Schematic representation of Wüstite decomposition [16]

2.1.3.3 Selective oxidation

The internal and selective oxidation is a slow process. This kind of selection is present in the reheating furnace or in the coils. Between these two stages, the duration is not long enough to develop selective oxidation. During the coiling, the most detrimental is the grain boundary oxidation, it can reach up to $10\mu\text{m}$ within the steel (Figure 2.10). At the interface, there is a low partial pressure of oxygen set by the Fe-FeO equilibrium. Some dissociated oxygen is present and diffuses into the metal surface. The excess of Oxygen in Wüstite (due to the non-stoichiometry) also acts as a reservoir. The selective oxidation is activated around 700°C . This oxidation is detrimental, because it amplifies defects during pickling.

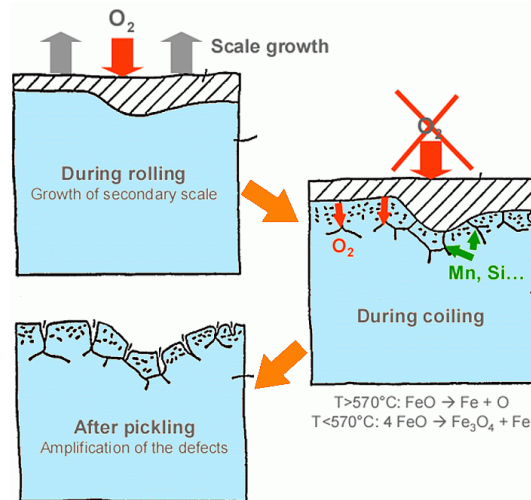


Figure 2.10: Mechanism of grain boundary oxidation during coil cooling [5]

The oxide that is generated at high temperature for low carbon steel is composed of three phases : Wüstite, Magnetite and Hematite. For the secondary scale that is the topic of this study, the scale is composed mostly of Wüstite at high temperature. The well-known decomposition of Wüstite is not considered in this study due to its low temperature and slow kinetics compared to the descaling.

2.2 Influence of alloying elements on the scale structure

The oxidation of steel is more complex than iron oxidation due to the alloying elements. In the case of low carbon steel, the additions never exceed 1% but it modifies the behaviour and the kinetics of oxidation. Indeed, the alloying elements and their oxides can be classified in different ways :

- miscibility with Wüstite. Some oxides are volatile (carbon oxides ; chromium oxide in presence of water vapour and over 1150°C) . Others can be miscible such as Mn oxides. But the majority are non-miscible. They accumulate between the metal and the Wüstite layer.

- melting point of component. If this temperature is below the rolling temperature, a liquid phase is generated at the interface. This is the case for Copper (1084°C), Silicon (fayalite Fe_2SiO_4 melts at 1177°C) or Phosphorus (creation of an eutectic $\text{P}_2\text{O}_5 + \text{FeO}$ with a melting point at 944°C). For low-melting point species, above a threshold concentration, a liquid phase appears and oxidation kinetics speeds-up. If on the contrary the melting temperature of the compound is above the rolling temperature, it remains solid, and tends to slow down the kinetics, acting as a barrier against the diffusion of ions.

- affinity with oxygen. The Ellingham diagram gives the free formation of enthalpy and the equilibrium atmosphere for pure metals [41]. On the axes, different atmospheres (O_2 , $\text{H}_2/\text{H}_2\text{O}$, CO/CO_2) are drawn. To compare the metal equilibrium in these atmospheres, a line should be drawn from the point O or H or C (on the left side) till the corresponding atmosphere axis. It classifies element oxides from less stable (top) to very stable (bottom) (Figure 2.11). Some elements are less oxidizable than iron. These elements remain metallic during the oxidation of steel. In the diagram, they are localised above the red Fe-FeO line (green elements such as Cu and Ni for exemple). The other elements (below the Fe-FeO line) are preferentially oxidized during the scale formation (blue elements such as Mn, Si, Al, Cr). In the next part, only the influence of a few (or major) elements is described.

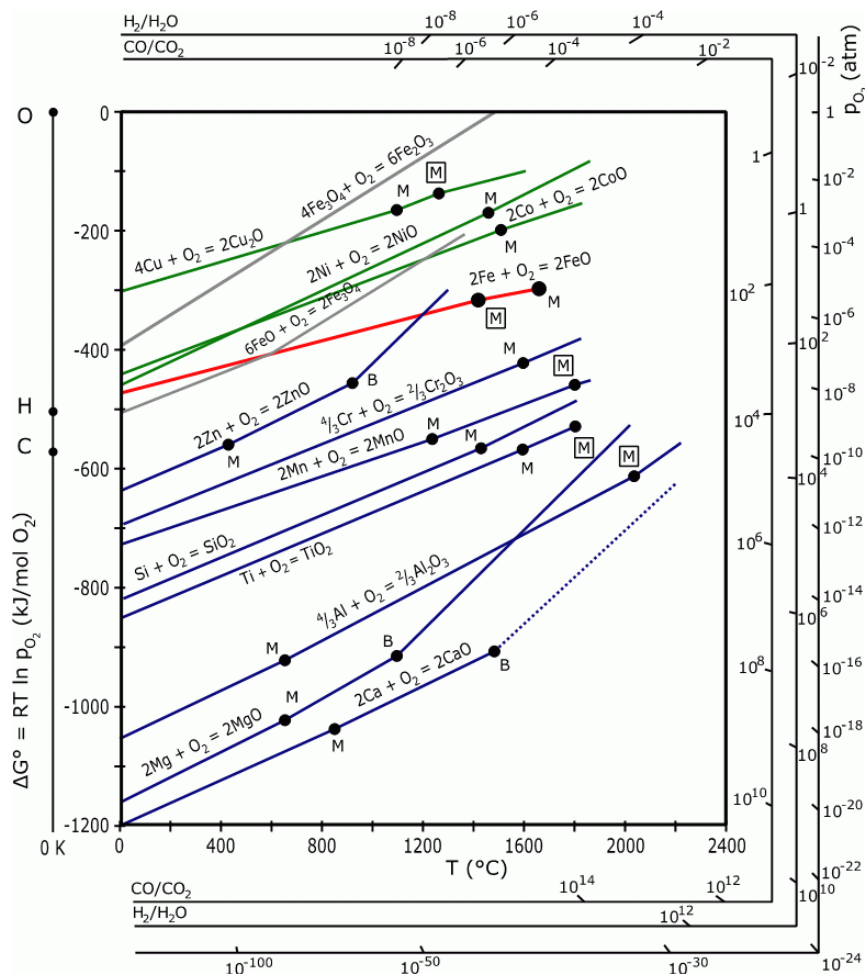


Figure 2.11: Ellingham diagram [41]

2.2.1 Elements less oxidizable than iron

Copper is insoluble with iron oxide and tends to be accumulated at the interface and is not oxidizing. Above the melting temperature ($T < T_m = 1084^\circ\text{C}$), the liquid infiltrates in grain boundaries and is encouraging the hot shortness effect (low ductility in the $[1100^\circ\text{C}-1200^\circ\text{C}]$ temperature range) and fissuration [42]. It drives down the ductility of the steel surface as soon as 0.2% wt. As the diffusion of cations is increasing in a liquid phase, the oxidation kinetics is also impacted by Cu. In the previous chapter, the Cu effect has been described for the descaling. According to Osei et al., the higher Cu steels (0.8% wt) are easier to descale due to this liquid phase, it tends to limit the formation of complex at the interface [25]. Below the melting temperature, for Nilsonthi [43], increasing Cu content tends to decrease the oxidation rate. Indeed, there is a precipitation that inhibits the diffusion of oxygen.

Nickel has the same kind of behaviour as Copper. It is accumulated at the interface between oxide and steel, and remains insoluble in oxide (Figure 1.22). Due to its much higher melting temperature, it does not melt like copper but forms an entangled layer between the oxide and steel between scale and metal. As described in the previous chapter, the addition of Ni tends to increase scale adherence and generates some descaling difficulties [22,23]. For a larger content of Ni (5%wt), the oxidation at 1200°C shows that the local microstructure within Wüstite is changed [44]. The concentration of Ni(Fe) particles is changing from the interface to the surface due to the oxygen potential gradient. At the interface, the concentration is similar to the steel and is increasing in the oxide, it confirms the enrichment of Ni within the scale. In oxide, some voids are present at the interface, such voids are caused by a counter diffusion of vacancies due to the outward diffusion of Fe ions across the whole oxide scale.

2.2.2 Elements more oxidizable than iron

Some alloying elements are oxidized for a $P(O_2)$ lower than the FeO-Fe equilibrium oxygen pressure (below in the Ellingham diagram). Generally they form an oxide sublayer at the metal-oxide interface.

The major effect of Carbon on common steels at high temperature is decarburization caused by selective oxidation. It is divided into three separate events: dissolution of carbides, diffusion of carbon through the iron matrix, and surface reactions [45]. The carbon reacts with Oxygen to form $\text{CO}_{(g)}$. This results in a decrease in carbon content below the interface. However, for low carbon steel, decarburization is limited, and C is an interstitial element in iron.

Chromium forms mainly two oxide phases: the rhombohedral oxide Cr_2O_3 and the spinel phase FeCr_2O_4 . During the first stage of oxidation, the presence of Cr in iron tends to increase oxidation because Cr^{3+} would dope FeO, increasing the concentration of iron vacancies. By increasing the time of oxidation, chromium oxides form and decrease oxidation. They stay at the metal-oxide interface and create a barrier which inhibits Fe outward diffusion. Above 800°C , Cr_2O_3 is decomposed into two gases: CrO_3 and CrO . The addition of Cr (up to 1 or 2%) can increase the temperature of FeO eutectoid decomposition.

In the presence of oxygen, Manganese is oxidized into MnO which also forms a solid solution with Wüstite: FeO-MnO. Increasing the Mn content inside FeO decreases the vacancy content. From a mechanical point of view, the presence of Mn tends to increase the oxide hardness. According to Baud, this effect is observable for Mn contents higher than 11.8% [46]. The addition of Mn tends to reduce the adherence of the scale (for percentage higher than 11.8%).

Silicon is oxidized into SiO_2 inside the metallic matrix and at the metal-scale interface. It can also form a mixed oxide Fe_2SiO_4 (fayalite). This mixed oxide segregates at the interface and forms a eutectic FeO- Fe_2SiO_4 which melts at 1177°C .

- At low temperatures: $T < 1177^{\circ}\text{C}$: Below the FeO-Fe₂SiO₄ eutectic temperature, silica first decreases oxidation rate [47]. An homogeneous internal silica layer is formed that generates passivity. This silica scale becomes porous and transforms into a biphasic layer containing fayalite and FeO. The diffusion of iron is then increasing using the short-circuits in the biphasic layer, and oxidation rate is increased.

- At high temperatures $T > 1177^{\circ}\text{C}$: Above the eutectic temperature, FeO-Fe₂SiO₄ melts and infiltrates grain boundaries. It increases bonding between scale and metal and improves the scale adherence [22,23]. As described in the paragraph 1.6.3, it generates descaling issues.

The alloying elements added to the composition of the steel have a strong influence on the behaviour of the oxide, from a chemical to a mechanical point of view.

2.3 Internal stresses

According to Bull [48], the oxide at the surface of steel undergoes several processes that generate stresses, but also relaxation mechanisms which decrease stresses. In order to understand the oxide behaviour, it is necessary to determine the possible origins of these stresses, and also to study the relaxation phenomena, which can be not negligible at high temperature. All the phenomena are summarised in the Table 2-1 and detailed in the following part.

Table 2-1: Stress generation and relaxation mechanisms for a thin oxide film on a metallic substrate

Stress generation	Stress relaxation
Growth	Scale creep
Thermal expansion mismatch	Substrate creep
Phase transformation	Scale cracking
Non-stoichiometry of Wüstite	Substrate cracking
Applied stresses	Substrate yield

2.3.1 Growth stresses during oxidation

The formation of stresses within the oxide is inherent to oxidation. The so-called “growth stresses” have been widely described in literature, and are multifactorial [49]. The determination of internal stresses is possible with different methods : X-Ray diffraction, Raman spectroscopy, flexure method. XRD is described more precisely in section 3.3.

1°) Pilling and Bedworth have proposed an explanation of growth strain during the oxidation [50]. The origin is the difference in molar volume of oxide and metal. This incompatibility induces an isotropic growth strain given by the next equation :

$$PBR = \frac{V_{M \text{ oxide}}}{V_{M \text{ steel}}} \quad \text{and} \quad \varepsilon^{\text{growth}} = \sqrt[3]{PBR} - 1 \quad (2-4)$$

This simple model indicates whether generated stresses are compressive or tensile. If the volume of oxide is larger than the metal one, the ratio is larger than unity, stress is compressive in the oxide (for Wüstite, $PBR = 1,68 > 1$). A limit of the model is that it tends to overestimate the associated

stresses [51]. In this approach, the strain is localised only at the interface between oxide and metal. Thus, for thick oxide, this difference in volume is not explaining all the growth stresses generated during oxidation. This model also considered that only an anionic inward oxidation is able to develop stresses but metals undergoing oxidation by cationic outward diffusion also has shown high stresses level [51].

2°) Another source of growth stresses is epitaxy, that is the lack of compatibility of the crystalline lattices at the interface (Figure 2.12). A strain is thus generated to accommodate the lattice parameters mismatch [52]. This local deformation is localised between the innermost atomic layers of the scale and the underlying metal. Epitaxy is maintained by an adjustment of the spacing of the remaining interface dislocations, it generates compression in the oxide and tension in the metal. This type of stress is at the microscale and its contribution at a macroscopic scale is a minority, particularly for thick oxide. The lattice mismatch of Wüstite, facing iron, in a $\langle 110 \rangle$ direction on $\{100\}$ plane is calculated to be 5.5%. However, this value may become smaller due to the iron lattice than also expands (strain never exceeds 2,75%) [53].

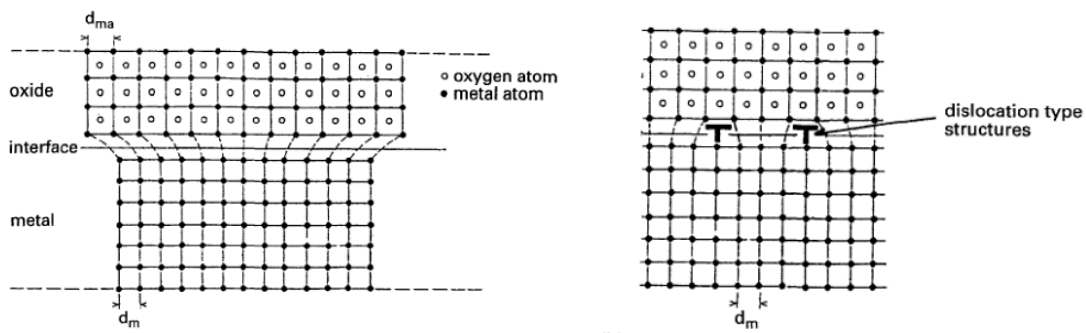


Figure 2.12: Epitaxy at the interface between the oxide and the metal (a) without accommodation (b) with accommodation by intrinsic dislocations [49]

3°) Rhines and Wolf suggest that a compression state is present due to the oxide growth in the oxide grain boundary [54] (Figure 2.13). It has been shown experimentally that the volume changes at the grain boundary for NiO oxide. Oxygen is diffusing along grain boundaries and the nickel through oxide crystals. The formation of the new oxide is thus localised at the grain boundaries (and at the surface). For nickel, the oxide grains are columnar. According to these authors, this kind of behaviour is possible for the oxidation of other metals, in which there is a diffusion of the oxygen at the grain boundaries. FeO has a similar columnar grain structure. Rhines and Wolf quote another author named Tylecote, about the oxidation of iron and his conclusion is: "The more likely and more generally acceptable explanation (for oxide growth stresses) is that inward oxygen diffusion is taking place along the grain boundaries and causing oxidation within the film".

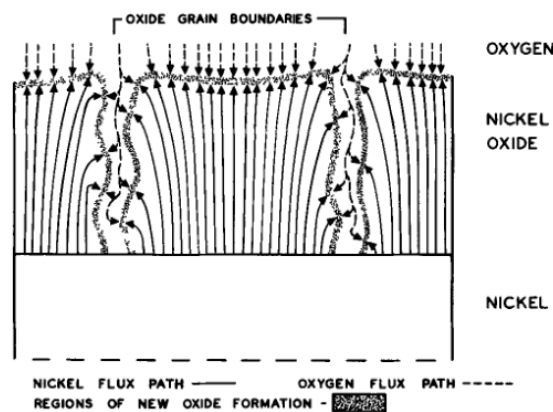


Figure 2.13: Schematic diagram for the formation of growth stress at the grain boundaries, where new oxide is created (Oxidation of Ni into NiO) [54]

4°) For the case of multilayered oxide, according to Appleby and Tylecote [55], the formation of a given oxide from a layer of another oxide generates a volume change that can lead to a source of growth stresses. Taniguchi and Carpenter calculate the volume change for the reaction between Wüstite and Magnetite and between Magnetite and Hematite [53]. The author considers that it is difficult to evaluate precisely the volume change but the tendency (compressive or tensile) can be deduced. The reaction at the Wüstite /Magnetite interface tends to increase the volume (6,5%), and there is also a net increase of volume at the interface between Magnetite and Hematite. Thus, two sets of stress systems are considered first, compressive stresses in the Wüstite and corresponding tensile stresses in the Magnetite layers at the Magnetite/Wüstite interface and secondly, compressive stresses in the magnetite layer and corresponding tensile stresses in hematite at the Hematite/Magnetite interface.

5°) During the oxidation, some vacancies are transported to the Wüstite/iron interface and generate vacancy sinks. According to Taniguchi and Carpenter, it results in the shrinkage of the metal substrate because a vacancy cannot fully occupy the volume of an iron atom which it replaces [53]. It induces tensile stresses in the metal and corresponding compressive stresses in the oxide. This source of stresses is mainly localised at the interface between the oxide and steel.

In conclusion, the sources for growth stresses are multiple and it is still complicated to select precisely one theory.

2.3.2 Thermal stresses during temperature change

Thermal stresses are generated during cooling due to the coefficient of thermal expansion (CTE) mismatch between the metal and the oxide [6]. Assuming uniform temperature, when CTE is smaller for the oxide, the retraction of the oxide is smaller. Therefore, the substrate is in tension and the oxide undergoes compressive strain during cooling. Considering that the oxide is thin and that both materials deform under a purely elastic mode, the stress within the oxide is:

$$\sigma_{thermal} = \frac{E_{ox}\Delta T(\alpha_{ox} - \alpha_{met})}{1 - \nu} \quad (2-5)$$

with ΔT the difference of temperature between the beginning and the end of the cooling, supposed uniform, E the Young's modulus, ν Poisson's coefficient and α the thermal expansion coefficient. When the CTE gap is important, the stresses are large. As an example, stress is independent of the thickness and it is evaluated as -240 MPa for an oxide composed of Wüstite on a low carbon steel for a cooling from 1000°C to room temperature (with $\alpha_{Wüstite} = 13.10^{-6} \text{ K}^{-1}$ and $\alpha_{steel} = 14.10^{-6} \text{ K}^{-1}$). Obviously, it is an approximate value of the real stresses within the oxide. It is highly dependent on the selected value for E , the Young's modulus, and the α coefficient. Many authors have measured the thermal expansion coefficient with different methods : X-Ray diffraction ([56]), thermo-mechanical analyser [57]. Significant differences can be observed in the Figure 2.14 and the values are dependent on the temperature. A major difference is noted for Wüstite above 500°C between the Sasaki et al. and Takeda et al., the first authors observe a collapse, and net increase for the second authors. For low temperature, similar values are noted. It may be due to the technique used : XRD versus dilatometer. It is thus complicated to conclude. Therefore in the chapter 3, we will give the CTE of Wüstite and ferrite based on our own measurement with High Temperature XRD.

In the case of multilayered oxide, the coefficients between Wüstite, Magnetite and Hematite are also different, and additional thermal stresses are generated.

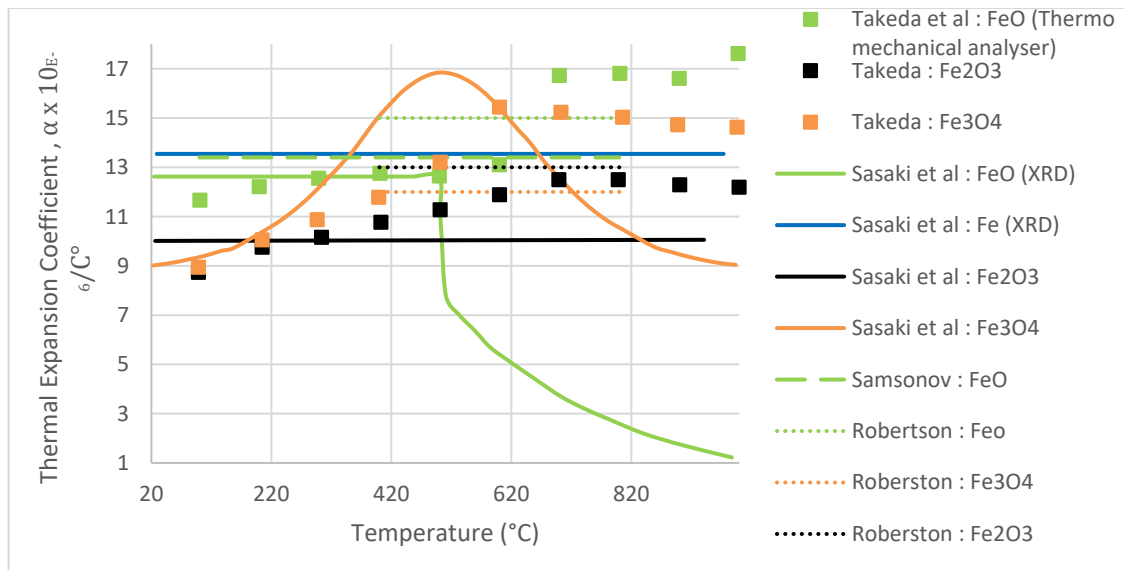


Figure 2.14: Thermal expansion coefficient of Wüstite in green, Magnetite in orange, Hematite in black and steel in blue, from several authors (after [1–4])

2.3.3 Other internal stresses

2.3.3.1 Non-stoichiometry of Wüstite

The gradient of non-stoichiometry of Wüstite is also a source of internal stresses. The variation in lattice parameter across the Wüstite is calculated by Foster and Welch [58], it changes from 4.292 Å to 4.308 Å for the compositions near the Magnetite/Wüstite and Wüstite/iron interfaces at 800°C, respectively. It induces a stress formation across the Wüstite layer. The layer possessing the smaller lattice is in tension relative to the adjacent layer with a larger parameter.

2.3.3.2 Phase transformation

The phase transformation is also a source of stress. Wüstite is no more stable below 570°C. It is decomposed in two steps (equation (2-4)). First, the Fe concentration in FeO increases from x to y and Fe₃O₄ precipitates. Then, the Fe-rich FeO (Fe _{y} O) changes to a eutectoid structure of Fe and Fe₃O₄. Tanei and Kondo show that this transformation generates compression [59]. A flexure method is used (Figure 2.15). Before that, one face of the oxide is covered with SiO₂ to protect it from the oxidation. On the other face, a stress-free state is considered initially. After 10 minutes of oxidation at 750°C, a slight bending is observed, due to the oxide growth stresses. After cooling to 400°C, the bending behaviour is enhanced by the thermal stresses due to the difference of expansion coefficients.

The first step of the decomposition is based on a change of the stoichiometry, it involves a decrease of volume (the volume change is approximately -0.34%). Indeed, the x and y values are 0.9 and 0.97, respectively. The second reaction is the volume change calculated as about +4.9%, which puts the oxide in compression. Finally, the correlation between the bending and the stress is done, the phase transformation stress is about -620 MPa (corresponding to a 0.26% strain). [59]. This test shows that the Wüstite decomposition is a long process: only after 30 minutes at 400°C is the whole decomposition done, and the strain is no more increasing.

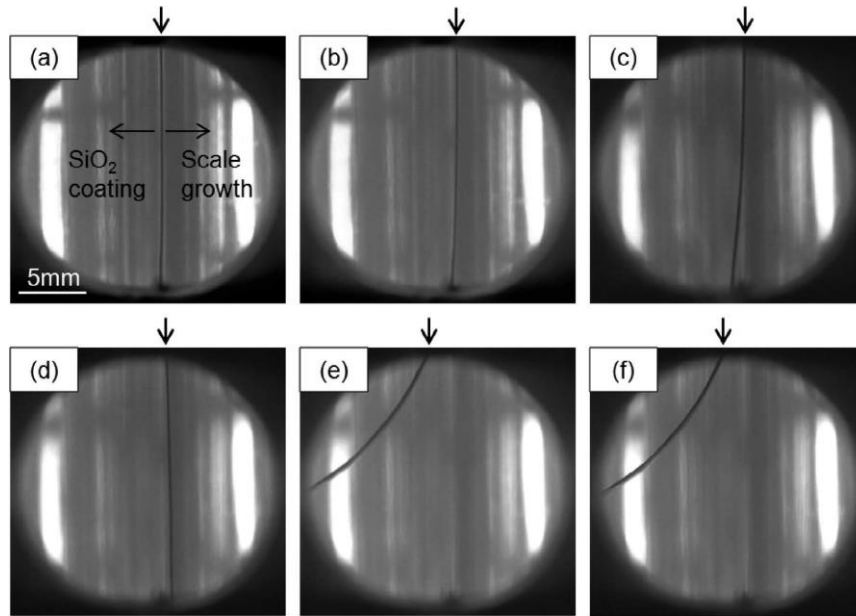


Figure 2.15: The so-called “flexure method” to evaluate stresses. The specimen is the dark line. (a) before oxidation (b) after 10 min oxidation at 750°C (c) after the cooling to 400°C (d) after 6 minutes soaking at 400°C (e) after 14 min soaking at 400°C (f) after 120 min soaking at 400°C

In conclusion, the sources for stresses generated at high temperature are multiple, these stresses change during in HSM and are relaxed depending on the conditions.

2.3.4 Relaxation by creep, fracture, spallation

The internal stresses generated can be relaxed by different mechanisms [48] : via plasticity or cracking. According to Evans and Taylor, these internal stresses can be relaxed by creep for thin oxide films [60]. But the influence of substrate (and the relaxation by creeping) is also addressed by the model of Bull [48].

2.3.4.1 Creeping behaviour of the substrate

In the literature, some models have been developed to predict the evolution of the internal stresses (growth and thermal). The model of Bull is based on the fact that substrate can relieve these stresses by creeping at high temperature (via a permanent elongation). This model has been developed for isothermal high temperature oxidation followed by cooling to room temperature. It gives a good agreement with experimental data for alumina scales on FeCrAlY.

For isothermal oxidation, only growth stresses are considered (a constant value of 1.4 GPa is assumed for each new scale layer increment created as oxidation proceeds).

In the Figure 2.16, an isothermal oxidation at different temperatures is done. For short time oxidation, the growth stress in the scale is low because the stress in the scale is easily relaxed by a small amount of substrate creep. By increasing the oxidation time and thus the scale thickness, stresses tend to be higher.

- For low oxidation temperatures, creep is marginal and the stress in the scale increases up to the growth stress (~1400 MPa) and remains constant at this value as the scale thickens.

- For higher temperatures, creep can occur in the substrate, and thus the scale stress increases to a maximum and is rapidly reduced by substrate creep above this. For the highest temperatures the stress in the scale is continuously relaxed as the scale thickens.

The same model is applied for the cooling of the oxidized sample to room temperature. The speed of cooling influences the final stress state of the thin film. The more slowly the sample is cooled, the more time there is for relaxation by substrate creep, and thus the final stress will be lower.

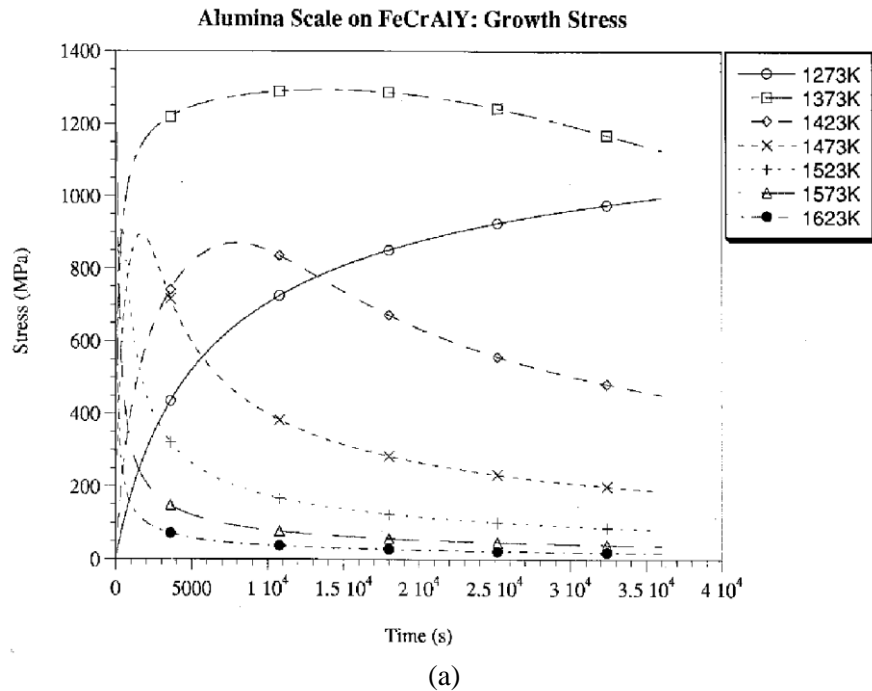


Figure 2.16: (a) Predicted variation of scale stress with time for short-term isothermal oxidation at a range of temperatures (8- μm alumina scale on a 1.8-mm thick FeCrAlY sample, new oxide growth stress 1.4 GPa)

2.3.4.2 Plastic behaviour of the oxide

Sasaki et al. [56] use a synchrotron radiation to evaluate internal stress within oxide of a silicon steel specimen (Fe-1.0 mass% Si-0.1 mass% C) (the $\sin^2\psi$ method technique utilised is described in section 3.3. After 15 seconds of oxidation at 900°C (to have 4 μm of thickness), no stress is measured during cooling of the thin scale between 900° and 700°C. Both the growth stress at 900°C and the thermal stresses generated by the cooling are relaxed by plastic deformation of oxide, because the temperature is higher than the ductile-brittle transition of Wüstite. According to Mackenzie and Birchenall [61], the Wüstite layer is known to creep extensively during high temperature sollicitation, and to relieve stresses due to the plastic flow. The plastic behaviour of oxide is widely described in the 2.5.1.2 part.

In the HSM, the main source of internal stresses is the thermal contribution, and growth stresses are second order compared to thermal stresses. Indeed, the difference in temperature between rolls and oxide induced high thermal stresses. As for the descaling, it is mainly a thermal process, induced by a fast, strongly heterogeneous cooling due to water jets. In reality, the cooling below the rolls and the one induced by the descaling are extremely rapid and this creep relaxation is probably negligible .

2.4 Fracture of thin film

When plastic relaxation is impossible (low temperature) or when growth or thermal stress increase too fast (contact with roll, fast cooling in descaling), relaxation by plastic mechanisms become inefficient and fracture will occur. All the fracture mechanisms have been summarised by Robertson and Manning [26] in Figure 2.17.

The tendency is that higher strain is needed to fracture thinner scales. Scales are likely to fail in tension by the formation of through-scale cracks which initiate at pre-existing flaws. By increasing the strain in tension, one first meets through-scale cracking, then multi-lamination, and finally spalling. For thin film, a failure mode is expected at high tensile strains, called “oxide cracking”. The oxide is breaking into a series of islands which will 'float' on the metal as the strain increases, but remains attached to the metal.

For the compression, the strain leads to brittle spalling. It requires the growth of a delamination crack either along the oxide/metal interface or parallel to it in the oxide. It depends on the behaviour of the interface (either buckling for weak interface or wedging for strong interface).

According to Robertson and Manning, for the thinnest scales, brittleness is a size dependent concept [26]. The stress required to propagate a flaw increases as the flaw size decreases. As the scale thickness is an upper limit to the flaw size, reducing the thickness increases the stress until it eventually exceeds the yield stress of the oxide: then the oxide is able to fail in a ductile manner only and not by cracking. This defines the “comminution limit” of the material. The thickness has to be lower than $\frac{2.8\gamma E}{\sigma^2}$ with E the Young's modulus, γ surface energy and σ the yield stress of the oxide.

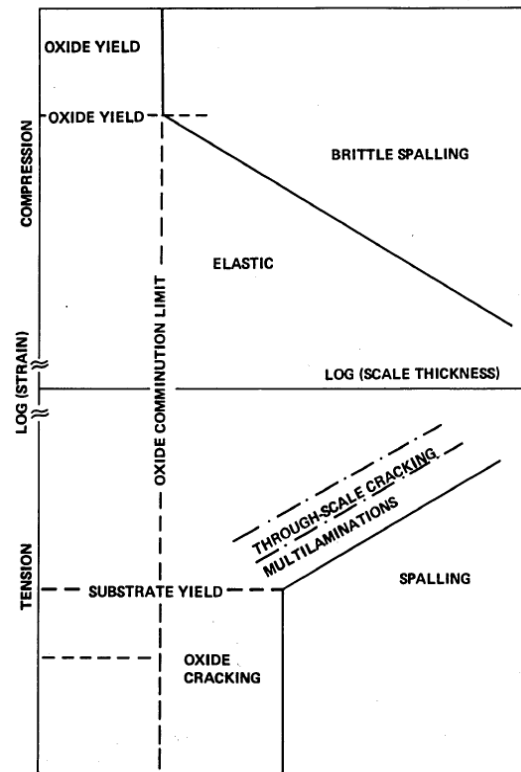


Figure 2.17: Failure mode map for tensile and compressive strains according to the thickness [26]

2.4.1 Failure under tension

In the presence of tensile stresses, the oxide is subject to cracking [62]. Two different modes leading to oxide spallation are observed: through-thickness crack or sliding along oxide-metal interface. This transition has been studied by Krzyzanowski and Beynon [63]. For that, the specimen is cut in two equal parts connected together (with a ceramic pin). During the oxidation, a continuous oxide layer covering both part is formed. The tensile tests reveal the two fracture mechanisms previously evoked. The transition between the two modes is strongly influenced by temperature (between 850°C and 870°C in the Figure 2.18). They show that some elements like Si and Mn increase the temperature range, where the cracking mode is observed [62]. In other words, this alloying results in strengthening of the oxide/metal interface at high temperatures.

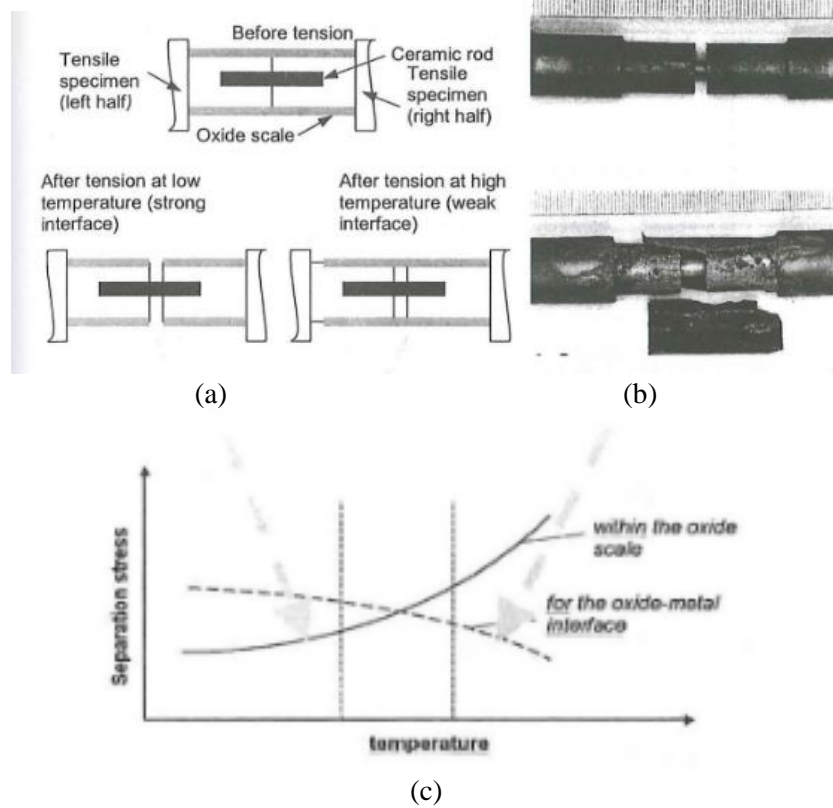


Figure 2.18: (a) Schematic representation of the two fracture modes in a tensile test (b) experimental oxide fracture mode during tensile tests (c) influence of the temperature on the fracture mode [64]

The first mode (through thickness crack) is generally accepted for tensile failure at up to 850°C [63] for a strong interface, and a weak oxide. Failure begins by through-scale shear cracking followed by initiation of a crack along the scale/metal interface that may result in spallation (Figure 2.19). The through-thickness penetration may be happening when the oxide is brittle [65]. Thus a critical failure stress σ_c (or strain ϵ_c) may be used as a criterion for the through-thickness crack occurrence:

$$\sigma_c = \frac{K_{1c}}{f\sqrt{\pi a}} = \sqrt{\frac{2\gamma E_{ox}}{f^2 \pi a}} \text{ and } \epsilon_c = \frac{\sigma_c}{E_{ox}} \quad (2-6)$$

where K_{1c} is the critical stress intensity factor, γ the oxide surface energy, E_{ox} the Young's modulus, f is a constant depending on the geometry of the notch ($f \sim 1$) and \bar{a} a characteristic size of the equivalent defect. According to Schütze [8], by increasing the deformation, stress relaxation by through-thickness cracks is replaced by a delamination process, starting from these cracks (Figure 2.19 b). Finally, when deformation reaches $\epsilon_{c,spall}$, delamination leads to spallation.

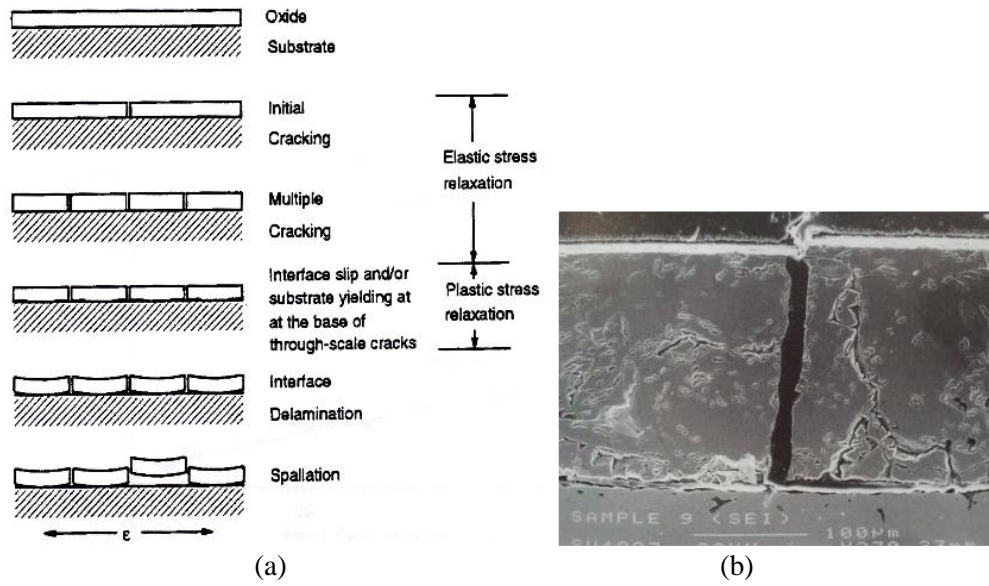


Figure 2.19: Figure 9: (a) Oxide scale failure mechanisms under tensile stresses [66]; (b) SEM images showing through-thickness cracks and initiation of interfacial damage [3]

The second mode of oxide spallation corresponds to the interface being weaker than the oxide scale and was observed at higher temperatures. In this mode the oxide scale slips along the interface. According to Beynon and Krzyzanowski, this sliding behaviour is explained by tangential viscous sliding between the oxide and the steel [67]. The sliding is possible if a critical stress is exceeded. This sliding is influenced by the irregularities at the oxide/metal interface.

2.4.2 Failure in compression : spallation

According to Evans [6], internal compressive stresses can also lead to spallation. The driving force for spallation is the release of energy accumulated in the oxide. The principle of Evans is that the spallation occurs when stored energy per unit volume in the oxide equals the one needed for decohesion (interfacial energy). The criterion to have the fracture can be calculated thanks to:

$$\lambda^2 \xi W^* = \lambda^2 \gamma_F \quad (2-7)$$

with λ^2 interfacial area, γ_F effective decohesion energy of the interface, ξ the thickness and W^* the stored energy per unit volume. The behaviour of the oxide depends strongly on the interface. According to Evans, two routes are possible (Figure 2.20):

- Strong interface leads to decohesion at the interface by an indirect way: wedging. In this case, where the interface is more resistant than the oxide scale, oblique shear cracks develop first under the longitudinal compression, with subsequent decohesion at the oxide-metal interface. The critical failure stress is [68] :

$$\sigma_c^s = \sqrt{\frac{(2\gamma_F)E_{ox}}{\xi(1-\nu_{ox})}} \quad (2-8)$$

- If the interface is weak, some decohesion areas are created at the interface by buckling. Buckling is progressive and is rumpling the surface of the metal as the temperature decreases. Oxide cracking and particle spalling come next. This time, the critical stress for the buckling is:

$$\sigma_c^b = \frac{1,22}{1 - \nu_{ox}^2} \left(\frac{\xi}{a}\right)^2 E_{ox} \quad (2-9)$$

with a the initial decohesion size (Figure 2.20). Some energy is released, and the fracture mode is known as a combination of opening (mode I) and shearing (mode II). Then, the local stresses enhance the propagation of buckling and tensile cracks appear where the curvature is maximal at the surface of the oxide and spallation occurs. If no cracks appear, buckling continues as long as there is energy stored in the oxide.

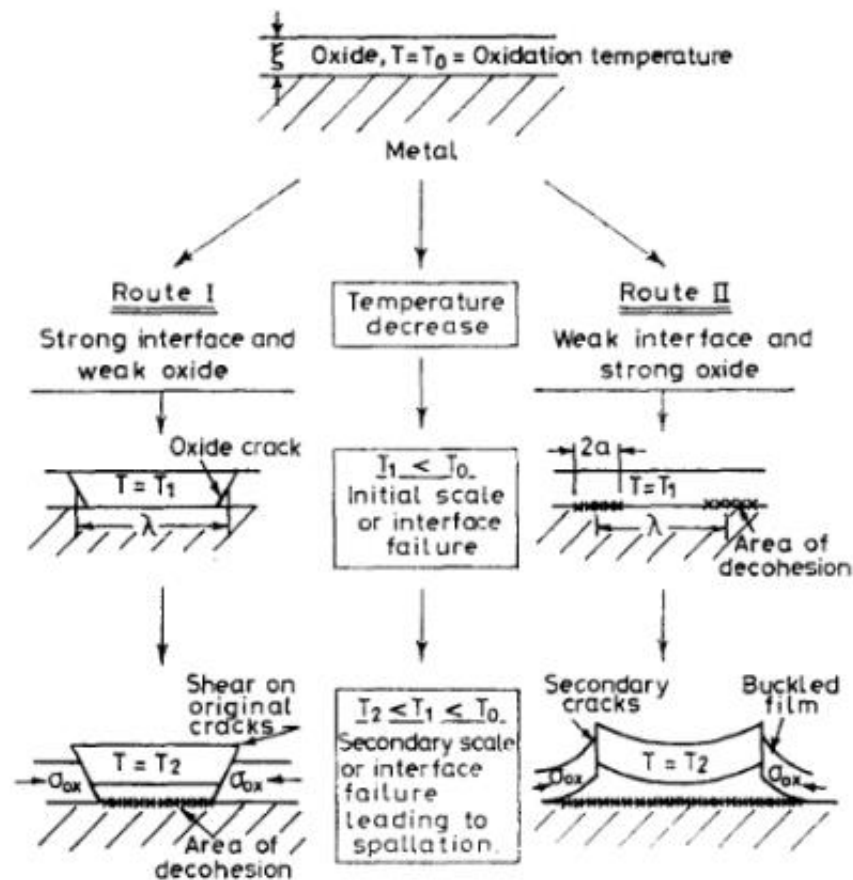


Figure 2.20: Schematic diagram showing two routes leading to oxide spallation during a downward temperature change.

Route 1: Compressive shear cracks develop first with subsequent decohesion at the oxide-metal interface.

Route 2: Interfacial decohesion occurs first, leading to unstable buckling and decohesion [69]

According to Evans, these internal stresses can be relaxed by creep or plastic relaxation for thin oxide films [60]. Relaxation of stress at high temperature may reduce the energy stored and so, influence the spallation behaviour. In case of a large relaxation, the spallation is delayed or avoided.

Using the critical compressive stresses σ_c^b and σ_c^s , a map for steel oxide failure (buckling or wedging) is drawn in the Figure 2.21 by Noh et al. [68]. The initial area a of decohesion is set arbitrarily to $10 \mu\text{m}$ for the buckling mode. For the wedging mode, three fracture energies are used, from 10 to 35 $\text{J} \cdot \text{m}^{-2}$. Figure 2.21 shows that with increasing thickness, the wedging fracture is favoured.

For a multi-layered oxide, the case is not as simple, the creep relaxation occurs mainly in one of the layers.

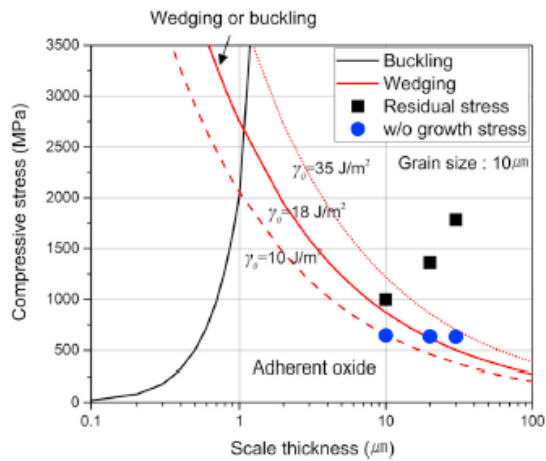


Figure 2.21: The failure map of the oxide scale with calculated compressive stresses [68]

2.4.3 Blistering

The blistering of oxide is possible during the oxidation due to decarburization. It can be detrimental when the oxide is rolled. This phenomenon has been well described by Kondo et al. [70]. It occurs in two stages : nucleation and growth (Figure 2.22). At the end the blister can collapse.

First, the nucleation is localised at the interface between oxide and steel, the scale is detached and is delaminated. This delamination is either attributed to the internal stresses or to gaz released at the interface depending on the adhesion of oxide :

- Under compressive stresses, the oxide can slip plastically at high temperature on the metal, interface damage results and pores are created [19]. Thus, the contact can be lost during the slip, the nucleus of a blister is created.
- In another way, decarburization by oxidation produces CO and CO₂, which migrate through the oxide scale. Inside the blisters, the gas compositions is mainly CO, CO₂.

Once the nucleation is done, the steel surface inside blisters is oxidized with the oxygen present there. Then, during the growth of the blister, again, the main driving force of blistering growth is internal stress.

The influence of the different phases on the blistering behaviour has been studied by Kondo et al. [71]. Blistering does not occurs when only Wüstite is present, blisters start to nucleate only when the scale layer structure changes from a Wüstite to a three-layered scale consisting of Hematite, Magnetite, and Wüstite: Hematite on the top surface acts as a barrier against gas outward permeation.

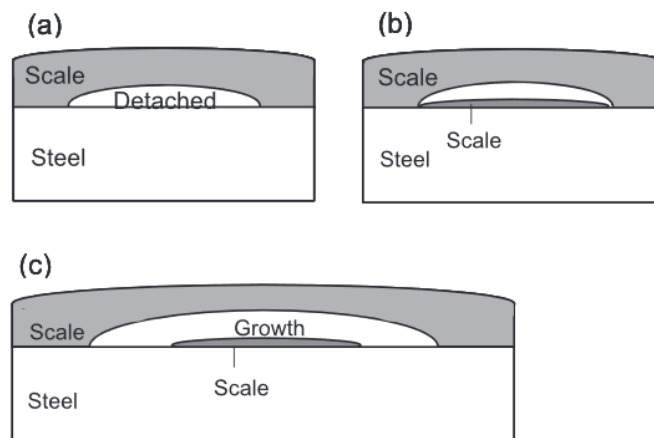


Figure 2.22: Mechanism of blister nucleation (a) blister nucleation (b) oxidation inside blister (c) blister growth

When the blister is large, fractures due to e.g. contact with rolls [72]. In this case, some more oxygen penetrates through the cracks and reacts with FeO to form Fe₃O₄, and also reacts with the substrate to form new oxide phases.

The influence of temperature on the blistering of steel oxide is studied by Matsuno [19]. Some low carbon steel specimens are oxidized at high temperature for a short period for a temperature between 800°C and 1200°C:

- The isothermal tests show that blistering appears after an incubation time (Figure 2.23(a)), the curves have a C- shape. The shortest incubation time is for 950°C. Under 800°C and above 1200°C no blisters appear. In this isothermal case, the blistering is generated by the growth stress.

- If oxidation is promoted during cooling (Figure 2.23(b)), this C-curve is enlarged and shifts to higher temperature and slightly lower oxidation time, due to the thermal stresses in the scale in addition to the growth stress. Under compressive stress, the lower part of the C-curve does not move but the top curve shifts to the left and upwards.

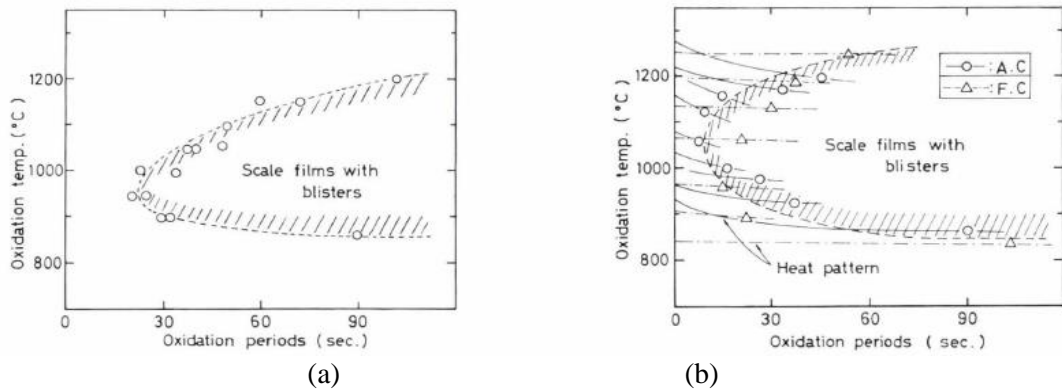


Figure 2.23: Blistering behaviours of scale films (a) in the isothermal oxidation (growth stress only) (b) in the oxidation during cooling (growth + thermal stress) [19]

As a conclusion, several cracking mechanisms are present within oxide. For a multi-layered oxide, the case is still more complex, failure can be localised at the interface between the phases or within one layer. Some of them are illustrated by Krzyzanowski (Figure 2.24) and Taniguchi (Figure 2.25) [73,74]

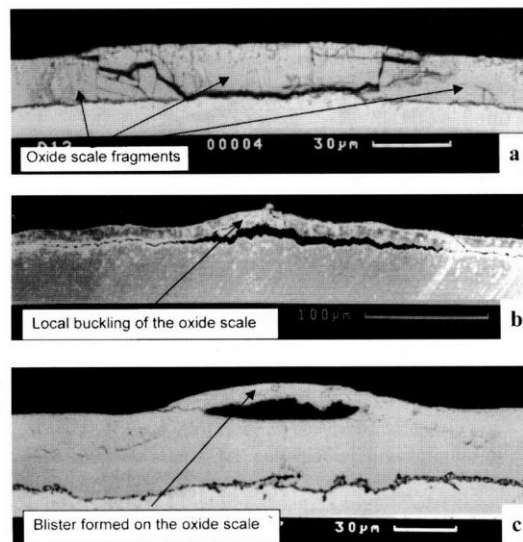


Figure 2.24: (a) oxide scale fragments (wedging mode), (b) local buckling of the oxide (c) blistering formed on the oxide scale [73]

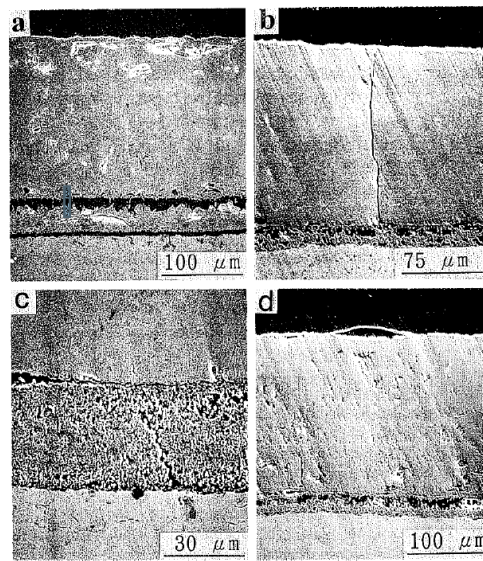


Figure 2.25 :(a) partial separation within FeO and at the scale/substrate interface, (b) through-scale crack almost normal to the substrate (c) crack at about 45 degrees to the substrate surface (d) blistering of a thin Fe_2O_3 layer [74]

2.5 Mechanical properties

Evaluation of mechanical properties of a film is essential to understand its behaviour. Lots of mechanical tests can be adapted to evaluate properties of oxide scale and its interface. However, due to the presence of the scale, the measurement is more difficult than for bulk materials (control of internal stresses, spallation, non-controlled deformation...). The next part is focused on the description of the methods that have been used at room temperature and at high temperature, and the corresponding oxide properties deduced. All the references are listed in the Table 2-2.

Table 2-2: Literature review of iron oxide properties (in bold : high temperature tests)

Oxide properties	Tests	Reférence
Hardness	Indentation	Takeda et al. [57] Vagnard [75] Charpentier et al. [76] Amano et al. [77] Deng et al. [78]
Elasticity	Indentation	Lee et al. [79] Zambrano et al. [80]
Plasticity	Indentation	Hidaka et al. [81] Charpentier et al. [76] Chicot et al. [82] Zambrano et al. [80]
	4-point bending test	Picqué [4]
Adhesion	Indentation	Ahtoy [47] Monteiro et al. [83]
	Scratch test	Noh et al. [68] Rosacz et al. [84]
	Tensile tests	Chandra-ambhorna et al. [85–87] Nilsonthi et al. [88]
	Inverted-Blister test	Mougin et al. [89]
	“Contact test”	Kondo et al. [70]
	Compression	Krzyzanowski et al. [62]
Ductile-Brittle transition	4-points bending test	Picqué [4]
	Compression	Suarez et al. [90]
	Rolling test	Filatov et al. [91] Li and Sellars [92]
Critical stress for fracture	Indentation	Sun et al. [93]
	Bending test	Picqué [4]
Toughness	3-points bending test	Graf and Kawalla [94]
	Tensile test	Hancock and Nicholls [65]
	Indentation	Amano et al. [77]

2.5.1 Oxide behaviour

2.5.1.1 Elasticity

Room temperature

The elasticity of a material can be evaluated with different methods : tensile test, vibrational methods, indentation.

According to Berns [95], the indentation reveals both parts, plasticity and elasticity. The total work of indentation W is divided into W_E and W_P , respectively the plastic part and the elastic part, the loading creates plasticity and the unloading is an elastic event. From the penetration/depth curve (P/h) (Figure 2.26), three types of information can be deduced, the maximum load P_{max} , the maximum displacement h_{max} and the elastic unloading stiffness S ($S=dP/dh$), which represents the slope of the initial stages of the unloading. According to Oliver and Pharr [96], the Young's modulus can be obtained directly from S for sharp indenters through the relation :

$$S = \beta \frac{2}{\sqrt{\pi}} E_r \sqrt{A_c} \quad (2-10)$$

with β a geometrical correction, A_c the contact area and E_r the reduced modulus :

$$\frac{1}{E_r} = \frac{1 - \nu_i^2}{E_i} + \frac{1 - \nu_s^2}{E_s} \quad (2-11)$$

with E_i , E_s the Young's moduli of the indenter and the material and ν_i , ν_s the Poisson's ratios of the indenter and the material (Figure 2.26). This formula can be adapted for different tip geometries, sharp (Vickers, Berkovich) or spherical.

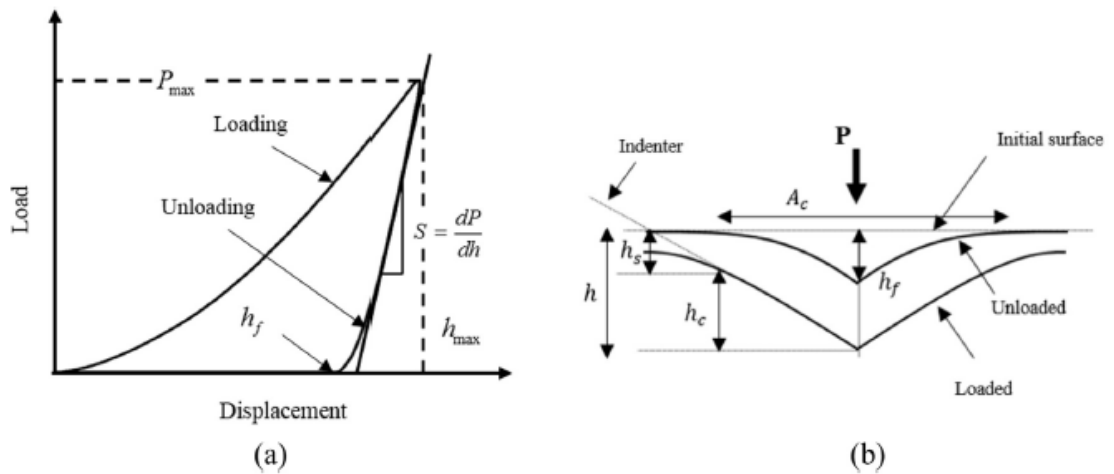


Figure 2.26: Schematic views of (a) the load-penetration depth curve and (b) parameters before and after the indentation by the Berkovich indenter [79]

It is difficult to evaluate intrinsic elastic behaviour of a thin film because of the influence of the bulk material (substrate). For thin films, the calculation of the reduced modulus is modified by Doerner [97] as a weighted average of film and substrate moduli, modified by indenter elasticity. Nano-indentations measurements show that :

$$\frac{1}{E_r} = \frac{1 - \nu_f^2}{E_f} \left(1 - e^{-\frac{\alpha t}{h_{eff}}} \right) + \frac{1 - \nu_s^2}{E_s} \left(e^{-\frac{\alpha t}{h_{eff}}} \right) + \frac{1 - \nu_i^2}{E_i} \quad (2-12)$$

with f , s and i referring to the film, the substrate and the indenter, h_{eff} is the indentation depth, t is the thickness of the film and α a coefficient which is fitted on indentations of tungstene film on silicon substrate ($\alpha=0.25$). This new E_r considers the influence of the substrate. For thick films and/or shallow indentations, this influence can be ignored and the first formula is used.

To avoid the influence of the substrate, the indentation can be made on a cross-sectioned surface through the thickness. In particular, Lee et al. and Zambrano et al. use indentation to measure the Young's Modulus of oxide on steel [79,80]. The comparison is made with other data from the literature in the Table 2-3. In reality, each oxide is different. Depending on the porosity, the condition of growth, the elastic properties can change. Globally, the tendency shows that Hematite is the stiffest of the three phases, followed by Magnetite, and Wüstite. Picqué considers the whole oxide, and the room temperature value is about 240 GPa [4].

Table 2-3: Room temperature Young's modulus of iron oxides

Oxide Young's Modulus (GPa)	FeO	Fe ₃ O ₄	Fe ₂ O ₃	Whole oxide	Fe
Roberston and Manning [26]	130	208	219		
Sasaki et al. [56]	130	136	234		210
Lee et al. [79]	-	151	-		
Fletcher et al. [98]	-	-	-		210
Picqué [4]	-	-	-	240	
Zambrano et al. [80]	125	159	220		

High temperature

The Young's modulus value are highly dependent on the temperature. The stiffness of oxide decreases at high temperature. Morrel proposes a formula to evaluate the high temperature values:

$$E = E_{RT} [1 + n(T - 25)] \quad (2-13)$$

with $n = -4,7 \times 10^{-4}$, E_{RT} the room temperature modulus and T the temperature in °C [99].

For a value of 240 MPa at room temperature, the corresponding Young's modulus is plotted in the Figure 2.27. By considering the whole oxide, the calculated value is between Hematite and Wüstite, and in agreement with Hancock and Nicholls [65]. The resonant frequency method is used by Sasaki et al. to evaluate Young's modulus value on sintered specimen at high temperature [56] (Figure 2.27).

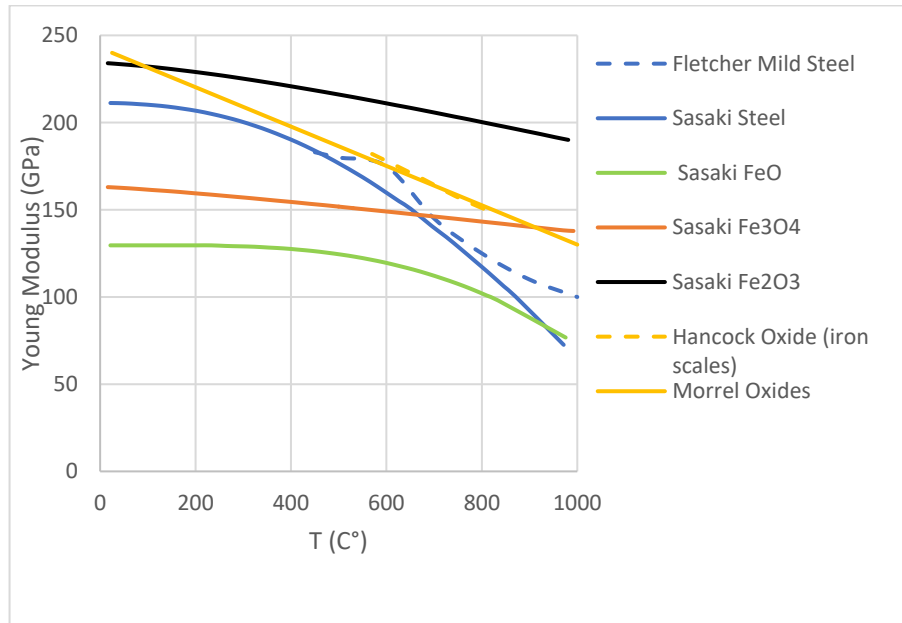


Figure 2.27: Evolution of Young's modulus with temperature. Blue (Steel), Green (Wüstite), Orange (Magnetite), Black (Hematite) and Yellow (iron oxides). After [56,65,98,99]

The elasticity of oxides has been evaluated both at room and high temperature.

2.5.1.2 Plasticity

Room temperature

The oxides are commonly considered to be elastic and brittle. However, some creep behaviour is found by micro-indentation at room temperature for Magnetite. It shows some viscoplasticity of the material. By applying low loading rates, the material has time to undergo plastic deformation, and the creep behaviour leads to an increase of the maximum depth of indentation. The apparent hardness of Magnetite is also modified by the dwell time [82]. In fact, one of the effects of creep in indentation is bowing-out, which manifests by the increasing of the contact indentation depth whereas the loads start to decrease; it is observed for short dwell time (Figure 2.28). If the dwell time is increased, it suppresses this effect by allowing the accommodation of the material and stress homogenization. With this precaution, the visco-plastic properties (obtained by varying the loading rate) of the materials have no influence on the elastic behaviour.

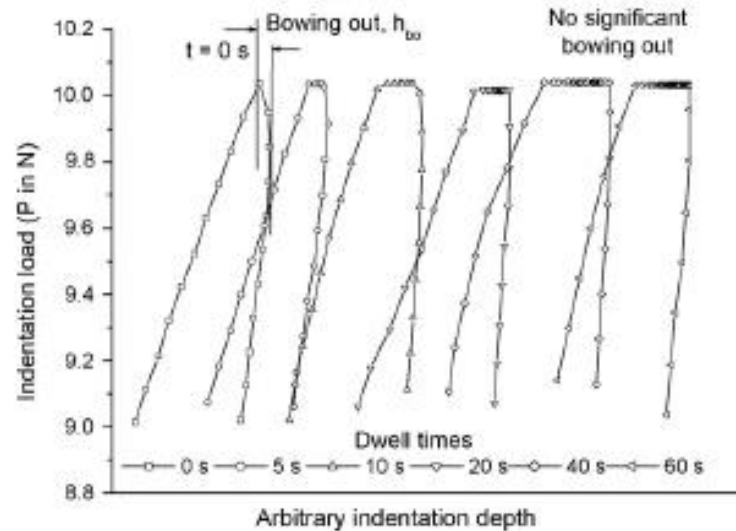


Figure 2.28: Bowing Out in instrumented indentation as a function of dwell time [82]

Zambrano et al. use indentation to quantify the elasto-plastic behaviour of oxides at room temperature from low carbon steel oxidized at 1200°C [80]. Indentations are made on oxide cross-sections that have been previously polished.

During the unloading, from the maximum displacement (h_{max}) and residual displacement (h_f), the ratio of elastic recovery is calculated, $0 \leq h_f/h_{max} \leq 1$. The lower limit corresponds to a fully elastic deformation while the upper limit corresponds to a purely plastic behaviour. This ratio is decreasing from the surface to the inner oxide. The elastic recovery ratio is higher for Hematite, than Magnetite and Wüstite.

The creep behaviour of each phase is analysed by holding of the maximum load for several seconds. The creep displacement is $(h-h_0)$ where h_0 is the displacement at the maximum peak load for 0 s holding time and h the displacement after holding time. After the initial increase of $h-h_0$ during the first 10 seconds, a linear asymptote is reached.

This deformation mechanism at room temperature is not clear : it could be due to volumetric densification mechanism or to a macroscopic displacement of the indenter due to the porous structure of oxide. Depth creep relaxation increased from the outer to the inner oxide layers and for the holding time.

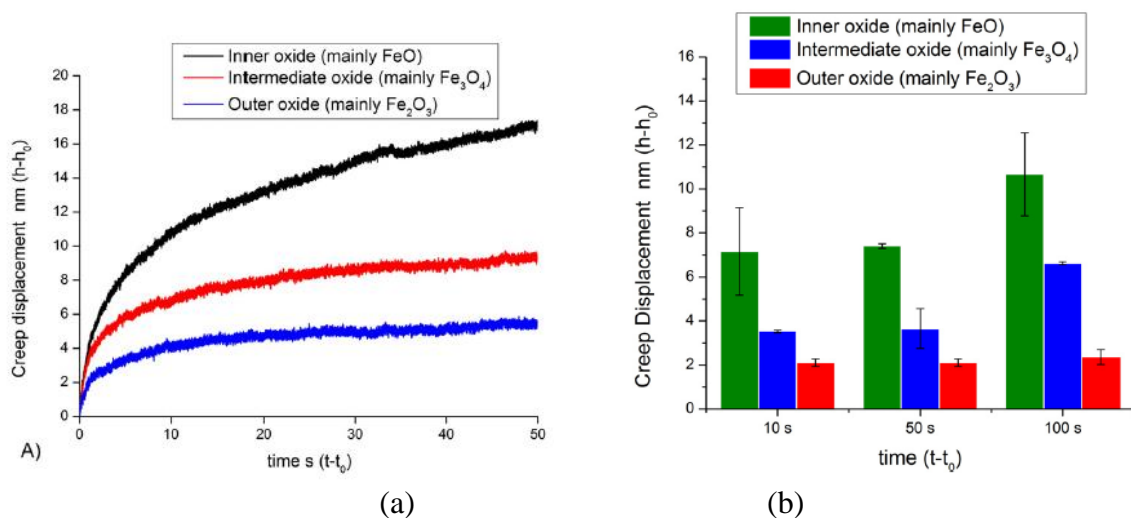


Figure 2.29: (a) Creep displacement vs holding time for each oxide layer at holding time up to 50 seconds at 5000 μ N indentation load at Room Temperature, for low carbon steel oxidized at 1200°C (b) Creep displacement vs holding time for each oxide layer, for holding times of 10, 50 and 100 seconds [80]

High temperature

However, at the temperatures reached during hot rolling, the scale is clearly co-deformed with the steel. Hidaka et al. quantify the plastic behaviour of iron oxides with tensile tests [81]. The samples are prepared by oxidation of pure iron specimens under controlled atmosphere (H₂, H₂O, O₂, N₂). For lower temperatures (up to 600°C for FeO and up to 700°C for Fe₃O₄), the oxide is brittle. Above this temperature, plasticity occurs by two different mechanisms :

- work hardening (for FeO at 700-900°C and for Fe₃O₄ at 800-1100°C); it corresponds to the dislocation glide or the grain boundary sliding.
- “steady-state” deformation associated to dislocation climb (dislocation creep) or diffusion creep (for FeO at 1000-1200°C and for Fe₃O₄ at 1200°C).

Fe₂O₃ does not display ductility but fracture by cleavage.

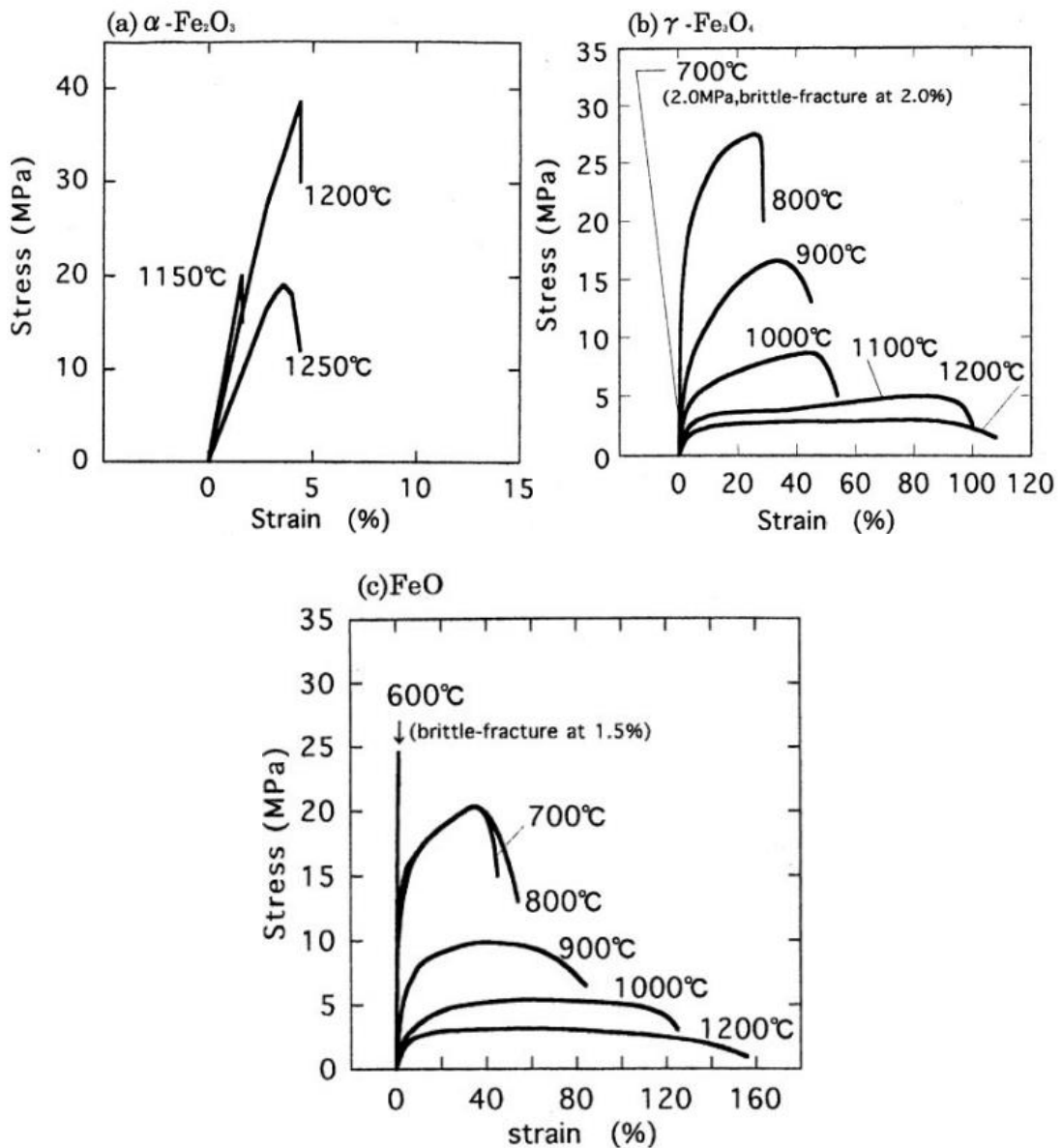


Figure 2.30: Stress–strain curves of the tensile test specimens for strain rate of $2.0 \times 10^{-4} \text{ s}^{-1}$ (a) Hematite (b) Magnetite and (c) Wüstite [81]

Piqué also characterises visco-plasticity of the oxide by using 4-points bending tests (4HBT) at high temperature [4]. One-side oxidation (the other side is protected by a coating) is performed at 900°C in a controlled atmosphere for several minutes, and then the sample is brought to the test temperature (between 600° C and 1000°C). The visco-plastic behaviour is taken as a power-law relation:

$$\sigma = K(T)\varepsilon^{n(t)}\dot{\varepsilon}^{m(T)} \quad (2-14)$$

with K the consistency, the strain hardening coefficient n and m the strain rate sensitivity coefficient. The visco-plastic steel properties of the metal are determined at low strain and very low strain rate typical for pre-bite deformation which first fractures the oxide, with an inverse method from the 4-point bending test of non-oxidized samples. For the oxide properties, in the presence of cracks during the test, the loading curves are not usable. Only samples without cracks are thus considered for the stress-strain curve determination. The 4-point-bending tests show that the visco-plastic behaviour follows the same trend, for the oxidized and non-oxidized specimens after the elastic linear slope (Figure 2.31 (a)). The same n coefficient is chosen because more precise determination of n is complicated with the available data. Thus, considering that the tests are done with the same strain rate, K_{ox-app} the apparent oxide consistency is introduced :

$$\sigma_{ox} = K_{ox-app}\varepsilon^{n_{steel}}\dot{\varepsilon}^{m_{steel}} \quad \text{with} \quad K_{ox-app} = K_{ox}\dot{\varepsilon}^{m_{ox}-m_{steel}} \quad (2-15)$$

Then, the visco-plastic parameters are identified using the hardness ratio giving quasi-identical results to those obtained with inverse analysis.

$$H = \frac{H_{ox}}{H_{steel}} = \frac{K_{ox-app}}{K_{steel}} \quad \text{and} \quad \text{finally } \sigma_{ox} = H \cdot \sigma_{steel} \quad (2-16)$$

The ratio H is dependent on the strain rate and the temperature (Figure 2.31 (b)). The hardness ratio determined is compared with the ratio between FeO and Fe determined by Vagnard using high temperature Vickers hardness testing [75]. This identification is made for the non-cracked specimen (above 800°C) and is extrapolated (dashed lines) to lower temperature using the hardness ratio of Vagnard to respect the same tendency.

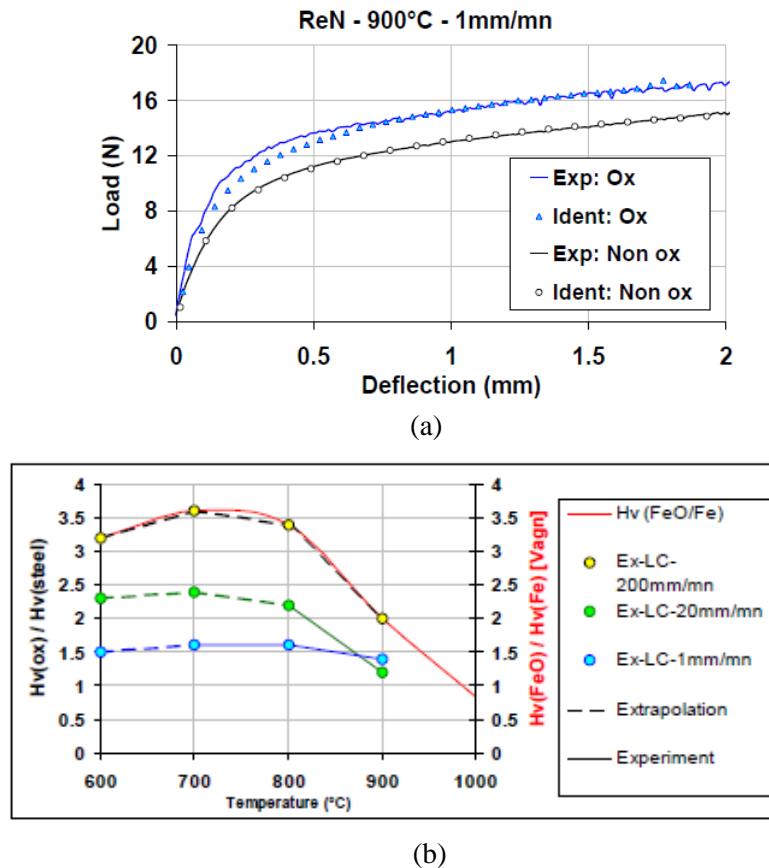


Figure 2.31: Superposition of experimental and numerical load-deflection curves obtained using 4-PHBT at 900°C (blue curves are for the oxidized specimen and black curves for the non oxidized one) (b) Identification of the hardness ratio between oxide and steel to evaluate visco-plastic behaviour of oxide at high temperature [4]

At high temperature, the oxide is ductile and can be deformed plastically.

2.5.2 Hardness

Before mechanical characterisation, different ways to design samples are possible : directly from the oxidation of steel or iron specimens, or by synthetic reaction. The properties could differ depending on the methods used.

Indentation can be used on an oxide scale, but some conditions have to be respected to limit the influence of the substrate. The total thickness of the film has to be 10 times larger than indentation depth. The width of the specimen has to be 3 times larger than half-diagonal of the indent. This precaution is essential to suppress the edge effect.

2.5.2.1 Room temperature

The hardness of oxides has been evaluated by several authors and results are compared in (Table 2-4). Some differences are noted between the authors, probably due to the systematic instrumental effects (tip defects, indentation size effect, formula...). However, ratios of hardness between each phase are similar, except for Graf and Kawalla: the latter study is based on the use of pure powder, compressed and heat treated. It differs from the “real” oxides.

Table 2-4: Hardness at Room Temperature of iron oxides, reported in the literature

Oxide Hardness (GPa)		FeO	Fe ₃ O ₄	Fe ₂ O ₃	Fe ₃ O ₄ /FeO	Fe ₂ O ₃ /FeO
Takeda et al. [57]	Oxidation at 1000°C	3.5	4	6.7	1.15	1.9
Zambrano et al. [80]	Oxidation at 1200°C	5.5	6.5	12	1.15	2.2
Westbrook [100]	-	4.9	5.4	9.0	1.10	1.8
Chicot et al. [101]	natural steel oxidation	-	6.3	8.2	-	-
Graf et Kawalla [94]	From compressed powder	3.9	5.9-6.9	8.8	1.6	2.25
Amano et al. [77]	Oxidation at 1000°C	3.5	3.9-4	6.7-7.6	1.15	~1.8

2.5.2.2 High temperature

Oxide on steels (Wüstite, Magnetite and Hematite) are synthesized by Takeda et al. using powder metallurgy and controlled oxidation to have high purity components [57]. The high temperature indentation reveals decreasing hardness with increasing temperature (Figure 2.32 a). The indenter used are diamond and sapphire square-based pyramids. FeO tends to have the lowest hardness, well below Fe₂O₃ and Fe₃O₄. The comparison at 1000°C between sintered specimens and scale formed on iron is made in Table 2-5. Some differences for the ratios are noted, higher value for the scales formed on iron. However the hardness of Fe₂O₃ formed on the steel is much larger than synthesised Fe₂O₃ at 1000°C. The authors consider that the hardness of Fe₂O₃ formed on the steel is not measured precisely because its thickness is a few or several tens of mm.

Table 2-5: Comparison of Hardness at 1000°C between sintered specimen and scale formed on iron by Takeda et al. [57]

Oxide Hardness at 1000°C (GPa)	FeO	Fe ₃ O ₄	Fe ₂ O ₃	Fe ₃ O ₄ /FeO	Fe ₂ O ₃ /FeO
Sintered specimen	0.0436	0.0505	0.0734	1.15	1.7
Scale formed on iron	0.05	0.08	0.53	1.6	10.6

For specimens after iron/steel oxidation, a similar tendency is noted by Vagnard [75] with a diamond indenter; the hardness of pure iron is higher than FeO above 950°C. i.e. after the transformation of ferrite into austenite (Figure 2.32 c).

Thus, at 600°C, the hardness of FeO is 40 Hv according to Takeda et al. (synthetic oxides), and 90 Hv according to Vagnard (oxidation of iron).

The plasticity of Magnetite is studied by Charpentier et al. [76] (Figure 2.32 (b)), the plasticity of Magnetite is present even at room temperature by microhardness tests, that cause "slip lines" to appear in the vicinity of the indentations. The hardness of Magnetite is also decreasing with the increasing temperature, in this case, the Vickers indenter is made out of sapphire. Magnetite is found harder than Wüstite at any temperature.

Finally, Amano et al. evaluate the hardness of each phase after an oxidation of low carbon steel at 1000°C for 18ks on cross-sections [77]. The indenter is made is sapphire. The hardnesses of Magnetite, Wüstite and Steel are respectively 0.08, 0.05 and 0.12 and GPa at 1000°C.

The main conclusion is that the hardness of Wüstite and Magnetite are higher than the hardness of steel when temperature is lower than 900°C. Globally, all oxide hardnesses decrease with the increasing temperature

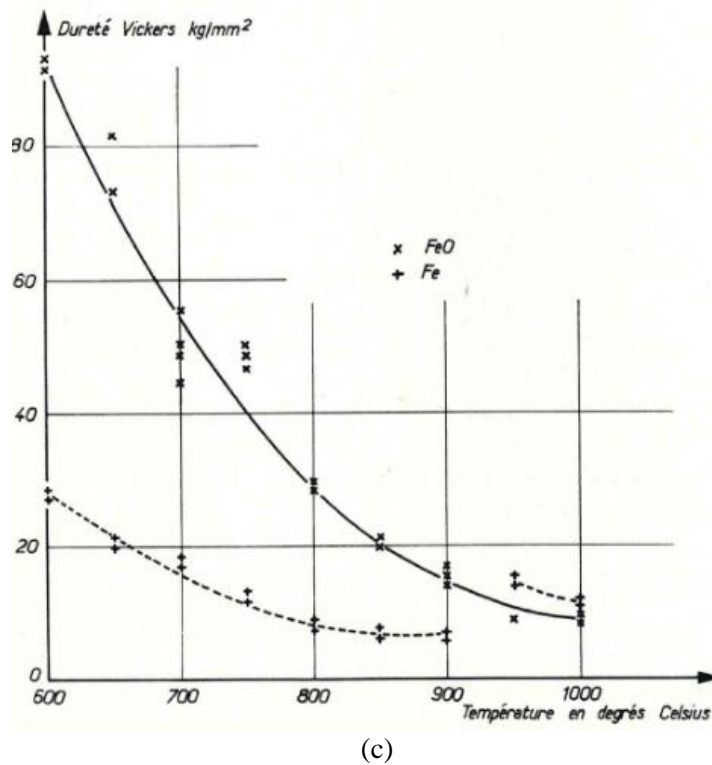
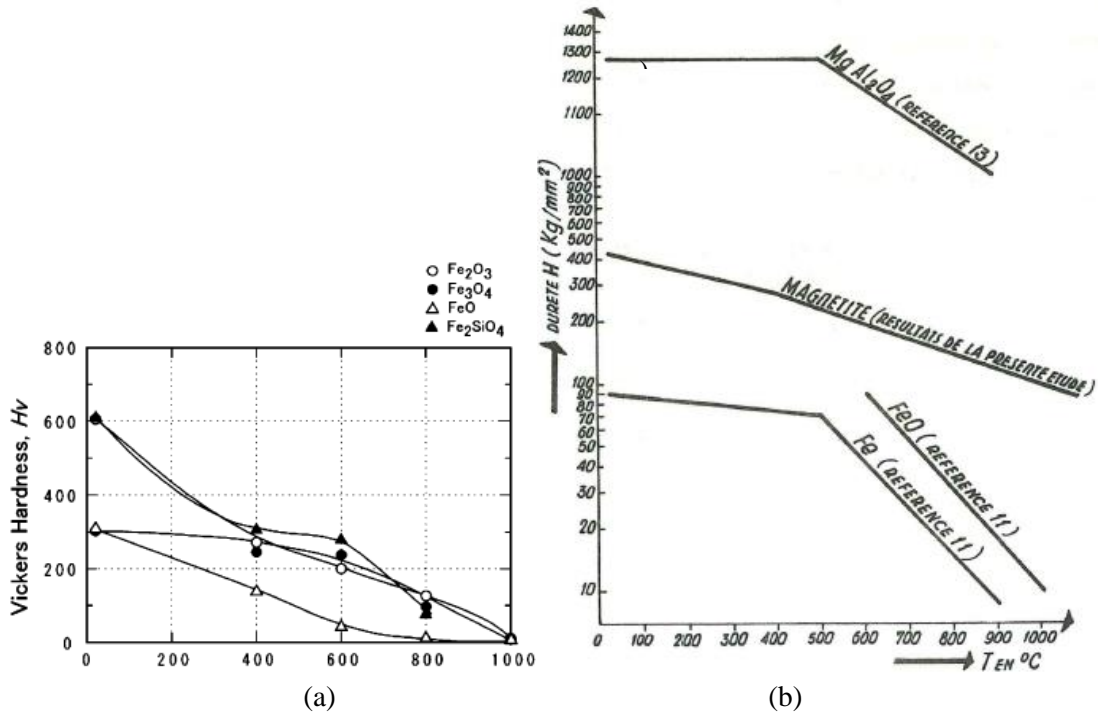


Figure 2.32: (a) High temperature hardness of the synthetic iron oxides [57] (b) hardness value of Magnetite, iron and Wüstite at high temperature ([76]) (c) hardness value of FeO and Fe [75]

2.5.3 Ductile-brittle transition behaviour of oxide

Oxide also displays brittle characteristics at room temperature (see Figure 2.36 below, which shows cracks in FeO after Vickers indentation). Above the elastic limit, stress relaxation can take place by mechanical failure. By increasing temperature, the ductile behaviour of oxide has been reported by many authors.

Oxide scale behaviour has also been determined. According to Picqué [4] who used hot bending, the behaviour of oxide can be divided in three categories (Figure 2.33):

- At low temperature (below 700°C), the oxide scale is brittle and the interface is strong. During 4-point bending tests, through-thickness cracks appear perpendicular to the stress direction. They are intergranular cracks which multiply and propagate across the specimen width as the bending strain increases.

- At intermediate temperature (above 700°C), the oxide scale is more plastic and can be deformed without any crack. Nevertheless, the interface seems to be weaker. This leads to interfacial decohesion. This ductile-brittle transition is affected by the strain rate. Indeed, crack number significantly increases with strain rate. Cracks can thus be initiated at higher temperatures if the strain rate is high.

- At high temperature (above 1000°C), a through-scale cracks network is observed due to thermal stress and to the steel phase change (ferrite⇒austenite with a contraction which puts the oxide in compression at heating and in tension at cooling). It is not possible to determine if these oxide cracks appeared on heating, or by expansion on cooling after the test. This effect must always be kept in mind when addressing high temperature tests, above 900°C.

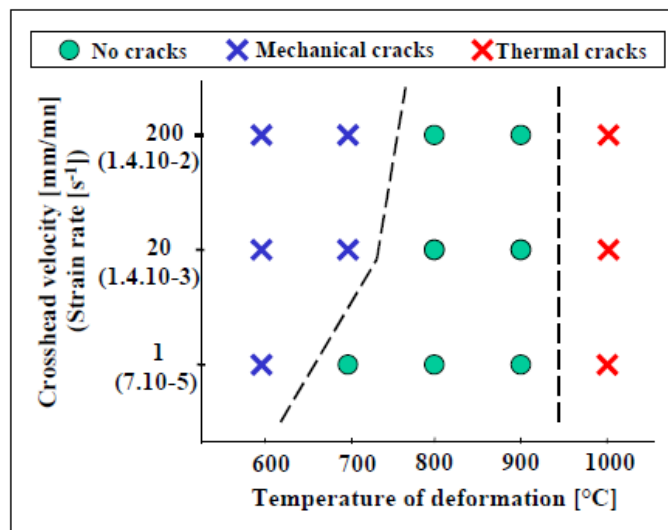


Figure 2.33: Schematic representation of oxide scale damage in 4-PHBT as a function of temperature and strain rate. Plastic strain $\sim 0.5\%$ [4]

Filatov et al. [91] make rolling tests with a 300 mm roll diameter, reduction from 40 to 60%. The thickness of oxide is between 5 to 30 μm . The temperature tested is between 800 and 1050°C. Two grades are tested : an interstitial free steel and a fine-grained low pearlite structural steel (Figure 2.34 (a)). They draw the same conclusion as Picqué: for low temperature, oxide is extremely brittle. No deformation occurs with the consequence that the scale breaks and undeformed scale fragments remain. At higher temperature (above 950°C), oxide undergoes ductile deformation and steel and scale layer deform in the same manner. At intermediate temperature (800/900°C), a mixed situation is depicted. In this test, the behaviour is clearly linked to the percentage rolling reduction. By increasing the reduction, the brittle domain range is extended to higher temperatures and low reduction leads to an increase of ductility.

Similar tests are done on C-Mn steel by Li and Sellars for 100 μm oxide thickness and 0.14 m/s rolling speed [92]. The study confirms the ductile-brittle transition of oxide and the strong sensitivity to rolling temperature and reduction (Figure 2.34 (b)). For the brittle behaviour, cracks are oriented

transverse to the rolling direction. However, the laboratory conditions are quite different, the contact time for real industrial strips is much lower (the slabs speed is higher) and thus, the profile temperature within oxide is different. It should be noted that no fracture is observed due to the Austenite-Ferrite transition as observed by Picqué (Figure 2.33).

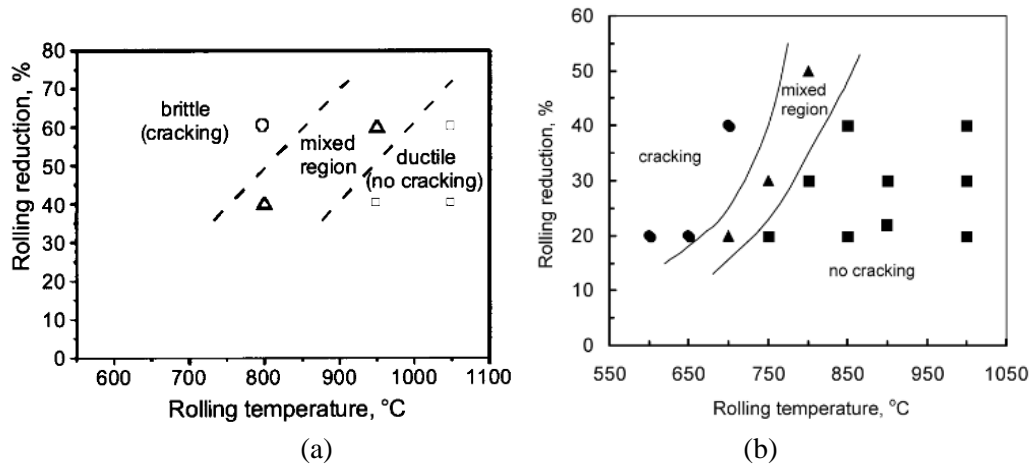


Figure 2.34: Oxide scale behaviour during hot rolling of (a) an interstitial free steel and a fine-grained low pearlite structural steel [91] (b) C-Mn slabs [92]

Finally, plane strain compression tests are done by Suarez et al. to evaluate this transition [90]. After an oxidation at 1050°C for 10 seconds, compression is done with an equivalent strain rate of 10 s⁻¹. The thickness of oxide is 18–25 μm, which is the range expected for tertiary scales. The oxide behaviour is assigned as brittle, mixed or ductile in agreement with the previous studies. The results of this study are plotted in the Figure 2.35 and the previous studies are added for comparison.

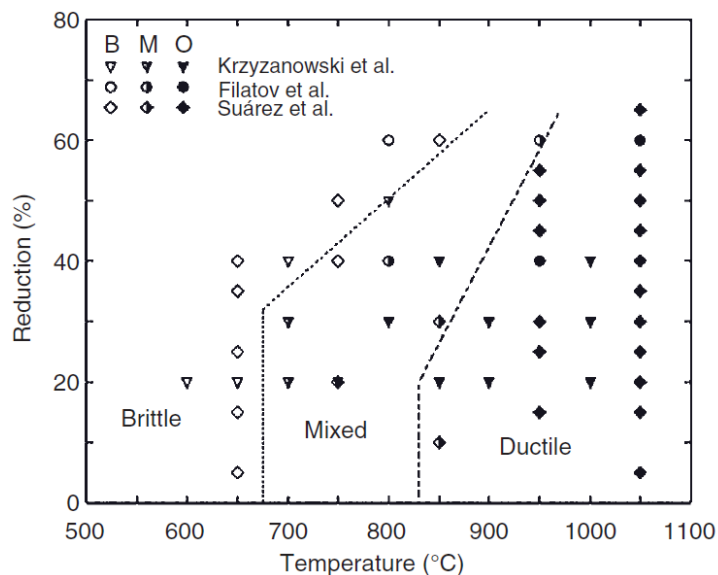


Figure 2.35: Plastic behaviour of the oxide scale as a function of temperature and thickness reduction [90–92]

A ductile-brittle transition of oxide is highlighted, this transition temperature depends on the strain and the strain rate. Different tests indicate a transition between 650 and 800°C.

2.5.4 Measurement of fracture toughness

Toughness is the ability to resist crack growth and to absorb energy during deformation. The measurement of toughness indicates the energy needed to create and propagate a crack. The crack may develop either through the film, or along the interface. The latter, interfacial toughness, is relevant to understand the adhesion of the film.

The toughness of Wüstite, Magnetite and Hematite are tested by Graf and Kawalla at room temperature [94]. The specimens are formed by sintering (compression of a pure oxide powder and with a heat treatment to realise a material cohesion). The final sintered specimens are tested with DIN ISO EN 15732 for ceramics (fracture toughness obtained with three-point bending fracture test of a single-edge-precracked beam specimen [102]). The calculated critical stress intensity factors at room temperature are quite similar for the 3 phases (Wüstite : $2.2 \text{ MPa}\cdot\text{m}^{1/2}$ Magnetite: 1.6 and Hematite: 1.2 (Figure 2.37)). With increasing the oxygen content the critical stress intensity factor decreases.

Hancock and Nicholls [65] evaluated iron scale toughness of Armco iron at high temperature using tensile tests. The initiation of crack is detected by a measurement of the resonant frequency. The tests are conducted between 570°C and 852°C for thickness of oxide between 36 and $390\mu\text{m}$. The lower the thickness is, the more "resistant" to fracture the scale is (Figure 2.37 and Table 2-6). This behaviour is similar to ceramic material, i.e. a greater probability of finding a "large" defect in the Griffith sense, i.e. one that will propagate for a low stress. The toughness is increasing by increasing the temperature. However, these conclusions are to be treated with caution because few data are available (1 measurement for a temperature/thickness pair).

Table 2-6: Calculated fracture toughness parameters for oxide scales on iron [43]

Temperature ($^\circ\text{C}$)	Scale thickness (μm)	a (μm)	K_{IC} ($\text{MN}\cdot\text{m}^{-3/2}$)
570	36	715	1.82
674	111	882	3.1 ± 1.4
743	206	1642	3.5 ± 1.4
800	325	2584	7.7 ± 2.5
825	390	3105	11.7 ± 1.7

Amano et al. use indentation to evaluate toughness of FeO at room temperature using a square-base diamond pyramid as an indenter [77]. The method is directly based on the evaluation of the radial crack length generated by the Vickers indent [103]. The indentation is made on a cross-section to avoid the substrate influence. The presence of radial cracks indicates the brittle behaviour of FeO at room temperature (Figure 2.36). The fracture toughness of FeO is between 1.3 to $2.1 \text{ MPa}\cdot\text{m}^{1/2}$ depending on the temperature of oxidation, the alloying elements and the presence of Fe_3O_4 precipitates. These values are close to Graf and Kawalla's study, in spite of measurements being done with two different tests.

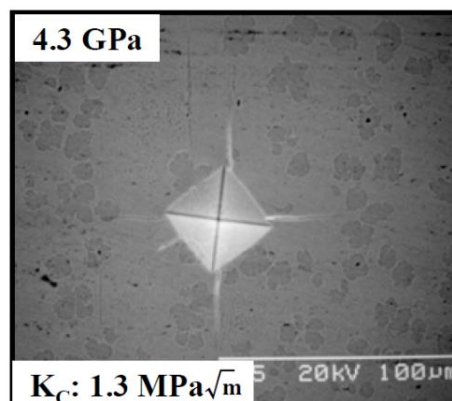


Figure 2.36: SEM micrograph of 5 N Vickers indentation on the cross-section of FeO (Fe exposed to oxygen at 1273 K for 18 ks) [77]

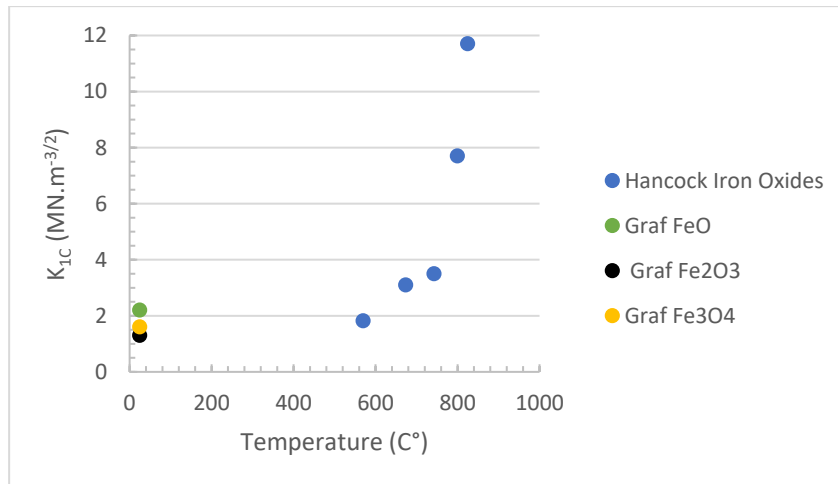


Figure 2.37 Evolution of toughness of oxide with temperature (after [65,94])

2.5.5 Critical fracture stress

From the toughness data calculated experimentally, it is interesting to evaluate the critical stress that can initiate cracks.

By considering the oxide purely elastic and brittle, the stress relaxation is possible only by formation of transverse crack (perpendicular to the interface metal/oxide) when a stress criterion is reached. Based on the elastic fracture mechanics :

$$\sigma_c = \frac{K_{1c}}{f\sqrt{\pi a}} \quad (2-17)$$

where K_{1c} is the critical stress intensity factor (or toughness), f is a constant depending on the geometry of the notch and \bar{a} a characteristic size of the equivalent defect (evaluated by micro-section observations). For the study of Hancock, the critical stress for the fracture can be calculated. By considering, that the defect size depends on the thickness, and that K_{1c} is independent of temperature, the critical tensile stress is calculated with the equation (2-17) for different thicknesses (red plot in the Figure 2.38). The critical stress increases for higher temperature and thicker oxide.

Piqué has also identified the critical stress for the initiation of cracks with 4-point bending test at high temperature [4]. In order to detect the cracks occurring during the tests, the equipment is instrumented with an acoustic emission (AE) device. The critical stresses have been determined by coupling FEM simulations results and AE measurements. Indeed, AE detects the instant of crack initiation. The numerical simulation of the tests gives the corresponding maximal tensile stress in the oxide scale. Maximal principal tensile stress values obtained in oxide scale during 4-PHBT simulations (with numerical cracking disabled) are represented in Figure 2.38 for each strain rate and temperature. Points in yellow report on crack-less experimental 4-PHBT. In red are represented those in which cracks have been experimentally observed.

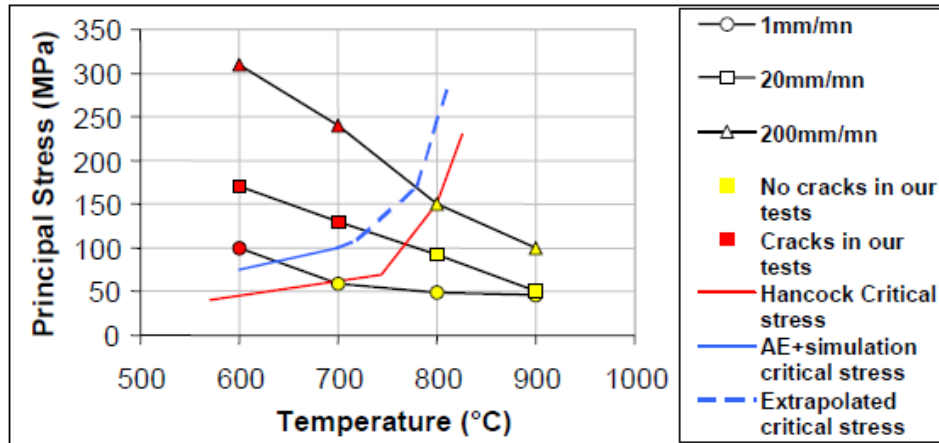


Figure 2.38: Critical tensile stress for a 100µm thick oxide obtained by 4-point-bending test [4]. 3 crosshead velocities are plotted (1mm/min), (20mm/min) (200mm/min), corresponding respectively to strain rates of $7.10^{-5}s^{-1}$, $1.4.10^{-3}s^{-1}$ and $1.4.10^{-2}s^{-1}$. The red curve corresponds to the critical stress calculated by Hancock [65]

In the study of Picqué [4], the influence of several parameters is discussed:

- Strain: the number of cracks increases with strain until a dense network of equidistant cracks is obtained. Distance between cracks decreases when the strain increases and increasing strain also facilitates the crack propagation through the specimen width.
- Strain rate: a high strain rate sensitivity has been evidenced. The crack number significantly increases with strain rate. Cracks can be promoted at higher temperatures by using higher strain rates.
- Scale thickness: when the thickness decreases, a slight increase of the crack number and a stronger adherence of oxide scales on steel substrates are observed.
- Steel grade: steel grade has a significant influence on the oxide scale behaviour during 4- PHBT, principally in terms of adherence at the interface.

The fracture toughness of oxide at room temperature is referenced. At higher temperature, few studies report the evolution of the fracture behaviour.

2.5.6 Adhesion

In the literature, several methods are used to determine adhesion of oxide at room temperature: indentation [47,83], scratch test [68,84], tensile tests [85–88], inverted blister-test [89]. Two more studies report the evolution of adhesion of oxide at high temperatures [62,70].

2.5.6.1 Indentation

Ahtoy uses room temperature (RT) Vickers indentation to study the interface of low carbon oxidized steel at room temperature [47].

It is an application of the method described by Drory and Hutchinson [104]. A 60° “brale” indenter (a cone ending in a spherical cap) is used to solicit a TiAl6V4 substrate coated with diamond. The thin film delaminates under the pressure, and a model is used to calculate the energy release G during the delamination. In this case, the interface has to be weak to allow the delamination and the thickness of oxide has to be small in comparison to the indentation depth.

Ahtoy is mainly focused on alloying elements such as P, Al and Si for a P-containing steel oxidized at 1000°C. Samples are oxidized for different times and different temperatures. For a 10 seconds indentation, plastic deformation creates compressive stresses in the steel, which deforms the oxide and induces delamination (Figure 2.39). The indentation depth is larger than the thickness of oxide. The value of adhesion energy is calculated as G_c (critical strain energy release rate), it depends only on the radial ε_r and circumferential ε_θ strains, the properties of the oxide (E and ν) and the thickness of the oxide t are calculated according to the formula:

$$\frac{2G_c(1 - \nu^2)}{E \cdot t} = \varepsilon_r + \varepsilon_\theta \quad (2-18)$$

Both components of strain (ε_r and ε_θ) are created by the indentation and the residual stresses. The strains due to the indentation (depending on R) are evaluated with U , the radial displacement of the metal during the indentation, using a finite element method (from the study of Vasinonta and Beuth [105]). The residual strains in the oxide are mainly due to the thermal stresses. internal stress is not calculated before the indentation, it is set to -358 MPa arbitrarily (from literature) .

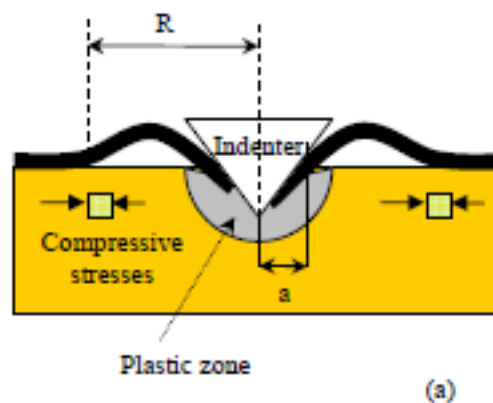


Figure 2.39: Indentation test and delamination of the oxide [106]

The adhesion energy of oxide is calculated between 0 - 350 J.m⁻² as shown in the Figure 2.40 (a). This study shows an improvement of the adhesion with the addition of phosphorus (0.15 wt%). 940°C is the temperature of an eutectic Fe₃(PO₄)₂, this component is present at the interface, and above this critical temperature, the liquid eutectic infiltrates the grain boundaries, creating an anchoring effect. The enrichment of phosphate at the metal-oxide interface increases scale adhesion. The same tests are

done for aluminium- and silicon-enriched specimens after 1000°C oxidation [47], the indentation test shows that for the first minutes of oxidation, adhesion increases due to the enrichment of the interface in Si-Al oxides. But, for longer oxidation time, the microstructure changes, the internal layer becomes porous, and thus the adhesion decreases (Figure 2.40(b)).

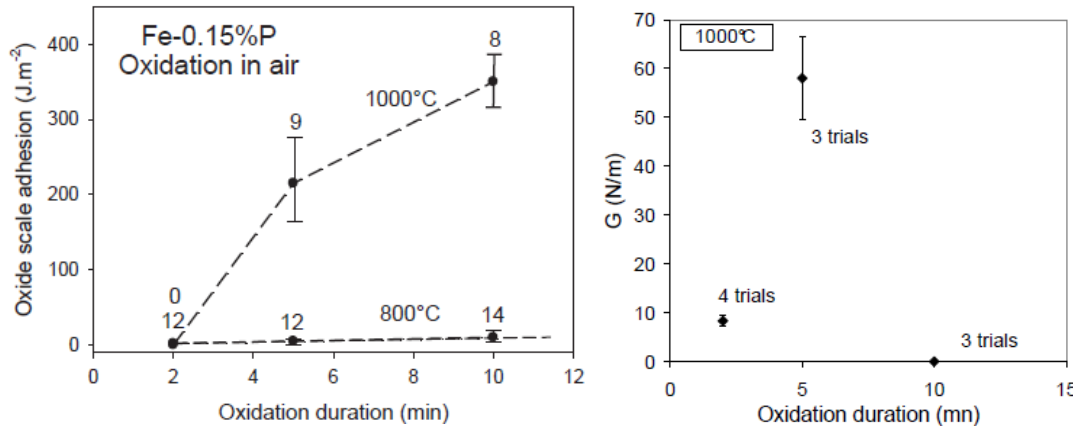


Figure 2.40 : Room temperature adhesion energy measured by indentation as a function of oxidation time on a) scales grown on P-containing steel at 800 and 1000°C (b) specimen containing 0,44% Si and 0,1% Al oxidized at 1000°C during 2, 5 and 10 minutes [47]

Indentation is also used by Monteiro et al. [83] for high speed steel (% in weight; C=1.5/2.5; Cr=4/7,5; Mo=2/2.3, W=2/3.9 and V=4.8/8.1) to estimate interfacial fracture strength. Samples are oxidized at 650 °C for 14.4 ks and indented with a Rockwell C diamond. After the indentation, the extent of oxide cracking around the indent is defined manually and the area of the disbonded oxide is calculated with an image analysis system. This study highlights that the presence of water during the oxidation affects the adhesion. For dry air, fracture occurred mainly at the oxide interface, and by increasing the water vapour (up to 12.2%), the fracture appeared to be largely cohesive and occurred at the chromium-containing spinel/Magnetite interface. According to the authors, an explanation could be that the porosity of the outer layer of Magnetite increases with increasing water vapour. In this case, pores could provide a mechanism for crack blunting so that interfacial damage arising from the indentation test might be expected to be less severe for the more porous structure. Thus, “measured adhesion” of the scale is increasing with the amount of water vapour.

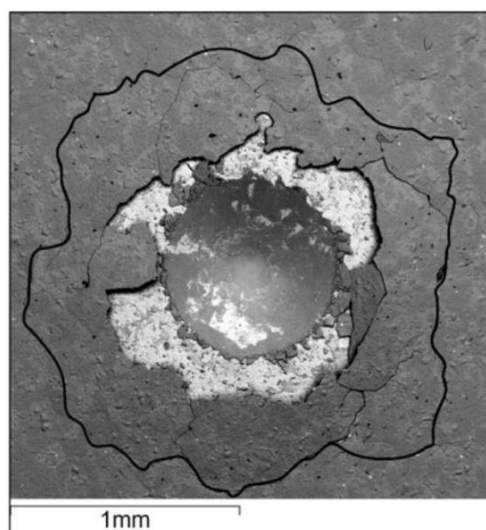


Figure 2.41 : Backscattered scanning electron micrograph of the oxidized sample after indentation. The black line delimits the extent of the fractured region [83]

Sun et al. use indentation to characterise the interfacial strength of an oxide on a ferritic stainless Steel (Crofer 22 APU, used in solid oxide fuel cell (SOFC) [93]. A Rockwell Ball (0.2-mm tip radius and 120° indenter tip angle) is used to strain a 2 to 15 μm thickness oxide. First, FE simulations are done with a fine crack at the interface between oxide and steel, it permits to calculate the main fracture mode at the crack tip (Figure 2.42). Linear elastic material properties are used for both the substrate and the chromia scale. The Figure 2.42 shows stress intensity factor versus indentation depth for an interfacial crack of $a = 5 \mu\text{m}$ length located at $L = 50 \mu\text{m}$ away from the indenter centre. K_{II} is much higher than K_I (take care of the two different vertical scales for K_I and K_{II}). Thus, the shearing mode II is the driving force for delamination. A critical shear stress-based interfacial failure criterion is proposed with a combined experimental/analytical approach. Experiments on oxidized stainless-steel specimens show that a critical loading P_c is needed to induce spallation of the oxide. Simulation of the indentation process with the same parameters is launched to evaluate the shear stress component within the scale. For the critical loading P_c for spallation, the value of shearing stresses is defined as the interfacial shear strength. This method allows the calculation of the properties of oxide-steel interface. For a $2 \mu\text{m}$ thickness oxide on a Crofer 22 APU stainless steel, it is evaluated as 455 MPa. Increasing the thickness of oxide tends to decrease the interfacial strength, it is interpreted as a deterioration of the interface.

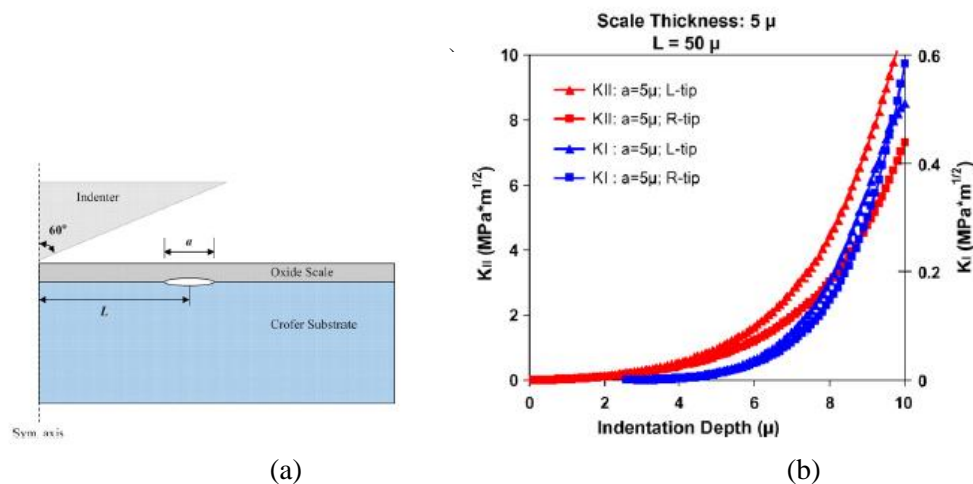


Figure 2.42:(a) schematic representation of interfacial pre-crack for indentation process (b) K_I and K_{II} vs. indentation depth for scale thickness of $5 \mu\text{m}$. L-tip is the left side of the interfacial crack, R-tip is the right side [77]

This kind of indentation test is relevant to evaluate adhesion and interface properties. These tests have only been carried out at room temperature (after high temperature oxidation), it would be interesting to make them at high temperature. Internal stresses are not measured nor calculated before the indentation, the value taken by the authors is arbitrary.

2.5.6.2 Scratch tests

Scratch test is commonly used to characterise the adhesion of thin films [107]. The method consists in generating scratches with a stylus by drawing it at increasing normal load on the surface of a coating. The driving force of the failure is the combination of the elastic-plastic indentation stresses, and the residual stresses in the coating. Two cases are possible: the cohesive failure which occurs within the coating by the tensile stress behind the indenter, and the adhesive failure due to the compressive stress which separates the coating from the substrate (spallation, buckling...).

This method is used to characterise the behaviour of oxide on steel by Rojacz et al. [84]. Some steel specimens with different alloying elements are selected (high percentage of Cr and Ni, 15 or 20%) and are oxidized at 700°C for 8 cycles of 24 hours. A Rockwell-C indenter is used with an increasing loading. The failure force is quantified using an acoustic emission and the DIN EN 1071-3:2005 method. Due to the differences within the scale thicknesses between the samples, the critical pressure is normalised to the oxide scale thickness t ($\text{N}\cdot\text{mm}^{-3}$) with the equation:

$$P_{critNor} = \frac{F}{A \cdot t} \quad (2-19)$$

with F the force for the first crack, A the contact area and t the thickness. This study reveals the influence of alloying elements on adhesion and quantifies the mechanical stability of the oxide. For example, the addition of Cr increases the adhesion of the oxide. The observation of the failure gives information on the oxide layer properties (spallation, crack...). The addition of Ni reduces the brittle behaviour of high Cr steel and stabilises the oxide layer against mechanical failure.

In order to calculate the adherence of the oxide, scratch test is conducted by Noh et al. [68] for an oxidised low carbon steel using a Rockwell tip at a constant speed. This study aims to examine the mechanism of oxide scale spallation occurred during uncoiling. The tangential load is recorded during the scratch test and the critical values are measured at the point of initial fracture (1.8N in the Figure 2.43). Then, a FE model of the scratch test is used to evaluate the properties of the interface. The interface is composed of cohesive elements to allow the interfacial detachment for the separation of the oxide scale. With a coupled numerical-experimental inverse identification procedure, the critical traction component and the fracture energy are evaluated respectively to 200 MPa and 18 J/m².

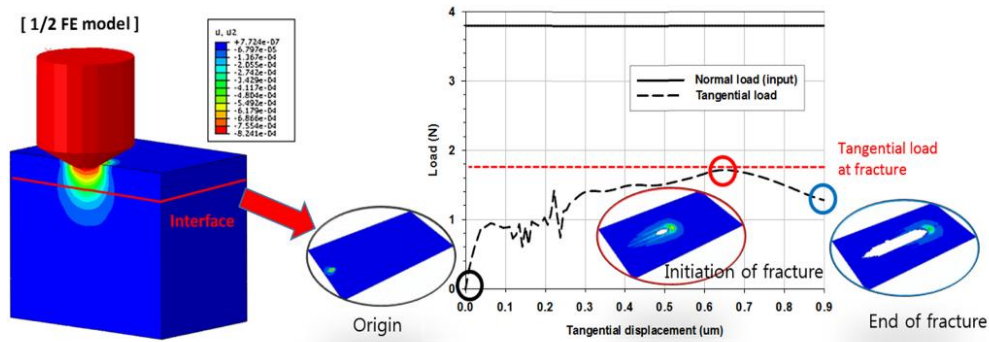


Figure 2.43: Schematic illustration of the FE simulation procedure for the determination of interface fracture strength. Cohesive elements are in red in the model at the interface. The 1.8N correspond to the loading for failure in the experimental scratch test [68]

This test is also conducted at high temperature by Berns [95] for iron, nickel and cobalt alloys. This application to the oxide at high temperature is possible, by oxidizing the specimen previously and then heating it just before the scratch test.

2.5.6.3 Tensile tests

Oxide adhesion is calculated by Chandra-Ambhorn and Klubvihok using tensile tests by considering spallation of oxide [86]. During the test, spallation ratio (spalled area divided by total area of the total interface) is calculated using image analysing software. This method is based on Evans' approach, in which spallation occurs when the strain energy accumulated in the oxide scale exceeds the energy needed to supply to the scale/steel interface for decohesion:

$$G = u \cdot t \quad (2-20)$$

where G is the mechanical adhesion energy (J.m⁻²), u is the strain energy per unit volume accumulated in the oxide scale until the first spallation (J.m⁻³) and t the thickness. Thickness is measured from the cross-sectional images. In this model, the oxide is considered purely elastic. The strain energy

u is calculated by evaluating the stress evolution in the oxide in both loading and transverse direction during the tests:

- the residual stresses within the oxide
- the elastic deformation in the early stage of the deformation (of the oxide and the steel)
- the plastic deformation of the steel while the oxide is still elastically deformed until the first spallation. It is assumed that the oxide scale is a brittle material which exhibits no distinct yield point.

For specimens oxidized at 850°C in O₂ – 20% H₂O up to 120 seconds, the quantified adhesion energies is in the range of 18-240 J.m⁻².

This method has been used to evaluate the effect of carbon on steel. The composition in carbon is varied (from 0,04% to 0,18%). By increasing the percentage of carbon, first spallation occurs earlier, the ratio of spalled oxide at the same strain is also higher. This experiment shows that the increasing amount of carbon tends to reduce the Room Temperature adhesion of the oxide, this is due to the enrichment of carbon at the interface, as proved by electron probe micro-analyser (EPMA).

Similarly, Nilsonthi et al. [88] used these same macro-tensile tests, in order to compare adhesion of steel oxide (mainly Magnetite) produced by blast furnace and electric arc-furnace. The adhesion calculated is between 300 to 700 J.m⁻². Comparison at the same strain rate of the conventional and recycled steels shows higher scale adhesion for the recycled steel due to the presence of high amounts of interfacial silica precipitates at the interface between steel and oxide.

Another study highlights the influence of temperature in the production line of hot rolling process [87]. For scale with similar thickness, the adhesion energy is lowered for the sample subjected to higher temperature drop between finishing and coiling temperatures. An explanation could be that more water vapour is present in atmosphere due to the higher amount of water used to cool down the steel strip. In this study, the energy calculated is about 40 to 890 J.m⁻². Here the humidity tends to decrease the adhesion. This study is not in agreement with the Monteiro conclusion but the grades are different (higher Cr and 14.4 ks at 650°C for the oxidation for Monteiro in comparison to low carbon steel and higher oxidation temperature, >820°C, for this study).

2.5.6.4 Inverted blister tests

The adhesion of brittle oxide is characterised by Mougín et al. [89] using the inverted blister test on oxidized ferritic stainless-steel (18% Cr stabilised by Ti and Nb). This test is based on the propagation of a crack at the interface in a sample where a square notch has been cut through the oxide to the interface. The oxide external surface is glued over the central hole of a metallic specimen holder. Then, pressurised water is sent toward the oxide+steel system. When the amount of fluid is increasing, a bulge is created, the metal is debonded from the oxide and forms a spherical cap-shaped blister. G , the value of the interface energy, is established by:

$$G = CPh \quad (2-21)$$

with C a constant (0.62, independent of membrane thickness and blister diameter), P the pressure of water, h the height of the bulge. For the ferritic stainless steel, the oxide-steel adhesion energy goes down with the increasing oxide thickness (Figure 2.44). This test shows the effect of alloying elements on the adherence: Ti plays a beneficial role by mechanical locking due to the precipitation of TiO₂ at the interface. This procedure is not relevant for very adherent oxides: above 180 J.m⁻², the pressure does not debond the metal.

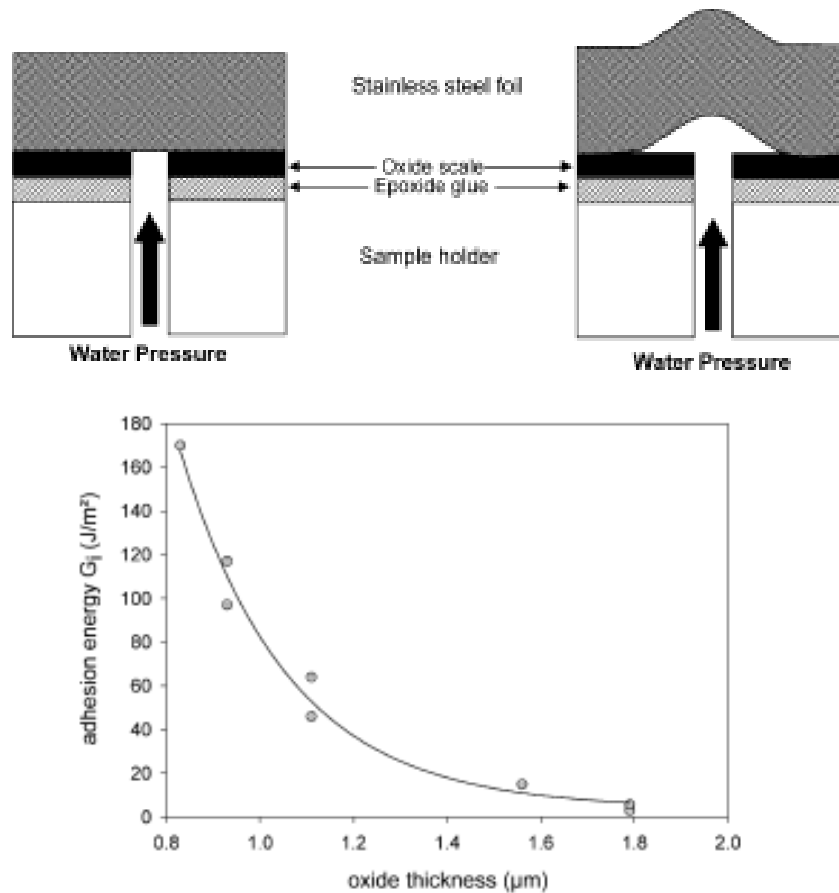


Figure 2.44: Principle of the inverted blister test and the influence of oxide thickness on the adhesion energy for an oxide grown on Fe-18Cr-TiNb at 900° in oxygen [89]

All the data concerning the adhesion of iron oxide scales is summarised in the Table 2-7 . Large variability is observed in adhesion, regardless of the technique used. It shows difficulty to characterise adhesion of thin oxide on steel. Few data exist for higher temperature tests.

Table 2-7 : Comparison of the quantified mechanical adhesion energies of oxide scales on metallic substrates using different methods (at room temperature)

Material	Oxidising conditions	Adhesion energy (J/m ²)	Method used	Ref.
Low carbon steel (0,04%)	Finishing mill temperature from 820 to 910°C	44-890	Tensile test	[87]
Low carbon steel (0,16%C)	850°C in O ₂ -20H ₂ O up to 120 s	18-240	Tensile test	[86]
Low carbon steel	As-received steels from hot rolling process (recycled and conventional steel)	2-690	Tensile test	[88]
P-containing steel	1000 °C in laboratory air up to 10 min	0-350	Indentation test	[47]
Ferritic Stainless Steel	900°C in a 15mbar O ₂ partial pressure to obtain the scale thickness of about 2 μm	3-170	Inverted-blister test	[89]
Low carbon steel	900 °C (10 to 30μm)	18	Scratch Test	[68]

2.5.6.5 High temperature

Kondo et al. estimate the scale adhesion at high temperature with the “contact test”. [70]. Two separated specimens are oxidized at high temperature (850° to 950°C). Then, samples are contacted to each other and oxide scales are joined at the same temperature. After joining, two samples are separated and the force during detachment is recorded. If the two oxide layers are found on the same side (cohesive fracture at the steel/oxide interface), the maximum force is considered as scale adhesion force at the considered temperature. Due to the complexity of the test, only a few tests are successfully performed at each temperature (Figure 2.45). Above 1000°C, blisters are formed at the surface and adhesion is not calculated. The scale adhesive force is expressed as the average pulling stress, force / section, in MPa ; it decreases as temperature increases, in the range from 1 MPa to 2 MPa.

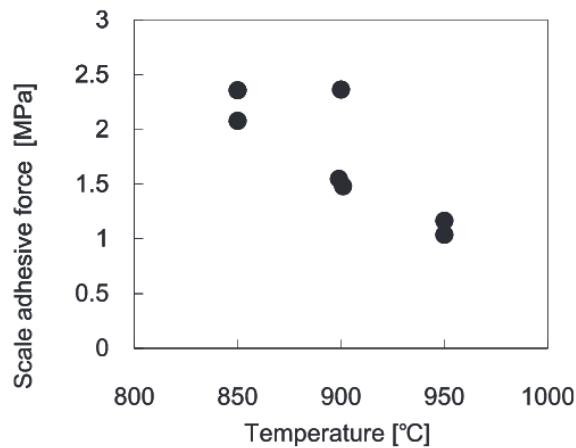


Figure 2.45: Measured scale adhesive force with the test temperature [70]

A similar test is developed by Krzyzanowski and Beynon to evaluate the adhesion of oxide at high temperature [62]. It is a compression test in which one half (the tool) represents the roll material and the other half is the oxidized specimen. The oxidized sample is picked up by the tool after oxidation. At 870°C, the oxide scale is partly separated from the tool specimen after the test. At 970°C, the whole oxide scale adheres to the tool during the contact and pulls away, exhibiting poor adhesion (but no quantitative results are given). This result is in agreement with Kondo et al.’s study [70].

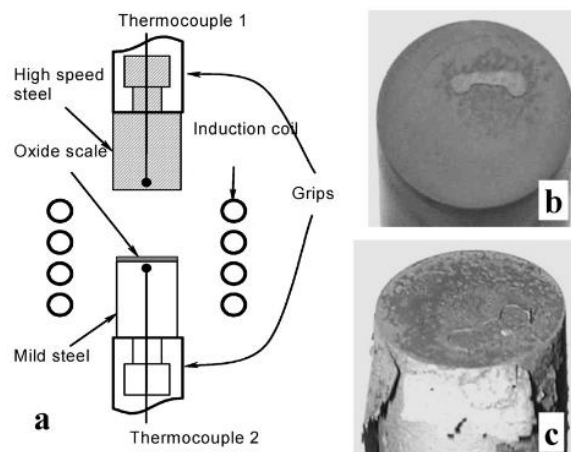


Figure 2.46 : (a) Schematic representation of the hot compression test to evaluate adherence of oxide. Oxidized sample after the test at 870°C (c) oxide scale partly separated from the specimen and (b) transferred to the tool [62]

The adherence of oxide is a determinant factor regarding the oxide scale behaviour in the Finishing Mill. Literature shows the complexity to characterise adhesion values, as lots of parameters

such as alloying elements, humidity, temperature of oxidation, phases modify adhesion of oxides. However, it is possible to enumerate some general tendencies such as:

- FeO is the most adherent iron oxide;
- The adherence decreases when the scale thickness increases;
- The additional elements have of course an important impact on the adherence. The interface with steel substrate is different according to the alloy elements.

At high temperature, the scale adherence remains poorly known, and is extremely difficult to measure quantitatively.

The adhesion at room temperature is well referenced with lots of different tests. At higher temperatures, few studies report the evolution of adhesion. This data is missing , yet it is particularly relevant to understand the descaling.

2.6 Conclusion

This chapter gives a wide review of the hot oxidation of steel and the behaviour of oxide at high temperature. At the temperature of the finishing mill, the oxide scale is composed of three phases, Wüstite, Magnetite and Hematite. In the presence of alloying elements, the kinetics of oxidation and the mechanical behaviour is changed due to the enrichment of some elements at the interface.

Internal stress is generated by several mechanisms (growth, thermal) and can be generally relaxed at high temperature by creep of the oxide and/or yielding of the substrate. During descaling, the fast cooling of the oxide can fracture it (by spallation, blistering or cracking), which is detrimental for the surface quality.

Some mechanical tests are used to evaluate intrinsic properties of oxide and its interface. In the roughing part of the HSM, oxide is co-deformed with steel due to its visco-plasticity at very high temperature. By decreasing the temperature as in the finishing stands, the oxide becomes brittle and cracking behaviour is reported. Some criteria for the fracture have been used to anticipate this brittle failure.

The adherence of oxide is another determinant factor regarding the oxide scale behaviour in the FM. Several studies report the adherence of oxide at room temperature, but there is a lack of information for the evolution of the adhesion of scale at the temperature encountered by HSM. Experimental tests to evaluate the adherence of oxide are therefore necessary.

Résumé

Ce chapitre décrit l'oxydation à chaud de l'acier et le comportement de l'oxyde à haute température. À la température du laminoir de finition, l'oxyde est composée de trois phases, la Wüstite, la Magnétite et l'Hématite. En présence d'éléments d'alliage, la cinétique d'oxydation et le comportement mécanique sont modifiés en raison de l'enrichissement de certains éléments à l'interface.

Les contraintes internes sont générées par plusieurs mécanismes (croissance, thermique) et peuvent généralement être relâchées à haute température par le fluage de l'oxyde et/ou la déformation du substrat. Lors du décalaminage, le refroidissement rapide de l'oxyde peut le fissurer (par écaillage, cloquage ou fissuration), ce qui est préjudiciable à la qualité de la surface.

Certains essais mécaniques sont utilisés pour évaluer les propriétés intrinsèques de l'oxyde et de son interface. Dans la partie ébauche de laminoir à chaud, l'oxyde est co-déformé avec l'acier en raison de sa visco-plasticité à très haute température. En diminuant la température, l'oxyde devient fragile. Certains critères de rupture ont été utilisés pour anticiper cette rupture fragile.

L'adhérence de l'oxyde est un autre facteur déterminant du comportement de l'oxyde dans le laminoir. Plusieurs études font état de l'adhérence de l'oxyde à température ambiante, mais on manque d'informations sur l'évolution de l'adhérence de l'oxyde à la température rencontrée lors du décalaminage. Des essais expérimentaux pour évaluer l'adhérence de l'oxyde sont donc nécessaires.

Chapter 3: X-Ray diffraction characterisation of oxide: from the in-situ-oxidation to the post-mortem observations

3.1 Introduction

The aim of this chapter is to understand the oxide behaviour after oxidation. This part is focused on the characterisation of low carbon oxidized specimens to prepare the mechanical tests, but also to provide elements for the understanding of descaling in the HSM.

Observation of oxide is possible after standard cross-sectioning and polishing, or Focused Ion Beam (FIB) machining, giving information about the thickness, the porosity and the oxide composition. However, these techniques are destructive. XRD is very useful for characteristics of material such as phases identification, internal stress, crystallographic texture... particularly for thin layers such as iron oxides. It is a non-destructive analysis that relies on the interaction between X-Rays and the crystal sub-surface of the sample. The main advantage is that the three phases of iron oxide (Wüstite, Magnetite and Hematite) can be analysed separately.

This chapter is divided into two parts:

- First, the characterisation of the pre-oxidized sample (at 650 and 700°C) by considering the multilayer composition, the presence of texture, and the internal stresses that are generated after the cooling. At room temperature, the post-mortem analysis can confirm the presence of each phase. The stress analysis, using the $\sin^2\psi$ law, gives all the internal stresses: growth stress during the oxidation, thermal stresses during the cooling, including possible relaxation effects. Internal stress have been shown to interfere with indentation deformation and indentation cracking [108]. It is therefore essential to identify the source and the contribution of these stresses to understand the mechanical behaviour of oxides.

- The high temperature XRD (HTXRD) is needed in order to observe the in-situ evolution of phases and stresses, in conditions closer to the HSM conditions. The objective is to identify the internal stresses generated, and their evolution : do they relax together with growth stresses and temperature changes (thermal stress) ? In this approach, in situ oxidation in a controlled atmosphere within the XRD chamber is possible to answer these interrogations. The determination of CTE is also done at high temperature, which is essential to understand the corresponding generated thermal stresses.

At high temperatures, a transition from a ductile-brittle transition has been reported. Another objective is to identify the ductile-brittle temperature transition of Wüstite (between 600°C and 800°C) through the occurrence of relaxation, assuming that the two are manifestations of the same phenomenon. The relaxation of stresses without externally imposed deformation means that there is a transition from elasto-plastic (or elastic-brittle) behaviour at low temperature to elasto-viscoplastic behaviour of oxide at high temperature.

This chapter is composed of a description of oxidation of the low carbon sample and its characterisation (SEM, EDX...). There is a description of the method used to identify the internal stresses of oxide with application to steel oxide from the literature. The room temperature, followed by the HTXRD analysis are then described to evaluate the evolution of phases and stresses within oxide.

3.2 Oxidation experiments

3.2.1 Steel composition

5 grades are tested in this study. The chemical composition of steels used are reported in Table 3-1. It has been evaluated by ArcelorMittal using Optical Emission Spectroscopy (OES). Carbon content varies from 0.002 to 0.11 mass%. Oxidation test specimens are cut from hot-rolled transfer bar at the entry of the finishing mill. This chapter is focused on the IF grade, which is an ultra-low carbon steel.

Table 3-1: Composition of grades used in this study (wt%)

Nuance	Fe%	C %	Si %	Mn %	P %	S %	Cr%	Mo %	Ni%	Al %	Cu %
	OES	OES	OES	OES	OES	OES	OES	OES	OES	OES	OES
IF	Bal.	<0.002	0.015	0.088	0.006	0.004	0.018	<0.002	0.012	0.059	0.01
DWI	Bal.	0.004	0.004	0.196	0.009	0.009	0.021	<0.002	0.02	0.017	0.041
HSLA0	Bal.	0.078	0.01	0.435	0.009	<0.003	0.014	0.003	0.013	0.034	0.007
HSLA1	Bal.	0.117	0.006	0.558	0.01	0.01	0.019	0.002	0.013	0.044	0.018
HSLA2	Bal.	0.053	0.216	1.04	0.01	0.0047	0.022	0.003	0.01	0.043	0.013

3.2.2 Oxidation of low carbon steel

In order to remove oxide residues and traces of the machining of samples from strips, each sample is manually polished with an abrasive P800 Silicon Carbide (SiC) paper and cleaned with alcohol. Samples are then introduced in the furnace chamber and a thermo-couple is placed near the surface of the sample to control the temperature. Oxidation is then conducted for different periods of time, at a temperature high enough to obtain the desired thickness of oxide. Controlled oxidation is achieved by using two different atmospheres (Figure 3.1). First, the chamber is flushed with nitrogen with a flux of 20 NI/min ; the material is then heated at 0.7 °C/s to the preset temperature of oxidation; this temperature is held for 300 s to ensure its homogenization. Nitrogen is replaced by dried air (21% O₂) to oxidize the sample for the time required. After the oxidation, the chamber atmosphere is reverted to pure nitrogen to prevent oxidation during cooling. The sample is cooled down, and the speed of cooling is equal to ~1.3°C/s until 300°C and then ~0.3°C/s to room temperature. Here, the rapid cooling is intended to limit the phase $W \rightarrow M + F$ transformation.

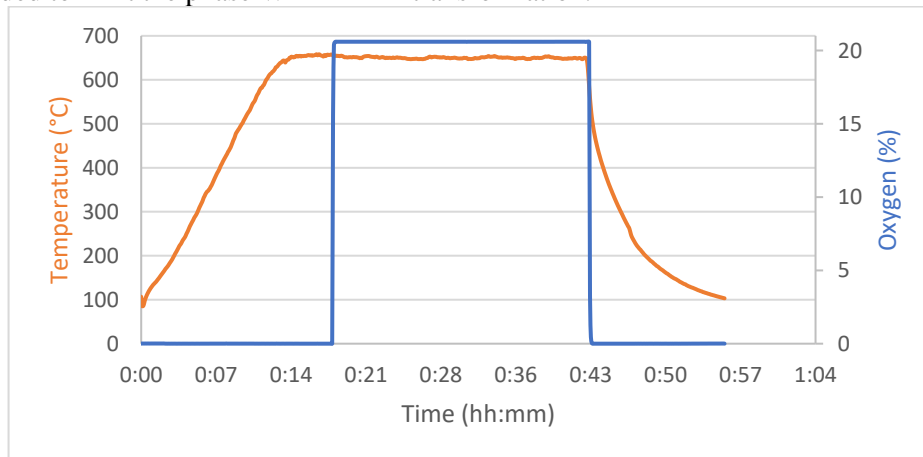


Figure 3.1: Thermal heat cycle for the oxidation: here 24 minutes 40 seconds at 650°C

In the rest of the manuscript, the following denomination of sample is done: Grade_oxidation temperature_oxide thickness. As an example, IF-650_12 is referring to a sample of IF grade oxidized at 650°C resulting in a 12µm thickness.

3.2.3 Observation of oxidized cross-sections

After oxidation, each specimen is analysed to measure the thickness and distinguish the phases. Preparation of specimens covered by oxide scale is extremely delicate due to its hardness and brittleness. Specimens are coated (at 170°C) in thermo-setting resins (epoxy) which are known to have a low shrinkage. RT-coated ones have been also tested with equivalent results, but longer time to dry. Coated samples are then ground using abrasive paper P320 and then polishing cloths with adapted diamond suspension from 9µm to 1µm. Finally, OPS (colloidal silica) is used to obtain a mirror polish. All parameters used are detailed in Table 3-2.

Table 3-2: Polishing protocol for the observation of oxidized cross-sections

Material	Speed (platen/sample) (rpm)	Pressing force (daN)	Time (minutes)	Diamond suspension	Lubricant
P320	250/150	2	1	-	-
TOP 9µm	180/100	2	2	9µm	0.1 mL every 12s
RAM 3µm	180/100	2	2	3µm	0.1 mL every 12s
HS-B 1µm	180/100	2	2	1µm	0.1 mL every 12s
OPS	180/100	2	2	OPS	

Due to the presence of the resin and to limit the decohesion of the oxide during the de-mounting, the assembly “sample+resin” is metallized with a Turbomolecular Pump Coater (Q 150T ES model from Quorum) to deposit a 7 nm platinum coating.

Then the scale/steel cross-sections are observed with a scanning electron microscope (SEM). Both the Secondary Electron mode (SE, emphasising topography) and the Back-Scattered Electron mode (BSE, emphasising contrast between chemical elements) have been used. With secondary electrons, area topography (for example oxide thickness) is determined. In the Figure 3.2, the measured thickness is 26 µm. The experiments have shown that the resins used adhere well, but their shrinkage is sufficient to induce decohesion of the oxide scale when the interface with the metal is weak. Thus, it is sometimes difficult to estimate the part of damage occurring during the experiment and that due to preparation of sample for examination.

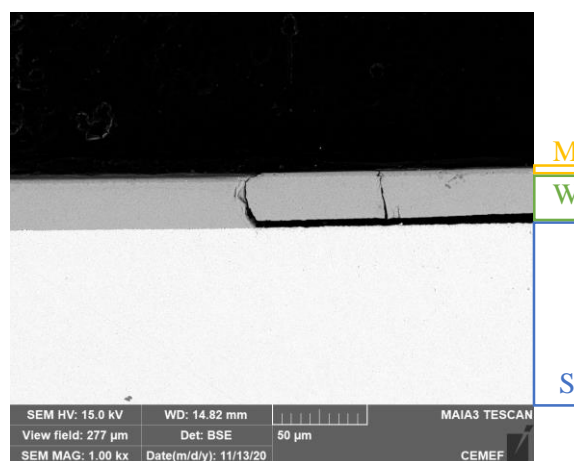


Figure 3.2: SEM image of the IF_650_26 oxidized specimen (SE image). M refers to Magnetite, W to Wüstite and S to Steel

Furthermore, the signal produced by back-scattered electrons (BSE) reveals information on the chemistry and atoms present at the surface. The chemical elements with a higher atomic number ($Z(\text{Fe})=26$) produce more back-scattered electrons than a lighter chemical element ($Z(\text{O})=8$). Thus, any

zone with a higher concentration of Fe appears brighter. A predominant clear grey oxide layer appears in the middle, with a dark grey layer at the extreme surface. This scale oxide is probably constituted of a dominant FeO layer (light grey) and of external Fe₃O₄ layers (dark grey) (Figure 3.3). The interface layer could also be a segregation of addition elements. The ratio of thickness of Magnetite and Wüstite varies from 93/7 to 78/22.

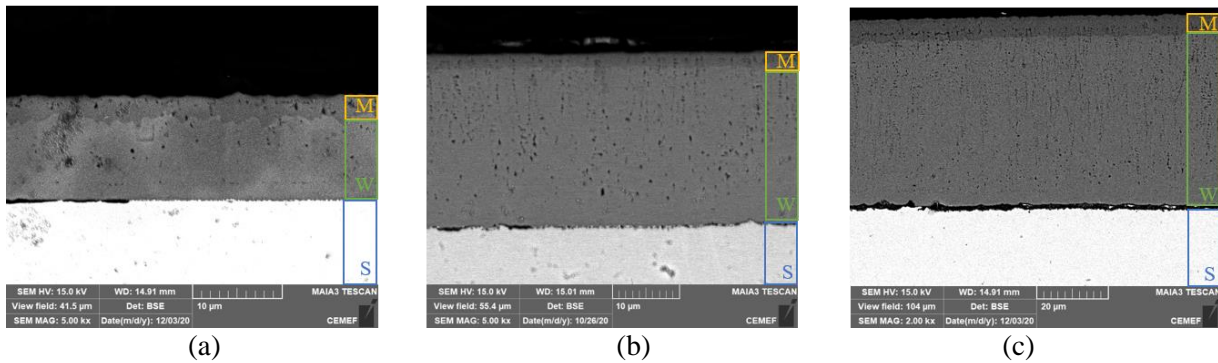


Figure 3.3: SEM images of oxidized specimens : BSE on the cross section (a) IF_650_12 (b) IF_650_26 (c) IF_650_55. M refers to Magnetite, W to Wüstite and S to Steel

In the cross-sections, the presence of Hematite is not identified. This surface scale is very thin, and confined with the resin. To confirm its presence, top surface images or X-Ray Diffraction analysis is needed (as shown in §1.4). Hematite represents a small percentage of the total scale (1 or 2%). The Hematite is observed from a view from the surface in the Figure 3.4.

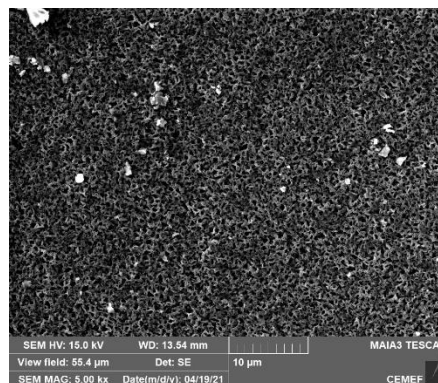


Figure 3.4: SEM images of oxidized specimen (IF_650_26) (view from the surface to observe Hematite)

Compared with the secondary scale grown in the HSM, the M/W ratio and the porosity are different. It is explained by the low temperature oxidation (650/700°C versus above 900°C for the secondary scale). From a mechanical point of view, in the HSM, the porosity is very low and an important roughness at the interface is observed due to the compression between the rolls.

SEM combined with Energy Dispersive X-Ray Microanalysis (SEM-EDX) allows the local chemical analysis of the sample. For the oxide, although quantification of oxygen and other light elements (C, B, N...) is not really precise, it helps to determine the evolution of the percentage of oxygen across the oxide thickness, hence detecting the different oxides. In the Figure 3.5, the intensity of the green colour represents the enrichment of oxygen, increasing from 0.15% in the steel, to 48% in Wüstite and 54% in Magnetite. In the view field of Figure 3.4, the percentage of oxygen has been found to be 60%. It confirms the presence of the Hematite (oxygen-richest phase).

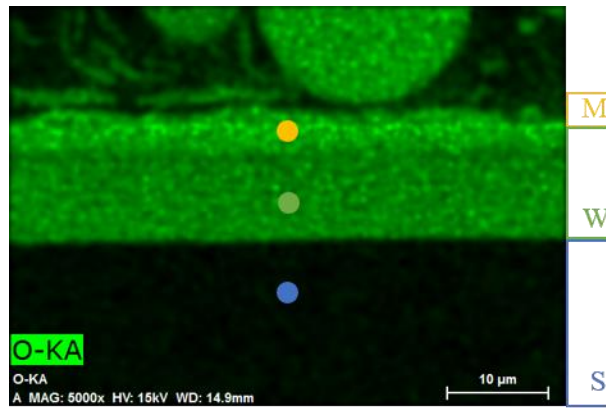


Figure 3.5: EDX analysis of a cross-section. The intensity of green is representative of the percentage of Oxygen. 3 local analyses are made in Steel, Wüstite and Magnetite (IF grade).

In order to have information at the interface between steel and oxide without mechanical degradation induced by polishing, cross-sections are prepared using a plasma (Xe source) Focus Ion Beam (FIB) thanks to a FIB column mounted on a SEM (Tescan FERA3 dual beam microscope). Cross-sections are obtained in 3 milling steps. Cross-section opening is performed at 30 kV and high current (2 μA). The resulting cross-section is then polished at 30 kV and a current intensity of 1 μA. Finally, the FIB current intensity is reduced down to 100 nA to refine the cross-section surface quality. In the Figure 3.6, an IF sample (IF_650_12) shows no interfacial decohesion. This observation, made repeatedly, suggests that the previously observed delamination occurred during coating.

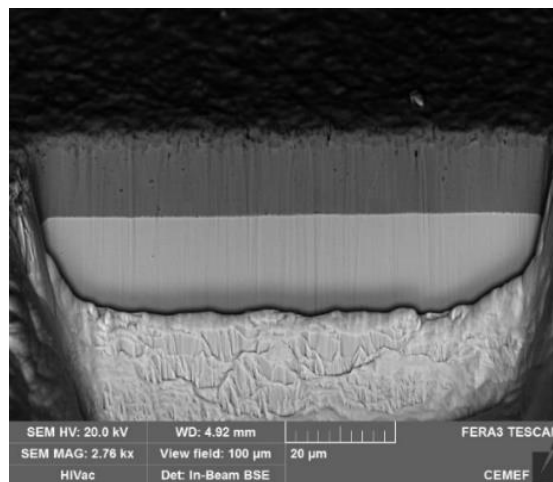


Figure 3.6: cross-section observation of oxidized specimen after FIB milling (IF grade).

All the characterisations made at room temperature are not the exact representation of the real oxide generated at high temperature. The room temperature observation is useful to evaluate the phases, and the structure of oxide. Furthermore, these analyses are destructive, the X-Ray diffraction is used next to evaluate the crystallographic structure of oxide

3.3 A description of the diffraction: phase and stress analysis

3.3.1 Diffraction principle

For the XRD laboratory, X-Ray are produced by the electronic transitions in the inner layers of metal wafer called an anticathode. Electrons are emitted by a heated cathode and accelerated by an electric field to impact the anticathode, generating X-Rays. At the contact with the crystal surface, X-Rays are scattered and undergo various types of interactions [109]:

- the photoelectric effect. X-ray photons act on the deep electronic layers of atoms by causing them to move from the ground state to an excited state by ejecting an electron. The ejected electron is called a photoelectron.
- inelastic interaction (Compton effect). The internal structure of the atom is modified and thus, no interference phenomenon is possible. X-ray knocks one of the electrons out of the inner shell of an atom, emitting a characteristic fluorescent radiation.
- Elastic interaction, called the Thomson diffusion. During the interaction between the incident beam and the atom, the internal structure, and therefore the internal energy of the atom is not changed. The radiation that has undergone this type of interaction can retain its coherence and may give rise to interference phenomena: diffraction.

The wavelength of X-rays has the same order of magnitude as the distances between atoms in matter, of the order of an angström (0.1 nm). Considering a coherent X-photon diffusion and a periodic atom distribution, the electromagnetic waves diffused by these atoms cause a phenomenon of constructive interference if they are in phase. The X-Ray diffraction phenomenon is described by the Bragg relation in the direct lattice:

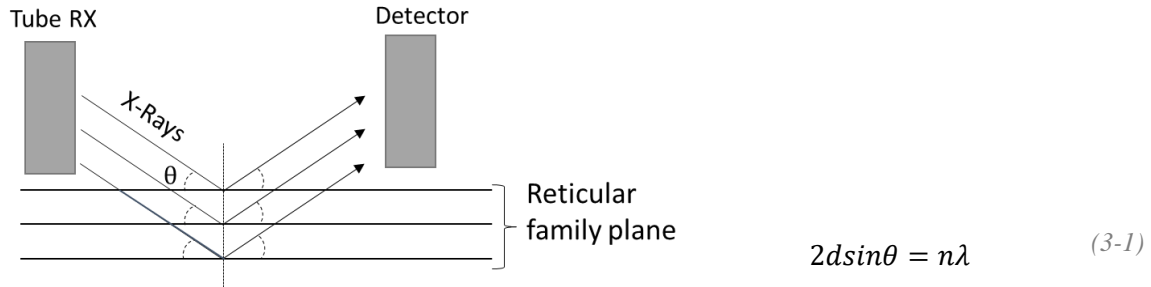


Figure 3.7: schematic representation of X-rays at the surface of sample

with θ the incidence angle, d the inter-reticular distance of the plane, λ the wavelength of the X-Ray source and n an integer.

The observation of a diffraction peak direction at 2θ from the incident beam is characteristic of the presence of a family of diffracting $\{hkl\}$ planes with inter-reticular distance d . According to Bragg's law, a family plane produced a diffracted peak. With a sufficient number of diffraction peaks of each phase, the different phases of the oxide can be identified. The Figure 3.8 shows a XRD pattern of an oxidized iron plate for 24 hours at 800°C [9]. There are 4 phases: Magnetite, Hematite, Wüstite and α -Ferrite. Each peak is attributed to a crystallographic plane of each phase.

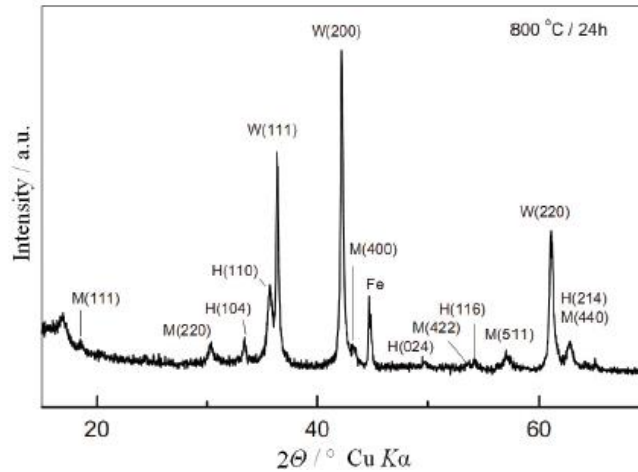


Figure 3.8: XRD diffractogram of an iron specimen for 4 hours at 800°C. M refers to Magnetite, W to Wüstite, Fe to Ferrite and H to Hematite [110]

3.3.2 Theory for stress analysis : $\sin^2\psi$ law

The source of internal stresses is multiple (thermal, growth see section 2.3) . During mechanical tests, it influences the behaviour of oxide, thus, quantification of stresses is relevant. For indentation testing, residual stresses have an influence on the results, the existence of compressive residual stresses will push the material to the surface, and increase the pile-up around the indenter [111].

XRD is widely used to measure the internal stresses within polycrystalline materials. The distance d between lattice planes can be measured and compared with stress-free standards. The variation is a strain. Assuming linear elastic distortions, the corresponding stresses are calculated. A method, based on the $\sin^2\psi$ law, is widely used at room temperature, but is also adapted to measure stress variations at high temperature. Indeed, monitoring stress continuously during high temperature processes is desirable to determine growth and thermal stresses undisturbed by the return to room temperature.

This $\sin^2\psi$ law method is described in the norm NF EN 15305 [112]. According to continuum mechanics, if an isotropic material is stressed, each point undergoes a displacement, from which local deformation of crystallographic mesh can be calculated. The diffracted plane strain measured at the microscopic scale is given by:

$$\varepsilon = \frac{d - d_0}{d_0} \quad (3-2)$$

with d_0 the distance between lattice planes without stress and d the same distance with internal stresses. This deformation can be observed directly in the XRD diffractogram with a shift of the peak. In the Figure 3.9, the dashed curve corresponds to a reference material (non-deformed distance d_0), and the full line to a stressed material. If the distance d increases, the shift is towards lower 2θ .

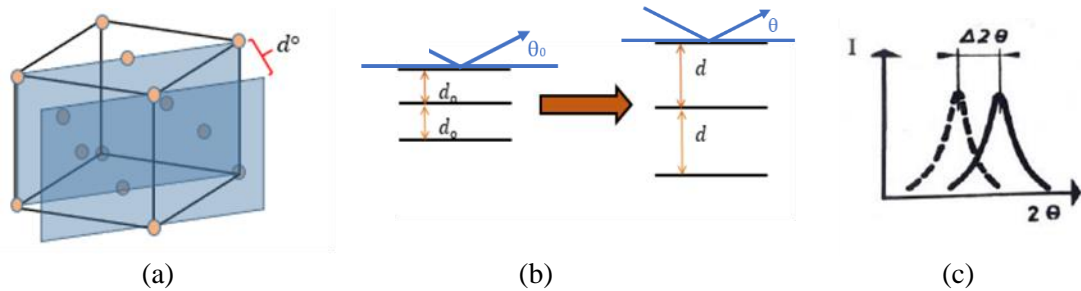
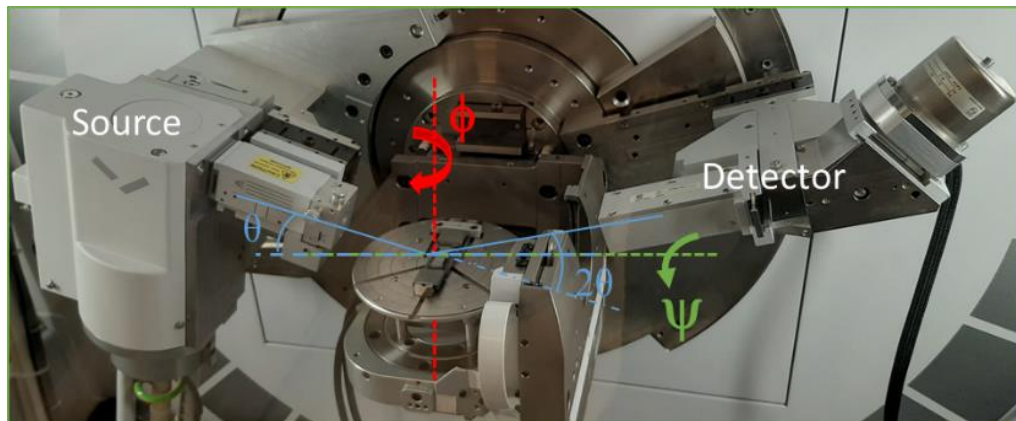
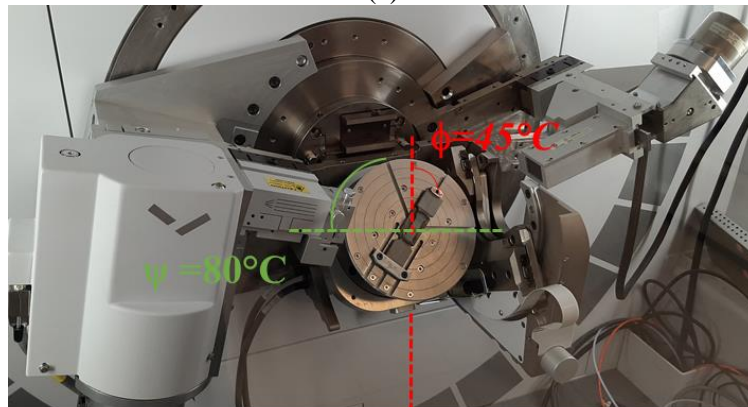


Figure 3.9: (a) reference distance d_0 for a CFC mesh (b) new distance d after a tensile solicitation (c) shift of the XRD peak

In the $\sin^2\psi$ law, it is necessary to measure d for several directions. The representation of the different angles ψ , ϕ and θ are presented in the Figure 3.10. θ is the diffraction angle between the X-Ray source and the detector and the specimen surface (blue color). ϕ represents the rotation angle around the vertical axis in red. ψ represents the rotation angle around the horizontal axis in green. In the Figure 3.10 b, configuration is set to $\psi = 80^\circ$ and $\phi = 45^\circ$. This configuration is called the χ configuration.



(a)

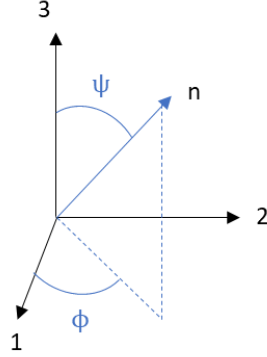


(b)

Figure 3.10 : Representation of the XRD equipment available at CEMEF for the χ configuration (a) ψ , ϕ and θ angles (b) goniometer configuration with $\psi=80^\circ$ and $\phi=45^\circ$

Another configuration called the ω configuration (also called the iso-inclination method) can be used to perform stress analysis with this equipment. In this configuration, ω is the angle between the incident X-ray beam and the sample surface. The tilt rotation is made by introducing an angle from the surface. Both ω and 2θ are in the same plane and the values of ψ are added to θ .

Diffracting plane deformation $\varepsilon_{\phi\psi}$ is calculated in the normal direction to the diffraction plane, thanks to the projection of the deformation tensor ε on \underline{n} :



$$\varepsilon_{\underline{n}} = \varepsilon_{\phi\psi} = n_i \varepsilon_{ij} n_j \text{ with } n = \begin{pmatrix} \cos \phi \sin \psi \\ \sin \phi \sin \psi \\ \cos \psi \end{pmatrix} \quad (3-3)$$

Figure 3.11 : Description of the measuring direction by the angles ϕ and ψ with 1,2,3 the sample coordinate

The principle of $\sin^2\psi$ law is to measure different $\varepsilon_{\phi\psi}$ to reconstruct the ε_{ij} and to have finally σ_{ij} . In the coordinate system described in the Figure 3.11, $\varepsilon_{\phi\psi}$ can be projected:

$$\varepsilon_{\phi\psi} = n_1 \varepsilon_{11} n_1 + n_1 \varepsilon_{12} n_2 + n_1 \varepsilon_{13} n_3 + n_2 \varepsilon_{21} n_1 + n_2 \varepsilon_{22} n_2 + n_2 \varepsilon_{23} n_3 + n_3 \varepsilon_{31} n_1 + n_3 \varepsilon_{32} n_2 + n_3 \varepsilon_{33} n_3 \quad (3-4)$$

$$\varepsilon_{\phi\psi} = \varepsilon_{11} \cos^2 \phi \sin^2 \psi + \varepsilon_{12} \sin 2\phi \sin^2 \psi + \varepsilon_{13} \cos \phi \sin 2\psi + \varepsilon_{22} \sin^2 \phi \sin^2 \psi + \varepsilon_{23} \sin \phi \sin 2\psi + \varepsilon_{33} \cos^2 \psi \quad (3-5)$$

The relation between strain and stress is given by Hooke's law for an isotropic material:

$$\varepsilon_{ij} = \frac{1}{E} [(1 + \nu) \sigma_{ij} - \nu \sigma_{kk} \delta_{ij}] \quad (3-6)$$

For a complete analysis, the whole strain tensor is calculated with a rotation of ϕ and ψ . However, considering the free-surface ($\sigma_{33}=0$) and for $\phi=0$, the equation becomes:

$$\varepsilon_{\phi\psi} = \frac{1}{2} S_2 \cdot \sigma_{11} \cdot \sin^2 \psi + \frac{1}{2} S_2 \cdot \sigma_{13} \sin 2\psi + S_1 (\sigma_{11} + \sigma_{22}), \quad S_2 = (1 + \nu)/E, \quad S_1 = -\nu/E \quad (3-7)$$

If the shear components are null ($\sigma_{13} = \sigma_{23} = 0$) and in the case of equi-bi-axial stresses ($\sigma_{11} = \sigma_{22} = \sigma_{\phi\psi}$, equation (3-7) is simplified and there is a linear dependence of $\varepsilon_{\phi\psi}$ on $\sin^2\psi$:

$$\varepsilon_{\phi\psi} = \frac{1}{2}S_2 \cdot \sigma_{\phi\psi} \cdot \sin^2\psi + 2S_1 \sigma_{\phi\psi} \quad S_2 = (1 + \nu)/E \quad S_1 = -\nu/E \quad (3-8)$$

with S_2 and S_1 are elasticity constants. The constants can be taken from the literature or can be measured experimentally. In the presence of internal stresses, depending on the orientation of planes, the deformed distance $d_{\phi\psi}$ (and thus the strain) is different depending on these angles (Figure 3.12).

In the presence of shearing component, the relation is no more linear due to the additional term in the equation (3-5).

In the Figure 3.12 (a), four grains of the same crystallographic plane are represented (same initial distance d_0 between atoms) but their orientations are different (for example orientation 1 and 2). Depending on the orientation and in the presence of residual stresses, here horizontal compression, Figure 3.12 (b), the distances d is changing. X-Rays are diffracted by the first orientation for $\psi = 0$ (Bragg's condition for diffraction respected), by making a rotation of an angle ψ , the diffraction is possible for the 2nd orientation (Figure 3.12(c)). As seen in Figure 3.9, the peak corresponding to this crystallographic plane is shifted with the variation of local strain. Thus, by multiplying analyses with different ψ , the same diffraction peak is shifted linearly. By varying angles ψ , different $\varepsilon_{\phi\psi}$ are calculated, by tracing ε as a function of $\sin^2\psi$, the slope gives the stress Figure 3.12(d). In this case, each point is the deformation of a given angle ψ . To satisfy this condition and to have a representative volume of material, the more measurements which different angle ϕ , ψ are done, the more accurate the results are. In Figure 3.12 (d), material undergoes a stress equal to -400 MPa ($S_2 = 6,8 \cdot 10^{-6} \text{ MPa}^{-1}$).

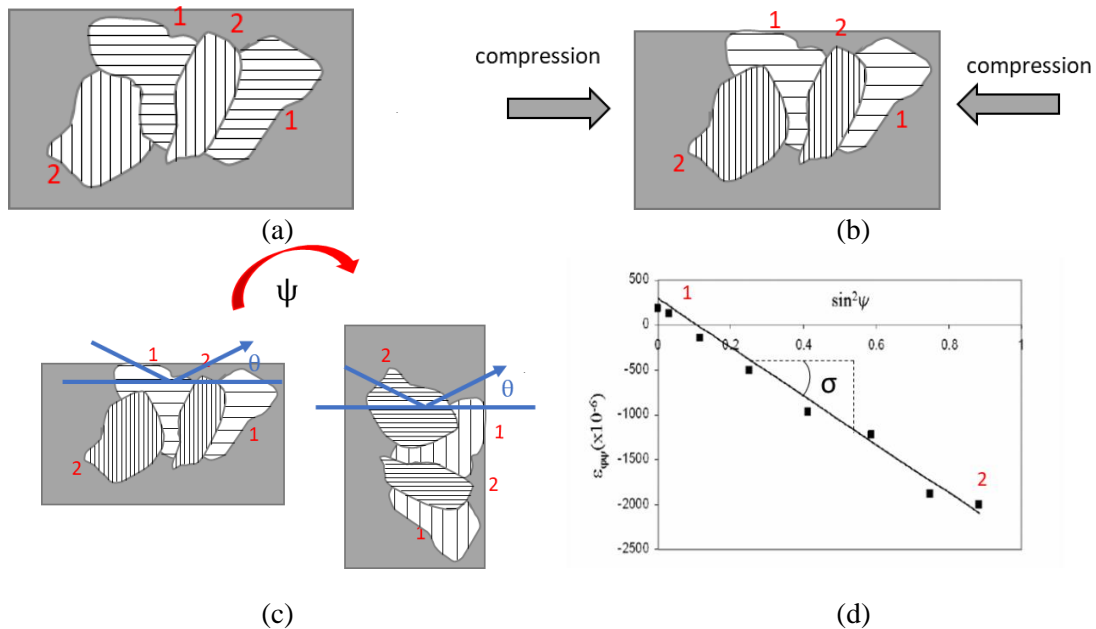


Figure 3.12: (a) representation of 4 grains of a same crystallographic plane (same distance d_0) but with different orientation (1 and 2 are two different orientations) (b) compression effect on the distance depending on the orientation (c) rotation of ψ angle to put the orientation 2 in diffraction condition (d) Example of $\varepsilon_{\phi\psi}$ versus $\sin^2\psi$ plot at constant ϕ in case of a biaxial compression stress (figure (d) is extracted from [112])

3.3.3 Others methods to evaluate internal stresses

Other methods can be used to evaluate the residual stresses. Similarly, the Raman spectroscopy can be used. Raman spectroscopy is a vibrational spectroscopy based on inelastic light scattering. It is mostly used to identify chemical bonds and functions in molecules. In a solid crystal, the frequency of Raman scattered light shifts from the incident light by the energy of a phonon (lattice vibration). The spectrum of the scattering (the number of peaks, their positions and intensities) is specific to each material. For the application to internal stress measurement, the principle is similar to the technique presented here: the wavelength of the peaks representing the vibrational transitions are sensitive to the state of stress. In the presence of internal stresses, there is a wavenumber shift of the main Raman band. The spectrum can thus be interpreted in terms of mechanical stress [113]. This has been done for iron oxides at room temperature [114] or during in-situ oxidation [113,115,116].

The photo-stimulated luminescence spectroscopy is also used to evaluate stresses. This technique is based on the determination of the frequency shift of luminescence light between a stress-free sample and a stressed one. This shift can be directly converted into stress. The method is used by Mennicke et al. for FeCrAl and FeCrAlY alloys at high temperature during oxidation at 1200°C [117].

In a previous chapter, the flexure tests have been described. This method consists in observing the deformation (bending, warping...) of a sample during a high temperature cycle and to deduce the corresponding internal stress [59].

After a description of the $\sin^2\psi$ method to evaluate internal stresses, a bibliographic review is done for iron and steel oxides.

3.3.4 Literature review for diffraction of iron oxides

3.3.4.1 Phase determination

X-Ray diffraction is commonly used to evaluate the phases after oxidation of iron or steel. In the literature, different sources for the X-Rays (Cu [59,78,85,86,110,118–125], Cr [126], Co [80,127–130] and Synchrotron [56,131]) and oxidation conditions are reported in Appendix A. The main conclusion is that Wüstite, Magnetite and Hematite are present at the surface of iron or low carbon steel. The high temperature in situ analysis is particularly relevant because it allows the observation of the phase transformation (Wüstite into iron and Magnetite) and the temperature range in which Wüstite is dominant (above 800°C typically). [59,124] [16,56,126,128,130,131]

3.3.4.2 Stress analysis at high temperature

As described previously, during cooling, oxide undergoes: thermal stresses, growth stresses, relaxation. The evaluation of internal stresses can be done at high temperature. The internal stresses analysis is not very widespread in the literature for steel and iron oxide at high temperature, but some authors have nevertheless carried out such studies: Buscail et al. [126], Juricic et al. [131], Sasaki et al. [56] and Hayashi et al. [130]. In the following, one paper is described in some details (the closest to our case study). The others are described in Appendix A.

Sasaki et al. used HT-XRD to observe the phase evolution during a thermal cycle [56]. Synchrotron radiation is used (20 keV) for 2θ ranges between 18.4 and 24.4°. A silicon steel specimen (Fe-1.0 mass% Si-0.1 mass% C) is oxidized at 900°C for 15 seconds. The cooling rate is 5°C/s in the presence of inert gas (Argon) to limit further oxidation. During the cooling, every 100°C, some stress measurements are done. In the Figure 3.13 (a), at 900°C the two major phases are FeO ($2\theta \approx 23.3^\circ$) and Fe₂SiO₄ ($2\theta \approx 20.0^\circ$). At 500°C, additional peaks show the formation of Fe₃O₄ ($2\theta \approx 20.7^\circ$, 22.1° and 24.0°). Fe₂O₃ ($2\theta \approx 21.1^\circ$) is observed at 200°C. This study points out the importance of in-situ analysis,

because the room temperature (post mortem) analysis is not really representative of the real evolution of phases. For example, Wüstite is unstable below 577°C, and is transformed into Magnetite and Iron, this phase is named “eutectoid”. This transition is highlighted by the variation of intensities of these peaks. For each phase, the behaviour is different:

- For Fayalite (Fe_2SiO_4): there is a linear variation of stresses during cooling due to the differential expansion with respect to the neighbouring layers, Fe and FeO.

- For Wüstite, the stress behaviour is divided into four regions: 1) 900 to 700°C, 2) 700 to 600°C, 3) 600 to 500°C, and 4) 500°C to room temperature. In the region 1), stress in Wüstite is found null. Above 700°C, Wüstite deforms plastically, growth and thermal stresses are relaxed. Going down from 700°C to 600°C, maximal compressive stress is reached (-165 MPa) corresponding to the thermal stresses: this means that during the analysis time (10 minutes at 600°C), no relaxation is present. This value suggests a ductile-brittle transition of Wüstite between 600°C and 700°C. In the region 3), Wüstite becomes in slight tension at 500°C, the authors explain that internal stresses are governed by Wüstite phase transformation. Finally, from 500°C to room temperature, internal stress evolution (compressive) is dominated by thermal stress again.

- For Hematite, from 200°C to room temperature, thermal stresses are generated due the difference of expansion with Magnetite.

- For Magnetite, stress is always in tension but fluctuating between 0 and 100 MPa from 600°C to room temperature. There is a sudden variation of stresses between 400° and 300°C while the other layers, FeO and Fayalite, have a linear variation of stresses.

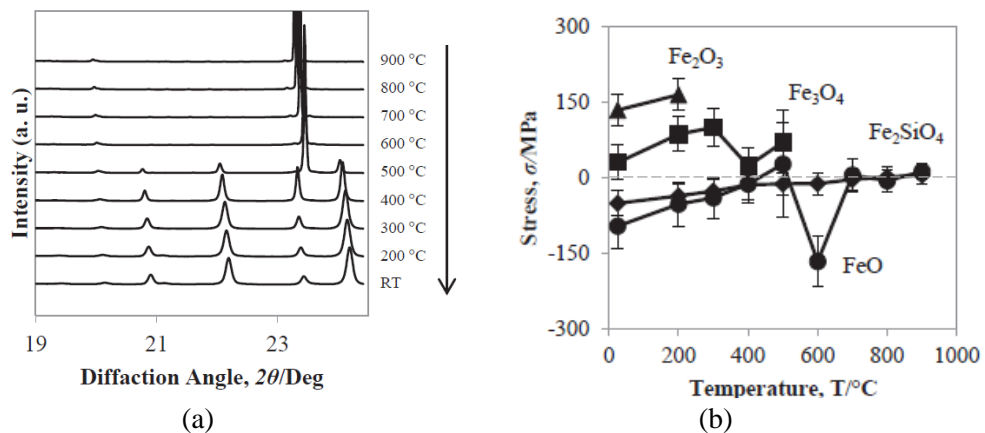


Figure 3.13: (a) High temperature X-Ray diffractogram during cooling of oxide formed at 900°C (b) the corresponding internal stress [34]

All these results of the four papers are summarised in the Table 3-3. Some differences are noted between the articles, for Wüstite:

- at high temperature (above 700°C) and without oxygen, there is a stress relaxation within Wüstite (Sasaki et al.), which is not the case for isothermal oxidation at 650°C and at 800°C (low pressure of oxygen). This relaxation is possible by plastic deformation. At lower temperature, micro-cracking and formation of pores can also be a source of relaxation.

- during an isothermal step, the source of stresses is multiple: stoichiometry gradient in Wüstite, volume change at the interface between Magnetite and Wüstite.

- during the cooling, from 700°C to room temperature, the thermal stresses are compressive (difference of dilation with the substrate)

- below 570°C, the eutectoid transformation is a source of tension, within Wüstite.

As low carbon steel oxide is composed of three phases, an equilibrium of stress is needed, the evolution of the stress in one phase is impacting the adjacent phase.

For Magnetite, the stress evolution tends to be in tension during the cooling due the thermal stresses.

In conclusion of this short bibliographic survey, HTXRD experiments are relevant to understand oxide behaviour at high temperature through two pieces of information: stress and phase evaluation. In order to stabilise the phases, a long oxidation cycle is needed. For the stress evaluation, the distinction between growth and thermal stresses is essential. Growth stresses are measured through long isothermal experiments in presence of oxygen. Thermal stresses can be measured only using cycles in an inert atmosphere to prevent further formation of oxide; it is furthermore disturbed by phase transformations. The relaxation of stresses is evaluated during long isothermal stresses, with short analysis times.

One of the objectives of the following stress analysis is to identify the ductile-brittle temperature transition of Wüstite (between 600°C and 800°C) through the occurrence of relaxation, assuming the two are manifestations of the same phenomenon. The strategies displayed in the articles detailed above will be exploited to try and evidence this behaviour transition which is a key to understand the descaling ability of oxide.

Table 3-3: Summary of stress analysis during in-situ thermal cycle (in bold, it is the source of the generated stress or relaxation)

Grade	Oxidation conditions	Wüstite	Magnetite	Ref
Pure iron	800°C isothermal oxidation for 30 h	Compression (-400/-100 MPa) Lateral growth of Wüstite	-	Buscail et al. [126]
	Cooling from 800°C to RT	Compression (-212 MPa) Thermal stresses	-	
Pure iron	650°C isothermal oxidation for 10 h	Tension after 2.5-3.5 h and 7-8 h) Compression otherwise Volumetric strain, Wüstite stoichiometry, inner oxidation in microcracks	Opposite sign of Wüstite	Juricic et al. [131]
1% Si Steel	900°C for 15 s	Stress-free Relaxation	-	Sasaki et al. [56]
	Cooling 700°C to 600°C	Compression Thermal stresses	-	
	Cooling 600°C to 500°C	Tensile phase transformation of Wüstite	Tension	
Pure iron	500°C to RT	Compression Thermal stresses	Tension	Hayashi et al. [130]
	Isothermal oxidation 700°C for 15 min	-	Tension Volume change	
	Isothermal transformation at 380°C for 80 min	-	Compression and relaxation Eutectoid transformation	

3.4 Methodology used in this work

3.4.1 CEMEF diffraction set-up

X-ray diffraction data are collected using a PANalytical X'Pert Pro diffractometer. The diffraction set-up is composed of a source of X-Rays, a goniometer on which the sample is placed, and a detector [109].

The X-ray source can be different : Copper, Manganese and Chromium. Once the X-Ray beam has been produced, the incident beam is focused in the direction of the sample according to the diffraction set-up used. A polycapillary is introduced to have a parallel beam. Crossed slits are added to delimit the beam before (the opening is set to 2x2 mm).

Some filters can be used, they act as a screen that strongly absorbs radiation of wavelengths shorter than λ . For each anticathode, a specific element is selected. For example, for Copper, Nickel is the optimal filter. It is very useful to suppress the K_{β} radiation but it does not allow the complete elimination of the continuous background, or the separation of the $K_{\alpha 1}$ and $K_{\alpha 2}$ lines.

A detector is used to receive the diffracted X-Rays. We have used two detectors, available in the laboratory [109]:

- Panalytical proportional detector is a punctual detector and consists in amplifying the energy of the photons received. This type of detector has to be "scanned" across the peak and the diffraction pattern is collected sequentially. They are rather slow with long counting time to have good statistics. In the set-up we used, a long parallel slit (parallel plate collimator 0.18°) is added before the detector to limit axial divergence. In addition, a flat graphite single crystal monochromator also improves the peak quality (narrow wavelength distribution). The monochromator works by reflection of the wavelengths that obey Bragg's Law for the particular d spacings of the monochromator. The main advantage is to transmit only the K_{α} radiation; the K_{β} , sample fluorescence and white radiation are reduced.

- with the Pixel detector, the diffraction pattern is recovered on a phosphor screen which converts the incident photons into "optical photons". These photons are then transferred by optical fibres to the "CCD plate" (plate of joined silicon cells in "honeycomb" of a few cm) where they are converted into electrons (about 350,000 electrons per cell). The number of these "stored electrons" is proportional to the incident X-Ray intensity. The measurement is faster, no long parallel slit and monochromator are used.

In the Figure 3.14, diffractometer elements of the proportional detector are present. The Soller slits are introduced to optimise the beam parallelism. Soller slits consist of closely spaced thin plates, made of a metal which absorbs X-rays. For the Pixel detector, no parallel plate collimator and monochromator are used.

This room temperature XRD configuration is then adapted for High Temperature XRD (HTXRD), a global description of the new set-up is done in the 3.6.1 paragraph (ceramic heating plate, inert dome...)

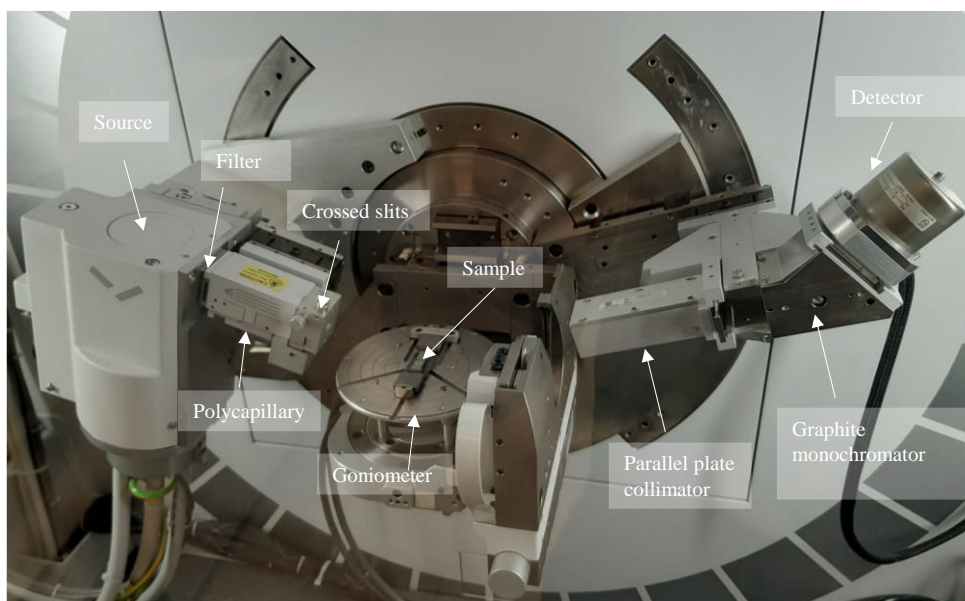


Figure 3.14: Diffractometer elements in a Bragg-Brentano geometry for the proportional detector

3.4.2 Fluorescence

The fluorescence radiation is due to the Compton effect, and the excitation of the electrons of the investigated material, usually by absorption of a photon immediately followed by spontaneous emission. The wavelength of the emission is lower than the initial anticathode wavelength, it tends to increase the background noise. In addition, there is less elastic interaction (responsible for the diffraction). These two effects combined can cause peaks to become invisible, making it difficult to analyse the diffractogram [132]. Thus fluorescence is detrimental for XRD.

The amount of inelastic scattering depends on the combination of the X-ray spectrum and the analysed material. Normally, to ensure sufficient scattering, the wavelength ($K\alpha$) radiation peak used should be longer than the so-called K absorption edge of the sample material. For iron samples, K is equal to 1.743\AA , above Cu $K\alpha$. Fluorescence is particularly detrimental with a copper anticathode for a Fe component. Fluorescence effect can be reduced by the energy sensitivity windows of the detector (set for energies above the 50% of the $K\alpha$ keV [132]). The use of a monochromator can also reduce the effect of fluorescence by selecting $K\alpha$.

For ferrous samples, the use of other anticathode is commonly recommended to limit the fluorescence. Unfortunately, in the set-up we used at high temperature, a graphite dome specifically designed for the copper source must be used.

3.4.3 Penetration depth evaluation

At the surface of the samples, X-rays penetrate and are diffracted. The interaction with the electronic clouds of atoms is the basis of XRD. Photons are partially absorbed due to the photoelectric effect. The intensity of the incident beam is greatly reduced within a very short distance below the surface. The transmitted X-ray intensity decays exponentially with respect to the path length it travels in the matter. Conventionally, penetration depth is defined as the distance from the surface out of which 63% of the intensity comes from. The Figure 3.7 is a schematic representation of the surface with a few atomic layers of a sample. X-rays are sent toward the surface, they are diffracted by the reticular planes, they have to get out of the material and they are finally detected. X represents the length travelled by X-rays, and p the penetration depth. Below this theoretical depth, the diffracted X-rays intensity is low.

Absorption is dependent on the X-Ray source and the analysed material. With some approximation, the intensity detected can be related to path length of the X-rays by the relation:

$$\frac{I}{I_0} = e^{-\mu X} \quad \text{with} \quad \mu(FeO) = \rho(FeO) \sum_i \frac{M_i}{M(FeO)} (\mu/\rho)_i \quad \text{and} \quad X = \frac{2p}{\sin\theta} \quad (3-9)$$

with I the intensity after travelling a distance X , I_0 the incident intensity, θ the incident angle, ρ the density, μ the absorption coefficient, p the penetration depth and M the molar mass of the element, the indice i refers to the elements (here Fe and O). The penetration depth (and the absorption more precisely) depends on the phase and the ratio between Fe and O. In the literature, only the mass attenuation coefficients of elements are available. The mass attenuation coefficient of a compound is the weighted average of the mass attenuation coefficients of the constituent elements. The mass attenuation coefficient of a powder mixture can be calculated based on the weight fraction of the components and their elemental compositions. The mass attenuation coefficient, multiplied by the density, yields the linear attenuation coefficient. Other models have been developed from grazing incidence XRD (GIXRD) [133].

Penetration depth is the same for Magnetite and Hematite, it is lower for Wüstite. From the above equation, the penetration thickness is evaluated when the ratio of intensities is around 67%. Figure 3.15 shows the evolution of the intensity ratio for different sources because for Wüstite, μ is strongly dependent on the wavelength of sources. The penetration depth can be read at the intersection with the yellow dotted line. The analysis with the Copper source is more superficial than the others (~ 6 μm of penetration depth for Wüstite). From this simple model, an estimation of the penetration depth is calculated ; it is in agreement with literature [132]. The penetration depth can also be determined with thin film specimens (oxide in our case). By analysing a sample with known thickness, when peaks of the substrate are not present on the diffractogram, it means that the thickness of the sample is above the penetration depth of X-Rays. For instance, for a sample with 12 μm of oxide, the ferrite peak is not detected by the Copper anticathode (6 μm of penetration depth). For all the anticathode, the penetrations estimated are listed in the Table 3-4.

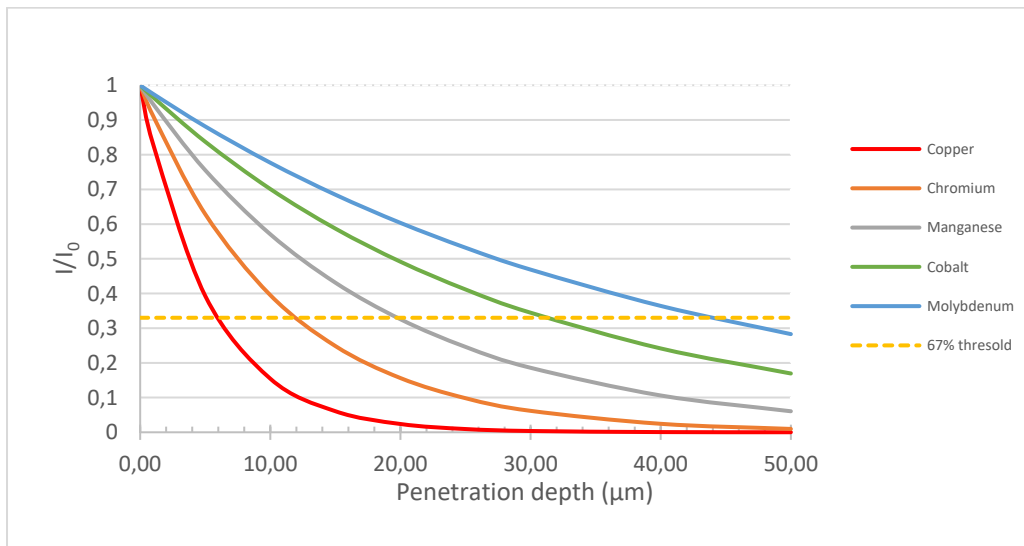


Figure 3.15: Variation of ratio I/I_0 as a function of depth, for different sources, with a diffraction angle of 45° for Wüstite; the penetration depth can be read at the intersection with the yellow dotted line

In this part, a global description of XRD has been done and the set-up that is used in this study has been described. The penetration depth is thus limited, and has to be considered in the interpretation of results. Now, the room temperature XRD analyses are discussed.

Table 3-4: Characteristic wavelengths for the anticathodes currently used for XRD

<i>Anticathode</i>	<i>Wavelength (\AA) $K_{\alpha 1} - K_{\alpha 2}$</i>	<i>Energy (KeV)</i>	<i>Penetration depth (μm) $I/I_0 < 0.33$</i>
Copper	1.5406 - 1.5443	8.05	6
Chromium	2.2896 – 2.2935	5.41	12
Manganese	2.102 – 2.106	6.54	20
Cobalt	1.7889 - 1.7928	6.93	30
Molybdenum	0.7093 – 0.7135	17.47	42

3.5 Room temperature: XRD results of a specimen pre-oxidized in the Orion Furnace

3.5.1 Phase analysis

3.5.1.1 Copper source

In order to verify the penetration depth, three samples of IF with different oxide thickness (12, 26 and 55 μm) are analysed with a Copper anticathode (45 kV and 30 mA). The characteristics of each source are summarised in the Table 3-4.

The identification is made for each phase. In the presence of multiphase components (for us, at least 3 plus the steel substrate), the identification can be complicated due to overlapping peaks. To help analyses, for each phase, all the diffraction peaks are reported in the Powder Diffraction File with their relative intensities. These data are usually based on powder diffraction.

The Figure 3.16 (a) is the XRD diffractogram for IF_650_55. Only the sub-surface is analysed (6 μm out of 55 μm) and the three phases are detected.

The Figure 3.16 (b) is the XRD diffractogram for IF with 3 different thicknesses. After the identification of each phase, peaks attributed to Hematite are more intense for the thicker specimen. In other words, the volume of Hematite analysed by XRD is larger. Inversely, for Wüstite, for the larger thickness, the volume analysed is lower (because the presence of Wüstite is at the limit of the penetration depth (6/7 μm). For a thick sample, the whole oxide is not analysed, but only the superficial phases. The schematic representations of the Figure 3.17 show the analysed volume of each phase.

Copper source has low penetration depth (6 μm), and fluorescence disturbs the analysis. Moreover, a few peaks are superimposed between the different phases. For example, (the peak at $2\theta=122^\circ$ can be attributed to Magnetite, Hematite or Wüstite).

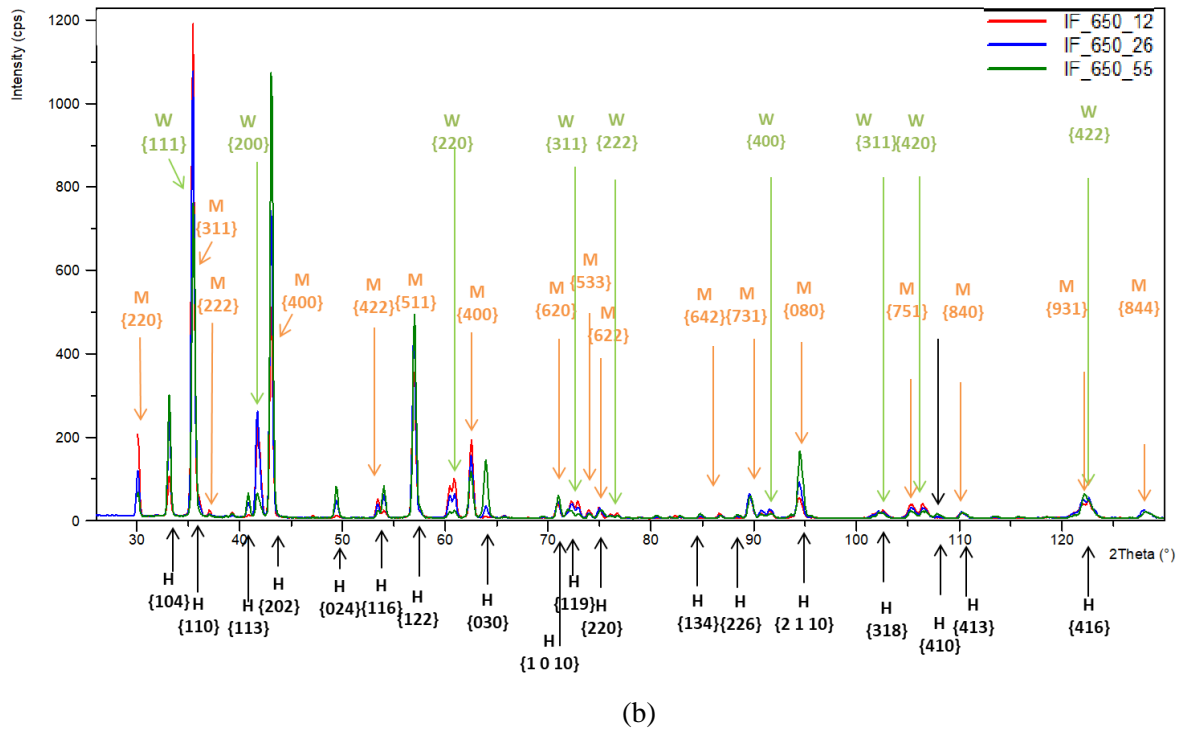
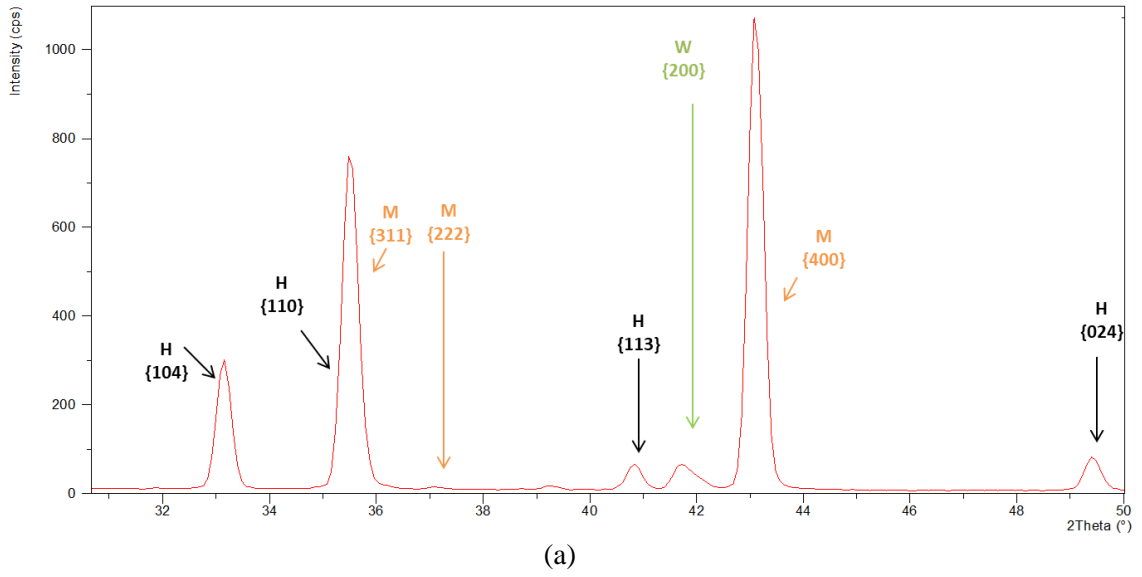
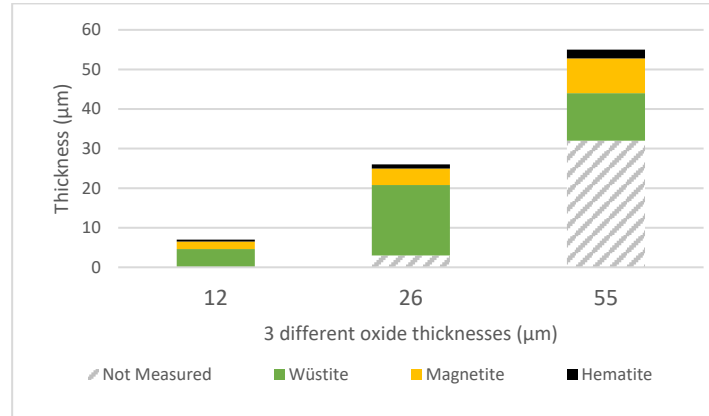
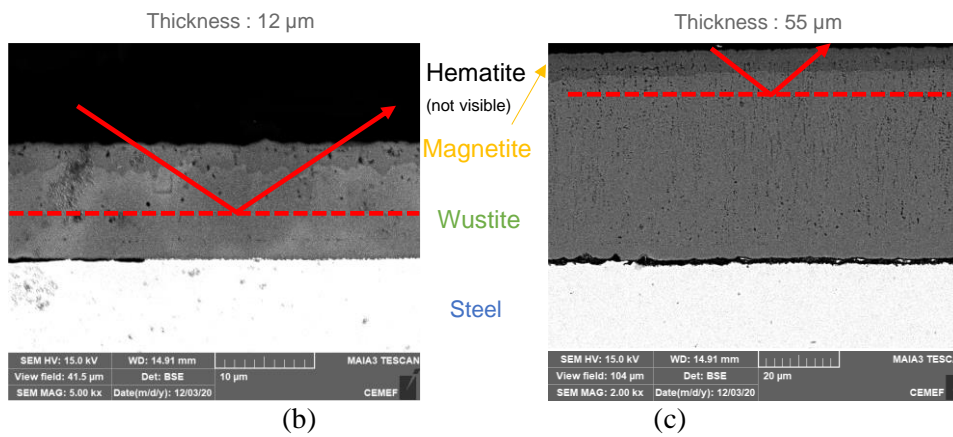


Figure 3.16: XRD diffractogram with Copper anticathode for IF oxidized at 650°C, with oxide thickness 12 (red), 26 (blue) and 55 (green) μm . Green legends represent Wüstite, black Hematite and orange Magnetite. (a) sample IF_650_55. (b) Comparison of thicknesses 12 μm , 26 μm and 55 μm .



(a)



(b)

(c)

Figure 3.17: (a) Schematic representation of diffracting volume with the penetration depth of a Copper anticathode. SEM images where the dashed line represents the penetration depth of X-Rays (b) sample IF_650_12 (c) sample IF_650_55.

3.5.1.2 Other anticathodes: Chromium and Manganese

In these set-ups, a monochromator is not used but a K_{β} filter (V for Cr) is added. Parameters are set to 45 kV and 40 mA for the Chromium and 30 kV and 30 mA for the Manganese sources.

For the Manganese source (Figure 3.18), the penetration depth is larger (20 μm), and thus the peaks of Hematite are more intense for the 55 μm sample. For the thinnest sample (12 μm), the ferrite is detected, proving that penetration depth is larger than the thickness of the oxide. It confirms the correct value of the estimated penetration depth (Table 3-4). For Wüstite, the maximum of intensity is for the 26 μm oxide sample. This is due to the larger W volume diffracting than for the 55 μm oxide sample which has a lot of Hematite and Magnetite in surface, and than for the 12 μm oxide sample (in which the thickness of Wüstite analysed is lower).

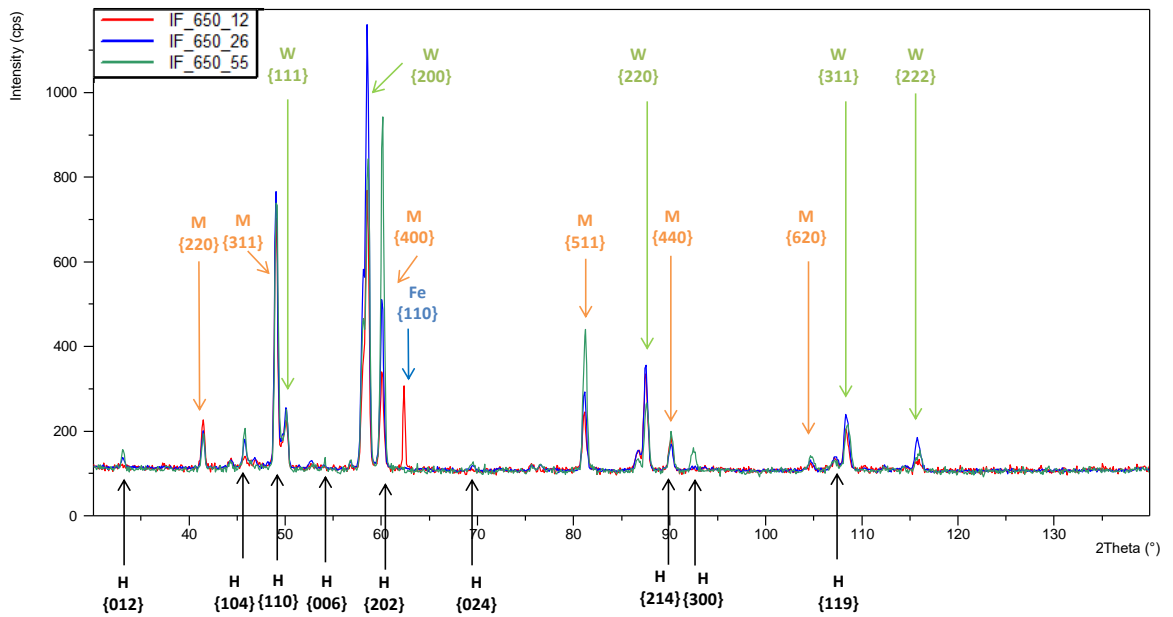


Figure 3.18: XRD diffractogram with Manganese anticathode for 12 (red), 26 (blue) and 55 (green) μm specimen oxidized at 650°C , green writing represents Wüstite, black is Hematite and orange is Magnetite.

The same conclusions are drawn with the Cr anticathode (Figure 3.19). However, even with the penetration depth of 12 μm (the same as the lowest oxide thickness), the diffraction peak of ferrite is not identifiable (it should appear at $2\theta=68.7^\circ$). The Chromium anticathode is better adapted for stress analysis. The main advantage of the Chromium source is that the {311} peak of Wüstite at $2\theta=124^\circ$ is isolated whereas with the Copper anticathode, the Wüstite {422} at 123° overlaps with {931} of Magnetite and {416} of Hematite. This anticathode is mainly selected for the room temperature stress analysis.

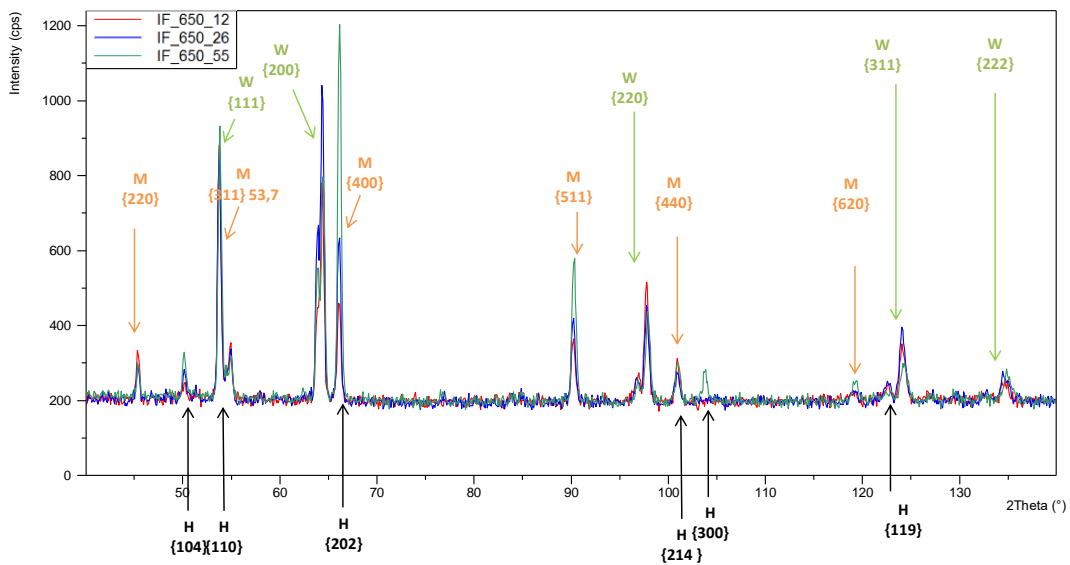


Figure 3.19: XRD diffractogram with Chromium anticathode for 12 (red), 26 (blue) and 55 (green) μm specimen oxidized at 650°C , green writing represents Wüstite, black is Hematite and orange is Magnetite.

All these results are totally in agreement with the literature. It confirms the presence of three phases : Wüstite, Magnetite and Hematite. The Hematite is a very thin layer in surface, which is not observable with the SEM on cross-sections (too thin and discontinuous). When the thickness of oxide is above the penetration depth, the steel substrate peaks are not detected by X-Rays.

3.5.2 Crystallographic texture

Before making a stress analysis, it is interesting to study the texture of each phase, the intensity of each peak is sensitive to the preferential orientation of grains. For cubic oxide (such as Magnetite and Wüstite), a fiber axis texture in the growth direction of the oxide is reported in the literature [131,134–136].

Texture analysis is based on a single family of planes (i.e. a 2θ angle is selected). The sample is rotated stepwise about two perpendicular rotation axes on the goniometer: rotation axis normal to the sample (angle ϕ) and rotation axis lying in the sample surface (tilting angle ψ). Steps may be 3° in tilting angle and 5° in azimuth angle, for example. The pole figure consists in the representation of the intensities for each angle pair ϕ - ψ (ϕ from 0 to 360° and ψ from 0 to 84°). Depending on the preferential texture, the intensity is varying as a function of these angles. A non-textured sample should have the similar intensity for each angle.

The Chromium source is used (45 kV and 40mA) and the pole figures of the {400} and {220} planes for Magnetite and {200} and {220} planes for Wüstite are determined on oxidized specimen (IF_650_26).

For the Wüstite phase, the maximum diffraction intensity for the {200} plane is close to the middle of the pole figure (normal direction of the sample) (Figure 3.20). The pole figure indicates that the normal to the {100} family (represented by peak {200}) points in the direction of the normal to the sample i.e. the direction of growth of the oxide layer. According to Buscail et al. [137], the {200} orientation is the direction of maximum growth rate of a cubic crystal. By the way, as the texture of the steel is different, the growth is not epitaxial. Indeed, if Wüstite is oriented in such a way, it appears that oxygen is quickly absorbed leading to a higher scaling rate.

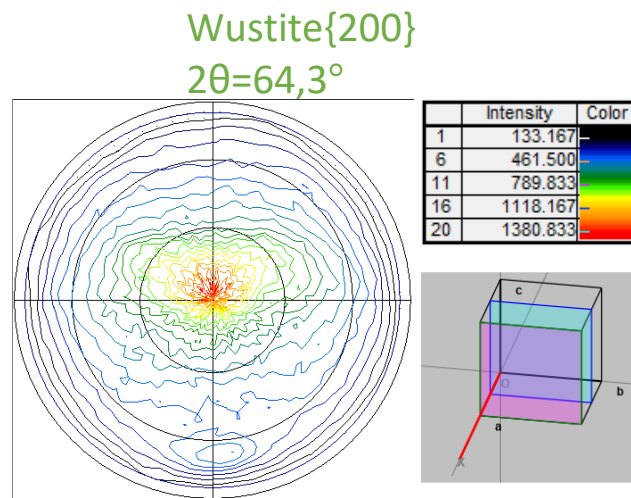


Figure 3.20: Pole figures of Wüstite with Chromium anticathode for the IF_650_26 sample {200} family plane

Similarly, for the Magnetite, the plane {400} exhibits a maximum diffraction intensity concentrated in the centre (Figure 3.21). The {220} planes are mainly located at an angle of 45° with respect to {200}, the maximum is a crown for a ψ angle of 45° . It corresponds to a clearly cube texture.

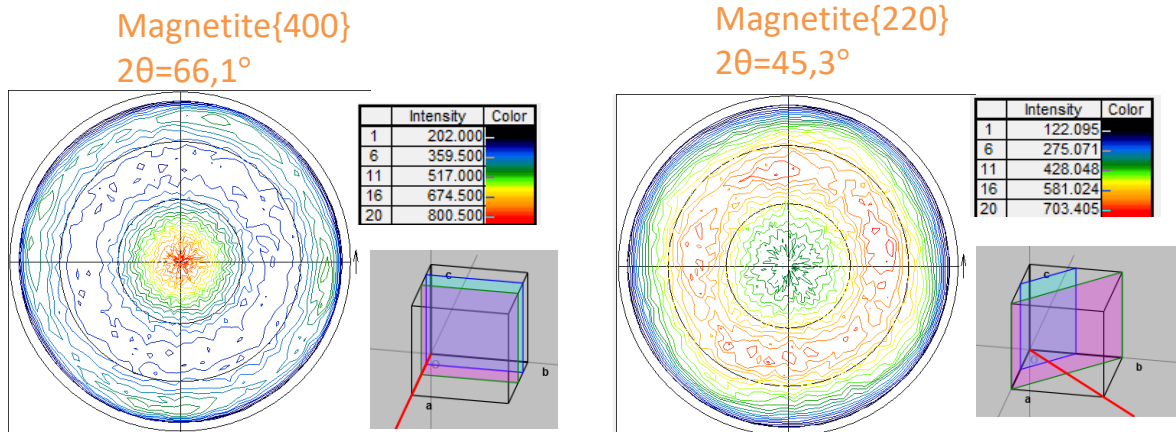


Figure 3.21: Pole figures of Magnetite with Chromium anticathode for the IF_650_26 sample (a) {400} family plane (b) {220}

To complete the analysis, the ferrite pole figure of {200} and {110} is made on the same sample (Figure 3.22). First, it indicates higher intensities. It is probably due to the coarse grains of ferrite. The volume analysed by X-Ray (only a few grains) is not representative of the sample texture. This means that for a thickness of $26\ \mu\text{m}$, the ferrite can be detected by the Chromium anticathode, meaning that penetration depth is a little bit larger than expected. For the 2θ phase analysis (Figure 3.19) ($\phi=\psi=0^\circ$), no peaks are observed.

These textures of Wüstite and Magnetite are confirmed for other thicknesses (12 and $55\ \mu\text{m}$). Thus the preferential orientation is independent of thickness.

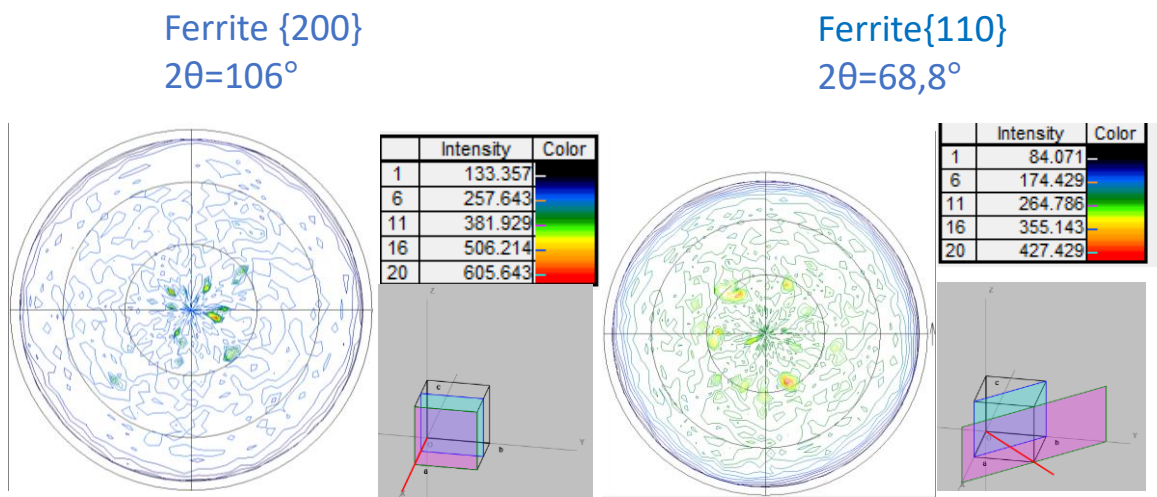


Figure 3.22: Pole figures of Ferrite with Chromium anticathode for the IF_650_26 sample (a) {200} family plane (b) {110}

The comparison is made with the literature and similar results are described. Basabe and Szpunar make texture analysis with EBSD, of low carbon steel specimens oxidized for 10 seconds at 800°C, 900°C and 950°C [135]. At 850°C, the oxide scale has a weak texture with no dominant texture components. With the increasing temperature at 900 and 950°C, the Wüstite and Magnetite phases develop a cube texture $\{001\}\langle 100\rangle$. They attribute this to the transformation phase of steel substrate from α to γ . The very short oxidation / higher temperature, probably the smaller oxide thickness, may explain the difference with our own results.

Higginson and West study IF oxidized specimen at 760°C for 2 hours [134]. Wüstite has a strong $\{100\}\langle 001\rangle$ component and the Magnetite exhibits both this and the $\{110\}\langle 001\rangle$ component. The oxidation process is strongly dependent on the oxidation temperature. The multi-layered character tends to complexify the analysis, as each layer is influenced by the others. The same authors confirm that for a low carbon steel specimen oxidized for 15 minutes at 800°C, 900°C and 1000°C [136], Magnetite layer shows for the outer layer showing a strong cube $\{110\}\langle 001\rangle$ and also a $\{110\}\langle 001\rangle$ orientation (not visible in our study). The texture of the oxide layers appears to significantly depend on the temperature with stronger textures seen at higher temperatures. Finally, Juricic et al. show that Wüstite and Magnetite evolve clear $\{001\}$ fibre textures parallel to the surface normal of the iron substrate after 5 hours of oxidation [131].

As a conclusion, a fiber axis texture in the growth direction of the oxide is observed. The texture is better defined for the Magnetite than Wüstite. The textural analysis of the oxide layers shows very clearly a strong crystallographic orientation. However, there is no clear correlation between the ferrite texture and the oxides [136]. By increasing the time of oxidation and the temperature (and the thickness), the texture is more pronounced.

3.5.3 Stress analyses

In this first step, the objective of stress analysis is to quantify the internal stresses of oxide after the cooling to room temperature. At room temperature, the analysis is the sum of the stresses in temperature (growth stress, possibly attenuated by relaxation) and during cooling (thermal stresses).

X-ray diffraction measurements are performed using the K_{α} radiation of Chromium (45 kV and 40 mA), Manganese (30 kV and 30 mA) and Copper (45 kV and 30 mA) for Wüstite and Magnetite phase. For each source, the peak with the highest 2θ angle is selected because the shift of the peak due to the deformation of the crystallographic lattice is larger for high 2θ , giving a better sensitivity of the method. Hematite is not investigated because under our conditions (short times, thin scales), it never really forms a continuous, hence “stressable”, layer.

The step size is 0.026° to have at least 40 points to properly define the peak. The choice of $\{hkl\}$ planes of each phase depends on the anticathode and the peak intensity. All the peaks analysed are referenced in the Table 3-5.

At least 6 angles ψ are considered for each analysis, ranging from $\sin^2\psi = 0$ to 0.75. At room temperature, the counting time for XRD analysis is not a problem (due to the extremely slow reactivity of iron oxides). The analysis for each angle ψ is about 30 minutes to obtain a good peak quality, thus the global analysis takes several hours. In theory, to measure the complete stress tensor, 3 ϕ angles and negative ψ angles should be used. For the goniometer used for these measurements, a rotation with negative ψ angle is not possible. Therefore, the measurement is made by making a ϕ rotation of 180° , which leads to the same results. In some cases, the ψ values are not considered in the calculations because of the texture (low intensities with increasing the angle ψ due to the decrease of the penetration depth and to the oxide texture).

The peak position is found by fitting a profile function. This function is adapted to each peak. In order to have comparative results, the same treatment is done for a family of planes for the same anticathode (same shape of the peak is assumed). It is recommended to use Pearson VII-functions, which are flexible in describing profiles. In this study, the profile function is either intermediate Lorentzian, or modified Lorentzian or Gaussian, after a Pearson VII fitting. The peak position is found according to:

$$y = y_0 \left(1 + \frac{\left(\frac{1}{2^{\frac{1}{m}} - 1} \right) x^2}{w^2} \right)^{-m} \quad (3-10)$$

with y_0 the amplitude at position x_0 , $x = 2\theta(x_i - x_0)$, w the half width at half-maximum and m the Pearson VII shape parameter. When $m = 1.5$ or 2, the peak is called modified Lorentzian; m and $m > 10$, the function tends to the Gaussian profile. In order to reduce the noise, the background intensity is also suppressed in the analysis.

In the treatment, a function is added to eliminate the part of the scan data which originates from the $K_{\alpha 2}$ wavelength coming from the X-ray tube. It is used to filter the data, to remove some overlap problems before calculating the peak position and to adjust stress analysis. At higher 2θ angle, the doublet splitting increases and simplifies the treatment.

The X-ray elastic constants are calculated with isotropic constants: at room temperature, the Young's Modulus of Magnetite is set to 160 GPa and 130 GPa for Wüstite. The Poisson's ratio is equal to 0.3.

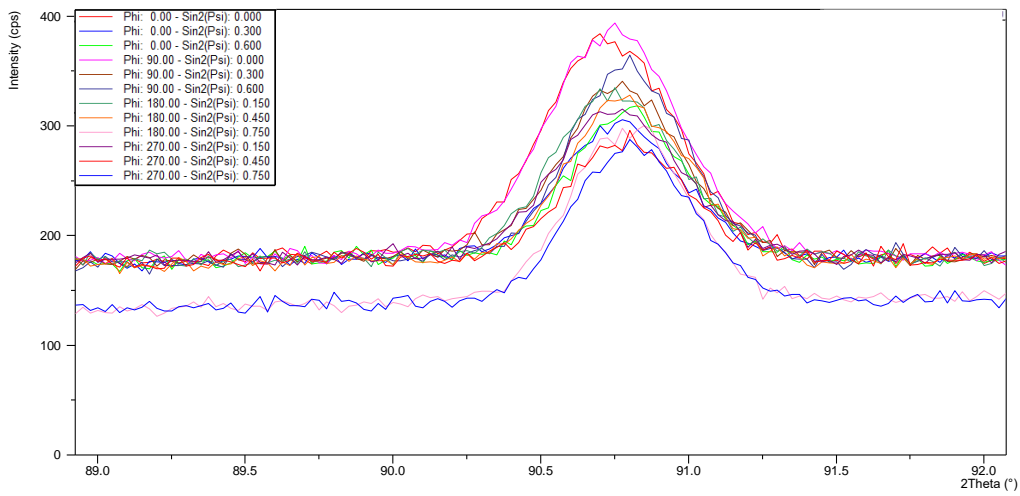
After the peak position determination, in the presence of stresses, there is a shift of the peak with the rotation of the angle ψ , and according to the theory, from the local strain, the macroscopic stress can be calculated with the equation (3-8).

3.5.3.1 Tri-axiality analysis

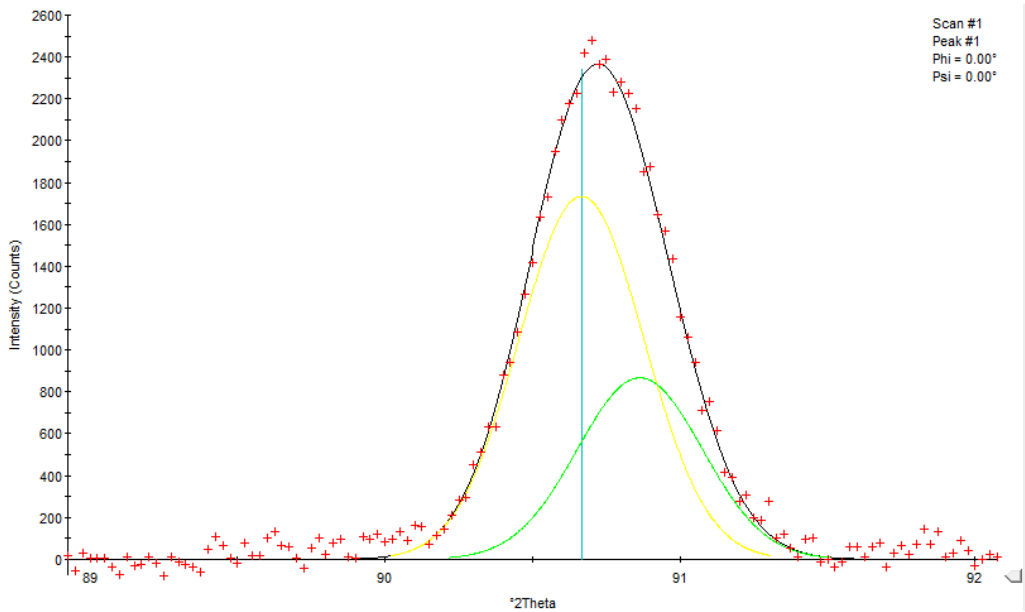
In order to verify the hypothesis made in the theory of the $\sin^2\psi$ law (shearing component equal to 0 and equi-biaxial in-plane stresses), the analysis is made with different ϕ angles (0/180 and 90/270°), 6 angles ψ each, for the Magnetite {511} peak and the Chromium anticathode. The measurement time is 10-20 minutes for a ψ analysis, thus a total of several hours. It is not a problem for room temperature, because of the stability of iron oxides.

In the Figure 3.23 (a), for a same ψ angle, the intensities of the peak are similar for the 0° and 90° ϕ angles (same penetration depth). In this case, the peak position is found with a Gaussian fit and the deconvolution between the $K_{\alpha 1}$ (green) and the $K_{\alpha 2}$ (yellow) (Figure 3.23 (b)). The shift is about 0.07 and 0.08° between $\sin^2\psi = 0$ and $\sin^2\psi = 0.75$. The relation between the shift of the peak and the angle ψ has a linear form, so that the local strain calculated with Bragg's law can be transformed into a macroscopic stress value.

After the calculation, the stress component in the two principal directions (the sample length and width) are quite similar, considering the uncertainty (of measurement and peak processing) (Figure 3.23 (c)). The hypothesis of equi-biaxial stress seems to be valid. The shearing component is also very low and negligible. Similar results are found with the Wüstite phase (no shearing component) and confirm the hypothesis. For the oxides, the compressive stresses are mainly attributed to the thermal stresses of the cooling to room temperature. The cooling is homogeneous in all sample directions and thus, for the rest of the study, the hypothesis of equi-biaxial stress component is made. Thus, only a single angle $\phi=0$ may be used, which reduces the measurement time.



(a)



(b)

$$\sigma = \begin{pmatrix} -90 & 0 & 0 \\ 0 & -95 & 05 \\ 0 & 5 & 0 \end{pmatrix} \pm \begin{pmatrix} 10 & 0 & 5 \\ 0 & 15 & 5 \\ 5 & 5 & 0 \end{pmatrix}$$

(c)

Figure 3.23: (a) Evolution of the Magnetite {511} peak position with the variation of $\sin^2\psi$ (from 0 to 0.75) (ψ from 0 to 50.8°) for 2 ϕ angles (0 and 90°) (b) fitting of the peak with a Gauss function and deconvolution of the the $K_{\alpha 1}$ (yellow) and the $K_{\alpha 2}$ (green) (c) measured stress tensor

3.5.3.2 Equi-biaxial measurement

By considering only equi-biaxial stresses (and no shearing stress), the calculation is made only with an angle ϕ and 7 angles ψ between $\sin^2\psi = 0$ and $\sin^2\psi = 0.7$ in the Figure 3.24. The peak is the Wüstite {311} analysed with the Chromium anticathode. There is a linear relationship between the d-spacing the variation of the $\sin^2\psi$, corresponding to a compressive stress of -175 ± 5 MPa.

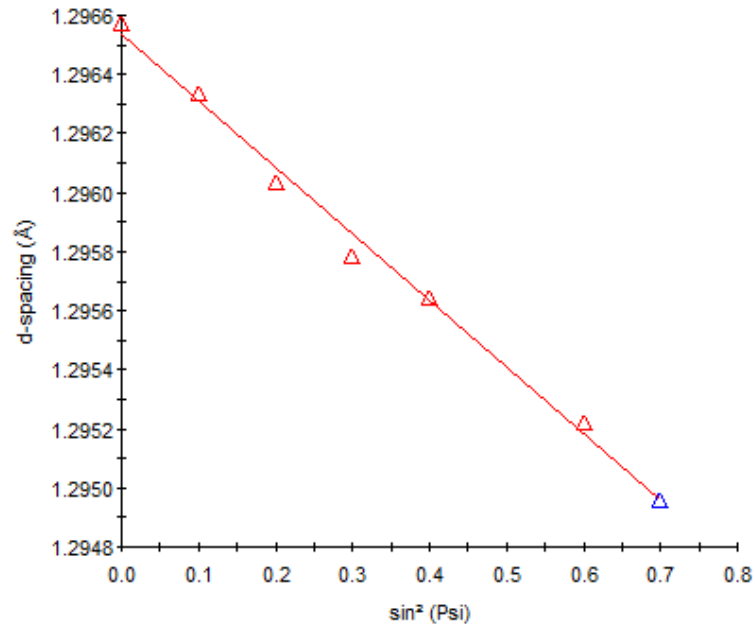


Figure 3.24: Evolution of the d-spacing of the Wüstite {311} peak with the variation of $\sin^2\psi$ angle (from 0 to 0.7)

All the analyses made are referenced in the Table 3-5.

In Magnetite as well as in Wüstite, the stresses are compressive (Figure 3.25). The measured residual stresses superpose the internal stress state existing at high temperatures prior to cooling (growth stress, phase change, maybe partially relaxed) to thermal stresses due to cooling of layers with different coefficients of thermal expansion. The final stage is compressive but the history is not known. The quick cooling from the high temperature tends to avoid any relaxation. In order to have more information on the growth stresses, high temperature measurement is needed as described in the next part 3.6.

Below 560°C , the CTE of Wüstite is lower than that of steel. The generation of compressive stresses is logical. From the pure elastic model described in equation (2-5), the cooling from 700°C to room temperature brings about -200 MPa. The values are not so far from the experimental data. Nevertheless, the relaxation at higher temperature but also porosity and micro-cracking (as Figure 3.6, Figure 3.2 and Figure 3.3 indicate) tends to decrease stress.

Table 3-5: Summary of all the analysed peak at room temperature. For some configurations, two angles ϕ are used (thus σ_1 and σ_2 evaluated). In other configurations, equi-biaxial stresses are assumed.

Sample	Anti cathode	Phase (E in GPa ; v))	{hkl} 2 θ	Angles ψ and ϕ	Treatment	stress
IF_650_11	Cr	Wüstite (130 ; 0,3)	{311} 2 θ =124°	8 ψ (0 to 0,7)	Modified Lorentzian	-140 \pm 5
IF_650_26	Cr	Wüstite (130 ; 0,3)	{311} 2 θ =124°	8 ψ (0 to 0,7)	Modified Lorentzian	-175 \pm 5
IF_650_55	Cr	Wüstite (130 ; 0,3)	{311} 2 θ =124°	8 ψ (0 to 0,7)	Modified Lorentzian	-115 \pm 15
IF_650_55	Cr	Wüstite (130 ; 0,3)	{220} 2 θ =98°	7 ψ (0 to 0,6)	Intermediate Lorentzian	-140 \pm 15
IF_650_55	Cr	Wüstite (130 ; 0,3)	{222} 2 θ =135°	7 ψ (0 to 0,6)	Modified Lorentzian	-130 \pm 10
IF_700_5	Cr	Wüstite (130 ; 0,3)	{311} 2 θ =124°	20 ψ (0 to 0,6) 2 ϕ (0 and 90)	Gauss	$\sigma_1=10$ $\sigma_2=20$ ± 5
IF_700_5	Cr	Wüstite (130 ; 0,3)	{220} 2 θ =98°	6 ψ (0 to 0,75)	Gauss	$\sigma_1=0$ $\sigma_2=10$ ± 5
IF_700_15	Cr	Wüstite (130 ; 0,3)	{311} 2 θ =124°	20 ψ (0 to 0,6) 2 ϕ (0 and 90)	Gauss	$\sigma_1=-180$ $\sigma_2=-170$ ± 5
IF_700_15	Cr	Wüstite (130 ; 0,3)	{220} 2 θ =98°	6 ψ (0 to 0,75)	Gauss	$\sigma=-140$ ± 5
IF_700_30	Cr	Wüstite (130 ; 0,3)	{311} 2 θ =124°	20 ψ (0 to 0,6) 2 ϕ (0 and 90)	Gauss	$\sigma_1=-90$ $\sigma_2=-110$ ± 5
IF_650_55	Mn	Wüstite (130 ; 0,3)	{311} 2 θ =108°	6 ψ (0 to 0,5)	Intermediate Lorentzian	-150 \pm 15
IF_700_5	Cu	Wüstite (130 ; 0,3)	{422} 2 θ =123°	12 ψ (0 to 0,75) 2 ϕ (0 and 90)	Intermediate Lorentzian	$\sigma_1=10$ $\sigma_2=10$ ± 5
IF_650_11	Cr	Magnetite (160 ;0,3)	{511} 2 θ =90°	8 ψ (0 to 0,7)	Gauss	-120 \pm 5
IF_650_26	Cr	Magnetite (160 ;0,3)	{511} 2 θ =90°	8 ψ (0 to 0,7)	Gauss	-115 \pm 5
IF_650_55	Cr	Magnetite (160 ;0,3)	{511} 2 θ =90°	8 ψ (0 to 0,8)	Gauss	-30 \pm 5
IF_700_15	Cr	Magnetite (160 ;0,3)	{511} 2 θ =90°	20 ψ (0 to 0,6) 2 ϕ (0 and 90)	Gauss	$\sigma_1=-90$ $\sigma_2=-90$ ± 10
IF_700_15	Cr	Magnetite (160 ;0,3)	{440} 2 θ =101°	6 ψ (0 to 0,75)	Gauss	$\sigma_1=-135$ ± 10
IF_700_30	Cr	Magnetite (160 ;0,3)	{511} 2 θ =90°	20 ψ (0 to 0,6) 2 ϕ (0 and 90)	Gauss	$\sigma_1=-25$ $\sigma_2=-30$ ± 5
IF_700_15	Cu	Magnetite (160 ;0,3)	{731} 2 θ =144°	12 ψ (0 to 0,75) 2 ϕ (0 and 90)	Gauss	$\sigma_1=-95$ $\sigma_2=-80$ ± 10

For the Magnetite, the compressive stresses are in any case lower than Wüstite or close to stress-free. According to the literature, its CTE is higher than Steel and Wüstite for $T > 400^\circ\text{C}$ and lower below. It is therefore not excluded to observe a change from tensile to compressive stress during the cooling. It has been calculated (Juricic et al. [131]) that during the cooling to room temperature, first tensile, then compressive stresses are generated. For these authors, after cooling from 650°C to room temperature, Magnetite changes from -400 to 200 MPa (8 μm thickness).

As a reminder, the samples with a thickness of 5, 15 and 30 μm are oxidized at 700°C (in comparison to 650° : 11, 26 and 55 μm).

There is no clear dependence on the evolution of stresses as a function of thickness (Figure 3.25). For a same anticathode, the penetration depth is the same even if the thickness of oxide is increasing. For thicker samples (above 15 μm), only the superficial $\sim 12 \mu\text{m}$ of the oxide are analysed. In Appendix B, the evolution of stresses through the scale thickness using different anticathode is described. A gradient of stresses (more compressive stresses close to the steel) is suggested.

Stresses are completely relaxed for the thinner specimen (5 μm). The SEM observations shows that such samples are more fractured than thicker ones. However, it is difficult to conclude if the cracks observed are due to the rapid cooling after oxidation or to the mounting and polishing.

By considering the cooling for a bi-layer Wüstite and steel between 700°C and 650°C (supposed purely elastic) equation (2-5), the stress is within the measurement uncertainty (10 MPa). Thus, no major difference is found for these two different oxidation temperatures regarding the stresses behaviour.

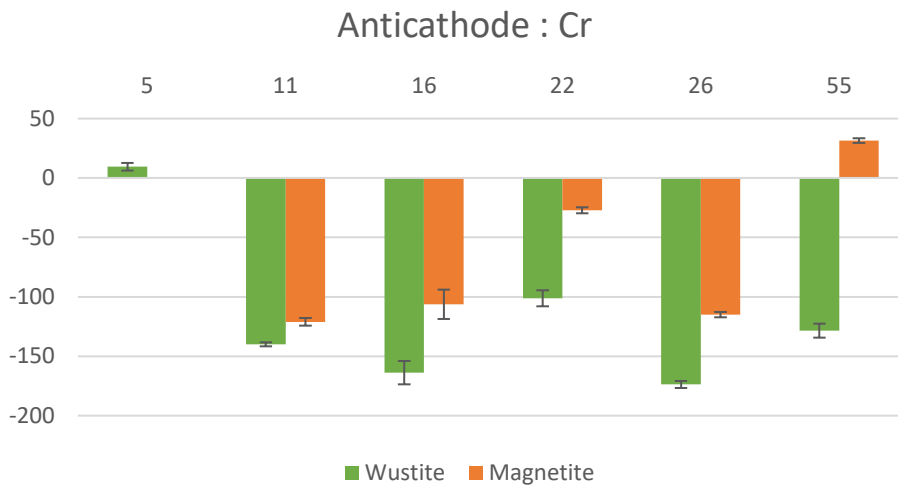


Figure 3.25 : Room temperature stress for Magnetite and Wüstite for different oxide thicknesses (Chromium anticathode: 12 μm of penetration depth). 5, 16 and 22 μm thicknesses are oxidized at 700°C and 11, 26 and 55 μm at 650°C

The room temperature stress analysis indicate a compression state within oxides. It is due to the thermal stresses generated during the cooling to room temperature. This confirms that the stress is mainly equi-biaxial. In the rest of the study, only equi-biaxial analysis are carried out to limit the time of acquisition. In the next part, the High temperature X-Ray diffraction (HTXRD) for in situ analyses are described.

3.6 High temperature X-Ray diffraction (HTXRD) for in situ analysis of stress evolution

The main question to be answered now is the existence or not of relaxation in a certain high temperature range. To obtain this result, stress has to be created (growth or thermal), then it has to be measured at time intervals under constant conditions. This has to be repeated at different temperatures to determine the temperature range where relaxation occurs. The way we have chosen is to perform the XRD stress measurements in situ, impose temperature cycles with steps long enough to perform stress measurements.

In the first stage, we have used a proportional detector which imposes a long stress measuring time. It showed two disadvantages: first, we have no time resolution to follow stress evolution; second, the stress may change while we are measuring it (varying ψ). Therefore, we changed to a faster counter ("Pixel"). It however forced us to change the stress measurement configuration. Both procedures are illustrated in the following.

3.6.1 Description of the equipment

A furnace can be added on the goniometer to make high-temperature X-Ray Diffraction (HTXRD). The Anton Paar DHS 1100 can heat samples up to 1100°C with a good temperature uniformity (Figure 3.26 (a)). The ceramic heating plate is chemically resistant to iron and its oxides.

In the set-up, a graphite dome is positioned to control the atmosphere (Figure 3.26 (b)). This dome is optimised for the Copper anticathode (65% of transmission). For the other anticathodes, the absorption of the X-Rays makes the detection X-Rays impossible.

This set-up is connected to a gas bottle of pure nitrogen (AlphaGaz2 with 99,9999 % purity 6N) to control the oxidation all along the thermal cycle. The dome is pressurised to avoid penetration of oxygen. The oxidizing air is introduced by opening a pipe for the time corresponding to the desired oxidation.

The first HTXRD analysis has shown that a temperature recalibration using a thermo-couple was needed. This difference of temperature between the requested temperature and the sample surface has been found highly dependent on the sample conductivity and thickness, and on the environment, in particular the gas flow.

For the calibration, a thermo-couple is welded at the surface of a pure steel sample, the temperature is measured all along the thermal cycle. In order to avoid the oxidation (constant thickness), a pure nitrogen atmosphere (6N) is used. The sample is heated to 1050°C (nominal) with a pause every 100°C to record the thermocouple temperature ; it is finally cooled down to room temperature (Figure 3.26 (c)). First, the temperature stabilisation is quick due to the small thickness of the sample (1 mm). However, the difference between the desired temperature and the thermocouple temperature measured on the surface is increasing with the rise of temperature; a difference more than 100°C is measured at 1050°C, see the curve in green in the Figure 3.26 (d). The difference is the same between heating and cooling. In order to confirm this difference, the allotropic transformation of pure steel (912°) is detected for a nominal temperature of 1005°C, using XRD monitoring of the phases.

In the following, the temperature corrected using Figure 3.26 will be reported systematically.

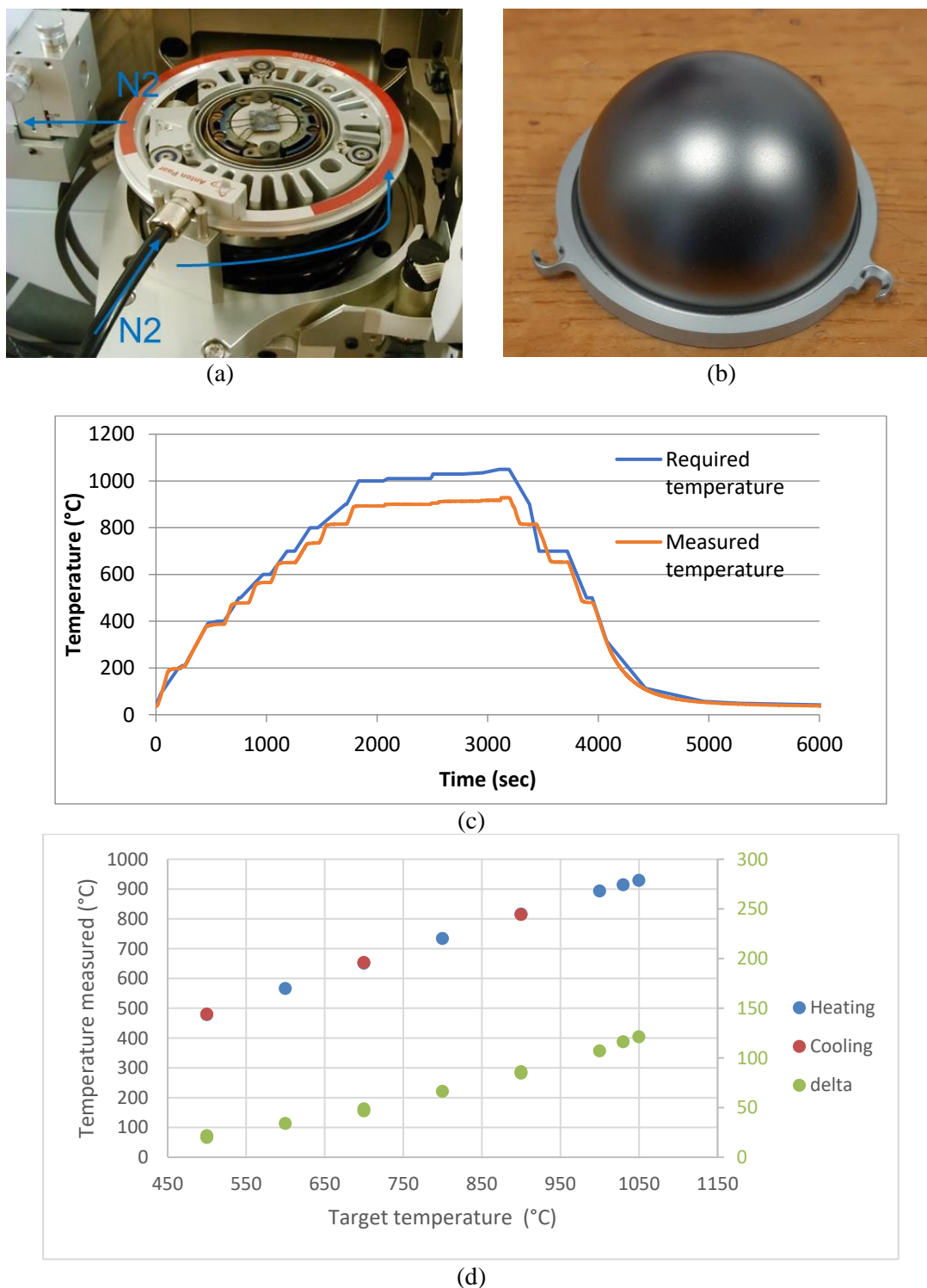


Figure 3.26: (a) Anton Parr heating device (until 1100°C) installed on the goniometer (b) Graphite dome for atmosphere control (c) Thermal cycle for calibration, to calculate the difference between the nominal temperature and the temperature measured with the thermo-couple (d) Evolution of temperature difference during the thermal cycle during heating (blue), cooling (red) and the difference (delta, green)

3.6.2 Determination of the coefficient of thermal expansion (CTE)

The thermal expansion coefficient (CTE) can be determined directly from the lattice parameter deduced from the Bragg's law with the equation:

$$\alpha = \frac{1}{a_{RT}} \left[\frac{a_{HT} - a_{RT}}{T_{RT} - T_{HT}} \right] \quad (3-11)$$

with α is the average thermal expansion coefficient, a_{RT} and a_{HT} are the lattice parameter values at room temperature and high temperature. This CTE is an average over a temperature range. The range of temperature is 810°C-560°C: below the transition to the austenitic phase of steel and above the Wüstite stability temperature.

This analysis has to be done on a stress-free sample since in the presence of stress, the local distance d_{hkl} is changed, hence the cell parameter a .

First, the test is carried out on a non-oxidized IF sample (N_2 atmosphere all along). Measurements are done during cooling from 810 to 560°C. Similarly, for the Wüstite, another IF sample is heated to 810°C and oxidized briefly, so that the oxide is thin; at such a high temperature, it is assumed that only Wüstite is present.

Results are plotted in Figure 3.27 (a). For the steel, the CTE is constant in this temperature range. The CTE of Wüstite is found to vary from 15 to 12.4 $10^{-6} K^{-1}$ with a decrease in the temperature from 810 to 560°C. In the literature, according to Sasaki et al, no stresses are present in the Wüstite for the temperature above 700°C, it doesn't disturb the calculations. This hypothesis will be confirmed later. At 560°C, a theoretical stress-free value is taken, calculated by the PANalytical Stress® software. The oxide CTE is higher than steel above 640°C and in good agreement with the literature values (Figure 3.27 (b)). However, some difference is reported with Takeda et al. and Sasaki et al. for the highest temperature. With these results and in the absence of Magnetite, tensile stresses are generated for the cooling of Wüstite above 640°C, and compressive stresses below 560°C.

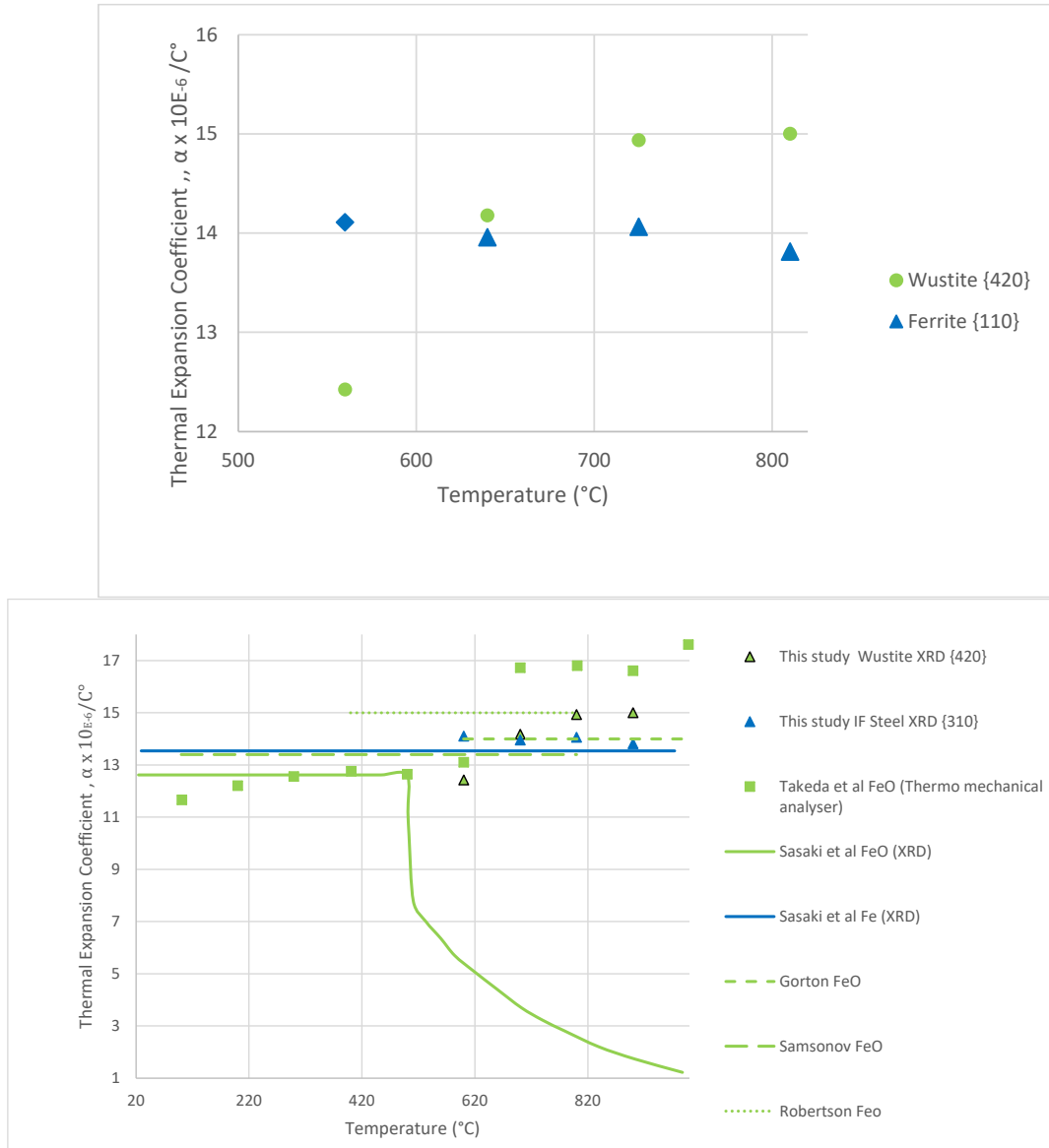


Figure 3.27: (a) Evolution of the CTE of Ferrite (blue) and Wüstite (in green) (b) comparison with the literature. The triangle refers to the results of our study. After [26,56,57,138]

The thermal behaviour of Wüstite and steel has been determined. During the cooling, above 600°C, tensile stresses are generated (CTE of Wüstite higher than steel). Below 600°C, compressive stresses are generated, in agreement with the previous results of section 3.5

3.6.3 Long Cycle stress analysis at high temperature: evaluation of thermal stresses and relaxation

With the described equipment, in-situ cycles are possible in the range of the capacity of the furnace (1100°C) with a pure nitrogen atmosphere. For next analysis, the copper source is used ($\lambda = 1,54056 \text{ \AA}$) because of the graphite dome.

The IF sample is initially polished (P800 Silicon Carbide SiC) to remove all the machining scratches and the possible oxides. Initially, the surface of the steel is analysed to confirm the absence of oxide in the μm range.

The atmosphere within the dome is initially pure nitrogen to avoid oxidation during heating. The heating speed is 100°C per minute until reaching the oxidation temperature (here 810°C). After the stabilisation of the temperature, air is introduced for a short time interval (3 minutes 36 s). This rather long duration is necessary because the pipe is long (~1 meter) and it takes time for the air to fill in the graphite dome. The oxidation process is controlled in-situ by the XRD analyses. Indeed, the shrinking of the ferrite peak is observed with the introduction of the oxidizing air. To stop the oxidation, pure nitrogen is flushed again all along the remaining 30 hours of the experiment. The thickness obtained is estimated after the thermal cycle with a SEM image of the sample: 12.5 µm oxide scale (Figure 3.28 (c)).

3.6.3.1 Phase analysis at high temperature : Wüstite only

The evolution of diffracted peaks with the decreasing temperature is plotted in the Figure 3.28. Phase analyses are done for $39^\circ \leq 2\theta \leq 45^\circ$. Indeed, with the copper anticathode, all the phases are identified: Hematite {113} at 40.9°, Magnetite {400} at 43.1°, Wüstite {200} at 42.1° and Ferrite {110} at 44.7°.

In Figure 3.28 (a), the HTXRD diffractogram during the cycle is plotted. Initially, Ferrite (Body-Centered Cubic) is present (peak at 44,1° at 810°). Wüstite (Face-Centered Cubic) appears in the surface (peak at 41,2° at 810°C) whereas ferrite disappears (buried too deep to be detected). As temperature decreases, the distance d tends to decrease so that the peak attributed to a phase is shifted to the right. It is clearly the case for the Wüstite {200} peak which is at 41.2 at 810°C and at 42,1° at room temperature. This shift is not an interpretation of a local strain, but a lattice dilatation with the evolution of temperature (CTE effect). For an IF specimen oxidized for a few hours above 520°C, the major, even single phase (in surface) is Wüstite.

Below the temperature of stability of Wüstite (~570°C), Wüstite starts to decompose into Iron and Magnetite. As a reminder, this reaction is divided into two steps:



Indeed, the Magnetite peak is present after 2.8 hours at 520°C (30,3 hours after the beginning of the cycle), the transformation is thus starting (Figure 3.28 (b)). Even after 2.8 hours, the Magnetite peak has a low intensity, meaning that the reaction is slow. Furthermore, no ferrite peak is present : the second step of the reaction has not started. Similar results are observed by Hayashi et al., the decrease of the Wüstite peak is slow (even after 4 hours at 500°C, the Wüstite peak is still present) [130].

Then at room temperature, the peak of Magnetite is still very small due to the “fast” cooling, and the major phase is still Wüstite.

For the oxidation at 810°C, Wüstite is the only phase detected by X-Rays. Below 570°C, the analysis is stopped to limit the decomposition of Wüstite.

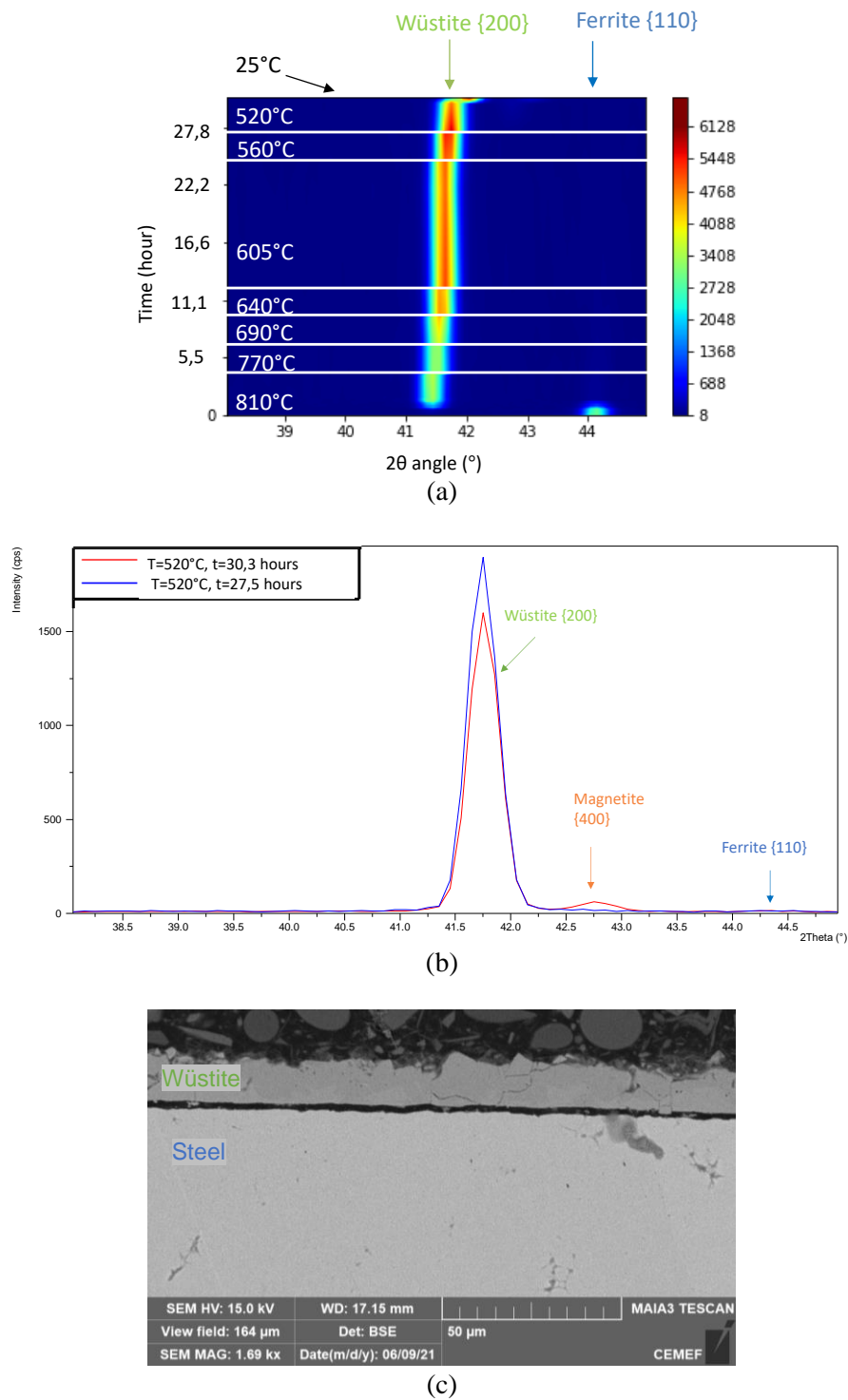


Figure 3.28: (a) Evolution of XRD pattern during the cooling stage of an in-situ cycle (810°C to room temperature, the scale of intensity is represented by the colour) (b) Diffractogram at 520°C at the beginning of the stage 27.5 hours (red) and at the end 30.3 hours (blue) (c) SEM cross-section of the sample after the thermal cycle (oxidation at 810°C for 3 minutes 36 seconds) (thickness of oxide is ~10 µm)

3.6.3.2 Stress measurement

Additionally, for each temperature, a long stress analysis is made. The method used is the same as described in the previous part. The peak analysed is the {422} plane of Wüstite. At least 5 ψ 's are considered for each analysis from $\sin^2\psi = 0$ to 0.6 (ψ from 0 to 50.8°). The peak treatment is based on the background estimation, a modified Lorentzian fit and a deconvolution between $K_{\alpha 1}$ and the $K_{\alpha 2}$. For the stress calculations, the elastic constants are re-calculated with the influence of the temperature (see the Morrel formula (2-13)). Equi-biaxial stresses are assumed in this study.

Table 3-6: Elastic constant selected for the X-Ray constant for the stress analysis

T(°C)	Young's Modulus (GPa)	Poisson ratio
25	130	0.3
520	100	0.3
560	97	0.3
605	95	0.3
640	92	0.3
690	89	0.3
725	87	0.3
810	82	0.3

The quality of peaks is not really good for the stress analysis even with very long counting times (more than 2.5 h for a 5- ψ analysis). Only general tendencies are given here (Figure 3.29) (a more precise analysis with the other detector is left for next section) :

- above 605°C, no stress is measured in Wüstite. Theoretically, growth stresses at 810°C (compressive) and the thermal stresses during cooling to 605°C (tensile) may be present. It is not case: they may have cancelled each other partly, but this result strongly suggests that stress relaxation takes place at these high temperatures due to the elasto-visco-plastic behaviour of Wüstite. This will be confirmed by more precise measurements (see below). Note that according to Mackenzie and Birchenall [61], the Wüstite layer is known to creep extensively during high temperature solicitation, and to relieve stresses due to the plastic flow.

- at 520°C, a tensile stress is measured in Wüstite (+80 ± 5 MPa at 520°C). Wüstite is no more stable. First, $Fe_{1-x}O$ begins to transform into Magnetite and a $Fe_{1-y}O$ ($y < x$) Wüstite, then this richer $Fe_{1-y}O$ is transformed according to the eutectoid reaction into Magnetite and Iron. This transformation is long (the peak of Magnetite has a low intensity after 2.8 hours). During this phase transformation, precipitation of Fe_3O_4 and the eutectoid reaction are responsible for the volume expansion in the Wüstite layer, compressive stresses within Wüstite are expected. Moreover, the thermal stresses should be compressive at this temperature because CTE of Wüstite is below the CTE of iron (Figure 3.27).

One explanation of the tensile stresses measured could be the modification of the inter-reticular distance d between $Fe_{1-x}O$ and $Fe_{1-y}O$ due to the change in stoichiometry. This shift can disturb the stress analysis of Wüstite. According to Hayashi et al. this d -spacing for Wüstite {400} is changing from 1.084 to 1.082 Å during a heat treatment at 500°C [130]. The peak of Magnetite {931}, at an angle close to the Wüstite peak used for the analysis, could also disturb the measurement (in spite of the very low amount of Magnetite?). Hayashi et al. observe tensile stress within Magnetite during the heat treatment at 500°C (after a 700°C oxidation) and explain it by the volume reduction in the Fe_3O_4 layer. However in the present study, the intensities of the Magnetite peaks do not allow any stress analysis in this phase.

- Finally, during cooling to room temperature, Wüstite changes from tension into compression (-45 MPa ± 5). The drop is about 120 MPa. This compression state is explained by thermal stresses during cooling due to the CTE mismatch between the metal and the oxide. Below 520°C, this coefficient is smaller for the oxide, and thus the retraction of the oxide is smaller. Therefore, the substrate is in tension and the oxide undergoes compressive strain. This stress increment is evaluated ~ -100 MPa for an oxide

composed of Wüstite on a low carbon steel for a cooling from 520°C to room temperature (with $\alpha_{Wüstite} = 13.10^{-6} \text{ K}^{-1}$ and $\alpha_{steel} = 14.10^{-6} \text{ K}^{-1}$) (equation (2-13) in section 2.5.1.1)

Additionally, the eutectoid transformation and the precipitation of Fe_3O_4 can also generate compressive stresses within Wüstite. However, this transformation is long and thus the fast cooling does not allow complete transformation.

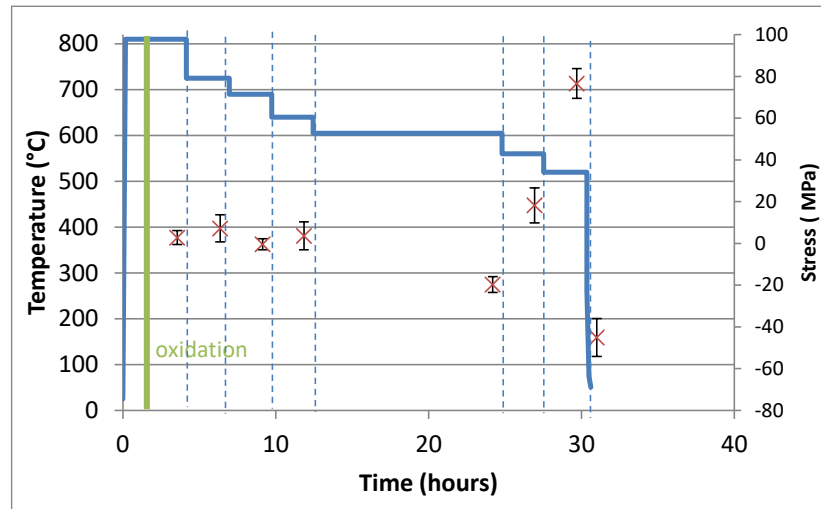


Figure 3.29 : Evolution of the stresses within the Wüstite {422} peak during the thermal cycle

This study highlights the limitations of the equipment used above, the long measurements do not allow to follow the evolution of the stresses, and the relaxation. The relaxation process is going on (the stresses are changing) while the analysis is carried out (varying ψ), thus a finer resolution of analysis is required. The counting time necessary to get exploitable peaks is too long (more than 2.5 hours for a stress analysis). The quality of the peaks used is also questionable, and no precise analysis can be done under these conditions.

3.6.4 Short Cycle analysis: to evaluate relaxation with a better time resolution

3.6.4.1 Test of the Omega configuration for the stress measurement

In order to reduce counting time, a new set-up is utilised with a Pixel detector. However, with this detector, the method based on the standard configuration χ is not valid, due to the defocusing of X-Rays with a rotation ψ which disturbs the detection of the diffracted beam, so that all the advantage of the fast counter is lost. Fortunately, the ω configuration is possible with the Pixel detector.

Comparison of the two configurations χ and ω with the same detector (slow, proportional)

Both configurations (χ and ω) have been tested at room temperature on Si powder (stress-free reference material) with the (slow) proportional detector. For both configurations, no shift of the diffracted peak is observed, and confirms the stress-free state of the Si powder standard. A steel sample has been sand-blasted to introduce compressive stresses, and analysed with Chromium and Copper anticathodes with the {200} and {310} planes of ferrite. Stress analyses give quite similar results for both anticathodes. With the Chromium anticathode, the stress measured is equal to: $-400 \pm 30 \text{ MPa}$ for

ω configuration and -480 ± 20 MPa for χ configuration. There is a 20% difference, thus only a comparison between the relative stress values is considered, they should not be taken as absolute data.

Comparison of the two detectors in the same ω configuration

Between the Pixel and the proportional detector, for the ω configurations, the same compressive stress is calculated with the $\sin^2\psi$ law : -390 ± 30 MPa for the proportional counter and -370 ± 30 MPa for the Pixel, a 5% difference, in the range of uncertainty.

The conclusion is that with the ω configurations, the good tendency is estimated, but the precise stress values calculated differ from the more usual χ method. According to Fischer et al. [139], to limit line broadening that disturbs the resolution power with the ω configuration, it is necessary to limit the range of tilt angle ψ . Indeed, the intensity of the diffracted peaks is too low for a good analysis. In this study at high temperature, the maximal value of $\sin^2\psi$ is set to 0.42.

With the Pixel detector, the time for counting is thus reduced to 20 minutes to record peaks usable for the global stress analysis. This represents a 7 to 8-time improvement compared with the proportional detector, although far from the factor 1/50 initially expected. Unfortunately, only 6 angles ψ are used, which is low, but this choice is made to limit the stress analysis time, and thus quantify the evolution of stresses as well as possible.

3.6.4.2 Comparison of long and short thermal cycles

Two thermal cycles are made:

- a first test with short temperature steps ~25 minutes, with a single stress analysis per temperature
- another one in which each temperature step is comparable with the experiment in section 3.6.3 (8 stress analyses, 20 minutes each, i.e. a total of 2 hours 30 minutes for each temperature), in order to observe the potential relaxation.

In both cases, the IF sample is analysed with the Copper source after oxidation at 810°C for 3 minutes. The oxidation is then avoided by pure nitrogen all along the experiment. In the range of 2θ (39-45°) Wüstite is the only oxide phase (Figure 3.30) and the ferrite is still visible (thin oxide) (Figure 3.30). These results agree with the previous experiments. The final thickness is determined by post-mortem SEM observations (6 μ m) (Figure 3.30 (c)).

The stress analysis is made on the {420} peak of Wüstite ($2\theta = 106.7$). A gaussian peak treatment (with the dissociation of the two K_α and a background) is made for each peak. 5 angles ψ are selected in the range of $\sin^2\psi = 0$ to 0.42. The crossed slits area is opened to 6mm \times 2mm, to increase the intensities of the peak. Some tendencies are observed in the Figure 3.31 :

- at 725°C or above, no matter how long it takes to analyse, the stress is zero, i.e. growth (at 810°C) or thermal (at 725°C) stresses have been relaxed. But the time of analysis is too long to observe the growth stress relaxation, which is therefore relatively fast. Wüstite deforms plastically and, at the accessible time scale, remains stress-free.

- at 640°C, for the long stage, a (thermal) tensile stress is present at the first measurement (60 ± 5 MPa) and is then relaxed before the next one, i.e. within minutes. It indicates the slower relaxation in comparison to the higher temperature. For the short cycle the stress value is still low, hardly significant, but tends to be in tension. The apparition of stresses at 640°C is tentatively attributed to the ductile-brittle transition of Wüstite. The tensile stress is explained at high temperature due to the CTE of Wüstite being slightly larger than that of steel (Figure 3.27).

- at 560°C, there is a partial relaxation from 100 MPa to 75 MPa in the "long" cycle within 1.5 hours and it seems to stabilise later on. For the short cycle (25 minutes only at 560°C), relaxation has not had enough time and the stress is slightly above 100 MPa.

Note that as long as relaxation occurs, the different ψ angles of each measurement are carried out while stress is changing, which certainly makes the estimation more imprecise.

- finally, during the cooling down to room temperature, for the short time cycle, the tensile component is slightly increasing, it is not the case for the long cycle, in which a stress-free state is measured at room temperature (difference of -50 MPa in comparison to 560°C).

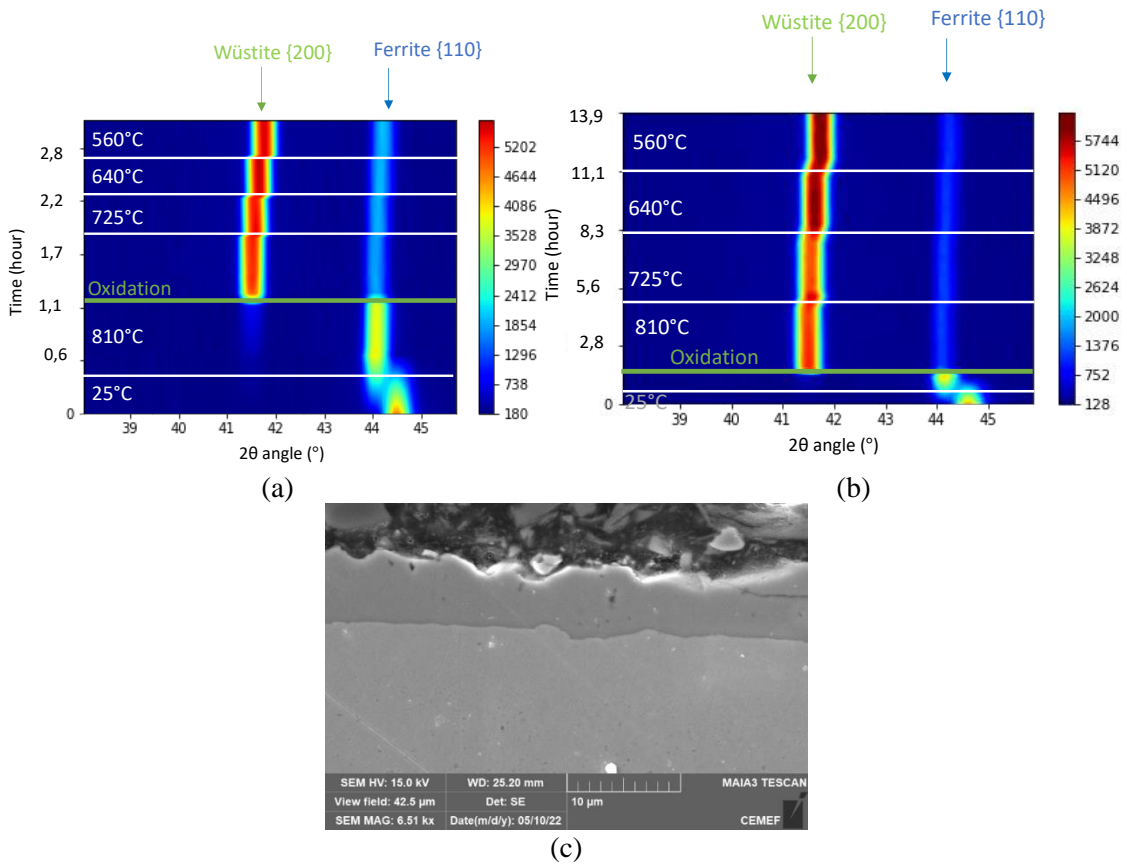
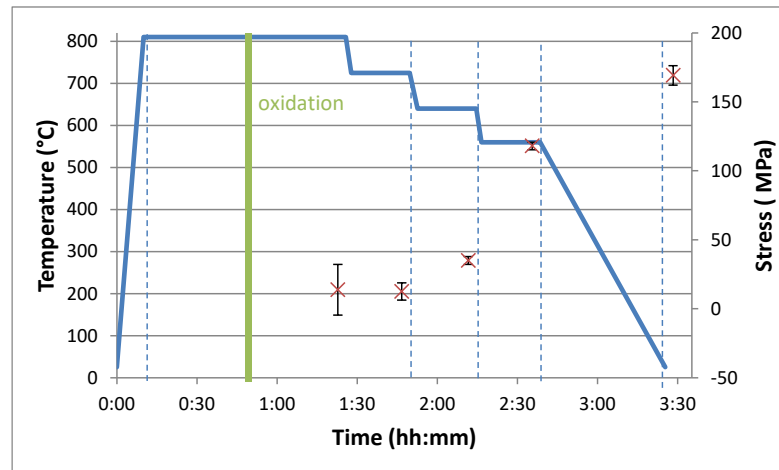


Figure 3.30: Evolution of XRD pattern during the cooling stage of in-situ cycles (810°C to room temperature) ; the scale of intensity is represented by the colour (a) for the short cycle (25 minutes per temperature, 1 stress measurement) (b) for the long cycle (2 hours 30 per temperature, 8 stress measurements) (c) SEM cross-section of the sample after the short cycle (oxidation at 810°C for 3 minutes) (thickness of oxide is estimated to be 6 μm in average)

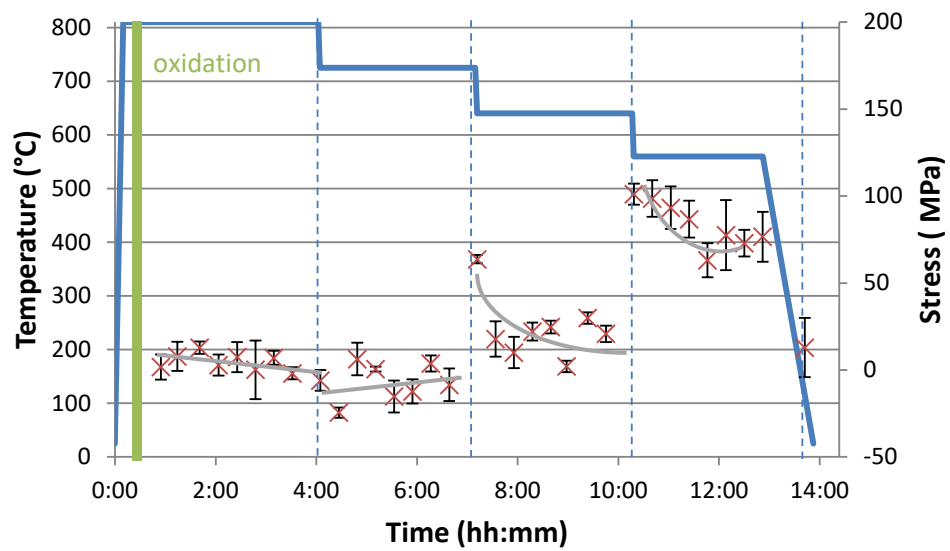
The results of the long cycles are very similar between the two detectors (compare Figure 3.29 and Figure 3.31). It confirms the complete relaxation of stresses above 600°C, the tendency to (partially relaxed) tensile stresses above 560°C and finally the thermal stress drop after the cooling at room temperature.

In all cases, no large compressive stresses are calculated (as evoked in the 3.5.3 paragraph), but there is a large difference in thermal cycle (only minutes at 650/700°C for pre-oxidized sample). The sample is thin (6 μm), and a stress-free state is calculated for the sample oxidized at 700°C to obtain 5 μm of thickness. During the pre-oxidation at 650/700°C, three phases are present, which is not the case for 810°C in situ oxidation.

The influence of thickness is not studied here, it is one of the limitations of this set-up. The penetration depth is low, 7 μm, due to the copper anticathode, unavoidable with the graphite dome. The advantage is that the stress calculated is the average over the whole Wüstite thickness.



(a)



(b)

Figure 3.31: Evolution of the stress calculated for the Wüstite {420} peak with the decreasing temperature from 810°C to room temperature (a) for the short cycle (25 minutes, i.e. 1 stress measurement per temperature) (b) for the long cycle (2 hours 30, i.e. 8 stress measurements per temperature)

3.7 Conclusion

The IF samples have been oxidized at high temperature in a controlled atmosphere at 650 and 700°C, giving thickness of 5 to 55 μm of oxide. They have been characterised by observations of cross-sections to evaluate the thickness and the phase of oxide.

X-Ray diffraction at room temperature has confirmed the presence of Hematite, Magnetite and mainly Wüstite in the surface of low carbon steel. This technique is adapted to the characterisation of multilayered materials. Indeed, each phase (Wüstite, Magnetite and Hematite) can be analysed separately.

However, the interaction between these phases is complex: phase transformation, difference in volume that generates stresses, and the difference in properties (expansion coefficient for example). In terms of orientation, a fibre texture has been found for Wüstite and Magnetite. The stress analyses have been made on oxidized samples with different anticathodes (with different penetration depths). It shows stresses are mainly equi-biaxial and compressive because they are mainly thermal stresses induced during the cooling. A gradient of stress is suggested with maximum compressive value at the interface. These results agree with the literature.

In order to go further in the analysis, HTXRD is made by making the oxidation in the XRD chamber in a controlled atmosphere. The coefficients of thermal expansion are determined for Steel and Wüstite between 560 and 810°C. As the difference changes sign around $\sim 630^\circ\text{C}$, thermal stresses change from tensile to compressive, in agreement with the study of Takeda et al [57].

After the oxidation at 810°C in air (to obtain 6-10 μm of thickness), Wüstite is the only phase until its decomposition below 560°C. In pure nitrogen atmosphere, the decomposition of Wüstite is long (more than 2 hours 30). This decomposition is not studied in this work. The evolution of stresses is depends of the temperature:

- above 700°C, a quasi-instant relaxation is observed
- at 640°C, the complete relaxation is possible after 25 minutes
- at 600°C, after 8 hours, the complete relaxation is also noted (Figure 3.28)
- at 570°C, stress is slightly relaxed in 25 min, 50% relaxed after one hour (Figure 3.31) and completely relaxed for 2.5 hours (Figure 3.28)
- below 520°C, no relaxation of stresses is noted.

This transition indicates a change in the behaviour from an elasto-visco-plastic to elasto-plastic behaviour. This relaxation is not instantaneous, and is becoming longer by decreasing the temperature. In the same range of temperature, Wüstite is known to have a ductile-brittle transition. Are these observations manifestations of 1 and the same phenomenon? or is it something else? This opens up questions for future work, probably by refining the temperature scan. However, the stress analysis is still long in spite of changing for a faster counter (from 20 to 2 hours 30), and this does not allow a quasi-instantaneous characterisation of the evolution of stresses in the oxide layer at high temperature. In the case of the secondary descaling, the cooling by the water jet is quasi-instantaneously. More tests with smaller time resolution are needed to evaluate more precisely the evolution of stresses at high temperature. Synchrotron diffraction can be used for deeper and faster analysis and quicker (for example with the DiffAbs line in SOLEIL synchrotron).

We can summarise by saying that

- the oxide arrives stress-less in front of the descaler because temperature is high ($> 1000^\circ\text{C}$) so that viscoplastic relaxation is fast enough to cancel stresses (growth, thermal) as soon as they appear;
- cooling during descaling is so fast that relaxation, which takes minutes in our experiments in the 600-500°C range, certainly cannot remove them within the μs of the jet-surface interaction; the oxide feels all the tensile thermal stress in this range where it becomes brittle;
- between the descaler and the entry of the finishing mill, the remaining oxide is reheated and stresses probably disappear again (although these specific conditions have not been given specific attention here).

Résumé

L'objectif de ce chapitre est de comprendre le comportement des oxydes en utilisant la diffraction aux rayons X. Cette partie se concentre sur la caractérisation d'échantillons oxydés à faible teneur en carbone pour préparer les essais mécaniques, mais aussi pour fournir des éléments pour la compréhension du décalaminage.

L'observation de l'oxyde est possible après une coupe transversale et un polissage, ou un usinage par Sonde Ionique Focalisée (FIB), ce qui donne des informations sur l'épaisseur, la porosité et la composition de l'oxyde. Toutefois, ces techniques sont destructives. La XRD est très utile pour évaluer les propriétés des matériaux notamment pour l'identification des phases, les contraintes internes, et la texture cristallographique... en particulier pour les couches minces comme les oxydes de fer. Il s'agit d'une analyse non destructive qui repose sur l'interaction entre les rayons X et la sous-surface cristalline de l'échantillon. Le principal avantage est que les trois phases de l'oxyde de fer (Wüstite, Magnétite et Hématite) peuvent être analysées séparément. Cela permet de mieux comprendre l'interaction entre ces phases: transformation de phase, différence de volume générant des contraintes, et différence de propriétés (coefficient d'expansion thermique par exemple).

Deux types d'analyses de diffraction sont effectuées dans ce chapitre :

- la diffraction à température ambiante. Dans ce cas, les échantillons d'acier ont été oxydés à haute température dans une atmosphère contrôlée à 650 et 700°C, donnant 5 à 55 µm d'oxyde. Les analyses ont par la suite permis de confirmer la présence d'Hématite, de Magnétite et principalement de Wüstite à la surface de l'acier. En termes d'orientation, une texture de fibre a été trouvée pour la Wüstite et la Magnétite. Les analyses de contraintes ont aussi été effectuées sur des échantillons oxydés avec différents anticathodes (avec différentes profondeurs de pénétration). Elles montrent que les contraintes sont principalement équi-biaxiales et compressives parce qu'il s'agit principalement de contraintes thermiques induites pendant le refroidissement. Un gradient de contrainte est suggéré avec une valeur de compression maximale à l'interface. Ces résultats sont en accord avec la littérature.

- La diffraction à haute température (HTXRD) est nécessaire pour observer l'évolution in situ des phases et des contraintes à haute température, dans des conditions plus proches des conditions du décalaminage. L'objectif est d'identifier les contraintes internes générées, et leur évolution : contraintes de croissance pendant l'oxydation, contraintes thermiques pendant le refroidissement, y compris les éventuels effets de relaxation. Dans cette approche, l'oxydation in situ dans une atmosphère contrôlée dans la chambre XRD permet de répondre à ces interrogations. La détermination des propriétés thermiques de l'oxyde, et notamment les coefficients d'expansion thermique est essentielle pour comprendre les contraintes thermiques correspondantes générées. Le coefficient de l'oxyde est plus important que celui de l'acier au-delà de 630°C (jusqu'à 810°C), ce qui va générer des contraintes en tension lors d'un refroidissement. En dessous de 630°C, les contraintes thermiques dans l'oxyde passent de la traction à la compression lors d'un refroidissement.

Après l'oxydation à 810°C en atmosphère oxydante (pour obtenir 6-10 µm d'épaisseur), la Wüstite est la seule phase jusqu'à sa décomposition en dessous de 560°C. L'évolution des contraintes dépend de la température :

- au-dessus de 700°C, une relaxation quasi-instantanée est observée*
- à 640°C, la relaxation complète est possible après 25 minutes*
- à 570°C, la contrainte est légèrement relaxée en 25 min, relaxée à 50% après une heure et complètement relaxée après 2,5 heures.*
- En dessous de 520°C, aucune relaxation des contraintes n'est observée.*

Cette transition indique un changement de comportement d'un comportement élasto-viscoplastique à un comportement élasto-plastique. Cette relaxation n'est pas instantanée, et augmente en diminuant la température. Dans la même gamme de température, la Wüstite est connue pour avoir une transition ductile-fragile. Ces observations sont-elles des manifestations d'un seul et même phénomène ou s'agit-il d'autre chose ? Cela ouvre des questions pour des travaux futurs, probablement en affinant le balayage de la température.

Cependant, l'analyse des contraintes reste longue malgré le passage à un détecteur plus rapide (de 2 heures 30 à 20 minutes), ce qui ne permet pas une caractérisation quasi-instantanée de l'évolution des contraintes dans la couche d'oxyde à haute température. Dans le cas du décalaminage secondaire, le refroidissement par le jet d'eau est quasi-instantané. D'autres essais avec une résolution temporelle plus petite sont nécessaires pour évaluer plus précisément l'évolution des contraintes à haute température. La diffraction synchrotron peut être utilisée pour une analyse plus approfondie et plus rapide (par exemple avec le synchrotron DiffAbs à SOLEIL). Cependant, on peut résumer en disant que

- l'oxyde arrive sans contrainte avant le décalaminage car la température est élevée (> 1000°C) de sorte que la relaxation viscoplastique est suffisamment rapide pour relaxer les contraintes (de croissance, thermique) dès qu'elles apparaissent ;*

- le refroidissement pendant le décalaminage est si rapide que la relaxation, qui prend des minutes dans nos expériences dans la gamme 600-500°C, ne peut certainement pas les éliminer dans les μ s de l'interaction jet-surface ; l'oxyde subit toutes les contraintes thermiques de traction dans cette gamme où il devient cassant ;*

- entre le décalaminage et l'entrée du broyeur de finition, l'oxyde restant est réchauffé et les contraintes disparaissent probablement à nouveau (bien que ces conditions spécifiques n'aient pas fait l'objet d'une attention particulière ici).*

Chapter 4: Indentation to evaluate properties of oxide (at room temperature and high temperature)

4.1 Introduction

The aim of this chapter is to evaluate the mechanical behaviour of low carbon steel oxide, i.e. the response of oxide under the effect of a mechanical stress. Descaling leads to the generation of stresses in the scale, and with these tests we are seeking to reproduce certain oxide damage mechanisms encountered during the thermomechanical stressing of the descaling process. The aim is then to use numerical simulation to determine the associated parameters/measures (stress at fracture, cohesive energy, etc.).

Among the methods commonly used to evaluate the properties in thin films, indentation has been chosen. Indentation techniques have been widely used to evaluate elastic and plastic behaviour, but also adhesion and toughness at room temperature (Table 4-1). In view of these results, it is logical to carry out indentations at higher temperatures, closer to the HSM conditions. Different grades have been tested with indentation in order to understand why some grades are difficult to descale.

Table 4-1: Literature review of iron oxide properties using indentation (references in bold refer to high temperature tests)

Oxide properties	Reference
Hardness	Takeda et al. [57] Vagnard [75] Charpentier et al. [76] Amano et al. [77] Deng et al. [78]
Elasticity	Lee et al. [79] Zambrano et al. [80]
Plasticity	Hidaka et al. [81] Charpentier et al. [76] Chicot et al. [82] Zambrano et al. [80]
Adhesion	Ahtoy [47] Monteiro et al. [83]
Critical stress for fracture	Sun et al. [93]

This chapter is divided into four parts:

- a literature review on fracture in indentation testing;
- a description of the indentation devices used in this study
- indentation at room temperature on pre-oxidized samples (at 650°C and 700°C). First, hardness is measured on cross sections of sufficiently thick oxide specimens. Then, the idea is to perform standard indentation through the surface to confirm the brittle behaviour of oxide and to observe the possible delamination of oxide. Focused Ion Beam (FIB) cross-sectioning is then used to identify the fracture behaviour within the oxide. These room temperature tests are useful to prepare the study at high temperature.

- indentation at high temperature : the objective is to identify the ductile-brittle transition of oxide between 600°C and 800°C and to evaluate adhesion of oxide under the same conditions. The experimental conditions for mastering the complex problems (thermal drift, control of oxidation, degradation of the tip...) of high temperature testing are described. The results are then compared with the literature and other mechanical tests.

4.2 A review of indentation fracture in literature

4.2.1 Fracture of material due to indentation: bulk material

The indentation test for brittle materials, coated or not, usually creates cracks during the loading and/or the unloading. These different crack systems can bring information on the material and/or interface toughness. The geometry of the indenter is one of the main parameters for the study of these cracks. Two categories exist: blunt indenter (sphere, flat punch...) and sharp indenter (cone, pyramid...). Some well-known types of cracks are created depending on the indenter geometry.

4.2.1.1 Stress field during indentation

Evolution of stresses during the indentation gives information to understand the behaviour of cracks, from the nucleation to the propagation. In all cases, the tensile component is the driving force for the ensuing fracture. At a large distance from the indenter, the stress field is like the Boussinesq concentrated force solution, due to St Venant's principle. According to Johnson [140], the penetration and the behaviour of the indented material is directly linked with value of the index $(E/Y)\tan\beta$ with β the angle of the obtuse indenter, E the Young's Modulus, Y the yield stress. If the index is lower than 2, the indentation is fully elastic, otherwise there is an elastic plastic deformation. The transition between elasticity and plasticity happens when the pressure under the indenter is about Y ; as pressure continues growing, a confined plastic zone is expanding until it reaches the free surface, giving rise to the "fully plastic" indentation.

According to Perrot [141], this fully plastic indentation pattern is characterised by the hardness H to yield stress ratio, about $H/Y=3$; this is typically the case for soft metals with sharp indenters. If H/Y is found well below 3, this reflects a different deformation mechanism where the plastic region is confined in the contact zone below the indenter and the rest is in an elastic state (confined plasticity). A model has been developed by Perrot [141] for obtuse axially symmetric indenters on perfect elastic-plastic material. The indentation creates a fully plastic zone, and displaces the material outward; the plastic-elastic boundary moves radially with the increasing indentation load (or depth). A state of triaxial compression is present under the indenter, near the loading axis. Outside the contact, near the surface, there is triaxial tension.

4.2.1.2 Main cracks due to indentation

In any case, the propagation of the crack is ruled by the Griffith condition, the cracks expand with the release of energy [142]. The main cracks observed during or after indentation are:

- the median/radial cracks (Figure 4.1): the crack nuclei are created by the deformation process. The crack is considered radial when it is initiated at the surface or emerges, there, from the depth. The median cracks begin under the indentation, or at the bottom of the plastic zone, grow stably until a specific depth and then rise towards the surface where they would end up as "radial". At their full development, they would therefore be identical but would come from different mechanisms - and therefore different stress components. For a Vickers indenter, two orthogonal median plane crack systems of comparable dimensions are created [143]. During the unloading, the stress tensor corresponds to an apparent elastic recovery of the stress, but the plastic deformation is retained [141]. This incompatibility between elastic and plastic zones tends to close the median cracks. Near the surface, hoop tension opens partially the radial cracks. Thus, median crack is expected to attain its maximum growth during the loading whereas the radial crack is expected to continue its growth until unloading is complete.

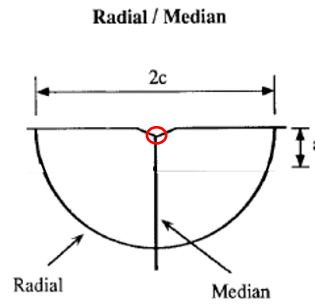


Figure 4.1: Schematic representation of indentation cracks geometry : radial/median cracks, initiation is located in the plastic zone (red) [144]

- lateral cracks (Figure 4.2). According to Lawn and Fuller [142], these cracks appear due to the residual stress field. It emanates from the plastic deformation zone and grows in a saucer-shaped configuration toward the surface, in a chipping mode of fracture (Figure 4.2). The elastic field is maximal at the end of the loading and is reversed during the unloading. The residual stress arises from mismatch traction exerted on the surrounding material by the plastic deformed material. The initiation of the crack is located where the residual stress is maximum, the expansion is mode I parallel to the surface. The depth for the initiation is about $d/a \sim 1$ according to Chen et al. [145]. The crack size increases as the toughness decreases.

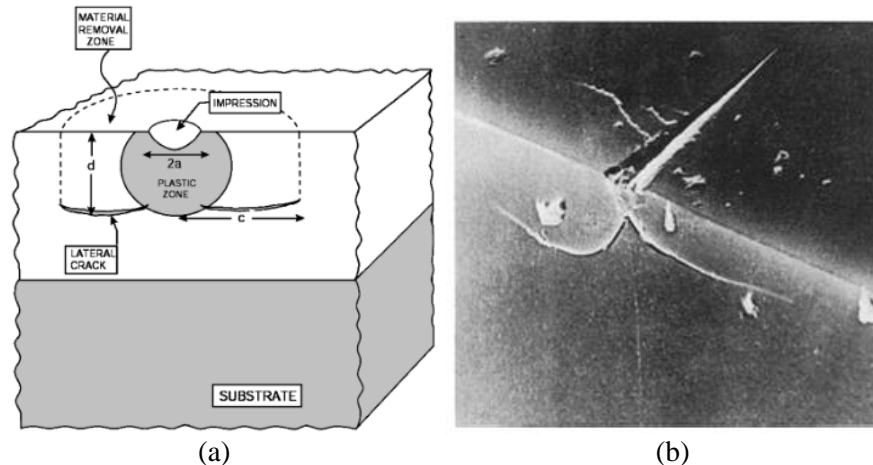


Figure 4.2: (a) Schematic showing of the lateral crack system [145] (b) Knoop indentation on quartz (0001) surface reveals lateral crack (2N load) [146]

- Palmqvist crack (Figure 4.3) expands radially in median planes and are localised near the surface during the loading, due to the presence of triaxially tensile stress [141]. These cracks grow also during the unloading and remain located in the surface region. Nucleation takes place in the indentation boundary in the corners of pyramidal indenters and then the crack spreads outward from the plastic zone. A criterion is developed by Perrot [141] depending on the properties of the materials and the indenter. The nucleation of cracks occurs if the maximum stress across the median plane exceeds $3F$, F being the engineering rupture stress:

- For the loading stage, $\frac{H}{Y} - 1,155 > 3 \frac{F}{Y} > 0$

- for the unloading, $\frac{H}{Y} + 1,155 > 6 \frac{F}{Y} > 2,310$

with Y the yield stress and H the hardness. According to these criteria, The probability of Palmqvist crack initiation is higher during the unloading. This crack appears in tougher materials than the median crack.

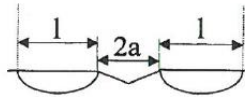


Figure 4.3: Cross-sectional view of Palmqvist cracks [39]

According to Chicot et al. [147], during an indentation test, Palmqvist cracks and median/radial cracks can appear depending on the loading. Palmqvist cracks appear first, at low load P_0 ; by increasing the load to P_{max} , they change nature by growing deeper and finally join to form the median/radial cracks. A core zone is considered (Figure 4.4), the size of which is linked with the half diagonal a . When the Palmqvist crack depth becomes greater than the core zone, the two opposite regions connect to create a median/radial crack. Thus, it could be that Palmqvist cracks expand to become median/radial cracks depending on the loading.

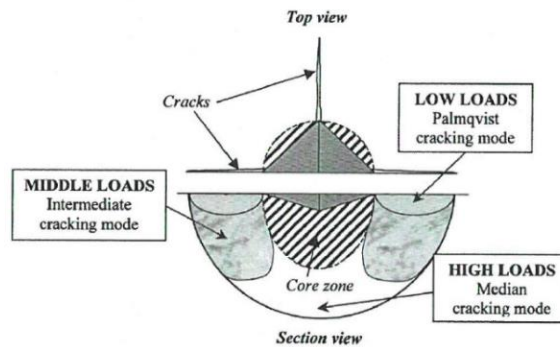


Figure 4.4: Schematic of top and cross-sectional view of Vickers indentation crack system [147]

- Hertz or cone cracks are present in the case of blunt indentation (Figure 4.5 (a)). The initiation of cracks does not occur at the edge of the contact zone but is shifted in the radial direction outward [22]. In fact, the gradient of stress changes a lot near the edge, the initiation of the crack needs a stabilisation of the value to allow the flaw to grow. This distance for the initiation of the crack is depending on the length of the initial flaw: for a small one, the nucleation is near the edge. The propagation starts either with a shallow cylindrical ring or directly with the Hertz cone, if a critical loading is applied (Figure 4.5 (b)). As long as the Griffith ($G > 2\gamma$) condition is valid (γ is the intrinsic surface energy), the propagation occurs.

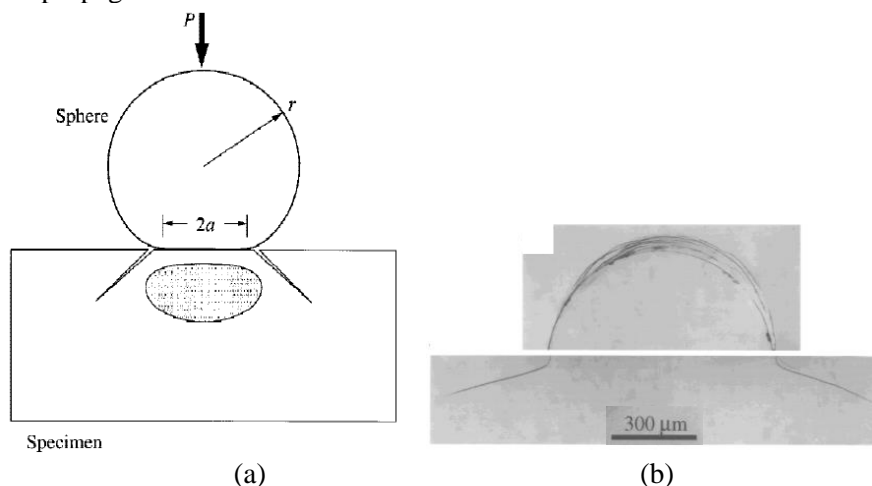


Figure 4.5: Cone fracture during an Hertzian contact of sphere on a brittle specimen (ceramic) [148] Half-surface and side views of Hertzian contact damage in Si_3N_4 with a Tungsten carbide sphere radius ($r=1,98mm$) [149]

4.2.1.3 Toughness measurement with indentation

From these cracks, the toughness of brittle material can be calculated [150]. Chicot et al. studied the apparition of median and Palmqvist cracks, as both can appear on the same materials [147]. In those cases, the stress intensity factor is:

$$K_{I_{median}} = \alpha \left(\frac{E}{HV} \right)^q \frac{P}{c^{\frac{3}{2}}} \quad K_{I_{Palmqvist}} = \beta \left(\frac{E}{HV} \right)^r \frac{P}{al^{\frac{1}{2}}} \quad (4-1)$$

where coefficients α and β and exponents q and r take different values according to each author. HV is the Vickers hardness, a the half diagonal of the indentation, c the crack length from the centre (median) and l from the corner (Palmqvist), P is the load.

All the fracture mechanisms are summarised in the Figure 4.6.

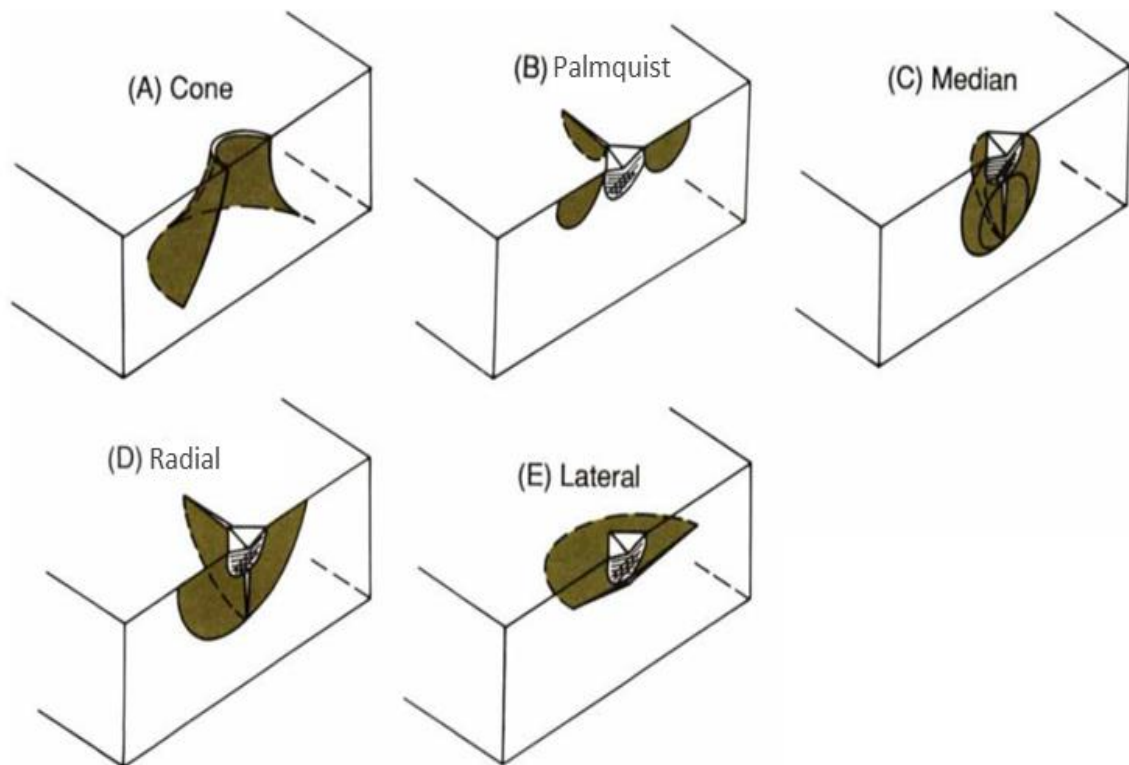


Figure 4.6: Isometric sections of idealized crack morphologies observed at indentation contacts: (A) cone crack and associated nucleating ring crack, (B) radial cracks and associated contact impression and plastic deformation zone (Vickers indenter), (C) median cracks (The full circle indicates the extent just after initiation, and the truncated circle the possible extent on continued loading.), (D) half-penny cracks, and (E) lateral crack. After [151]

In this first part, the well-known crack families that are observed during the indentation of bulk brittle material have been described. Now, we are going to see the fracture behaviour of a hard film on a soft substrate.

4.2.2 Fracture of a thin film

The Sneddon half-space indentation solution is not relevant for thin film when the thickness is comparable with the indentation radius, because the distribution of stresses is strongly influenced by the properties of both substrate and film. For example, the FIB cross-section of an indentation of a composite (Mo layer on a Si substrate (ductile film on a brittle substrate)) shows lateral and cone cracks, formed readily in the Si substrate, and delamination [152]. According to the authors, the difficulties associated with substrate cracking complicates the interpretation of delamination. Conical cracks are troublesome for the identification of interfacial toughness because they deflect the interface crack into the substrate, stopping the delamination of the interface. Lateral cracks are also problematic when they allow part of the substrate to remain attached to the underside of the overlayer after it has buckled.

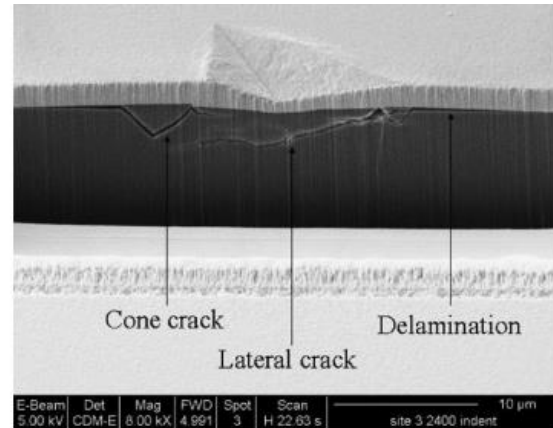


Figure 4.7 : FIB cross-section of a Berkovich indentation (3 μm deep) on a Molybdenum overlayer on a Pt film on a Silicon substrate (cone, lateral cracks and delamination are visible [152])

To simplify, in the rest of the document, only “hard”, more or less brittle thin film on a “soft” ductile substrate are considered, it is the case in iron oxide that grows on a low carbon steel. In this configuration, new crack systems are possible, and are localised only within the film or at the interface.

4.2.3 Thin hard film on a soft substrate

4.2.3.1 Main cracks due to indentation

(i) radial cracks (R in Figure 4.8) are formed from the interface. According to Rhee et al. [153] for a spherical indenter on a brittle coating (radius of 3.96 mm), a radial fracture initiating from the lower part of the coating can appear due to the bi-axial tension below the indenter and to flexure induced by the indentation. The crack is initiated from a flaw when a critical load is reached, and when the stress equals the flexure strength of the film. Both traditional cone crack (C) and quasi-plasticity zone (Y) near the edge at the surface are also present. The transition between the fracture mechanisms is directly linked with the loading. Figure 4.8 shows the evolution of the fracture mechanism for brittle materials on a polycarbonate substrate. For films up to 1 mm, the radial cracks are present (represented by the oblique line). The horizontal lines on the right ($d > 1000 \mu\text{m}$) refer to either the yield (Y) or the cone (C) cracks and correspond to thick coatings for which the indentation does not interfere with the substrate.

(ii) circular/ring/circumferential, Hertzian-like cracks can be formed from the surface. The stresses are concentrated at the contact edge. Stresses within the contact are largely compressive and the maximum tensile stresses are localised in the surface of coating. For example, the indentation of 2.3 μm NbN coating on a stainless-steel substrate shows a ring crack at the surface (Figure 4.9).

Depending on the thickness of the film, the cracking mode is changing : from surface to interface (Figure 4.10). According to Chai and Lawn [154], fracture mode induced by concentrated loading with a spherical indenter at the top surface undergoes transitions. By decreasing the thickness, the top-surface ring cracking changes to bottom-surface radial cracking at the lower ceramic surface (“intermediate” region) and, finally, back to surface ring cracking (“thin-coating” region).

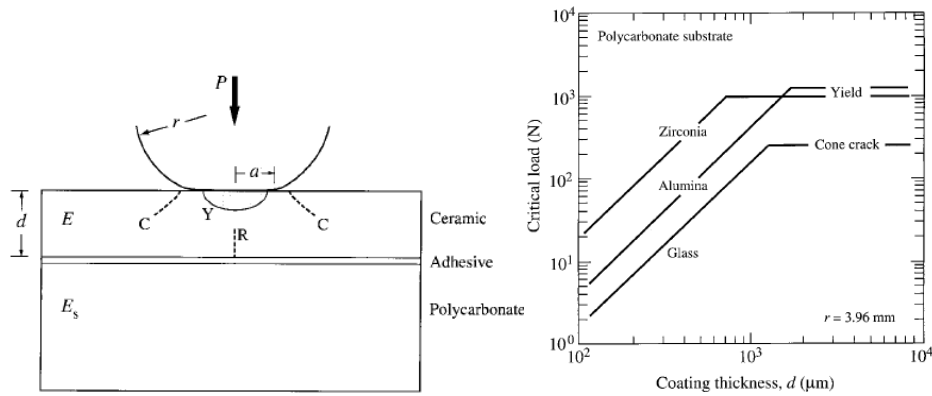


Figure 4.8: Schematic representation showing damage mode for a thick brittle ceramic coating on a flexible polycarbonate substrate: R (radial cracks), Y (quasi-plasticity) and C (Cone cracks) (b) prediction of the fracture mechanism as function of coating thickness for a spherical indentation (spherical radius of 3.96 mm). Oblique lines ($100 \leq d \leq 1000 \mu\text{m}$) correspond to radial cracks, horizontal lines to yield and cone cracks. [153]

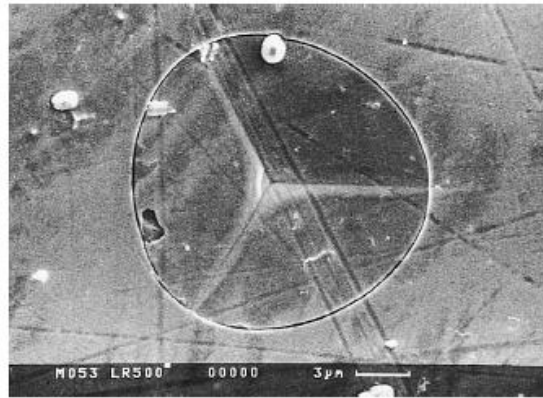


Figure 4.9: SEM micrograph of 500 mN indentation in a $2.3\mu\text{m}$ NbN coating on a stainless-steel substrate. There is a ring crack at the surface [155]

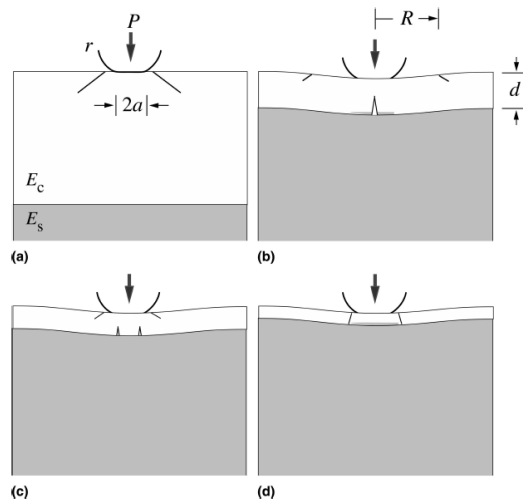


Figure 4.10: Schematic illustration of cracking of a bilayer structure consisting of an outer brittle layer on a thick compliant substrate. Fracture mode transitions in brittle layer: (a) cone crack at top surface, (b, c) ring crack at top surface and radial crack at bottom surface, and (d) through-thickness ring cracks. [154]

The transition is due to the evolution of stresses within the oxide. For thick and thin coatings, the contact stresses in surface induced by the indenter dominate. For an intermediate thickness, the flexure stresses dominate. Finite element simulations are done for three bilayer systems with brittle

coating layer: Soda-lime glass, Alumina and Zirconia. The substrate is polycarbonate. The result shows radial location R/a versus d/a for the same three coating systems (d is the coating thickness and a the contact area in the Figure 4.10). Each point is a simulation. The unfilled symbols refer to the top-surface ring cracks and filled symbols to the bottom-surface radial cracks. It highlights the shifts in ring and radial crack locations with decreasing coating thickness. It also indicates the localization of the cracks for each mechanism. Ring (or cone) cracking dominates in the extreme regions of very large d and very small d , radial cracking in the region of intermediate d . The crack locations R change with diminishing relative coating thickness d/a : for large d/a the dominant cracks are localised at the surface. For low d/a bottom surface radial cracks are a majority. As for the ratio R/a , it depends on the thickness.

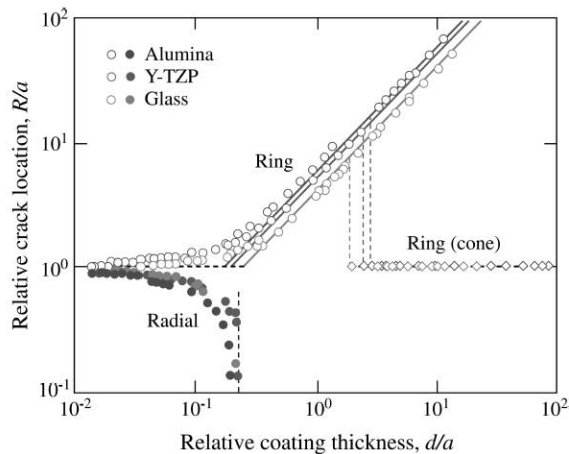


Figure 4.11: Finite element simulation for 3 composite coatings (glass, alumina and Zirconia) on a soft substrate (polycarbonate). Surface ring crack are the unfilled circles and squares and the radial cracks are filled circles. R represents the crack location, a the contact radius and d the thickness [154]

(iii) delamination during the indentation of a thin film has been widely observed [104,156]. For example, Xiao et al. make an indentation (diamond cone 45° and $1 \mu\text{m}$ tip radius) on a Diamond-Like Carbon coating on steel substrate [157]. After FIB milling, the cross-sections reveal interfacial delamination (and circumferential cracks). According to these authors, the interfacial delamination is likely to initiate at the location where the maximum shear stress is found, and the delamination behaviour remains a mode II dominated defect.

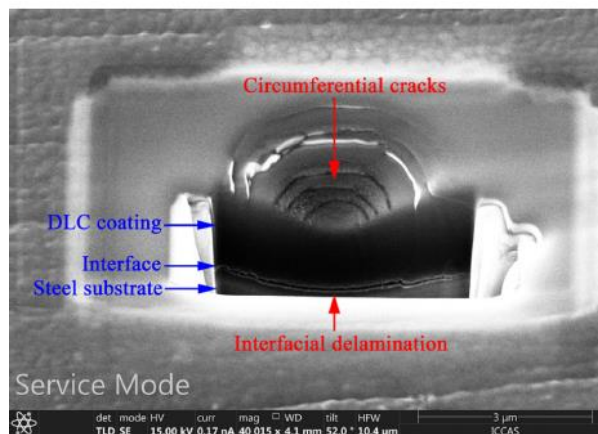


Figure 4.12: SEM images of a cross-section of an indentation (diamond cone 45° and $1 \mu\text{m}$ tip radius) on a Diamond-Like Carbon coating on steel substrate. Interfacial delamination and circumferential cracks are shown.

We have seen some of the cracks that are observed during the indentation of a brittle and hard film on a soft and ductile substrate. From these fracture mechanisms, the properties of the film and its interface can be evaluated.

4.2.3.2 Evaluation of properties of thin film with indentation

After the cracking, the mechanical properties of thin film can be determined. For thin film, interfacial crack area can be used for measuring interfacial strength or interfacial fracture toughness, whereas cracks in the film can be used for measuring the fracture toughness of the film. Two methods, respectively based on the measurement of the crack length and on pop-ins on the loading/unloading curves, are exemplified below.

The first method, based on crack length, is different for each crack mechanism. The observation of the crack propagation after the test is necessary to quantify the real delaminated area and FIB milling cross-sections are needed.

Propagation of fracture at the interface between oxide and steel is representative of adherence of scale. Adhesion of a thin film is controlled by interfacial bonding strength. G , the energy release rate, is the drop of strain energy in the system brought about by a unit increase of crack surface area. It is related to the stress intensity factor K (proportional to the load) by $G = K^2/E$ for purely elastic material. G provides the energy needed to create a new surface (surface energy γ), plus some inelastic strain energy if needed to propagate the crack (plasticity or viscoelasticity at crack tip). In case of non-dissipative, elastic behaviour, equilibrium propagation implies that $G = 2\gamma$. Therefore, following crack propagation provides a quantitative determination of interface energy.

Rosenfeld et al. determined interfacial fracture energy of epoxy coating on soda-lime glass substrate by considering that debond crack is continuously driven by contact stresses during loading [158]. The main assumptions, valid in their case, are that the substrate is rigid and the coating (considered as compliant) is submitted to in-plane-stress but does not buckle. The propagation of the crack is continuous and stable, and the crack growth is piloted by the growth without buckling of the in-plane stresses triggered by indentation. The delaminated area is an annulus of inner radius a , the contact radius, and outer radius c (crack extension) (Figure 4.13).

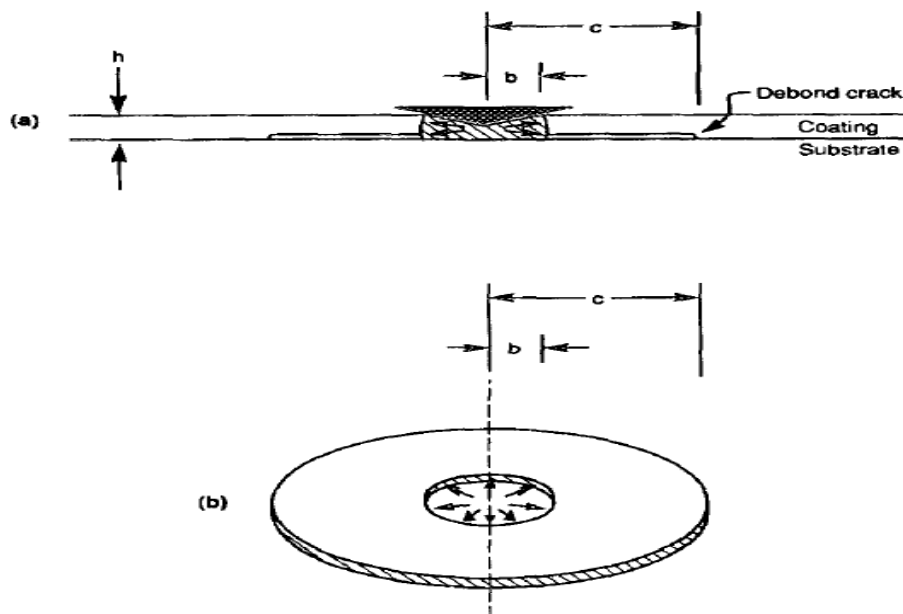


Figure 4.13: Schematic representation of (a) indentation damage (b) the annular plate model

The interfacial adhesion energy G is given by:

$$G = \frac{2(1 - \nu_c^2)\sigma_{rb}^2 h_c}{E_c} \left[1 - \nu_c + (1 - \nu_c) \left(\frac{c}{a} \right)^2 \right]^{-2} \quad (4-2)$$

With E_c and ν_c are the Young's modulus and Poisson's ratio of the coating, h_c its thickness. σ_{rb} is the radial stress at the outer edge of the contact zone at full load; it is calculated by applying the Tresca yield criterion to the plastically deformed contact zone: it is assumed that $\sigma_{rb} = \sigma_{yc} - H_c$ where σ_{yc} is the yield stress and H_c is the hardness of the coating and an approximation of the hydrostatic stress. The H_c/σ_{yc} ratio is approximately 3. In order to confirm the hypotheses, the authors compare experiments using epoxy (variable thickness), on glass, with a numerical FEM study. This method has also been used to evaluate properties of a Diamond-like carbon (DLC) thin film on a steel substrate [157], a hard-on-soft case closer to our own application, although DLC films are much thinner.

The second method is based on the detection of the pop-in event on the loading curves. Usually, cracking is found to be accompanied by a discrete change in slope of the loading part of the load-displacement curve. For instance, Li and Bhushan developed a methodology to measure fracture toughness in the indentation mode of ultra-thin films [159]. The energy release in cracking is estimated by observing the load-displacement curve. Experimentally, during the indentation of amorphous carbon films on silicon substrate, they observed three fracture stages: first, ring-like through-thickness crack formation, then delamination/buckling, and finally, second ring-like through-thickness crack formation and spalling (Figure 4.14 (a)). According to Li and Bhushan the strain energy for the first ring crack is small and gives no clear step in the loading curve. The delamination which occurs in the horizontal direction does not greatly affect the normal displacement. However, the second ring-cracking (associated with spalling) is responsible for the released energy reflected in the loading curve. In Figure 4.14 (b), the load-displacement curve shows the loading (OACD) and the unloading (DE). The second ring crack that occurs at AC is responsible for the event ACD on the curve. In the absence of cracking, the loading curve is OAB. Crack formation changes the loading curve OAB into OAC. The dashed area represents the difference in elastically stored energy in the film/substrate system.

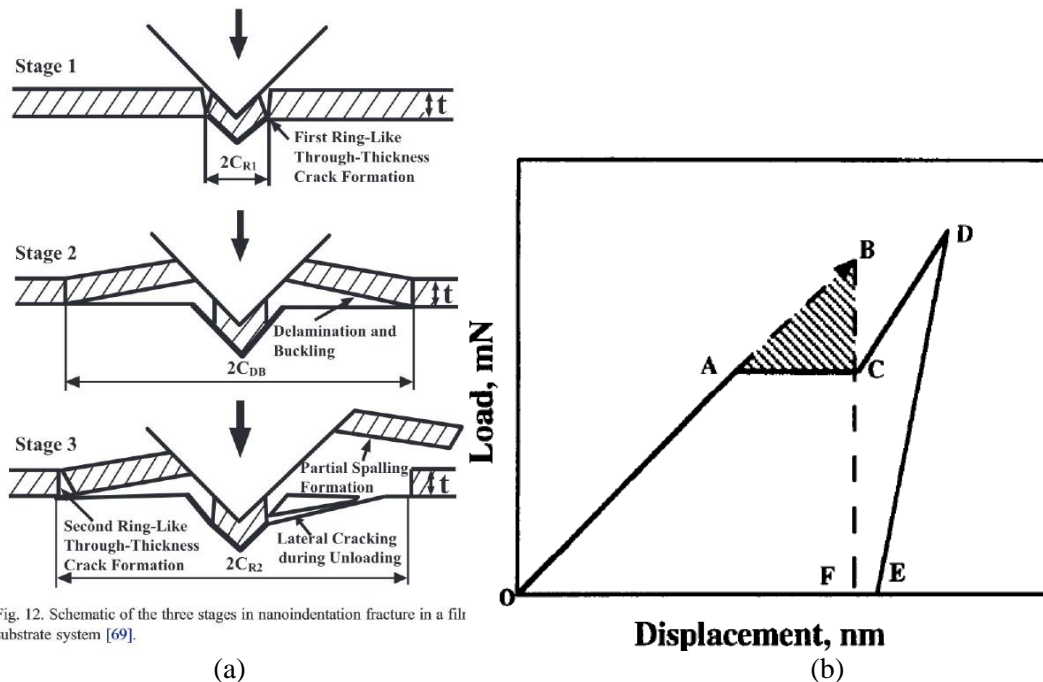


Fig. 12. Schematic of the three stages in nanoindentation fracture in a film/substrate system [69].

Figure 4.14 : (a) Schematic representation of the three stages of fracture during indentation of amorphous carbon films on silicon substrate (b) load-displacement curve showing a step during the ring cracks (stage 3)

K_{IC} , the critical stress-intensity factor, or the fracture toughness of the material is calculated by considering that the Mode I fracture is predominant, and that the crack propagates instantaneously until the interface:

$$K_{IC} = \left[\left(\frac{E}{(1 - \nu_c)^2 2\pi C_r} \right) \left(\frac{U}{t} \right) \right]^{1/2} \quad (4-3)$$

with E and ν_c are the Young's modulus and Poisson's ratio, $2\pi C_r$ the crack front length in the film plane, U the strain energy difference before and after cracking on the loading curve and t the thickness.

We have seen in this bibliographic review that during the indentation of brittle materials, different fracture mechanisms are observed and more precisely: delamination, circular and radial cracks for thin film. Some models to determine the film properties and its interface have been presented, and will be used to evaluate the oxide properties at room and high temperatures.

4.3 Methodology used in this work

In this study, different pieces of equipment are used to meet the different experimental conditions required (high temperature indentation, high speed of indentation, low penetration...) (summarised in Table 4-2).

At room temperature, two indenters are employed:

- a standard micro-indentation tester (Buehler) with a diamond Vickers indenter. The load range is 0.2 – 10 N in order to vary the penetration depth / oxide thickness ratio in comparison to the homemade indenter.

- a homemade instrumented indenter with a diamond and a sapphire tip. Indentation tests are performed in 3 steps. First, a loading step to the desired force at an indentation speed of 3 $\mu\text{m/s}$ is realised. The load is then maintained for 10 s before the final unloading (same speed as the loading step), a calibration is made with quartz and with non-oxidized low carbon steel. The main advantage of this equipment is the large force range (up to 45N) to have deep penetration within the sample, especially useful for specimens with thicker oxide because larger penetration is needed.

At both room and high temperature, another set-up is used:

- instrumented indentation on an Alemnis HTM 800 in-situ platform (Figure 4.15 (a)). Measurements have been performed at Alemnis, in Thun, Switzerland. The main advantage of the HTM is to operate indentation from room temperature to 800°C. Thus, this equipment has been set in a SEM (in vacuum) to limit the oxidation at higher temperature and to observe in situ the indentation (Figure 4.15 (b)). The indentations are carried out on pre-oxidized specimens (700°C) before the indentation thermal cycle. The samples are introduced and a pressure less than 10^{-4} mbar achieved. As detailed later in section 4.5.2, two Berkovich tips are designed and custom-made in Boron Carbide (B_4C) and Tungsten Carbide (WC) to enable experiments at high temperatures. The equipment is displacement-controlled and the speed of indentation is between 250 nm/s to 30 $\mu\text{m/s}$. The maximum loading force is 2.5N. The main advantage of the in-situ test is the observation of the rupture. The frame compliance analysis has been performed using a diamond Berkovich tip on Fused Silica, maximum load in the range 30-500 mN. The frame compliance has been found to be 4 $\mu\text{m/N}$ with a very good repeatability. For each test, a pre-load of 1 mN is applied to ensure the surface detection, particularly at high temperature due to the thermal drift.

It must be noted that due to limited apparatus availability, the number of tests at high temperature (600-800°C) has been rather limited (65 indentations), making the corresponding part of the study a feasibility one for measuring the brittle-to-ductile transition. At room temperature, hundreds of experiments have been carried out and exploited.

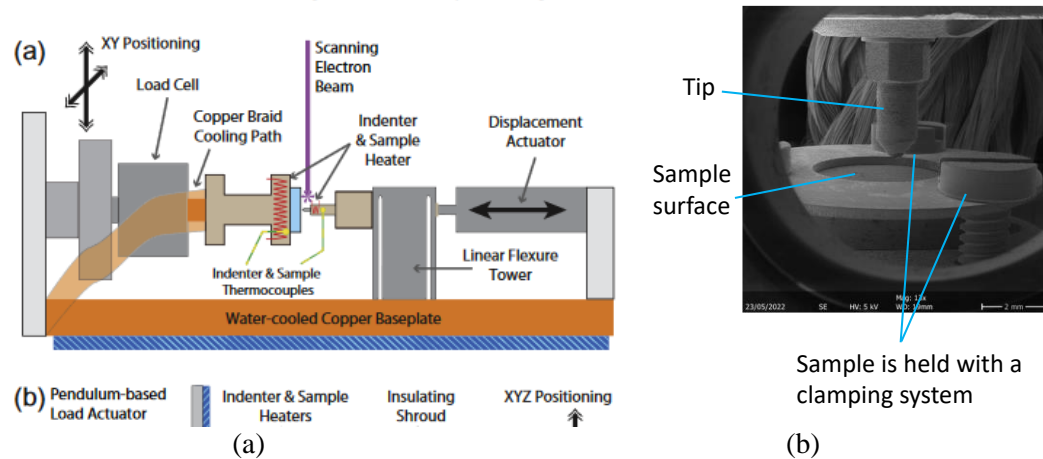


Figure 4.15: (a) HTM800 set-up used for the high temperature indentation [160] (b) clamping system to set the sample and the tip

Finally, at still higher temperature, a last equipment is used, in fact a “quenching furnace” recently developed at ArcelorMittal Lab, employed here for its capacity to perform in-situ oxidation + indentation experiments. The main advantage of this device is the high-speed indentation capability, and the in-situ oxidation just before the indentation. Indeed, it implies only one thermal cycle, whereas the Alemnis set-up requires a first oxidizing full cycle, then re-heating to make the indentation at high temperature. Only few tests have been done on this set-up at the end of this study, they are described in Appendix D.

Table 4-2: Description of parameters available for the 4 devices used in this study

Equipment	Instrumented indentation	Temperature (°C)	Force (N)	Indentation rate ($\mu\text{m/s}$)	Time at full load (s)
Homemade indenter	No	RT	2-45	1-5	3-10
Buehler micro-indenter	No	RT	0.2-10	0.1	10
Alemnis HTM800	Yes	RT-800°C	0.4-2.6	0.25- 30	
Quenching furnace	No	RT-1600°C	50-2000	100-10000	10

4.4 Room temperature indentation

4.4.1 Indentation on cross-sections to evaluate hardness

The hardness of steel and oxide will be necessary to exploit indentation curves, but cannot be easily accessed by standard indentation from the surface due to combined oxide-steel effects. Sample is therefore prepared with a standard cross-sectioning and polishing and indentation is performed on the cross-section, on either sides of the interface.

The hardness of Wüstite and low carbon steel are determined with a diamond cube corner indenter with an Alemnis Standard Assembly (ASA) (load control) after an oxidation at high temperature (650°C) designed to have a large thickness (55 μm).

Several loads are tested (up to 500 mN). For larger loads, cracks and pile-ups are observed (Figure 4.16).

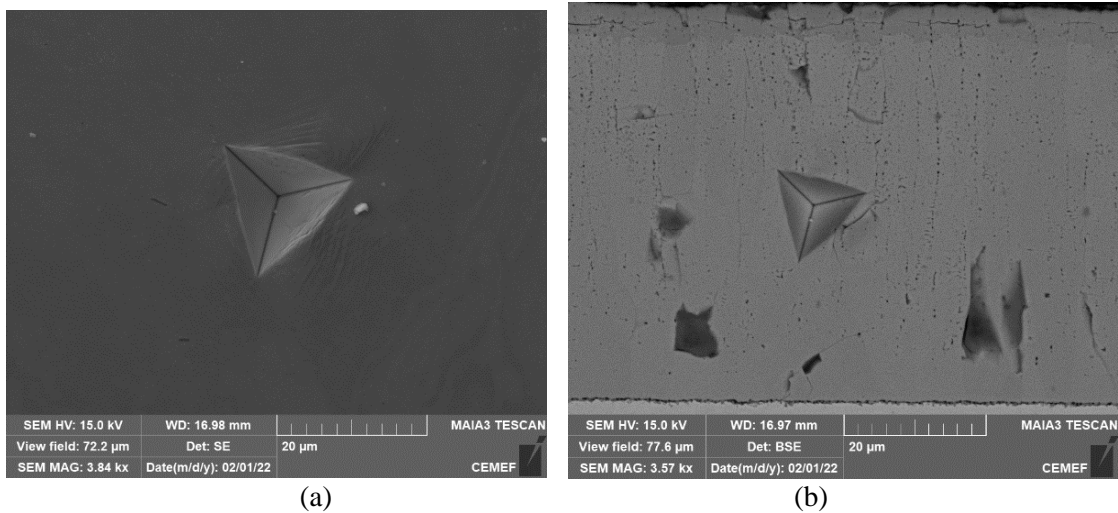


Figure 4.16: Cube corner indentation imprint for (a) steel with a 200mN load (b) Wüstite for a 400 mN load.

To avoid the hardness measurement perturbation, the indentation load is equal to 100 mN. At least 5 indentations are made for each phase, the reproducibility is good. The hardness is calculated directly from the plastic depth (h_p) and the loading force according to the Oliver and Pharr method [161] (Table 4-3).

Wüstite hardness in this study is higher compared with the literature recalled in the Table 4-4 (but in that case, oxidation was performed at higher temperature (1000°C-1200°C). The higher hardness of Wüstite can also be attributed to the Oliver and Pharr method used. As Wüstite is a “plastic ceramic” at room temperature, the sink-in considered in the model tends to underestimate the size of the indentation (moreover, it should be noted that there is no pile-up observed at the edge of the indentation). The indentation size effect should also be taken into account when comparing with indentations of greater force ([57,77,94]). At a micro scale, dislocations tend to increase hardness.

No tests could be carried out in the superficial phases (Magnetite and Hematite) due to the low thicknesses.

Table 4-3: Room temperature hardness of iron oxides

	Hardness (average) (GPa)	Standard deviation (GPa)
FeO	6.5	0.1
LC-steel	1.9	0.1

Table 4-4: Hardness at Room Temperature of iron oxides, reported in the literature

Oxide Hardness (GPa)	Indentation	Oxidation	FeO	Fe ₃ O ₄	Fe ₂ O ₃	Fe ₃ O ₄ /FeO	Fe ₂ O ₃ /FeO
Takeda et al. [57]	50 g applied for 30 s	Oxidation at 1000°C	3.5	4	6.7	1.15	1.9
Zambrano et al. [80]	(5. 25 and 50mN)	Oxidation at 1200°C	5.5	6.5	12	1.15	2.2
Westbrook [100]		-	4.9	5.4	9.0	1.10	1.8
Chicot et al. [101]		natural steel oxidation	-	6.3	8.2	-	-
Graf et Kawalla [94]	10 kgf (100N)	compressed oxide powder	3.9	5.9-6.9	8.8	1.6	2.25
Amano et al. [77]	50 or 500 g (for 30s)	Oxidation at 1000°C	3.5	3.9-4	6.7-7.6	1.15	~1.8

4.4.2 Fracture of oxide at room temperature: brittle behaviour

4.4.2.1 Methodology

Indentations are made from the surface to study fracture, with different set-ups : the Homemade indenter, Buehler micro-indenter and Alemnis HTM800, to ensure a larger span of the indentation depth / oxide thickness ratio p/t .

Figure 4.17 shows a typical force-displacement curve of the Alemnis platform: loading step to the desired force, then a holding time and finally unloading. In theory, the pop-in or slope inflexions can be attributed either to failure of the oxide, to different behaviours of the phases indented, or the influence of the softer substrate once the "1:10th rule" is violated. Thus, instrumented indentation can provide information on mechanical processes taking place during indentation, compared with a standard indentation (Buehler) which gives only a hardness value. However, no pop-in or inflection has ever been detected, whatever the sample and even in the case of multi-cracking as described later. This means that the energy released during the cracking is low and does not disturb the indentation. Therefore, the energy-based methods described above are inapplicable.

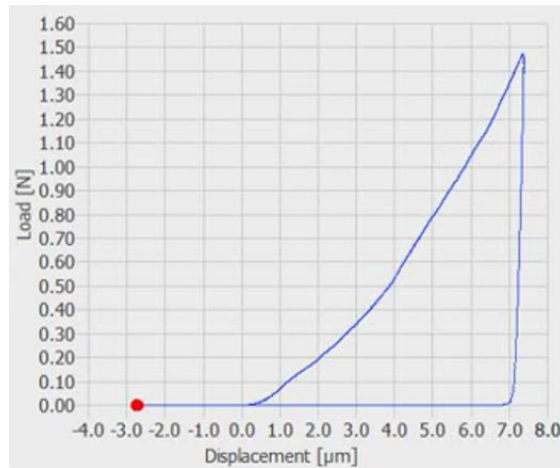


Figure 4.17: Load-displacement curves for a 1.5N indentation on IF_700_4 sample on the Alemnis equipment

Indentations are done on pre-oxidized IF grade samples with thickness between 5 to 55 μm , for a large variability of loading (up to 40 N). This large range of oxide thickness has been obtained using 2 oxidation temperatures, 650°C and 700°C ; this is not thought to lead to much different oxide structures based on X-Ray diffraction and SEM micrographs. In order to facilitate comparison between specimens with different thicknesses, a normalisation is done by dividing the penetration of indenter p by the oxide thickness t :

$$p/t \quad (4-4)$$

As described in the previous chapter, after the oxidation thermal cycle, the oxide is under compressive internal stress (about -100 MPa), and composed of 3 phases: Hematite in surface (very thin, generally discontinuous), Magnetite (7 to 20 % of the oxide thickness) and Wüstite.

4.4.2.2 Surface cracking

After indentation, fractures are observed on the oxide surface, using a Scanning Electron Microscopy (SEM, MAIA3, Tescan, see Figure 4.18).

- when the penetration is low, i.e. $p/t \leq 0.1$, the plastic deformation is confined in the oxide. The substrate has no influence on the indentation (the Buckle's "1/10"th rule is respected). No fracture is found.

- by increasing the penetration, superficial cracks are present. These cracks are not really opened and are linked to the porosity of the haematite in the subsurface. Such cracks are not considered in this study, the corresponding indentations are considered "crack-free".

- by increasing the penetration above $p/t \sim 0.2$ "circular" cracks appear at the surface. All along the loading, more such cracks appear periodically as concentric circles. The first ones appear when $p/t \sim 0.3$, this limit slightly depends on the thickness. As a reminder, when ratio $p/t > 0.1$, results are more and more strongly influenced by the substrate. This suggests that fracture behaviour of oxide depends on substrate: when the substrate starts to yield, it forces the whole oxide layer to bend under the indenter. Increasing the load, the bending effect increases and more cracks form.

- Starting from the corners of indentation, radial cracks are observed as well, their length increases with the normal load.

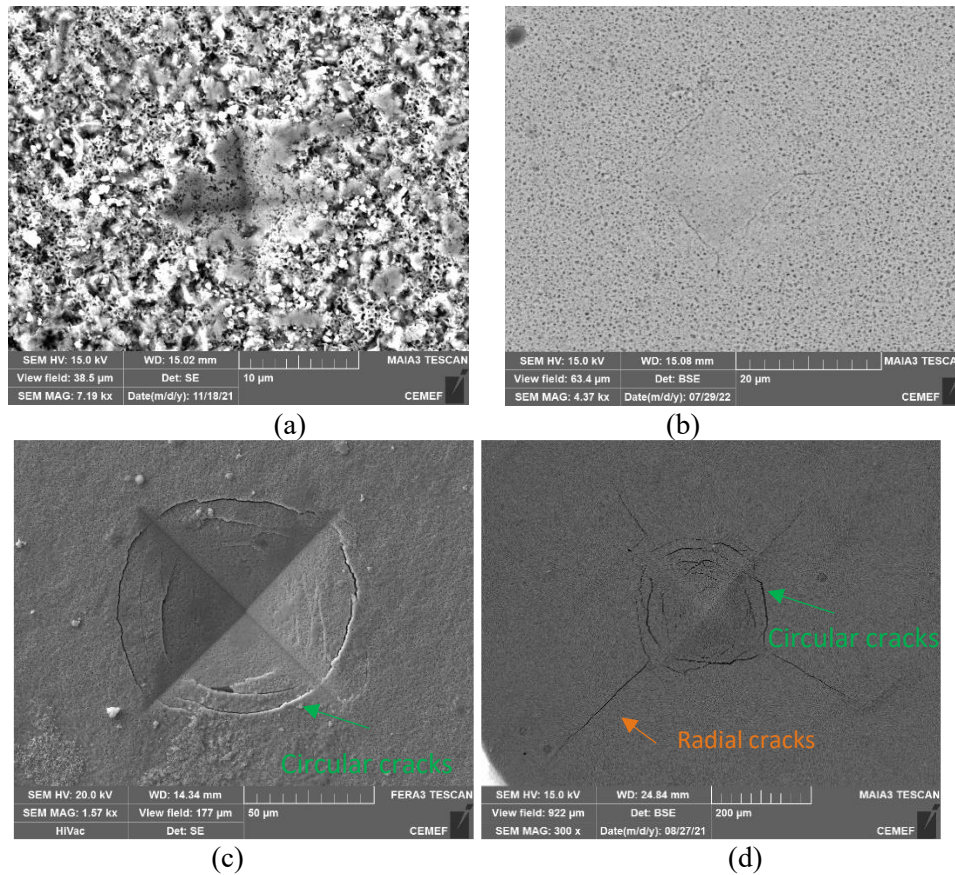


Figure 4.18: SEM observation of oxidized specimens (a) IF_650_12 after a 0.5N force indentation ($p/t \sim 0.07$) (b) IF-650-26 after a 1N force indentation ($p/t \sim 0.1$) (c) IF_650_26 after a 18N indentation ($p/t \sim 0.48$) (d) IF_700_22 after a 40N indentation ($p/t \sim 2.2$)

Crack pattern also depends on oxide thickness and is best drawn according to the depth-to-thickness ratio p/t , as a first step (Figure 4.19). For the lowest thickness ($t = 4 \mu\text{m}$), cracks are always observed because due to instrumental limitations, indentation below $p = 1.5 \mu\text{m}$ could not be achieved, so that the smallest p/t is 0.4, well above the estimated limit, $p/t \sim 0.2$. Hence, substrate yielding leads to oxide fracture.

Figure 4.19 gathers all the data collected at room temperature on the 3 indentation devices described in the 0 part. For the lower thickness, the Berkovich tip (Alemnis HTM800) is used to have the same order of magnitude of p/t . A good correlation is noted between the two tip geometries, Vickers and Berkovich.

Figure 4.19 shows that the oxide behaviour dependence on p and t cannot be summarised by p/t alone. Both p/t and t are necessary: the former describes the extension of plasticity into the substrate, the latter recalls the sensitivity of the bending strain and stress to the thickness of the oxide plate.

The fact that circular cracks appear first, before the radial cracks, has been reported in the literature by Pachler et al. [162] during fracture analysis of a TiN coating on a steel substrate. This tendency has been confirmed by FE simulations by the same authors.

∴

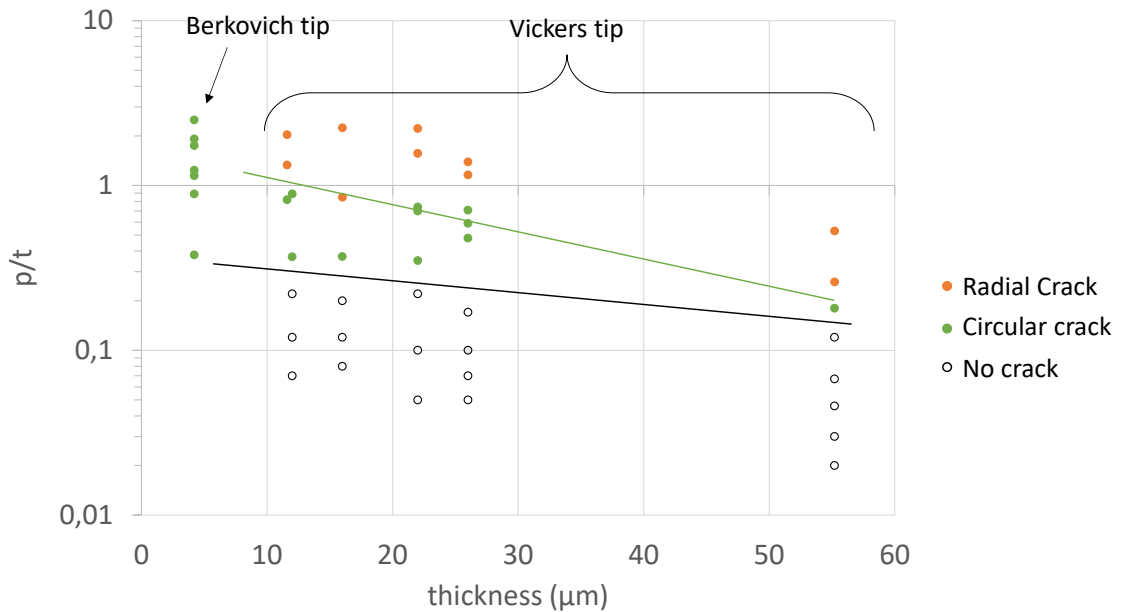


Figure 4.19: Evolution of the fracture mechanisms with the increasing thickness.

After the study of the cracks from the surface, FIB cross-section are needed to observe crack failure mechanisms within oxide.

4.4.2.3 FIB cross-sections to observe delamination and normal cracks

By optical observation from the surface, information is missing, particularly what is happening at the interface between oxide and steel. Therefore, cross-sections are prepared using a plasma (Xe source) Focused Ion Beam (FIB) thanks to a FIB column mounted on a SEM (Tescan FERA3 dual beam microscope). Cross-sections are obtained in 3 milling steps:

- cross-sections opening is performed at 30 kV and high current (2 μA).
- the resulting cross-section is then polished at 30 kV and a current intensity of 1 μA.
- finally, the FIB current intensity is reduced down to 100 nA to smooth the cross-section surface.

Cross-sections are prepared by milling the vicinity of the indentation with FIB technology (Figure 4.20 and Figure 4.21), over a maximum length of 300 μm.

These cross-sectional observations bring an important complement of information:

- 1) in reality, circular cracks deviate outwards and do not propagate down to the interface with steel.
- 2) radial cracks traverse the oxide layer, to the interface
- 3) delamination is observed below indentation. This indicates a poor adhesion of oxide on this steel grade under these conditions. This delamination is described in literature [157]
- 4) normal cracks starting perpendicular to the interface are also present. This is due to the oxide layer bending following plastic deformation of steel; fracture occurs on the extrados, as shown in literature (Figure 4.8 and Figure 4.10).
- 5) Oblique crack, which occurs between the circular cracks, and the normal cracks propagate at 45°, apparently without reaching the surface or the interface.

These fracture mechanisms at room temperature have been found for all three grades (IF, HSLA0 and HSLA1). Some regions far from indentations have also been milled, showing that initially, the oxide is weakly but continuously bonded, with no interfacial gap (Figure 3.6).

With the post-mortem observations (and no visible signature on the loading-displacement curves), it is impossible to build the chronology of the fracture mechanism. Numerical simulations will be carried out in chapter 5 to reconstruct it for the different types of cracks. For the time being, a short quantitative analysis of the two families of buried cracks is detailed below, delamination first, then normal cracks.

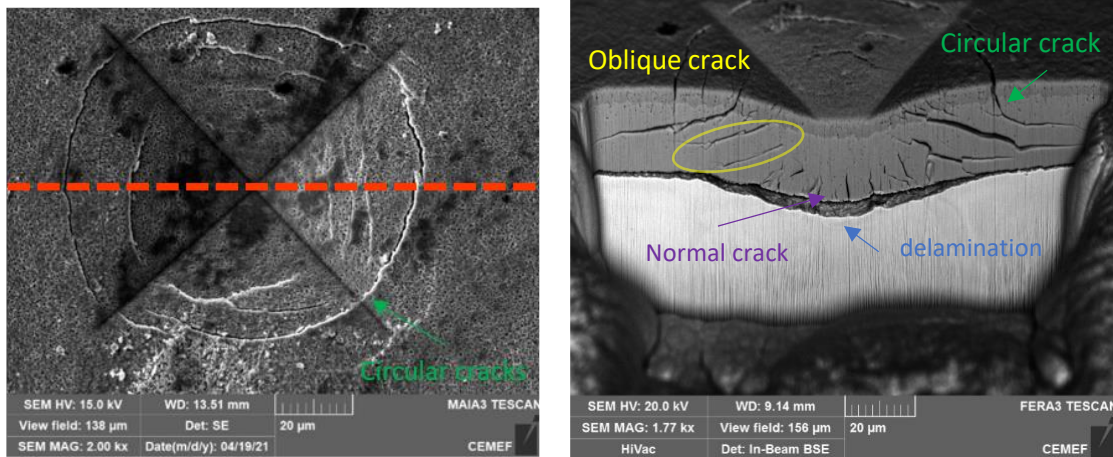


Figure 4.20: SEM observation of oxidized IF specimen indentation with 18N force ($p/t \sim 0.6$). (a) top view showing circular cracks. (b) cross-section of the indentation, prepared by milling the imprint along the red-line, perpendicular to the surface

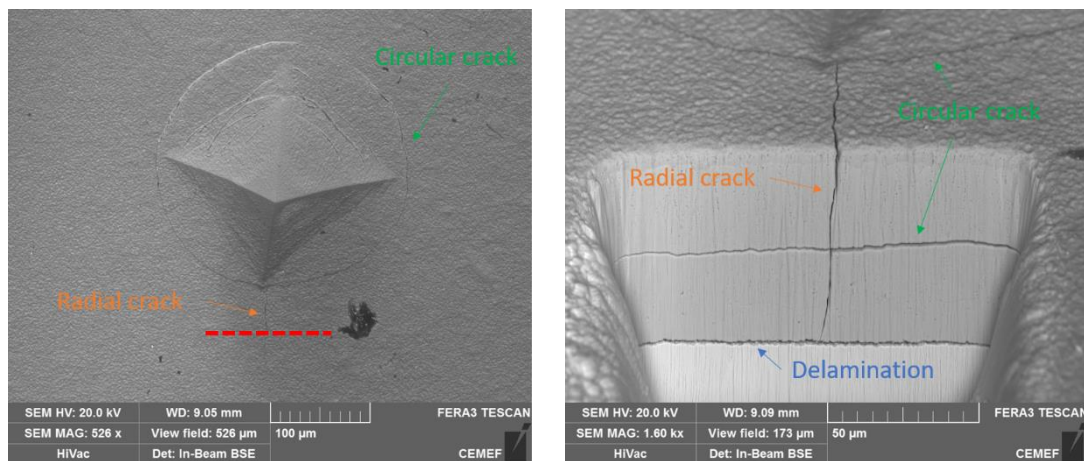


Figure 4.21: SEM observation of oxidized IF specimen indentation with 30N force ($55\mu\text{m}$ of thickness). (a) top view showing circular and radial cracks. (b) cross-section of the indentation, the cross-section is prepared by milling the impression along the red-line, perpendicular to the top surface.

Delamination

The evolution of the delaminated area, with the propagation of fracture at the interface between oxide and steel, is representative of the adherence of scale. The delaminated area is plotted as a function of the penetration p , for a single thickness $t = 16\ \mu\text{m}$ (Figure 4.22(a)). When the ratio p/t is lower than 0.1, no delamination is observed: the delamination also starts during the loading when the influence of the substrate becomes significant. Then, the trend is to increase the delaminated area with increasing penetration.

In order to compare different thicknesses, both the delaminated area and the penetration are normalised by the thickness of each sample (Figure 4.22 (b)). It confirms that this trend is maintained when we vary the thickness.

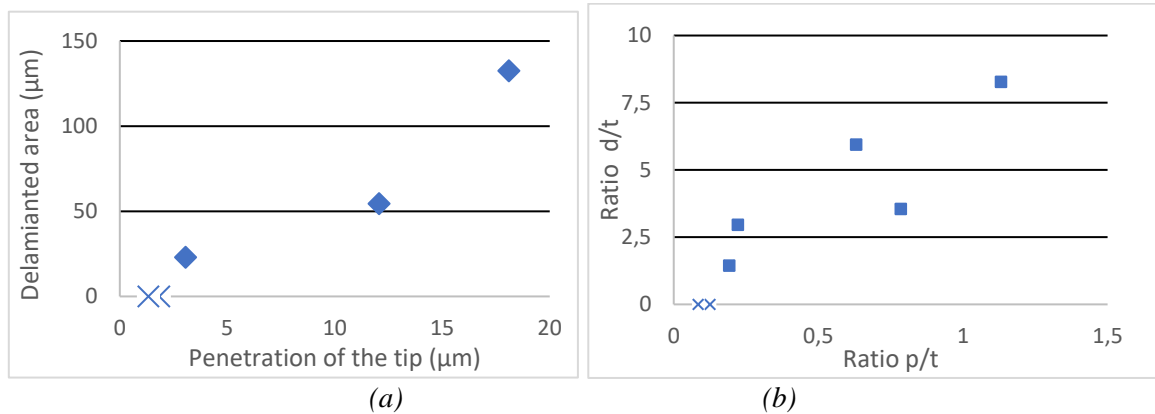


Figure 4.22: (a) Evolution of the delaminated area after indentation for different penetration (and a constant thickness of $16 \mu\text{m}$) (b) evolution of the ratio d/t with the ratio p/t for indentations on different oxide thicknesses. d refers to the delaminated length, t is the oxide thickness and p the tip penetration. The crosses refer to indentation with no delamination.

In the literature, the model of Rosenfeld et al. described previously in part 4.2.3.2 calculates the interfacial fracture of a thin film [158]. The exploitation of this analytical model is based on the debond crack size measurements. Some of their hypotheses are far away from our own conditions (substrate is considered rigid in the model, which is not the case in our study). However, this method has also been used to evaluate properties of a Diamond-like carbon (DLC) thin film on a steel substrate [157]. We therefore use it here as a first approach of the interfacial energy, to be refined later using numerical simulation in section 5.4. The results of the model are plotted in the Figure 4.23 as a function of the ratio p/t , the estimates range from 300 to 500 $\text{J}\cdot\text{m}^{-2}$. Only specimens on which delamination is observed are considered.

A few considerations can be addressed at this stage:

- For Rosenfeld et al., interfacial crack grows only during loading [158]. This mechanism differs from lateral cracks, reported by Marshall et al. [163] which propagate at the end of the unloading in bulk brittle material, parallel to the surface. Interface cracks bear some resemblance to lateral cracks: initiation at the bottom of the plastic zone ($p/t = 0.1$ means that the plastic zone is reaching the interface), sub-surface outward propagation. But differences are substantial: lateral cracks propagate in mode I and only at the end of unloading, whereas interfacial crack propagates during loading and in a mixed mode according to Rosenfeld et al. For our case, these characteristics remain at this stage an open question which is investigated in chapter 5 through numerical simulation.
- Indeed, degradation at the interface is in a mixed mode between I and II according to Rosenfeld [158]. The relative amount of each mode can be described by the phase angle $\tan \alpha = K_{II}/K_I$ (0° for a pure crack opening and 90° for a pure shear loading). For indentation of an epoxy-glass interface, the authors found $\alpha = 45^\circ$ to 55° . Indeed, we will show in section 5.4 that shear can explain oxide-steel interface crack growth in our case. The influence of fracture mode on G_c has been widely described in literature ; by increasing α , G_c tends to increase too, an explanation is crack tip plasticity and non-planar interface [158].
- In this model, buckling and residual stress are not accounted for, and hardness is supposed to be constant through the thickness. Compressive stress strongly influences delamination by increasing the driving force of interfacial cracks when buckling occurs [156].
- A limitation in the application of the model is that the FIB-milled zone must be larger than the delaminated area (Figure 4.20). Here, due to technical limitations, no cross-section larger than $300 \mu\text{m}$ could be prepared; we therefore often observe a lower bound of crack length, hence an upper bound of interface energy.

The average value of adhesion for IF is equal to $336 \pm 39 \text{ J/m}^2$ (with values between 287 and 474). This method used to determine adhesion of oxide scale shows a variability in results. This may be due partly to the uncertainty of the methodology, but also to the spatial variability of the adhesion and, presumably, the interface composition or microstructure. Thus, it is necessary to multiply the

analyses to refine results. These results agree with adhesion values found in literature (see Table 2-7). Remember that a very large variability was also observed in adhesion values of steel and oxide with others tests (tensile tests [85–87,120], inverted blister-test [164], scratch test [68] and indentation [47,83]). This points to intrinsic variability and heterogeneity of such interfaces and confirms the great difficulty to characterise adhesion of thin oxide steel.

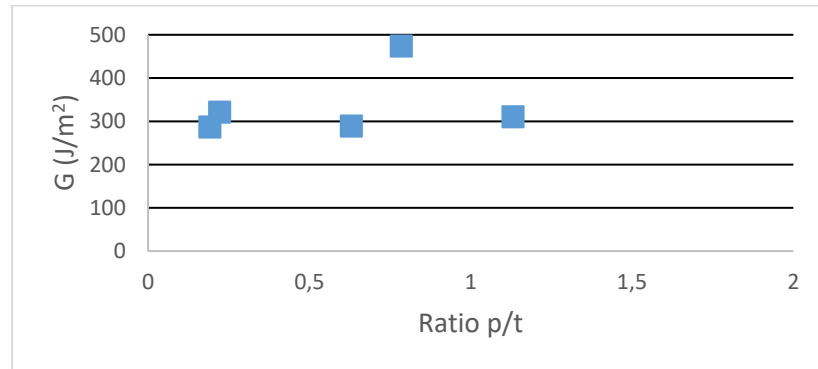


Figure 4.23: Evolution with the ratio p/t of the interfacial fracture of oxidized low carbon steel calculated with the Rosenfeld model.

Normal crack

At the interface between oxide and steel, there are other cracks which are not visible without FIB cross-sections. The normal cracks are initiated at the interface, perpendicular to it. In the following, R is the position of the normal crack in relation to the axis of the indentation and a is the radius of the area of contact.

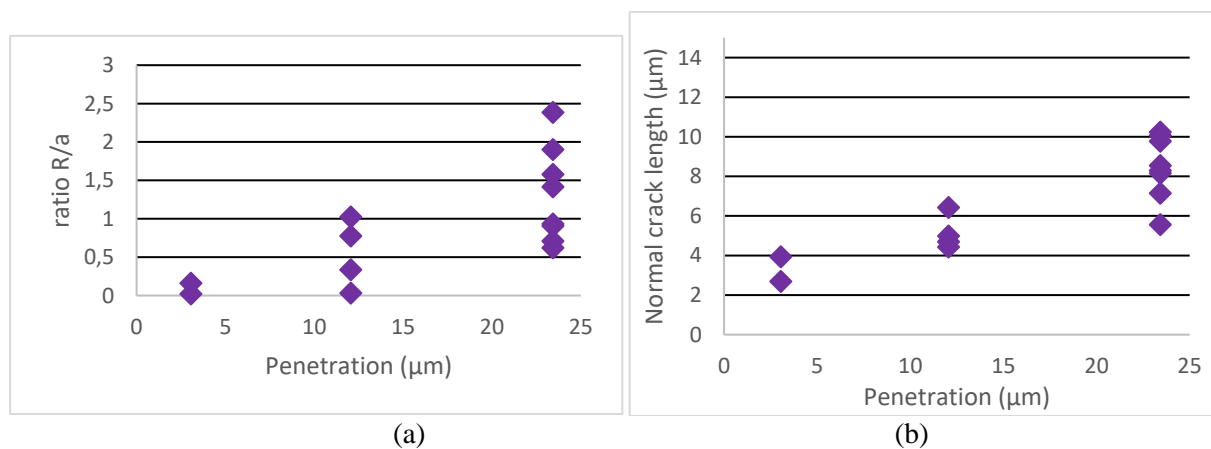


Figure 4.24: (a) Evolution of the position of the normal cracks versus the penetration (for a same oxide thickness of oxide $t=16\mu\text{m}$) p/t (b) Evolution of the normal crack length with the penetration (for a same oxide thickness of oxide $t=16\mu\text{m}$)

First, the description is made for indentation at different tip penetrations, for the same oxide thickness ($16\mu\text{m}$). The position of crack initiation depends on the penetration of the indenter (Figure 4.24(a)). In all cases, there are cracks just below the indentation ($R/a \sim 0$), probably formed at low penetration; but by increasing the penetration depth, they become more numerous and are located further away from the centre of the indentation. This corresponds to the literature results cited in Figure 4.11, considering that increasing the load, i.e. p/t , i.e. a , is equivalent to decrease t/a (d/a in Figure 4.10 and Figure 4.11).

The length of these cracks is also dependent on the ratio p/t (Figure 4.25(b)). They never reach the surface, and thus the final length is always lower than the thickness of oxide. The length of cracks tends to increase with increasing p/t (Figure 4.24 (b)). For $p/t < 0.1$, no cracks are visible, just like for circular cracks. Thus, these normal cracks also are initiated when the plastic deformation due to the indentation reaches the interface, forcing the oxide plate to bend.

Secondly, the same trend is noted when gathering different thicknesses (normalised with the ratio p/t) in the Figure 4.25.

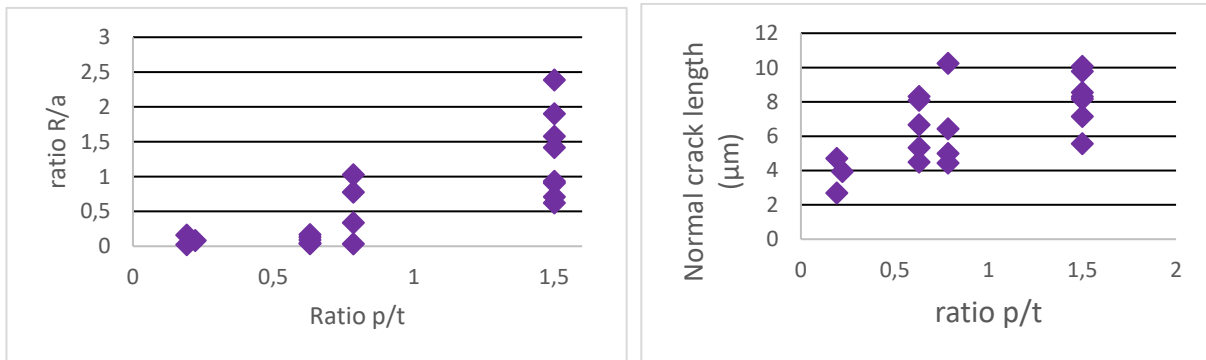


Figure 4.25: (a) Evolution of the position of the normal cracks versus the ratio p/t (b) Evolution of the normal crack length with the ratio p/t

4.4.2.4 Comparison between steel grades

Similar indentation tests are done for two other grades: HSLA0 and HSLA1. These grades tend to blister in the HSM. Indentations are carried out from 0.5 to 20 N with Vickers tips. For $t \geq 20 \mu\text{m}$, oxide has been completely flaked-off during indentation, which reflects a weak adhesion. Thus, results are shown for samples with thickness lower than $20 \mu\text{m}$.

Fracture behaviour

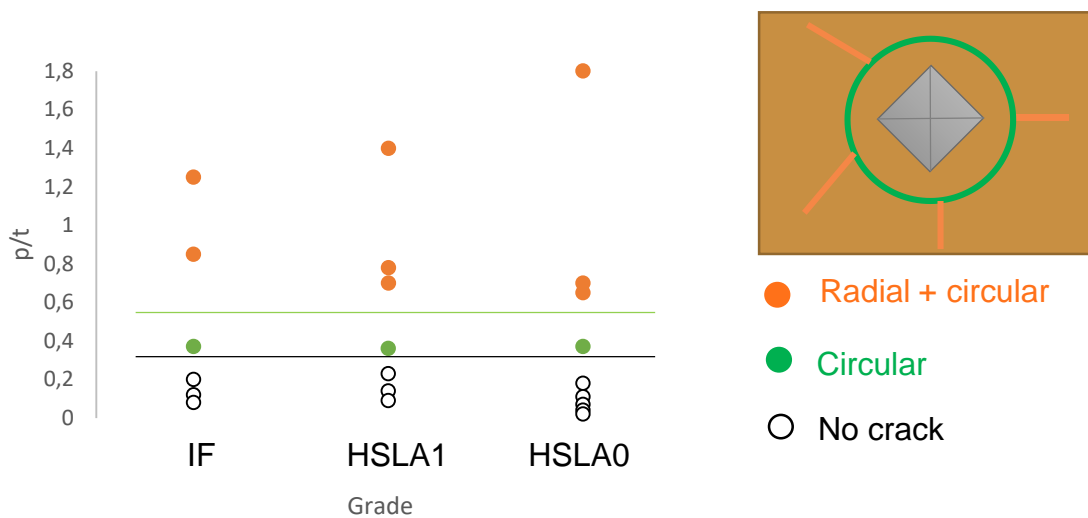


Figure 4.26: Evolution of the fracture mechanisms for the three grades. Circular cracks are represented in green and radial cracks in orange. The same thickness is used for the three grades ($16 \mu\text{m}$)

Concerning the brittle behaviour of the oxide at room temperature, the same types of cracks are present. When the plastic deformation is confined within oxide ($p/t < 0.1$), there is no crack. By increasing the penetration, first circular and then radial cracks appear at the surface Figure 4.26). The transition p/t between fracture mechanisms is the same for the three grades, at least no difference can be made based on the results of this campaign.

Delamination

Even for low force indentation, delamination of oxide is larger than the FIB cross-section lateral size for HSLA0 and HSLA1. Once delamination has started, the fracture propagates far from the indentation area (Figure 4.27 (a) and (b)). An area far from any indentation has been FIB-bed and has confirmed the adhesion of oxide in the absence of mechanical solicitation (Figure 4.27 (c)). It can therefore be concluded that the oxide adhesion of these grades is poor.

Comparison between the three grades is presented Table 4-5 and Table 4-6 using the Rosenfeld et al. model [158]. Adhesion energy for HSLA0 and HSLA1 is much lower than for IF. Standard deviation has the same order of magnitude as the average for HSLA0 and HSLA1, it reflects the large heterogeneity of adherence for these grades.

A new grade (DWI) has been studied as well. On the contrary, it does not delaminate, even for very deep indentations (30 N and $p/t > 2$), so interfacial adhesion cannot be calculated, but it seems that the oxide is strongly adherent on this steel grade.

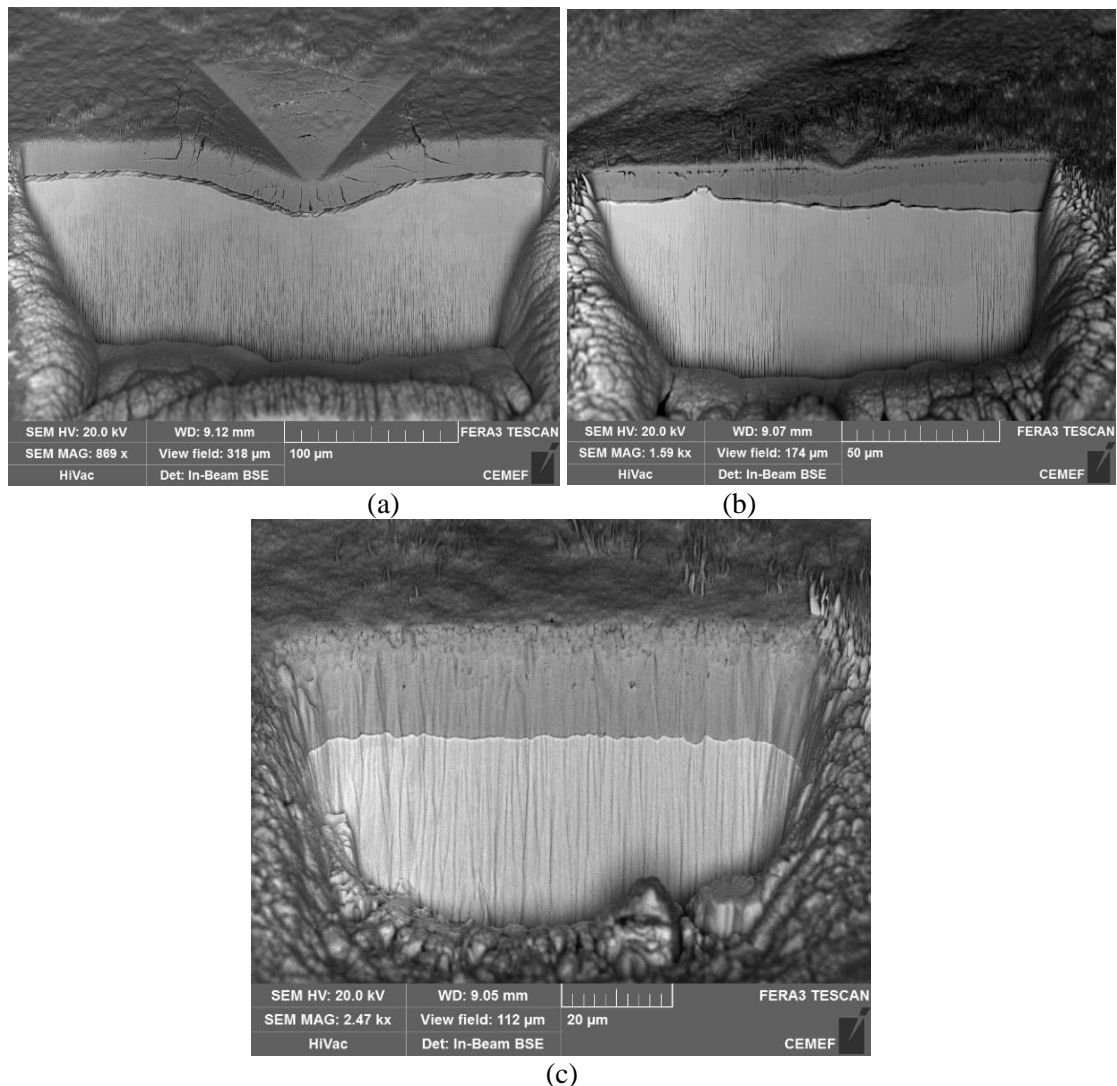


Figure 4.27: FIB cross-sections of oxidized HSLA1 specimen after indentation (a) with a 20 N force. (b) with 1 N load (c) without indentation. The cross-section is prepared by milling perpendicular to the top surface.

Chapter 4: Indentation to evaluate properties of oxide

Table 4-5: Evaluation of the interfacial adhesion energy for different grades using the Rosenfeld et al. model [158]. Each line corresponds to a FIB cross-section.

Sample	Force (N)	p/t	a (μm)	c (μm)	G (J/m^2)
IF_650_26	5	0.6	107	139	289
IF_650_16	2	0.8	88	55	474
IF_650_55	10	0.2	91	168	321
IF_650_16	0.9	0.2	22	23	287
IF_650_16	0.4	0.1	13	0	-
IF_650_16	0.2	0.1	10	0	-
IF_700_16	5	1.1	133	133	310
HSLA1_700_20	5	0.5	72	208	29
HSLA1_700_20	20	1.3	184	305	139
HSLA1_700_20	0.9	0.2	25	146	2
HSLA1_700_20	0.4	0.1	14	106	1
HSLA0_700_20	5	0.5	83	179	77
HSLA0_700_20	20	1.0	164	295	136
HSLA0_700_20	2	0.5	41	148	8
HSLA0_700_20	0.9	0.2	20	93	4
HSLA0_700_20	0.4	0.1	13	114	1
DWI_700_16	10	0.7	80	0	-
DWI_700_16	2	0.3	40	0	-
DWI_700_16	30	2.0	240	0	-

Table 4-6: Comparison of adhesion for 3 grades (at least 5 indentations are selected for each grade)

Grade	G (J/m^2)	Min-Max
IF	336 ± 39	287-474
HSLA0	45 ± 30	0-139
HSLA1	43 ± 33	1-136

A large difference in adhesion value is observed between IF and other grades, for the same oxidation cycle and preparation. On the contrary, the toughness of the oxide itself seems not to be affected (Figure 4.26): the critical point is the interface behaviour. The grades differ by Mn, Si and C percentage (Table 3-1). It could explain the differences in the adhesion values calculated. The effects of these alloying elements are discussed by Kizu et al. [24]. In their study, specimens are oxidized at high temperature and blistering is observed at. Scale blistering is the balance between delamination (by either compressive buckling or gas formation at the interface) and adhesive forces between steel and oxide. For a fixed oxidation time, blistering tends to decrease (Figure 4.28 (a)) for oxidation at $T > 800^\circ\text{C}$, when $\text{Mn} > 0.2\% \text{wt}$. At 800°C , for $\text{C} > 0.02\% \text{wt}$, the same tendency is observed (Figure 4.28 (b)). Thus, high C and Mn content tends to promote blistering, i.e. decrease adhesion of oxides. Several explanations have been proposed. At the interface, with more carbon, CO is more liable to be generated by selective oxidation of carbon, and adhesive force decreases. This tendency is also confirmed by Chandra-Ambhorn [85]: lower scale adhesion is related to the higher amount of carbon at the scale-steel interface, favouring CO gas or graphite formation. In addition, according to Kizu [24], Wüstite, the main oxide phase, normally has a strong fiber texture $\{100\}$. The increasing percentage of Mn tends to favour other crystalline orientations such as $\{110\}$ and $\{111\}$. The volume occupied by these two minority orientations causes compressive stress due to the different crystal growth rates. It deteriorates adhesion between oxide and substrate. Mn also affects the grain size of Wüstite. With a lower grain size, other crystalline orientations $\{110\}$ and $\{111\}$ are more present, which increases compressive stress.

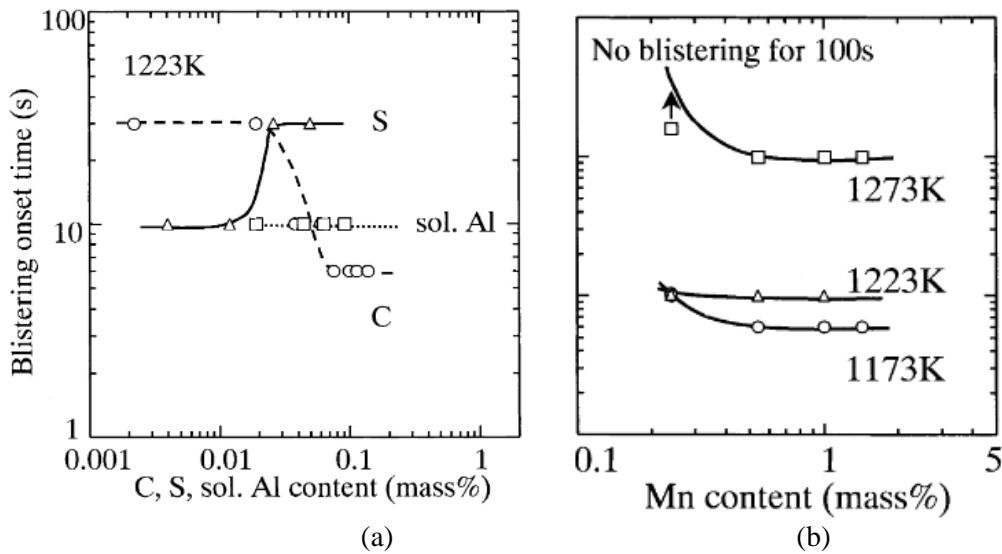


Figure 4.28: Effect of alloying elements on the onset time of blistering (a) carbon at 950°C (circles) (b) Manganese at 1000°C, 950°C and 900°C

To summarise, during indentation at room temperature, the oxide is brittle and tends to crack in a multiple way: in surface, first circular cracks start from the oxide surface but never reach the interface and then radial cracks start from the indentation side and go through traversing the oxide. At the interface, delamination and normal cracks start from the interface but never reach the surface. These fracture phenomena have been reported in the literature for different systems. The model of Rosenfeld et al. has been used to evaluate the interfacial adhesion energy. There are some differences in adhesion for HSLA grades that are supposed to blister. In the next chapter, the FEM simulation of the indentation will be used to understand the fracture mechanisms and to identify the chronology of the oxide fracture.

Now, the high temperature indentation is described to understand the thermo-mechanical behaviour of oxide at high temperature.

4.5 High temperature indentation

4.5.1 Difficulties inherent to high temperature indentation

The indentation at high temperature is particularly relevant in order to evaluate the properties of oxide, and more precisely the ductile-brittle transition. However, this kind of experiment is complicated due to the thermal drift, the control of further sample oxidation and the choice of the material tip. All these difficulties are described in the next paragraph.

4.5.1.1 Thermal drift

The main issue for high temperature indentation is the thermal drift. It depends basically on the temperature gradients within the tip-sample contact [165]. To limit temperature errors, the choice of the heating system is therefore a very important step. The idea is to maintain isothermal conditions during the contact. Two options are possible:

- Sample heating only. In this case, only the sample is heated directly, it is supposed to heat the tip (the small size guarantees low thermal inertia). The main advantage of this technology is its simplicity of use, as no heating system is attached to the tip. However, it does not guarantee a homogeneous temperature in the contact area, which is essential for the proper conduct of the test.

- The use of two independent heating systems, for the sample and tip, is therefore recommended by Everitt et al. [165]. Indeed, indentation without separate indenter heating tends to produce unacceptable thermal perturbations in the system and to induce errors in the evaluation of properties at high temperature. The majority of devices use this heating technique, and this is the case of Alemnis HTM800. The temperature of each part is continuously controlled to ensure the thermal equilibrium at the contact.

4.5.1.2 Control of sample oxidation

The other issue is the control of oxidation, particularly in the case of reactive material such as low carbon steels. To ensure the integrity of the material surface and to limit further growth of oxide, several solutions exist:

- The first solution is to perform the tests in an inert environment (pure argon or nitrogen) to limit the presence of oxygen. The indentation area can be flushed all along the tests. However, according to Wheeler et al. [160], for tungsten, after 1 h at 700 °C in an argon atmosphere, strong oxidation of the surface occurs and disturbs the analysis. Therefore, an inert environment shows limitations for very high temperatures and highly reactive materials.

- The second solution to limit the degradation of the surface condition is then to perform the testing under a vacuum (in a SEM for example). Korte et al. show no oxidation at 630°C for 48 hours on a nickel superalloy [166]. They evaluate the elastic and plastic properties of this alloy in agreement with the literature. In our study, Alemnis HTM800 is installed in SEM to observe the indentation, and to control the oxidation (10^{-4} mbar).

4.5.1.3 Material for the tip

For the room temperature indentation, diamond tips are commonly used because of its high hardness and stiffness. For high temperature indentation, several issues have to be tackled. The material has to:

- remain inert towards the atmosphere. A high vacuum is frequently used to prevent oxidation of most indenter materials above ~400°C except sapphire. Diamond readily oxidizes into CO and CO₂ above 400°C [167].

- be much harder than the sample. Indeed, by increasing the temperature, the hardness of the material used for the tip is reduced. It has to be 20% higher than the sample to be able to make plastic deformation (and much higher to avoid blunting of the tip).

- remain chemically inert towards the sample. During the contact, the tip has to be chemically stable to avoid blunting again. For example, it is well known that diamond can react with pure iron and other transition metals [167], as carbon dissolves readily into iron. So, the current diamond Vickers indenter cannot be used in our study.

Other materials are recommended for high temperature indentation (up to 1000°C):

- Tungsten Carbide WC
- Cubic Boron Nitride cBN
- Sapphire (Al_2O_3)
- Boron carbide, B_4C

Table 4-7 lists the main advantages of each of these materials. Diamond and boron carbide are the materials of choice for indenting hard materials at elevated temperatures due to their excellent hardness retained at high temperatures. Regarding chemical reactivity, Tungsten carbide is the most stable material against metals and alloys. It only appears to be vulnerable in the presence of tungsten, titanium, and iron at very high temperatures where the carbon could diffuse into the sample. Thus, carbide (B_4C , WC) tips are recommended for HT testing especially for ferrous materials and are used in our study.

Table 4-7: Description of the most used materials for indentation at high temperature [167]

Material	Hardness GPa (at 900°)	Thermal properties	Oxidation	Reactivity with Steel
Diamond	30	High conductivity	Forms CO and CO_2 at $T > 400^\circ\text{C}$	Carbon dissolves into Fe $\sim 400^\circ\text{C}$ Dissolves into Ni $\sim 300^\circ\text{C}$
Sapphire (Al_2O_3)	5	Low conductivity and expansion	Inert	Mostly inert, reduces Ti and Cr (High Cr steel)
Tungsten carbide (WC)	9	Low conductivity and expansion	Forms WO_3 $T > 500^\circ\text{C}$	Loses carbon by diffusion
Boron Carbide (B_4C)	35	Low conductivity	Forms B_2O_3 $T > 450^\circ\text{C}$	Forms carbides/borides Reacts with Ti and Zn
Cubic Boron Nitride cBN	15	High conductivity	Forms B_2O_3 $T > 700^\circ\text{C}$	Dissolves Ni $\sim 700^\circ\text{C}$ Mo, Ti and Cr to form boride

However, after our tests above 800°C , the Boron carbide tip was found blunted (Figure 4.29). One explanation for this degradation is that IF steel has a very low carbon content, thus, compared to “common” steel, it is more likely to dissolve/react with the C in the tip. Indeed, at the end of the unloading, just before the contact is broken, some interaction/adhesion has been observed on the force-displacement curve.

The tungsten carbide WC tip up to 700°C did not show any degradation.

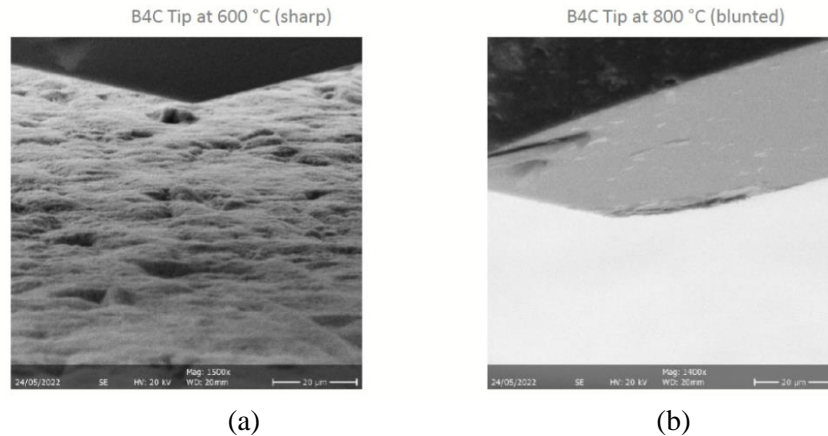


Figure 4.29: Degradation of the B₄C tip during indentation on low carbon steel at high temperature (a) at 600°C (b) 800°C

4.5.2 Micro-indentation up to 30 μm.s⁻¹ at 800°C

4.5.2.1 Description of the conditions

These tests are performed with an Alemnis HTM800, previously described.

The high temperature indentation requires to have the indenter tip and the sample in thermal equilibrium to limit the thermal displacement drift due to thermal expansion. This is achieved through independent heating with resistance heaters and temperature monitoring of both the indenter tip and the sample. Thus, the heating of each part is continuously adjusted.

Before the test, both pre-oxidized sample and tip have been heated to the desired setpoint temperature and maintained for a stabilisation period at the target temperature. The clamping system of the sample consists of a stub, a membrane and 3 screws, all made of Molybdenum to allow testing up to 800°C (Figure 4.15 (b)).

Tests have been made at room temperature and at 600°C, 700°C and 800°C. A PID feedback loop ensures displacement control with a specified target load/loading rate (maximum load of 2,5 N). The tip speed is the same at loading and unloading. The displacement rate has been varied between 250 nm/s to 30μm/s. The penetration of the indenter has been controlled between 4,5μm and 10μm. a surface detection with the tip is done at 1 mN. Each test has been repeated a minimum 2-4 times. SEM observations are made at high temperature, and post-mortem with a better resolution.

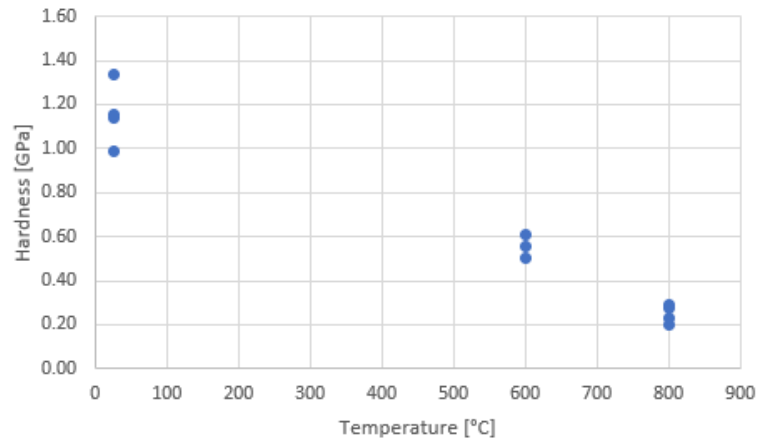
Two grades (IF and HSLA0) have been selected with two different thicknesses (4.5 and 7μm respectively). Samples have been oxidized at 700°C in a controlled atmosphere furnace before the test to obtain the desired thickness; in this series of experiments, the thickness range is 4.5-7 μm. A control before and after the test has shown that no further oxidation takes place during the thermal cycle of the indentation.

The study described here is focused on the influence of the temperature and penetration depth. As Picqué [4] has shown strain rate sensitivity of Wüstite at elevated temperature, a few tests have been carried out at different indentation speeds.

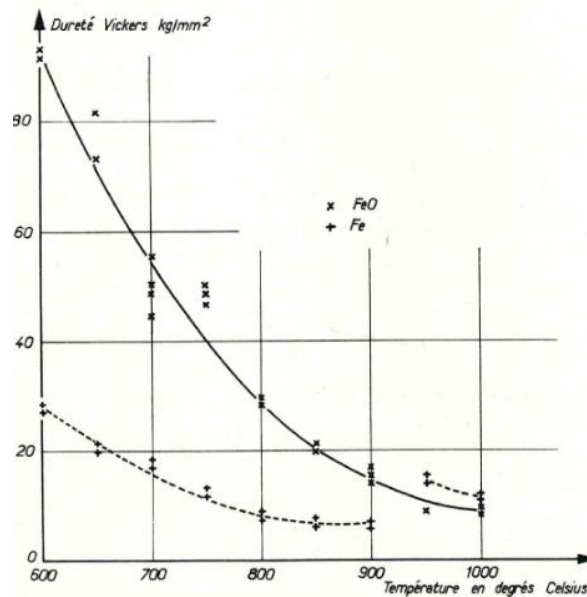
4.5.2.2 Hardness of “steel+oxide” at high temperature

Contrary to room temperature, the intrinsic hardness of steel and oxide has not been measured by indentation on a cross section (see Figure 4.16) at high temperature: for want of apparatus time, only indentations from the surface have been performed. This gives only an apparent, “composite steel+oxide hardness”. This is not much of a problem; oxide ductility and interface toughness are the key point of this part. In all indentations, due to the low thickness (4-7 μm), the ratio p/t is above 1, and thus this “composite hardness” is highly influenced by the steel substrate. In the Figure 4.30 (a), the same

parameters are used (7 μm penetration and 250 $\mu\text{m/s}$ displacement rate). Hardness is of course decreasing with increasing temperature. The “hardness values” lie between the oxide and the steel hardness at 600°C and 800°C as evaluated by Vagnard [75] (at 800°C, 0.3 GPa for Wüstite and 0.1 GPa for steel (Figure 4.30 (b)).



(a)



(b)

Figure 4.30: (a) Evolution of the composite Steel+Oxide hardness with the temperature (7 μm of penetration and 250nm/s of displacement rate) (b) hardness value of FeO and Fe [75]

4.5.2.3 Ductile-brittle transition

As described previously (section 4.4.2), the oxide is found to be brittle at room temperature whatever the conditions used and the steel grade, for any penetration ratio $p/t > 0.1$. The evolution at high temperature is now studied, grade by grade starting with low indentation speed (0.25 $\mu\text{m/s}$).

IF grade

Consider the example of Figure 4.31, an indentation at 600°C with a displacement rate of 250 nm/s and a penetration of 4.2 μm (sample IF0_700_4,5, oxide formed at 700°C furnace temperature). There is no trace of cracking even at large penetration of the indenter ($p/t > 1$).

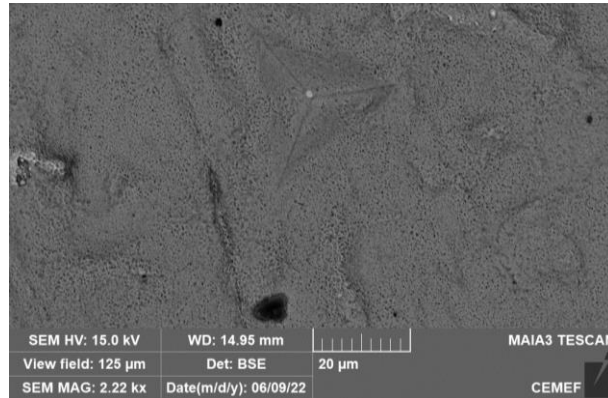


Figure 4.31: Post-mortem SEM observations of the indentation at 600°C with a displacement rate of 250 nm/s and a penetration of 4.2µm

Oxide is thus liable to show plastic deformation at 600°C. A more general picture is given for a 250 nm/s displacement rate by Figure 4.32 which summarises fracture behaviour of IF_700_4 during all indentation (at least 3 indentations for each p/t at each temperature). The oxide is brittle at room temperature as discussed above; at 600°C for the same indenter velocity, the oxide fracture becomes random: some indentations show cracks and others not. There is no obvious influence of p/t, the occurrence of fracture probably depends on surface and interface roughness and on local defects. At 800°C, no cracks are found whatever the conditions, the oxide deforms plastically.

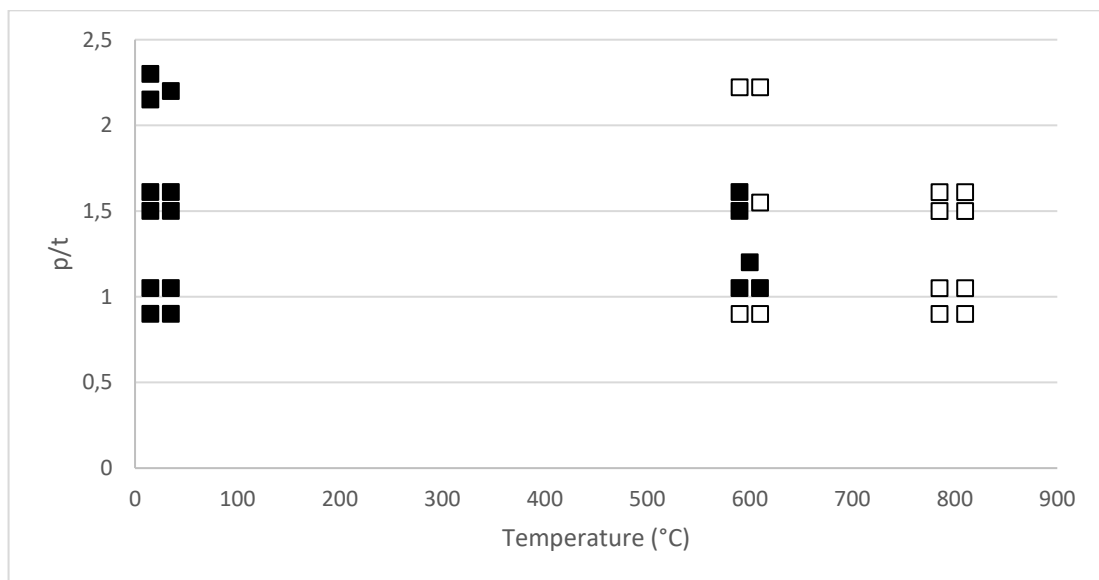


Figure 4.32: Fracture behaviour of IF_700_4 at different temperatures, indentation speed 250 nm/s : □ no crack, ■ crack, Each group of points corresponds to a set of parameter

HSLA0 grade

The study has been extended to a second grade, HSLA0. Only a small number of tests have been performed, furthermore not at the same temperature as IF; indeed, the highest temperature is 700°C instead of 800°C due to the damage to the indenter mentioned in section 4.5.1.3. However, the same trend is noted. By increasing the temperature to 600°C, fracture becomes random (maybe more frequent at large penetration), and at 700°C, the oxide is fully ductile in the two experiments which have been carried out, at low and high penetration depths. It can be tentatively concluded that the evolution in temperature is the same as IF grade.

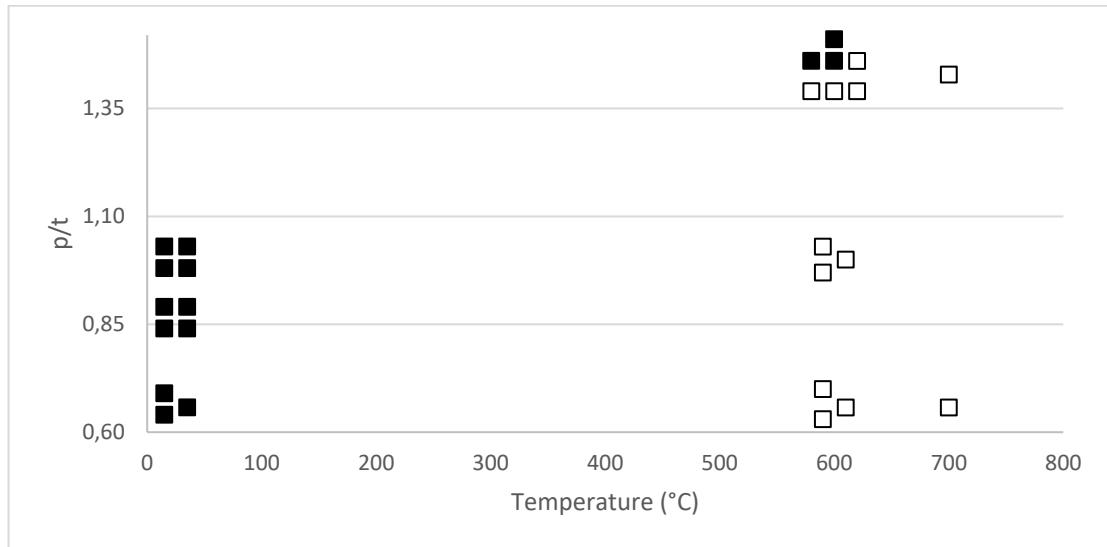


Figure 4.33: Fracture behaviour of HSLA_700_7 at different temperatures, indentation speed 250 nm/s: \square no crack, \blacksquare crack, Each group of points corresponds to a set of parameter

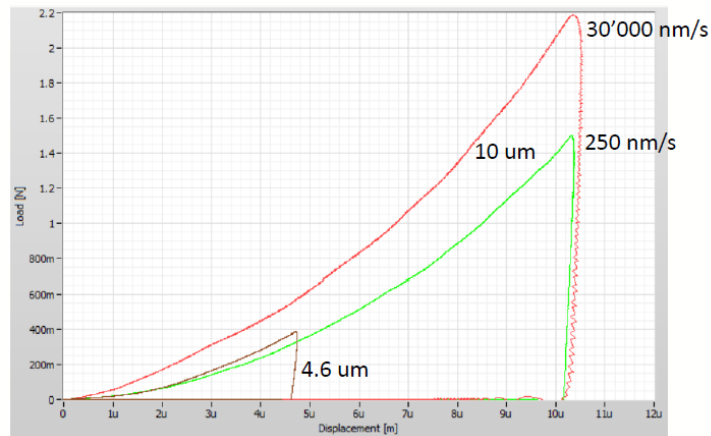
Influence of the strain rate

In addition to previous tests, the indentation speed has been varied from 250 nm/s to 30 $\mu\text{m/s}$. This study has been carried out on HSLA0_700_7 at 700°C and on IF_700_4. Figure 4.34 (a) presents results for HSLA0_700_7 (oxide thickness $t = 7 \mu\text{m}$ formed at 700°C), indentation temperature 700°C, imposed penetration $p = 10 \mu\text{m}$. As indentation speed is multiplied by 120, the indentation load increases by 50%, from 1.45 to 2.2 N. This corresponds to a strain rate sensitivity exponent $m = 0.08$, consistent with steel behaviour at 700°C. Figure 4.34 (b) and (c) show post-mortem SEM observations at room temperature, with a much better resolution than the in-situ SEM observations. The low-speed test shows a ductile behaviour, whereas high speed shows “circular” cracks.

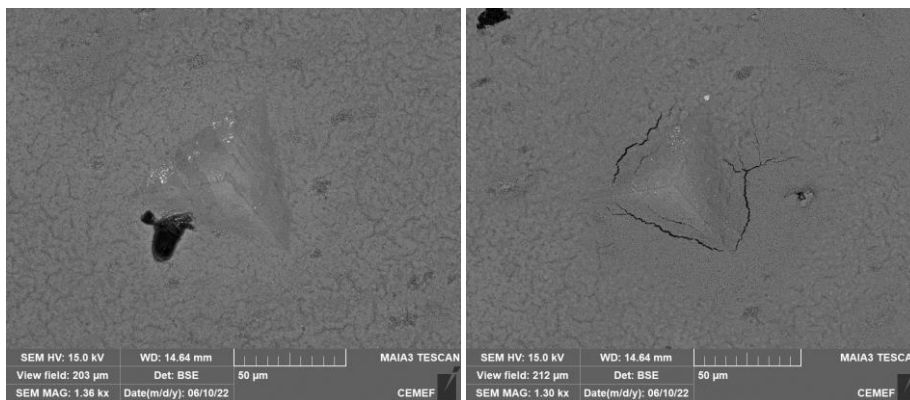
This tendency has been observed for both grades. The comparison is made with the ratio p/t as the thickness of oxide is different (4.5 μm for IF and 7 μm for HSLA0). In Figure 4.35, the comparison is made for tests at 600°C with two displacement rates: 0.25 $\mu\text{m/s}$ and 3 $\mu\text{m/s}$, by considering the percentage of circular cracks after the indentation (IF in yellow and HSLA0 in blue). As a reminder, 600°C is in the ductile-brittle transition. For IF grade (yellow points), by increasing the displacement rate to 3 $\mu\text{m/s}$, the probability of cracking is higher. However, this tendency is not so clear for the HSLA0 grade with 3 $\mu\text{m/s}$. Indeed, for low penetration indentation on HSLA0 grade (blue points), whatever the displacement rate used, no cracks are observed. By increasing the penetration (p/t above 1), similar results are observed for the two-displacement rates.

The same behaviour is observed between the two grades. Thus, in this range of temperature and speed, similar fracture behaviours are observed, which is not surprising since in both cases, Wüstite is involved; the low level of additional elements does not seem to change matters a lot.

Chapter 4: Indentation to evaluate properties of oxide



(a)



(b)

(c)

Figure 4.34: (a) Load-displacement curves for indentation at 700°C with a 10µm penetration on HSLA0_700_7 sample for different indentation speeds (green for 250 nm/s and red for 30 000 nm/s). The brown curve is at 250nm/s, with smaller penetration. Post-mortem SEM observations for (b) 250nm/s (c) 30 000 nm/s

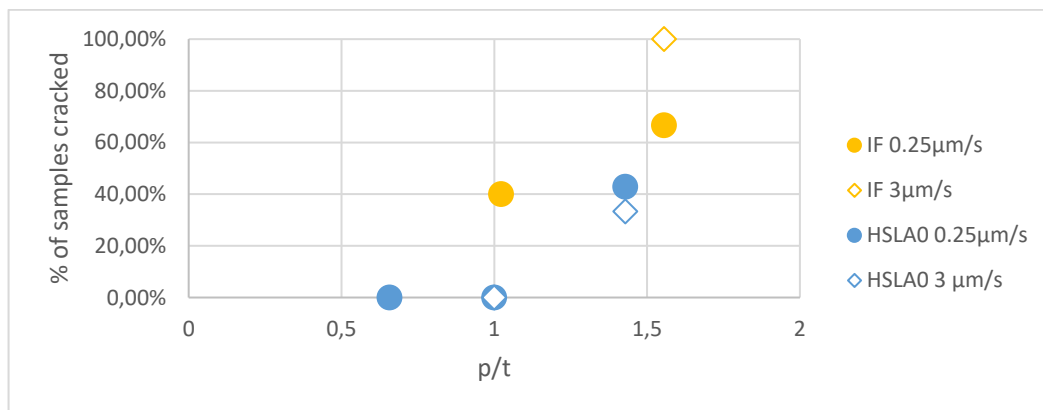
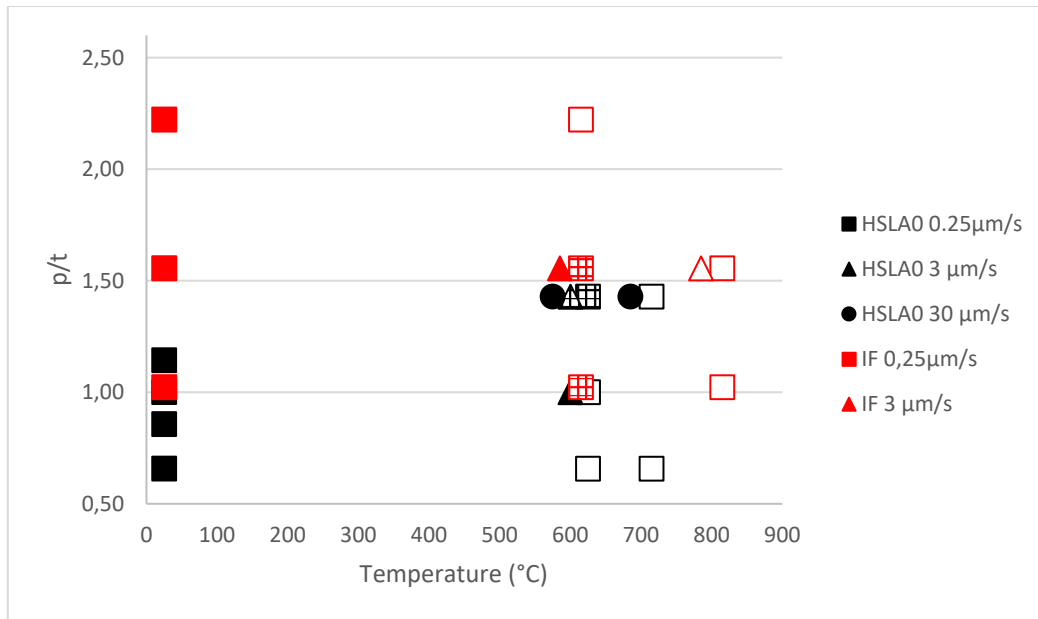
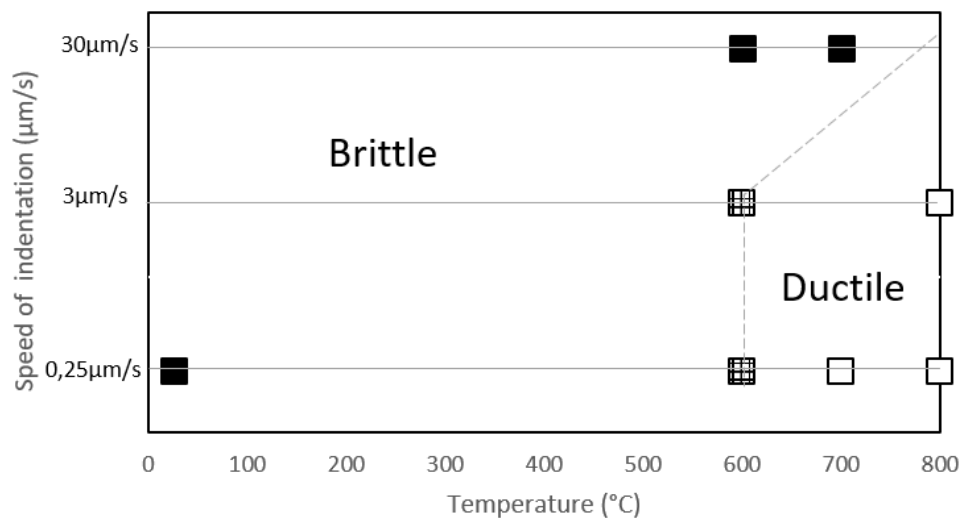


Figure 4.35: Comparison of percentage of cracking at 600°C for the two grades IF (in yellow) and HSLA0 (in blue) for two different displacement rate (low displacement rate in filled points).

Figure 4.36 gathers all indentations for the IF and HSLA0 grades at all temperatures and indentation speeds. A fracture map can be built depending on temperature and indentation speed (Figure 4.36 (b)). This transition is highly influenced by the indentation speed. For a fixed set of parameters (temperature, penetration of indenter), a speed increase tends to harden and embrittle the oxide. By plotting the percentage of cracking for each temperature, a brittle to ductile transition is thus detected between 600 and 700°C.



(a)



(b)

Figure 4.36: fracture behaviour of IF and HSLA oxides. (a) Summary of all tests at high temperature. Only circular cracks in surface are considered. The red symbols refer to IF0, the black symbols to HSLA0. (b) Mapping of the oxide cracking behaviour (circular cracks in surface) of low carbon steel (IF and HSLA0) during high temperature indentation tests: □ never cracking, ■ always cracking, ▣ occasionally cracking

These results are in agreement with other mechanical tests: bending [4] (Figure 2.33), rolling ([91]- [92] and Figure 2.34) and compression [90–92] and Figure 2.35 in Chapter 2). It confirms the progressive ductile/brittle transition of oxide between 600°C and 750°C, depending on strain rate as also reported by Picqué [4]. In all the studies, there is a mixed mode of degradation in which oxide sometimes does not crack. However, the temperature of transition depends on each method and its specific conditions, oxidation, stress and strain pattern (Table 4-8).

Table 4-8: Comparison of the determination of ductile-brittle transition of oxide using different methods

Reference	Method	Temperature of the transition	Tests conditions
This study	Indentation	600°C/700°	0.3 to 30 μm/s
Picqué [4]	3 points bending	~700°C	Strain rate (10 ⁻⁵ /10 ⁻² s ⁻¹)
Suárez et al. [90]	Plane strain compression	680°C/850°C	Strain rate 10 s ⁻¹ % reduction 5/60
Filatov et al. [91]	Rolling tests	700°C/900°C	Rolling reduction % 30 to 60
Li and Sellars [92]	Rolling tests	650°C /800°C	Rolling reduction % 20 to 50 Speed : 0.14 m/s

The ductile-brittle transition of oxide has been well identified. This transition is influenced by the displacement rate of the indenter and seems to be identical between the grades investigated. Now, we are going to observe the adhesion of oxide, through the study of delamination.

4.5.2.4 Delamination

IF0 grade

Figure 4.37 represents a 10 μm penetration indentation of the IF_700_4 sample at 600°C (p/t = 2.5). From the surface, no crack is visible. The FIB cross-section shows oxide delaminated at the periphery of the indentation. In comparison to the Figure 4.20 and room temperature indentation, the delaminated area is clearly not the same.

Cross-sections have also been made far from an indented area. Delamination is also present (Figure 4.37(c)). It suggests that the delaminated area is not directly in relation with the indentation; in this case, the thermal cycle could be responsible. The samples undergo a double thermal cycle : a first heating at 700°C for the oxidation, followed by a fast cooling, then a long heating stage before indentation and finally a long cooling. What we observe in the cross-section is therefore the result of a complex thermal history. In section 3.5.3, we have seen that compressive stresses are generated during the cooling, and tensile stresses should be generated during the heating. According to Evans [6], for a weak interface, some decohesion areas are created at the interface by buckling. Buckling is progressive and is rumpling the surface of the metal because of thermal stresses.

No clear conclusion for the adhesion of oxide at higher temperature can therefore be drawn. In order to limit the thermal stresses contribution, the ideal test is to make the indentation just after the oxidation (and avoiding the cooling/heating).

Remark: Anyway, no normal cracks are present at 600°C, after FIB cross-sections observation. These indentations are carried out on low thicknesses, we are close to the configuration described in Chai & Lawn [154] in Figure 4.10, where there are no more "normal" cracks under the indenter, they merge into the ring crack. It seems that we are in this d/a range.

HSLA0 grade

After the double thermal cycle (cycle 1 for indentation and cycle 2 for the indentation up to 700°C), FIB cross-sections for HSLA0 indicate large decohesion Figure 4.38. The oxide is poorly adherent to the substrate, contrary to the IF sample, (see Figure 4.37). The oxide has clearly melted, which shows that the heat induced by the ion beam could not be evacuated through the interface into the steel substrate, proving a physical discontinuity. This large decohesion has been observed in areas with an indentation as well as without. It confirms the low adhesion of HSLA0 already evidenced by the low values of G at room temperature.

As described previously, this large delamination may probably be attributed to the thermal stress cycles.

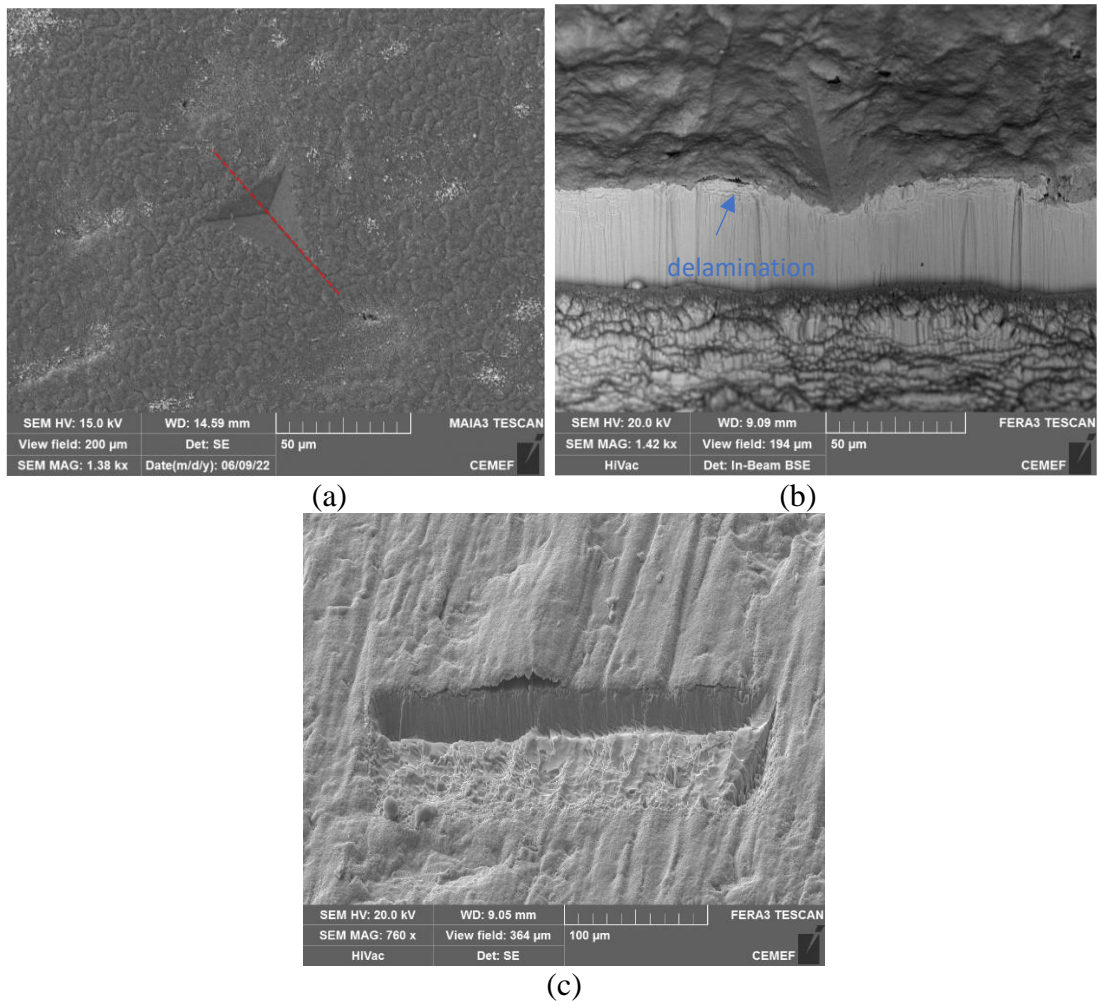


Figure 4.37: SEM observation of the IF_700_4 indentation with 10μm penetration at 250 nm/s rate at 600°C (a) top view (b) cross-section of the indentation. The cross-section is prepared by milling the imprint along the red-line, perpendicular to the top (c) cross-section in a area without indentation

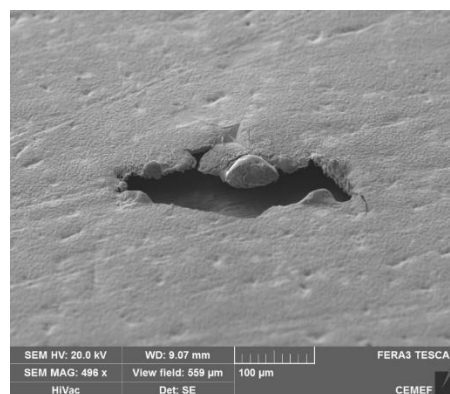


Figure 4.38: FIB cross-section at the surface of the HLSA0_700_7 sample after the high temperature indentation. Large decohesion is noted.

Delamination could not be clearly evidenced in hot indentations. On the one hand, further experimental study should be conducted, in particular on more relevant samples (no buckling) and as much as possible using in-situ oxidation to avoid multiple cycles which destroy the interface. Under the present conditions, the numerical study of chapter 5 will be called upon to provide at least a lower bound of interface adhesion properties.

4.6 Conclusion

The objective of this chapter is to assess the mechanical behaviour of low carbon oxide to better understand its response to external stress. Initially, low carbon steel samples are oxidized at high temperatures in a controlled atmosphere at 650°C and 700°C, resulting in an oxide thickness ranging from 5 to 55 µm. Cross-section indentations have been used to evaluate the hardness of oxide and steel separately at room temperature. Then, classical Vickers indentations have been made from the surface of the oxidized samples (15-55 µm of oxide). The oxide is found to be brittle and fractured in multiple ways, with first circular cracks at the surface and then normal cracks appearing on the interface. The absence of "pop-in" on the loading curves complicates the interpretation of these fracture mechanisms. At the interface, delamination indicates low interfacial toughness and oxide adhesion, which is characterised by the delaminated area from which a first estimation of the interfacial energy has been made. The presence of both transverse cracks and a delaminated area confirms the appropriateness of using indentation for our purpose of double characterisation: oxide and interface toughness. But the complexity of the observations means that no simple model can reliably measure these quantities. This is why numerical simulation is used in the next chapter.

High-temperature indentations have been performed on the same kinds of pre-oxidized samples, but with certain difficulties. First, only thinner oxide (4-7 µm) have been studied. At 600°C, the oxide exhibited mixed-mode degradation (ductile-brittle). As the temperature is raised above 700°C, no cracks are visible any more, confirming the transition of the oxide to a ductile behaviour. This transition is found to be influenced by indentation speed, with cracks being observed as the speed of deformation increases. From an industrial standpoint, descaling must cool the oxide sufficiently to bring it below this transition and allow for its fracture, considering the cooling speed and the corresponding stress rate.

However, it has not been possible to evaluate adhesion at high temperatures due to buckling caused by thermal stresses generated during the double thermal cycle. To address this problem, a new in-situ indentation test is developed to realise the in-situ indentation just after oxidation (detailed in Appendix C). The thickness is much higher however (90 µm) The first results are encouraging and confirm the ductile-brittle temperature transition in agreement with the literature (Figure 4.39). They also indicate that the oxide is still adherent under the indentation at 800°C.

Regarding the HSLA grades that are difficult to descale, similar fracture mechanisms are observed with the IF grade (at both room temperature and high temperature). It seems that the toughness of Wüstite on HSLA does not differ from the toughness of Wüstite on IF steel, although %Mn is known to influence this behaviour. However, the adhesion, evaluated, considering the delaminated area under the indentation, is significantly lower for HSLA grades. At high temperature, this grade has also been found particularly sensitive to blistering after the two thermal cycles. This is an important result in agreement to the tendency of these grades to blister in HSM.

Due to the complexity of managing high-temperature tests, such as controlling oxidation and thermal drift, only a few tests have been performed at high temperatures. Further tests are needed to evaluate more precisely the ductile-brittle transition and the differences in behaviour between grades. While the indentation conditions are far from the real industrial descaling conditions, such as isothermal conditions and slow-rate indentation, they allow for the generation of controlled stresses and observation of the behaviour of the oxide.

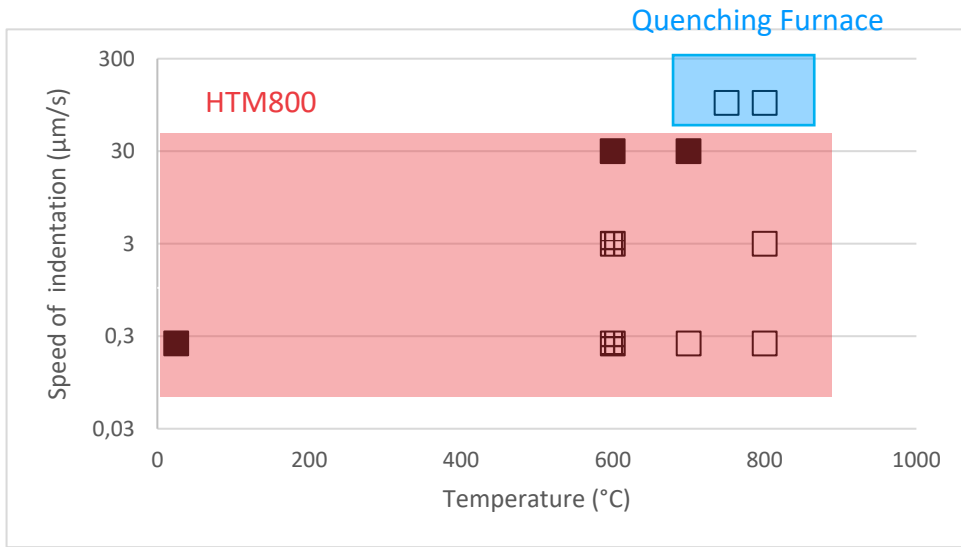


Figure 4.39 Mapping of the oxide cracking behaviour (circular cracks in surface) of low carbon steel during high temperature indentation tests: □ never cracking, ■ always cracking, ▨ occasionally cracking

Résumé

L'objectif de ce chapitre est d'évaluer le comportement mécanique de l'oxyde afin de mieux comprendre sa réponse aux contraintes externes. Dans un premier temps, des échantillons d'acier sont oxydés à haute température dans une atmosphère contrôlée à 650°C et 700°C, ce qui permet d'obtenir une épaisseur d'oxyde allant de 5 à 55 µm. Des indentations sur les tranches des échantillons ont été utilisées pour évaluer la dureté de l'oxyde et de l'acier séparément à température ambiante (dureté trois fois plus importante pour l'oxyde). Ensuite, des indentations Vickers classiques ont été réalisées sur la surface des échantillons oxydés (15-55 µm d'oxyde). L'oxyde s'est avéré fragile et s'est fissuré de multiples façons, avec d'abord des fissures circulaires à la surface et ensuite des fissures normales apparaissant à l'interface. L'absence de "pop-in" sur les courbes de chargement complique l'interprétation de ces mécanismes de rupture. À l'interface, la délamination indique une faible ténacité interfaciale et une faible adhésion de l'oxyde. L'adhésion est caractérisée par la zone délaminée à partir de laquelle une première estimation de l'énergie interfaciale a été faite. La présence de fissures et d'une zone délaminée confirme la pertinence de l'utilisation de l'indentation pour notre objectif de double caractérisation : celle de l'oxyde mais aussi de son interface.

Des indentations à hautes températures ont ensuite été réalisées, jusqu'à 800°C, température de l'oxyde lors du décalaminage. Tout d'abord, des échantillons pré-oxydés, avec une épaisseur faible (4-7 µm) ont été étudiés. A 600°C, l'oxyde présente un mode de dégradation mixte (ductile-fragile). Lorsque la température dépasse 700°C, aucune fissure n'est plus visible, ce qui confirme la transition de l'oxyde vers un comportement ductile. Cette transition est influencée par la vitesse d'indentation, des fissures étant observées lorsque la vitesse de déformation augmente. D'un point de vue industriel, le décalaminage doit refroidir suffisamment l'oxyde pour l'amener en dessous de cette transition et permettre sa rupture, compte tenu de la vitesse de refroidissement et du taux de contrainte correspondant. Cependant, il n'a pas été possible d'évaluer l'adhérence à haute température en raison du cloquage causé par les contraintes thermiques générées pendant le double cycle thermique. Pour résoudre ce problème, un nouveau test d'indentation in situ a été mis au point pour réaliser l'indentation in situ juste après l'oxydation (Appendix C). Les premiers résultats sont encourageants et confirment la température de transition ductile-fragile en accord avec la littérature. Ils indiquent également que l'oxyde reste adhérent sous l'indentation à 800°C.

En ce qui concerne l'étude des différentes nuances, les nuances HSLA difficiles à décalaminer, des mécanismes de rupture similaires sont observés avec la nuance IF (à la fois à température ambiante et à haute température). Il semble que la ténacité de la Wüstite sur l'acier HSLA ne diffère pas de la ténacité de la Wüstite sur l'acier IF, bien que l'on sache que le pourcentage de Mn influence ce comportement. Cependant, l'adhérence, évaluée en tenant compte de la zone délaminée sous l'indentation, est significativement plus faible pour les nuances HSLA. À haute température, cette nuance s'est également révélée particulièrement sensible à la formation de cloques après les deux cycles thermiques. Il s'agit d'un résultat important en accord avec la tendance de ces nuances à former des cloques dans le laminoir.

Chapter 5: Numerical study of the indentation process to understand fracture and delamination of oxide

5.1 Introduction

The purpose of this chapter is to further investigate the mechanical behaviour of low carbon steel oxide during indentation. In order to have a better understanding of the experimental data, limited by the fact that we observe only the final state, numerical finite element (FE) simulations have been selected as an effective tool to simulate the micro-mechanical behaviour and failure of the oxide-steel system. This approach is commonly used in thin film studies, particularly in hard-coating on a soft substrate [168–174], to observe the stress field and correlate it with oxide fracture. Indeed, the analytical models describing the behaviour of thin films are not always suitable for oxide film indentation due to certain assumptions, such as a rigid substrate and oxide thickness [104,175].

In Chapter 4:, multi-fracture of oxide is observed during indentation, including delamination and normal cracks at the interface, as well as circular cracks from the surface (Figure 5.1). However, the chronology of fracture could not be accurately determined due to the absence of significant information in the load-displacement curves. The objective is to replicate the experimental results using a 2D axisymmetric model.

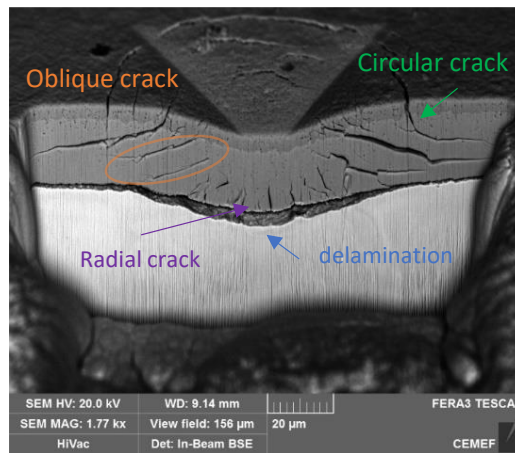


Figure 5.1: Multifracture of oxide for room temperature indentation on oxide ($t = 26 \mu\text{m}$, $p = 15 \mu\text{m}$, $p/t \sim 0.6$)

In the first stage, "crackless" indentations are performed to observe the stress field evolution during loading and to understand the competition between the delamination cracks of interest and spurious cracks that may interfere with the former. This allows identification of the area with the highest stress, where cracks are most likely to appear and propagate, which is necessary to prepare the second stage.

In the second stage, crack propagation is modelled in the areas where fracture may occur. Two approaches are implemented:

- Cohesive zone model (CZM) elements are used to simulate the delamination of oxide at the interface, for which the crack path is obvious.
- An XFEM methodology is employed to observe the propagation of circular and normal cracks. The main advantage of this approach over CZM is that the crack path is not predetermined.

Both methods are based on a Traction-Separation law, which considers the influence of three parameters: the stiffness of the elements, the fracture energy, and the critical stress. For all three fracture mechanisms (delamination, circular cracks, and normal cracks), the parameters of these laws are identified to evaluate the failure properties of the oxide and its interface.

This chapter begins with a numerical simulation of indentation of thin hard film on a soft substrate. Then, a description of the 2D model is done, which is developed after testing the influence of the indenter geometry using a 3D configuration and considering residual stresses. Then, the model is used to study in detail a specific indentation at room temperature (18N loading force on a 26 μm oxide thickness) and its multiple fracture behaviour, in order to evaluate the interface and the oxide properties at room temperature. The model is then applied to high temperature experiments (up to 800°C) to evaluate the fracture properties of oxide at high temperatures. These parameters will be available for future work on the simulation of the real descaling process.

5.2 A review of numerical simulations of indentation of thin & hard films

5.2.1 Cohesive zone model (CZM) for thin film

5.2.1.1 Description of CZM

Cohesive zone models are used in fracture mechanics to model crack propagation on the basis of a Traction-Separation (T-S) law at the crack tip (Figure 5.2). Cohesive elements are utilised to mitigate stress singularities in linear elastic fracture mechanics and to approximate nonlinear material separation phenomena [176]. The first uses of these kinds of elements date back to the 1960s, with the consideration of nonlinear evolutions located at the front of a pre-existent crack by Dugdale [177] and Barenblatt [178].

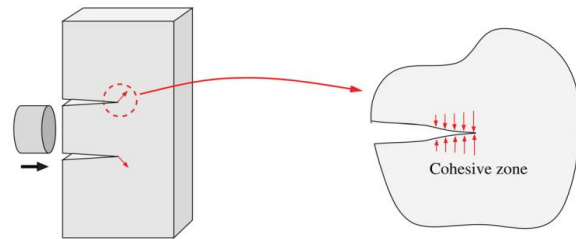
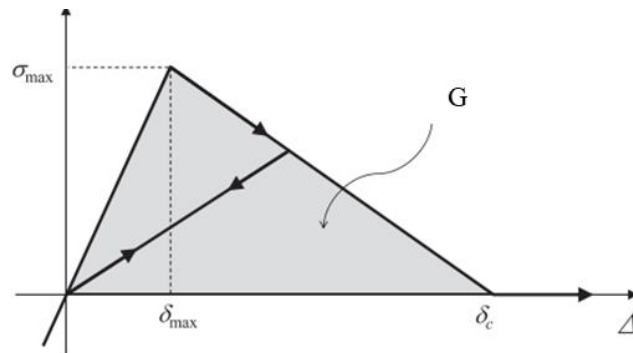
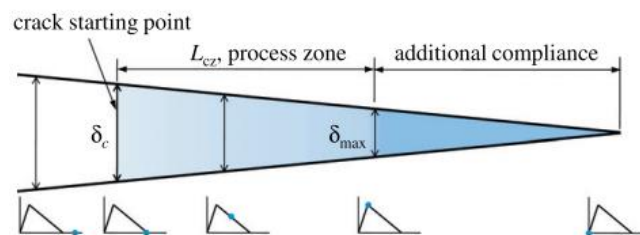


Figure 5.2: Schematic representation of cohesive zone model [176]

CZM describes the cohesive forces which exist between two elements, from the initial state to the final degradation. Indeed, in the presence of a force (normal or shear), the stress in cohesive elements increases until a maximum is reached (σ_{\max} reached for a displacement of δ_{\max}), and then subsequently reduces to zero by damage and fracture of the interfacial bonds, which results in complete separation and crack initiation (for a separation δ_c) (Figure 5.3). The variation in traction in relation to displacement is plotted on a curve and is called the traction-displacement curve (Figure 5.3). The work needed to create a new surface corresponds to the fracture energy, area under the T-S curve.



(a)



(b)

Figure 5.3: (a) Typical traction-separation law evolution of degradation of CZM elements (extracted from Abaqus documentation) (b) evolution of a crack-opening profile along the interface [179]

A bilinear cohesive model has been already developed using the commercial finite element software, ABAQUS®. It allows progressive damage and failure in a cohesive layer whose response is defined in terms of Traction-Separation law (T-S law). These models are based on three steps directly observable on T-S law:

- elastic behaviour of cohesive elements
- initiation of degradation of elements
- damage of elements until the total destruction

The first slope is defined as the stiffness of CZM elements, the reaction of elements is considered as elastic. The stiffness parameter K are the modulus of the cohesive element material (E , G) material divided by its thickness.

In the presence of a normal force, the cohesive element undergoes a normal displacement δ_n , and a normal traction develops $t_n = K \cdot \delta_n$ with K the stiffness previously described. This traction increases until reaching a criterion t_n^{\max} . Once the initiation damage criterion is reached (for a displacement $\delta_n = \delta_n^{\max}$) (top point in Figure 5.3), the damage evolution law describes the rate at which cohesive elements are degraded. Damage evolution can be defined based on the energy that is dissipated as a result of the damage process, also called the fracture energy. By considering the cohesive traction t_n^{\max} and the work of rupture G_I , the displacement δ_n^c at full rupture of the cohesive elements δ_n^c is defined by $G_I = 1/2 t_n^{\max} \delta_n^c$. The damage variable D which increases as the maximum interfacial displacement δ_n increases from δ_n^{\max} to δ_n^c . It varies from 0 (undamaged) to 1 (cohesive elements are destroyed, and crack is propagated, at the displacement δ_c in Figure 5.3). The fracture energy is equal to the area under the traction-separation curve Figure 5.3). The corresponding t_n is thus reduced by the relation $t_n = (1-D) \bar{t}_n$, where \bar{t}_n is the stress components predicted by the elastic traction-separation behaviour for the current stress without damage.

A similar model is applied for shearing mode, with work of adhesion G_{II} and cohesive traction t_t^{\max} . The CZM degradation can be activated as soon as one of two criteria t^{\max} is reached. The total work of rupture G , which is the sum of G_I and G_{II} is assumed to be independent of the mode mixity (i.e. the dissipated energy associated with full crack opening always takes the value Gc that we prescribe, irrespective of the particular way this opening is performed).

In the definition of CZM parameters, there are two possible approaches to indicate the T-S law, either by defining the area under the curve (fracture energy), or by defining the specific length of the CZM separation. Both of them are linked through the previous formulae.

5.2.1.2 Examples of application of CZM to indentation of thin films

Thus, CZM provides an effective methodology to study and simulate fracture in solids, at the interface between two materials and within a material. For the study of thin films, CZM can be used in different configurations:

- cohesive interface layer between perfect coating and substrate. For interfacial fracture, the cohesive model describes the interfacial adhesion and the interfacial toughness between the two materials. In this case, the main advantage is that the crack front is localised at the interface. For example, Abdul-Baqi and Van der Giessen studied the delamination of a strong film from a ductile substrate during indentation [172]. The interface is modelled by means of a cohesive element with normal and tangential failure modes. The simulations show that the delamination is caused in mode II, driven by the shear stress at the interface outside the contact region during the loading stage. These interfacial cohesive elements have also been used for the study of diamond-like-carbon coating with a low adhesion by Xiao et al. [168], confirming the delamination by shear at the interface. In the Figure 5.4 (a), two areas of delamination are observed :

- cracks on coating with a perfectly bonded layer. The traction-displacement curve gives the constitutive behaviour of the fracture. In the case of fracture within a material, the T-S law is referring to the fracture toughness of a brittle material. In this configuration, the crack path has to be pre-localised by cohesive elements. This methodology has also been used by the same authors mentioned previously.

Xiao et al. [168] used a cohesive zone model (CZM) for inserting the cracks in the brittle coatings on ductile substrate to investigate the fracture behaviour of thin films. Cracks nucleate at pre-specified locations and propagate along predefined paths. In the presence of high tensile radial stresses, fracture is observed within the film with the increase of loading (the cracks are initiated from the surface and at the interface) (Figure 5.4 (b)). This methodology have also been used by Abdul-Baqi and Van der Giessen [173].

- cracks on coating with weak adhesion layer. Indeed, the coating cracking is often linked to interfacial delamination under indentation, especially in a weakly bonded thin hard coating-substrate system. Thus, Xiao et al. combine cohesive elements at the interface and within the thin film to analyse the correlation between film cracking and interfacial delamination [168]. In the Figure 5.4 (c), in the presence of a brittle film with a weak adhesion, both the delamination and cracking is noted. The authors demonstrate that with an increase of the film strength, the generation of crack and the propagation is reduced, but it hastens the interfacial delamination.

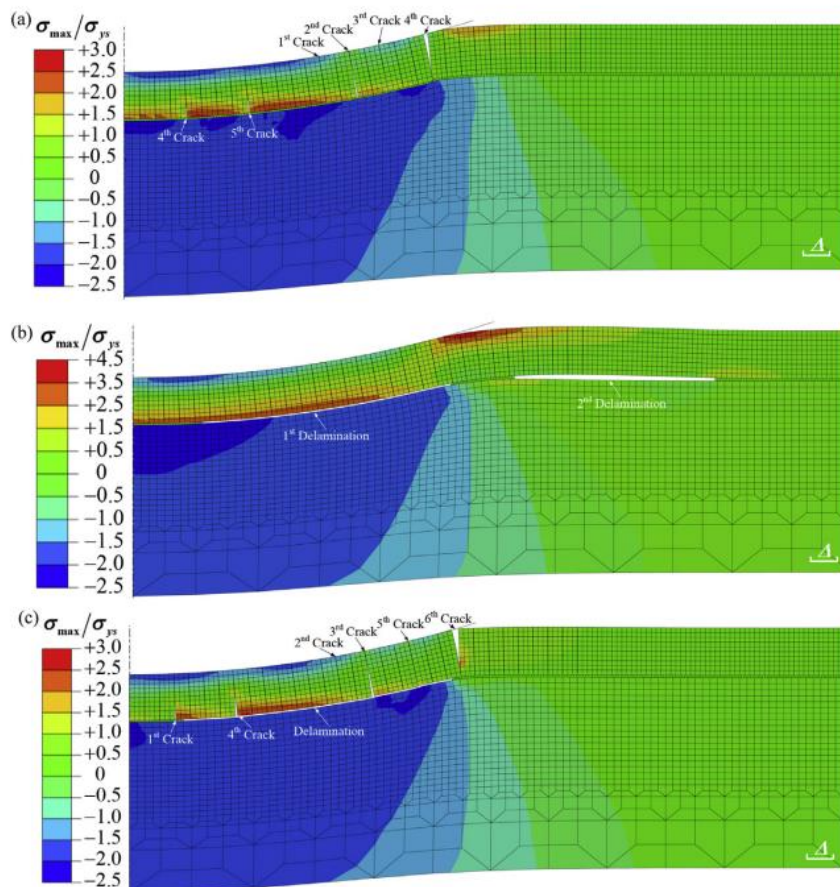


Figure 5.4: Evolution of the failure behaviour of a hard coating on a ductile substrate in case of (a) brittle coating and perfectly bonded layer (b) perfect coating and weakly bonded later (c) brittle coating and weakly bonded layer [168]

5.2.2 eXtended-Finite Element Method (XFEM) models to evaluate cracking

The XFEM is introduced to overcome the problems that can be found with the presence of singularities, such as cracks. It is customary to remesh at these points to improve convergence, but these operations are costly. XFEM avoids mesh manipulations by adding special functions to the finite element approximation using the framework of partition of unity, which was developed by Melenk and Babuška [180].

In fracture mechanics, the displacement field is discontinuous across a crack. The modelling by XFEM of the crack propagation is made by Moës et al. including two types of enrichment [181]:

- an enrichment for the crack front using functions characterising the asymptotic behaviour of the displacement field near the crack front
- an enrichment for the interior of the crack using a function with a value 1.0 above the crack and -1.0 below the crack.

The fact that a node is enriched or not and the type of enrichment depends on the relative position of its support with respect to the crack (Figure 5.5). For the determination of the stiffness matrix of an element cut by the crack, it is necessary to integrate separately on both sides of the crack.

For further details, XFEM has been described e.g. in [181].

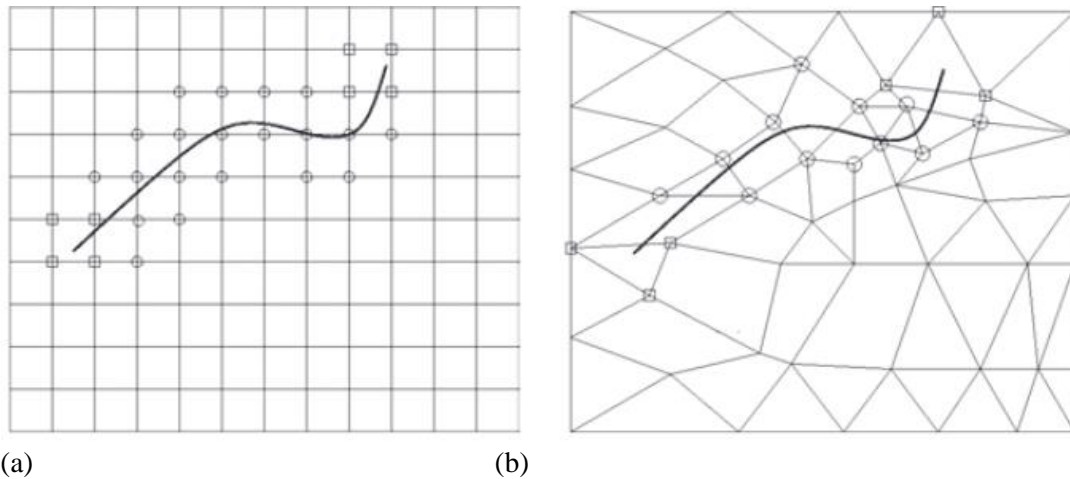


Figure 5.5: Crack on a uniform mesh (a) and on a non-uniform mesh (b). The circled nodes are enriched by the jump function whereas the squared nodes are enriched by the crack tip functions [181]

The main advantage of the XFEM is to consider cohesive failure, allowing the evaluation of both nucleation and propagation of cracks independently of mesh distribution or refinements. Thus, it overcomes the limitations of methods which require pre-inserting cracks, such as CZM described in the previous part. Due to the particular displacement functions that are applied to analyse discontinuous characteristics at crack tips, the propagation is free. An initiation site can be implemented to initiate the location of the crack.

Similarly to the CZM, the XFEM technique is based on the traction-separation constitutive behaviour (described in 5.2.1.1). The similarities extend to the linear elastic traction-separation model, damage initiation criteria, and damage evolution laws.

In Abaqus®, the traction-separation model initially assumes linear elastic behaviour. The elastic behaviour is written in terms of an elastic constitutive matrix that relates the normal and shear stresses to the normal and shear separations of a cracked element. The elastic properties for an enriched element are dependent on the elastic properties of the material in which the crack can propagate.

The evolution of film cracks is simulated using a cohesive relationship, and the maximum principal stress criterion (Maxps) is used as the criterion for crack initiation:

$$f = \left\{ \frac{\langle \sigma_{max} \rangle}{\sigma_{max}^0} \right\} = 1 \quad (5-1)$$

where σ_{max}^0 represents the maximum principal stress (ultimate tensile strength of the oxide). The symbol $\langle . \rangle$ represents the Macaulay bracket, $\langle \sigma_{max} \rangle = 0$ if $\sigma_{max} < 0$ and $\langle \sigma_{max} \rangle = \sigma_{max}$ if $\sigma_{max} \geq 0$. The Macaulay brackets are used to signify that a purely compressive stress state does not initiate damage. Damage is assumed to initiate when the maximum principal stress ratio (as defined in the expression above) reaches a value of one.

An additional crack is introduced or the crack length of an existing crack is extended after an equilibrium increment when the fracture criterion, f , reaches the value 1 within a given tolerance:

$$1 \leq f \leq 1 + f_{tol} \quad (5-2)$$

If $f > 1 + f_{tol}$, the time increment is cut back such that the crack initiation criterion is satisfied.

The tolerance f_{tol} is set to 0.2. When the maximum principal stress is specified, the newly introduced crack is always orthogonal to the maximum principal stress direction when the fracture criterion is satisfied. Ahead of the crack tip, the stress field evaluation has to be accurate to predict the correct crack propagation direction ; thus, a fine enough mesh is needed.

Then, the crack propagates according to a damage evolution criterion based on energy release rate. The fracture energy release rate G (area underneath the traction–separation curve) is calculated according to the Griffith–Irwin relationship :

$$G = \frac{K^2}{E} \quad (5-3)$$

with K the toughness and E the Young's Modulus. This value can be extracted directly from the literature, and depends on the ability of the material to resist crack propagation.

Using Abaqus®, the linear damage evolution is the same as described previously for the interfacial delamination. The damage evolution describes the rate at which the cohesive stiffness is degraded once the corresponding initiation criterion is reached. The same scalar damage variable, D , represents the averaged overall damage at the intersection between the crack surfaces and the edges of cracked elements. It initially has a value of 0, and evolves from 0 to 1 upon further loading after the initiation of damage. Phantom nodes, which are superposed on the original real nodes, are introduced to represent the discontinuity of the cracked elements. When the element is intact, each phantom node is completely constrained to be superimposed to its corresponding real node. When the element is cut through by a crack, the cracked element splits into two parts.

Rusinowicz et al. perform a complete study to evaluate the properties of a brittle layer (silicon nitride Si_3N_4) on a metallic alloy [171]. Their study proposes a complete methodology to reproduce with XFEM the cracking behaviour observed experimentally. The comparison with the large pop-in event, on the experimental and the simulation curves, makes it possible to determine the right parameters for the brittle layer strength and localization of the crack (Figure 5.6). The crack paths of both the conical crack nucleating at the interface and the circular crack generated from the surface are simulated.

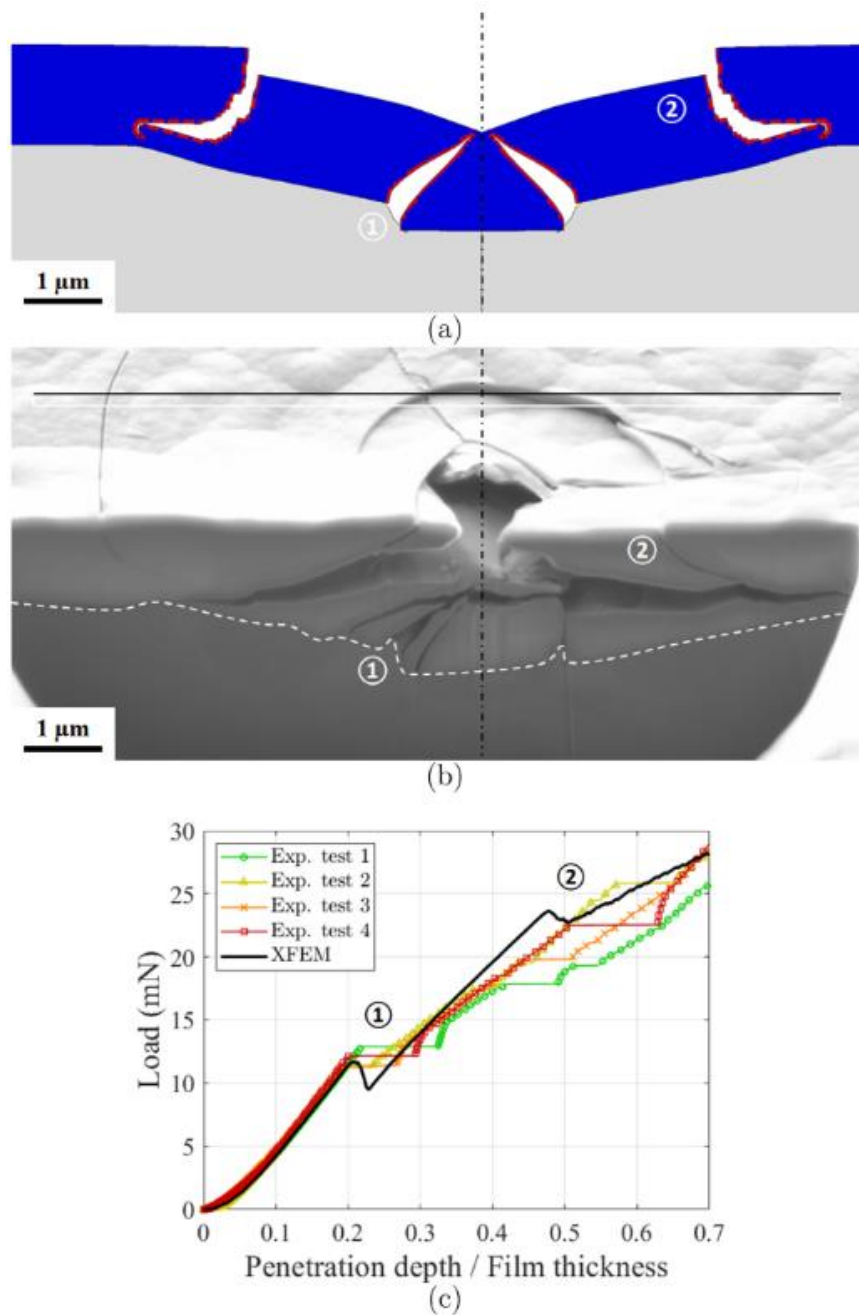


Figure 5.6: Comparison of fracture mechanism during the indentation of a Si_3N_4 coating between the (a) numerical model using XFEM (b) the corresponding experiment (c) the Load-displacement curves of the experimental work and numerical model are fitted to determine the right set of parameters [171]

The combination of XFEM within the film and CZM at the interface to model indentation of thin film has been widely done. For example, Fukumasu et al. [174] combined the XFEM with CZM techniques to reproduce the failure behaviour of film cracking and interfacial delamination successfully.

According to Shu et al. [170], the interfacial delamination hastened the cracking at the bottom surface of the film because of the enhancement of the film stretching. However, at the location outside the contact area, the cracking on the top surface of the film was postponed by the interfacial delamination due to the reduction in the film bending.

As a conclusion for this part, both types of failure observed during indentation of a brittle film on a ductile substrate can be numerically modelled. The correct prediction of the location of failure during the test allows determining the corresponding material strength and toughness. The adhesive failure at the interface is mostly investigated using the CZM and the cohesive failure within the film is made with XFEM. In Abaqus®, both of them may be based on the same traction-separation law. Orders of magnitude of the parameters of the T-S law for hard coating on ductile soft substrate, as found by different authors for different coating/substrate systems, are summarised in Table 5-1.

Table 5-1: Values of thin film and interfacial toughness and strength from literature

Description of the film	Adhesive strength (MPa)	Adhesive toughness or Energy release rate for cohesive failure (G_c) (J/m^2)	Fracture strength (GPa)	Fracture toughness Energy release rate for cohesive failure (G_c) (J/m^2)	Ref.
	Interface		Thin film		
General film 0.25 to 4 μm	-	25-250	-	50-250	Fukumasu et al. [174]
Diamond-like carbon (DLC) coating on a steel substrate (0.5 to 10 μm)	200	8	2	30	Xiao et al. [168]
Silicon nitride on a ductile metallic alloy (AlSiCu) ($t=1.3\mu m$)	100-500	0.01-10	2.5	1	Rusinowicz et al. [171]
Thin hard films on ductile substrate	100-600	2-20	4.5-7.5	30	Shu et al. [170]

5.3 Simulation of indentation with a continuum approach

As described in the previous part, the finite element simulation is useful to understand the fracture mechanisms observed during indentation of thin films, and to evaluate properties of thin films. This dual approach was widely used on thin films.

In our case, the indentation tests on oxide indicate that multiple cracking occurs: delamination, circular cracks, normal crack and corner cracks.

This first part is dedicated to the implementation of a simple model on Abaqus® software to reproduce an experimental indentation at room temperature, which has been well documented in terms of fracture thanks to FIB cutting. The stress field is analysed and related with fracture of oxide.

In order to simplify the experimental model, some hypotheses are made: axisymmetric configuration, single phase (Fe_{1-x}O) oxide with no residual stresses, boundary conditions ... Except for the single phase oxide, their validity is checked, below and in appendices.

5.3.1 Description of the model

5.3.1.1 Boundary conditions

Here, axi-symmetry is used to reduce calculation time. In Appendix D, a comparison with 3D simulations justifies this assumption.

Indenter angle is therefore 70.3° (Vickers equivalent). A computation volume of $250\ \mu\text{m}$ (radius) \times $100\ \mu\text{m}$ (thickness) was found sufficient to avoid edge effects. To reproduce the experimental tests presented in Figure 5.1, the bimaterial is composed of two parts, the oxide and the steel. The oxide thickness is equal to $26\ \mu\text{m}$. To simplify, oxide is considered as a single homogeneous phase, whereas in reality, it may consist of 2 or 3 sublayers, moreover sometimes porous and fractured; such complexity is left for future studies. For indentation test, to limit the edge effect, the thickness of the sample must be 10 times larger than the maximum indentation depth, and the width must be 3 times larger than the maximum contact dimension (diagonal for Vickers tips). Both of them are respected and the convergence of the results has been checked with respect to both computation domain dimensions and mesh size.

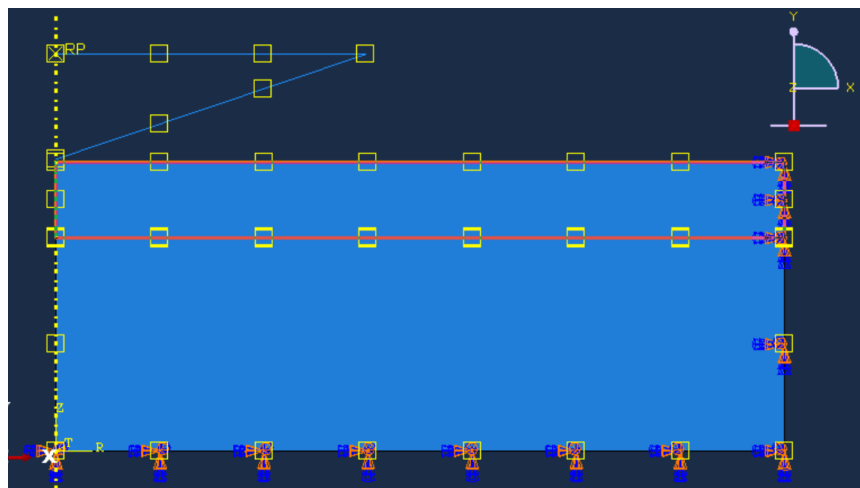


Figure 5.7: Model of the $26\ \mu\text{m}$ thickness oxide indented

A reference node is localised at the top of the indenter; a displacement of $15\ \mu\text{m}$ is applied in the negative z direction with an indentation rate of $3\ \mu\text{m/s}$. It is important to simulate both the loading and the unloading of the indentation process, considering the potential fracture of oxide (and delamination) during the unloading. At maximal load, $p/t=15/26 \sim 0.6$, resulting in a 18N load), the contact radius is $37\ \mu\text{m}$.

The indenter is considered as a rigid body for simplicity due to its high hardness and modulus. The contact behaviour between indenter and the surface of the oxide is divided into two parts: normal and tangential behaviours. The normal behaviour applied to the model is “hard” contact. For tangential behaviour, a penalty-type contact algorithm is carried out, that place imaginary springs between the “master” surface and the “slave” surface. The coefficient of friction for contact between the indenter and coating is specified as 0.1. Fixed-boundary conditions are applied to the substrate bottom and the right side of the whole sample (Figure 5.7). The same mesh density is used in oxide and steel (0.5 μm), and 4-nodes bilinear axisymmetric quadrilateral elements with reduced integration are selected.

5.3.1.2 Material law

Oxide and steel are given an elasto-visco-plastic behaviour in view of simulation at both room and elevated temperature. Values at room temperature are detailed here. The Young’s moduli of the oxide and the steel at room temperature are respectively 240 GPa and 210 GPa [63], both Poisson’s coefficients are 0.3. The visco-plastic part follows a Hollomon-type model where K is the consistency, the strain hardening exponent is n and the strain rate sensitivity coefficient is m :

$$\sigma = K \cdot \varepsilon^n \cdot \dot{\varepsilon}^m \quad (5-4)$$

For steel, K value is directly calculated using Tabor’s formula [182], considering that flow stress is equal to Vickers Hardness divided by three for a representative strain of 0.08. As the ratio of hardness between oxide and steel at room temperature has been measured in Chapter 3 as 3.4 ($H_{V_{\text{steel}}} = 1.9 \text{ GPa}$, $H_{V_{\text{oxide}}} = 6.5 \text{ GPa}$), the assumption is made that $K_{\text{oxide}} = 3 K_{\text{steel}}$.

The choice of the coefficients n and m is more difficult, as hardness testing does not give these parameters so easily. It is very hard to perform e.g. tension tests on pure oxide; extracting the oxide behaviour from measurements on oxidized samples is furthermore limited by the fact that oxide represents a small fraction and its properties consequently have a small contribution to the global behaviour.

Here, we choose $m = 0.01$ since at room temperature, strain rate sensitivity is not expected to be significant, neither for steel nor for oxide. For the strain hardening coefficient, $n = 0.15$ for both oxide and steel appears reasonable for an IF steel in the hot rolled state and, following Picqué [19], it is hard to measure a difference between the steel and its oxide.

5.3.1.3 Results of the continuum simulation

Figure 5.8 shows the loading curve obtained for the indentation of the oxidized sample (26 μm).

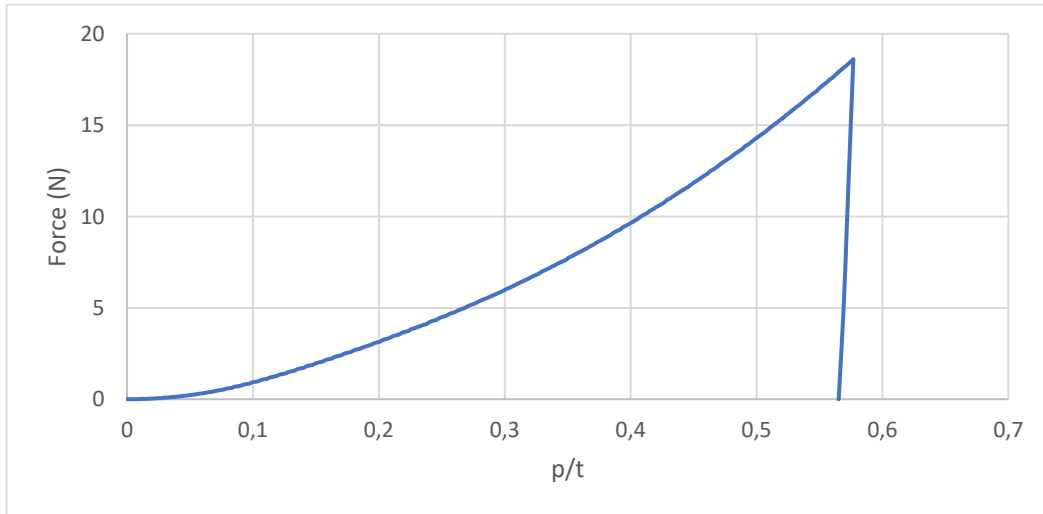


Figure 5.8 : Load-displacement curve for a 26 μm thick oxide

Radial stress σ_{11} : for the circular cracks in surface and the normal cracks at the interface

Figure 5.9 shows the evolution of σ_{11} at four indentation depths, along both surface and interface, but on the oxide layer side.

- First, at the interface (Figure 5.9 (b)), for a low penetration ($p/t \leq 0.2$), a zone with radial tension is found below the indenter, reaching 400 MPa, extending to 20 μm from the axis. It is connected with the cracks normal to the interface found in experiments. These cracks are not reaching the surface due to the compression area at the tip apex visible in Figure 5.9 (a). Further on, this tensile zone extends outward, up to 30 μm at maximum penetration, for which contact radius is 37 μm ; the tension decreases at the same time (~ 200 MPa) for larger penetration, $p/t = 0.3$ and 0.4 . Under the edge of the contact and beyond, a compressive state is observed .

- on oxide surface, Figure 5.9 (a), for a low penetration (yellow curve for a ratio $p/t=0.1$), σ_{11} is highly compressive directly under the indenter. Elsewhere, stress is quite low. Increasing the penetration throughout the loading process, the compression values are decreasing because of the substrate influence. Note that the maximum compression is shifted to higher and higher radius. Outside the indentation area for $p/t > 0.3$, a σ_{11} tensile stress area appears, following the edge of the indentation as penetration depth increases; it finally reaches 1700 MPa. At room temperature, we observed circular cracks in this zone; tensile σ_{11} explains the initiation of such circular cracks. We have observed experimentally that circular cracks are not propagated until the interface: from a certain stage of oxide bending, a compression area is present at the interface on the σ_{11} map (Figure 5.9), below the edge of indentation. This bending field (surface in tension and compression at the interface, Figure 5.9c) channels crack outward more and more, quasi-horizontally. By considering that the cracks are initiated at the edge of the contact area, the first crack being localised at a distance 25 μm , the σ_{11} stress value in this area is about 500 MPa, meaning that the critical stress can be in the first instance estimated to 500 MPa. The outermost cracks (distance of 30 and 45 μm) may be initiated when this critical stress is reached later on at their own position.

σ_{11} can thus explain the external circular cracks and normal cracks, from the initiation to the propagation. In the light of these results, we can identify that normal cracks appear before circular cracks.

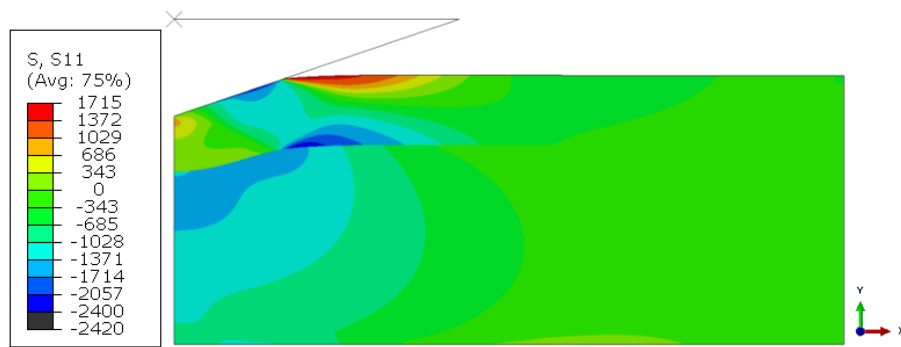
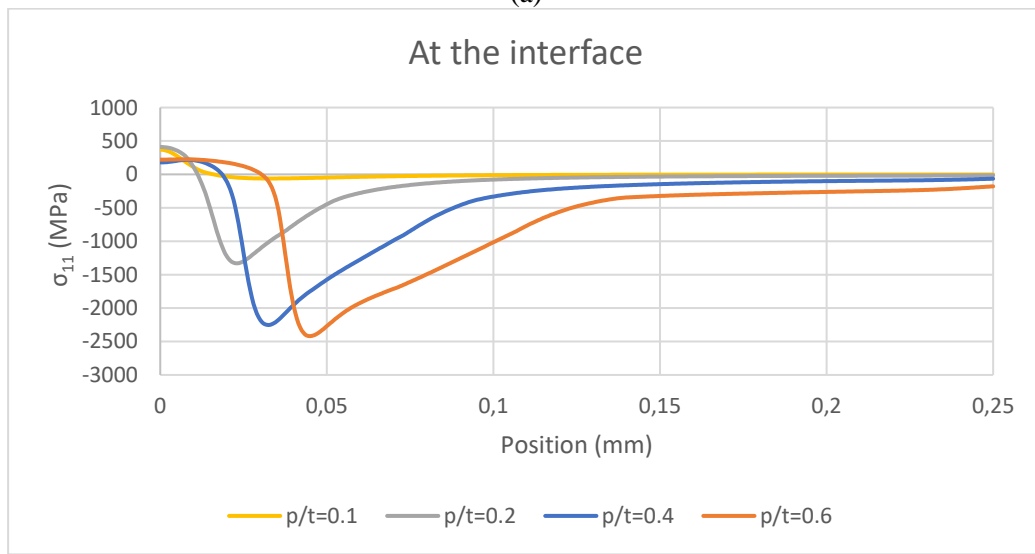
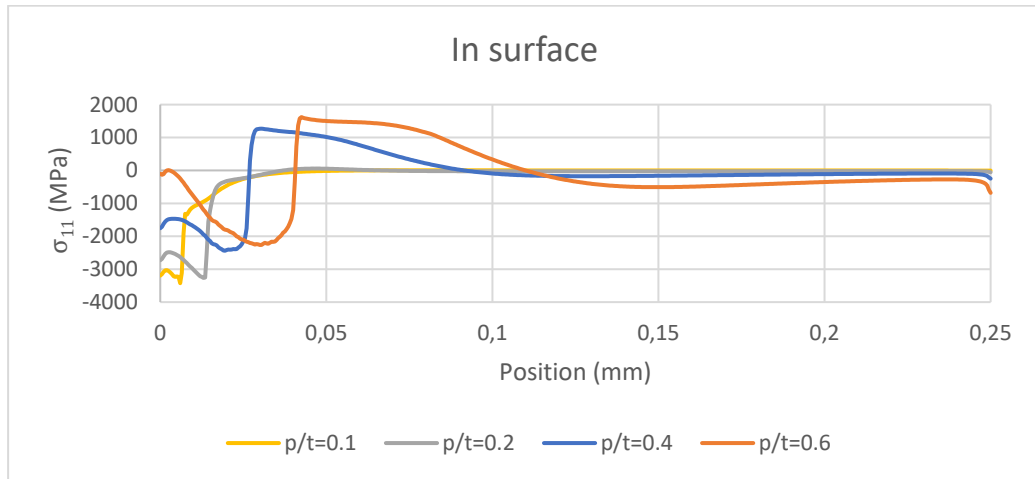
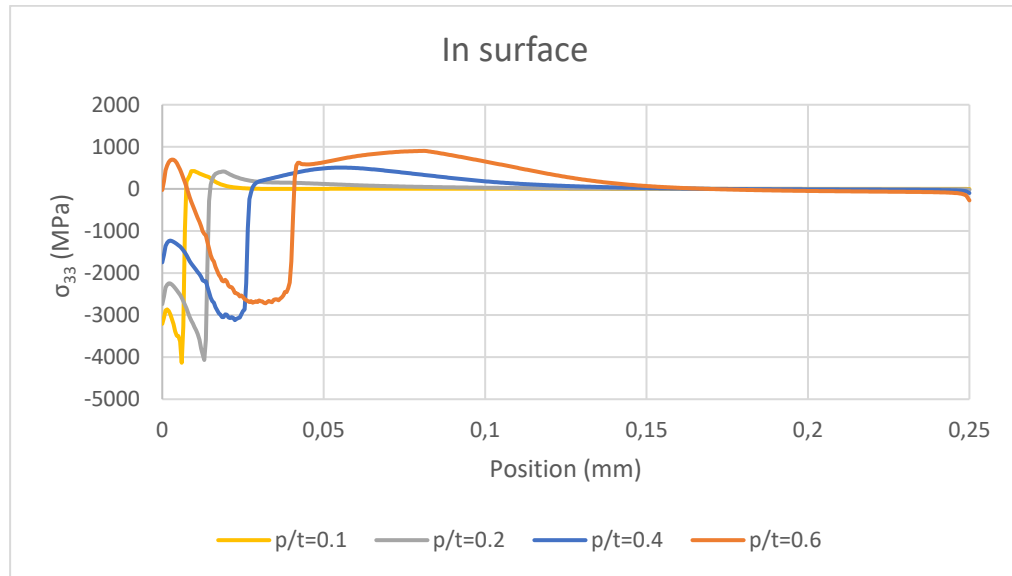


Figure 5.9: Evolution of the σ_{11} component for different penetrations of the indenter (a) at the surface (b) at the interface (c) Stress map at the end of loading of Vickers indentation (18 N) of an oxidized steel sample (thickness of oxide: 26 μm). Indentation depth 15 μm ($p/t = 0.6$).

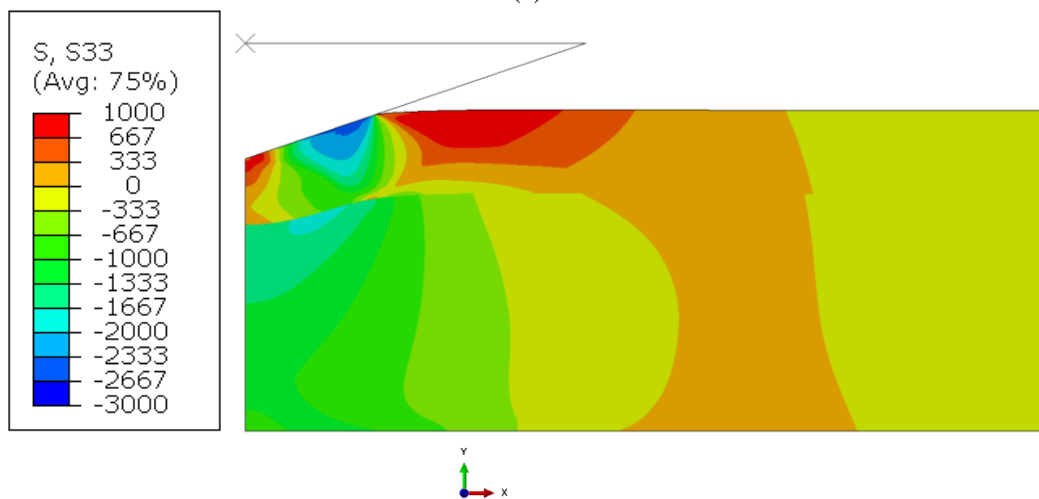
Circumferential stress σ_{33} : for the corner cracks

Similarly, σ_{33} (circumferential: Figure 5.10) is also in compression below the contact. However, there is, all along the loading, a tensile area near the contact zone. The stress values are lower than the radial component but nevertheless reach 1 Gpa.

Experimentally, with this configuration, no corner cracks are observed, meaning that this circumferential component is not high enough to generate cracks. We can imagine that by increasing the ratio p/t , these corner cracks would be generated by σ_{33} , as we observed in several cases at larger p/t . Moreover, this circumferential stress is in tension within the whole thickness of oxide (Figure 5.10(b)), which explains that corner cracks, when they form, are reaching the interface (Figure 5.1).



(a)



(b)

Figure 5.10: Evolution of the σ_{33} (circumferential) component for different penetrations of the tip (a) at the surface (c) Stress map at the end of loading (18 N) of an oxidized steel sample (thickness of oxide: 26 μm). Indentation depth 15 μm ($p/t = 0.6$).

Normal σ_{22} and shearing σ_{12} stress for the delamination

At the interface, no matter the p/t ratio, values of normal σ_{22} stress component are largely compressive (Figure 5.11 (a)). Thus, this normal component cannot be held responsible for the delamination observed experimentally. Note that for large penetration of the indenter, a small tensile area is localised away from the contact, the maximal values are equal to 100 MPa (blue and orange curves in the Figure 5.11 (a)). Note that Xiao [1] found a delamination at this position for his weak interface case.

However, the shearing σ_{12} component is increasing with the penetration and localised just below indentation contact edge $r = a$ (at the end of indentation, $a = 37 \mu\text{m}$) (Figure 5.11 (b)). This shear stress is caused by the outward radial plastic flow of the substrate under the indenter relative to the coating. It reaches the interface with a high value, the maximum being a few μm closer to the axis, $r = 36 \mu\text{m}$. This point stress moves as the indentation edge and scans the interface outwards. It is seen that delamination is likely to initiate where this component is maximal, and delamination behaviour remains in mode II, as reported in the literature [168,172]

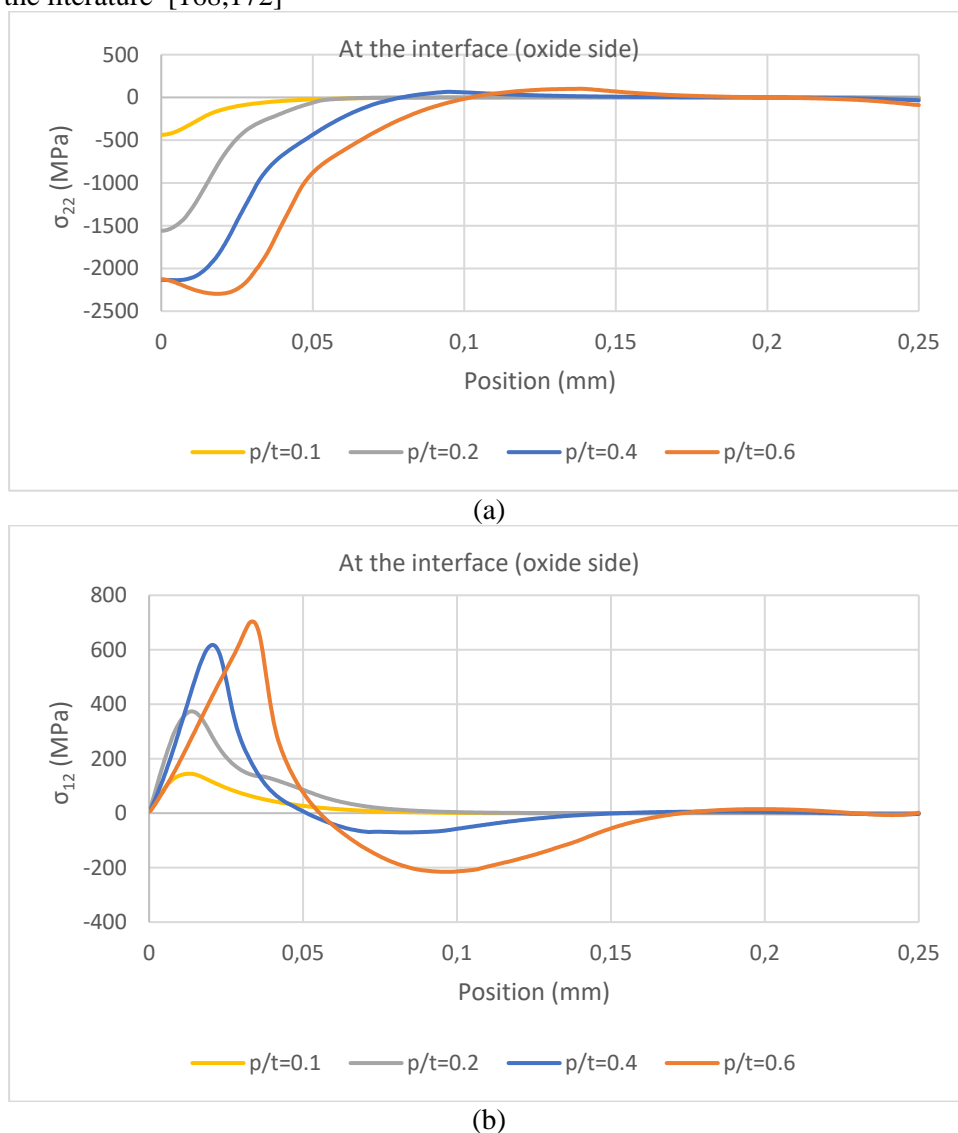


Figure 5.11: Profiles at the interface of the (a) σ_{22} and (b) σ_{12} components for different tip penetrations

The Figure 5.12 shows the stress map at the end of loading ($p/t = 0.6$) for the shearing σ_{12} and normal σ_{22} .

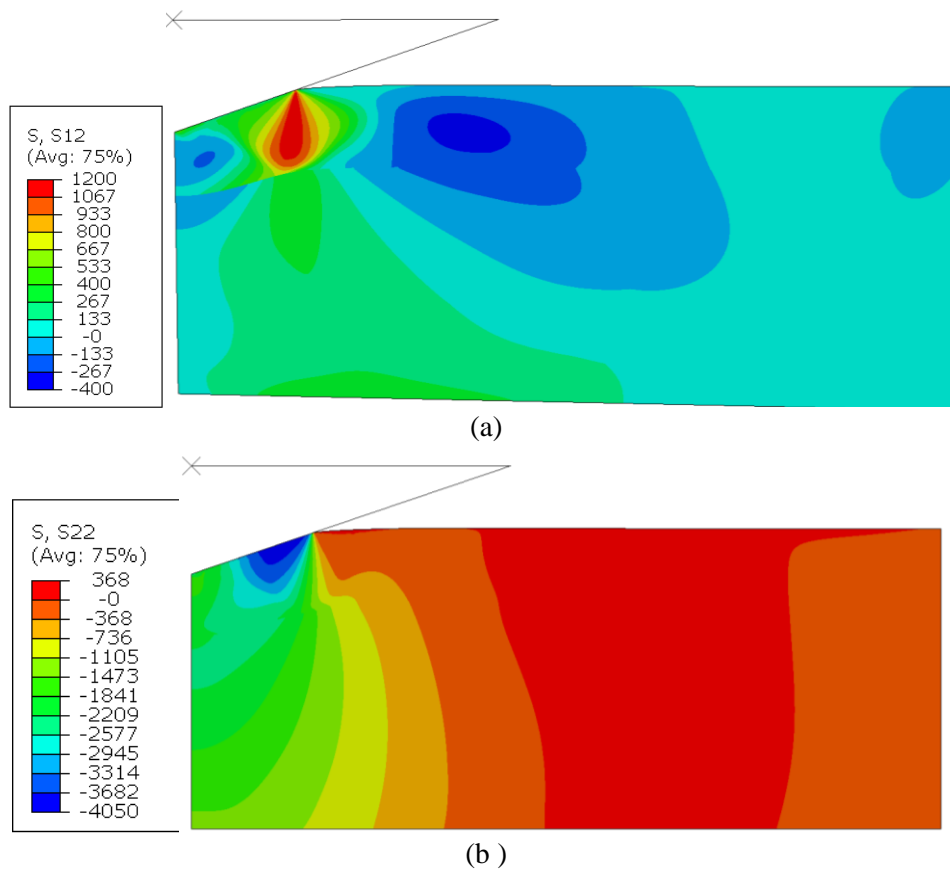


Figure 5.12.: Maps of (a) σ_{22} and (b) σ_{12} at the end of loading (18 N) of an oxidized steel sample (thickness of oxide: $26 \mu\text{m}$).

Note that transitional cracks, between the normal crack and the circular crack, propagate obliquely ($\sim 45^\circ$). Their initiation is at the boundary of the indentation compressive (plastic indentation) area in the direction of the interface. The local observation of the maximum of the principal stress values indicates a presence of a tensile stress (above 300 MPa) for $p/t=0.2$. This tensile stress area extends from the area of the interfacial tensile stress (responsible for the normal cracks at the interface) to the area of the surface tensile stresses (at the origin of the circular cracks). The orientation of the stress is at 45° , which means a possible opening of the crack observed experimentally. It is composed of a mixed mode of the σ_{11} , σ_{22} and σ_{33} , it is thus complicated to evaluate the critical stresses for the initiation of this crack.

During unloading, we have found no stress component evolution suggesting further crack initiation or propagation.

As a conclusion, the main fracture mechanisms have been understood, the critical stress has been estimated to be less than 500 MPa for the normal cracks at the interface and for the circular cracks. It is however complicated to estimate the delamination, because there is no indication of when it appears. The next part will refine the stress values by using specific numerical tools the stress values.

5.3.2 Influence of the residual/internal stresses during indentation

In section 3.5, internal stresses within the oxide have been detailed. At room temperature, compressive internal stresses (~ -150 MPa) are present mainly due to thermal stresses (differential dilatation) during cooling. At high temperature, the internal stresses are relaxed by the oxide and metal viscoplasticity.

The influence of residual stresses during mechanical tests has been described, and particularly during indentations tests. For example, Suresh and Giannakopoulos [108] report that hardness tends to decrease under tensile surface stress and increases under compressive surface stress. Indeed, in the presence of compressive stresses, during the loading the P-h curves are modified by the increase of the contact area. By considering a strain-hardening behaviour in the presence of a residual plastic strain, they have developed a methodology to evaluate residual stresses, supposedly equi-biaxial, using instrumented sharp indentation. This model is then extended by Lee and Kwon [183] to non-equi-biaxial surface stresses. The authors also show that pure shear stress state have no influence during the indentation.

According to Xu and Li [111], the residual stresses influence also the unloading behaviour of nanoindentation. The ratio h_e/h_{max} , with h_e the elastic recovery and h_{max} the maximum indentation depth, evolves linearly with the residual stresses. Thus, this ratio which can be directly determined from the unloading curve of indentation, is a way to evaluate residual stresses.

The effect of thermal stresses in iron oxide have been studied by Noh et al. [68] using the Lee and Kwon method. The stresses are evaluated to 2.81 GPa (in compression) for an oxide thickness of 20 μm . They simulate the uncoiling process of low carbon steel by making bending tests. The thermal stresses generated during the cooling to room temperature magnifies the stresses at the interface.

The idea of this paragraph is to quantify the influence on the residual stresses on the cracking behaviour during the same Room Temperature indentation analysed above : formation of cracks within oxide and delamination at the interface:

- after an oxidation at 650°C/700°C and a cooling to room temperature, stress is between -100 and -200 MPa within Wüstite. In order to reproduce these stresses, before the indentation, an initial bi-axial compression state (σ_{11} and $\sigma_{33}=-150$ MPa) is introduced (no shearing component and $\sigma_{22}=0$) within oxide).

- The same simulations have been reproduced with an equi-biaxial stress of -1400 MPa, i.e. of the order of magnitude of the internal stresses investigated in the cited articles.

5.3.2.1 Low residual stresses: -150 MPa

In the first time-step of the simulation the initial compressive stresses in the oxide decrease to -130 MPa (for σ_{11} and σ_{33}); in the substrate, the stress is still close to zero (Figure 5.13 (a))

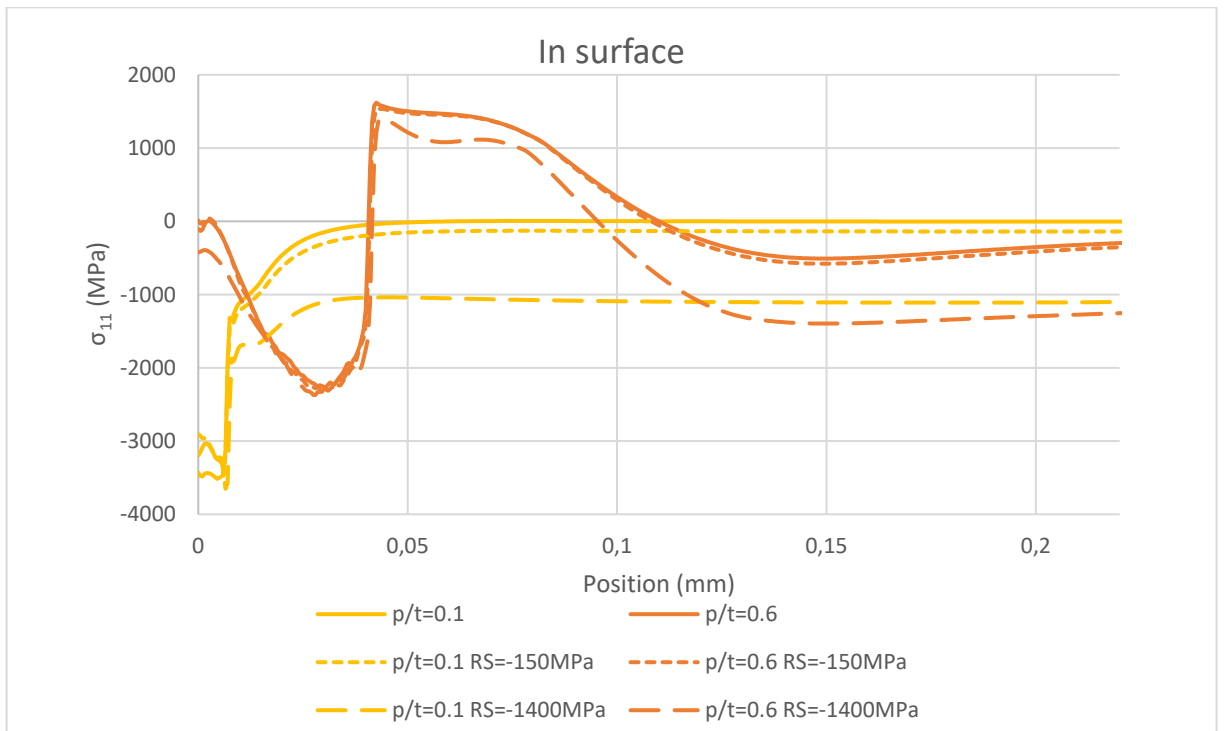
For different moments of the indentation, the comparison of stresses is made with / without residual stresses (Figure 5.13 (b)).

The σ_{11} component (source of the circular cracking in surface) shows that in the area below the indentation, the compressive stresses are somewhat higher when the residual stresses are considered : -100 MPa over the outmost half of the contact, although stress is less compressive very close to the axis, by +100 to +150 MPa. Far from the indentation area, for the first instant of the penetration, -130 MPa is observed. By increasing the penetration depth, the difference is decreasing (less than -100 MPa), by plastic deformation induced by the indentation (the equivalent plastic strain is increasing). The conclusion is that there is no incidence for the circular cracks generated at the surface, at this level of internal stress.

At the interface, the shearing component σ_{12} remains unimpacted (maximum difference 10-20 Mpa) all along the indentation (Figure 5.14). As a reminder, no shearing component is added in the simulations. As a conclusion, an initial compressive stress of -150 MPa or less within the oxide before indentation does not modify the shearing stress field. Thus, the residual stresses measured in chapter 3 have no influence on the delamination (considering that the delamination is caused by the shearing component).



(a)



(b)

Figure 5.13: (a) Redistribution of the σ_{11} stress after the introduction of -150 MPa residual stresses. (b) Evolution of the σ_{11} component during the indentation in surface. 2 steps of the loading are plotted. The dashed curves represent the case in which a bi-axial compressive stress of -150 and -1400 MPa are added.

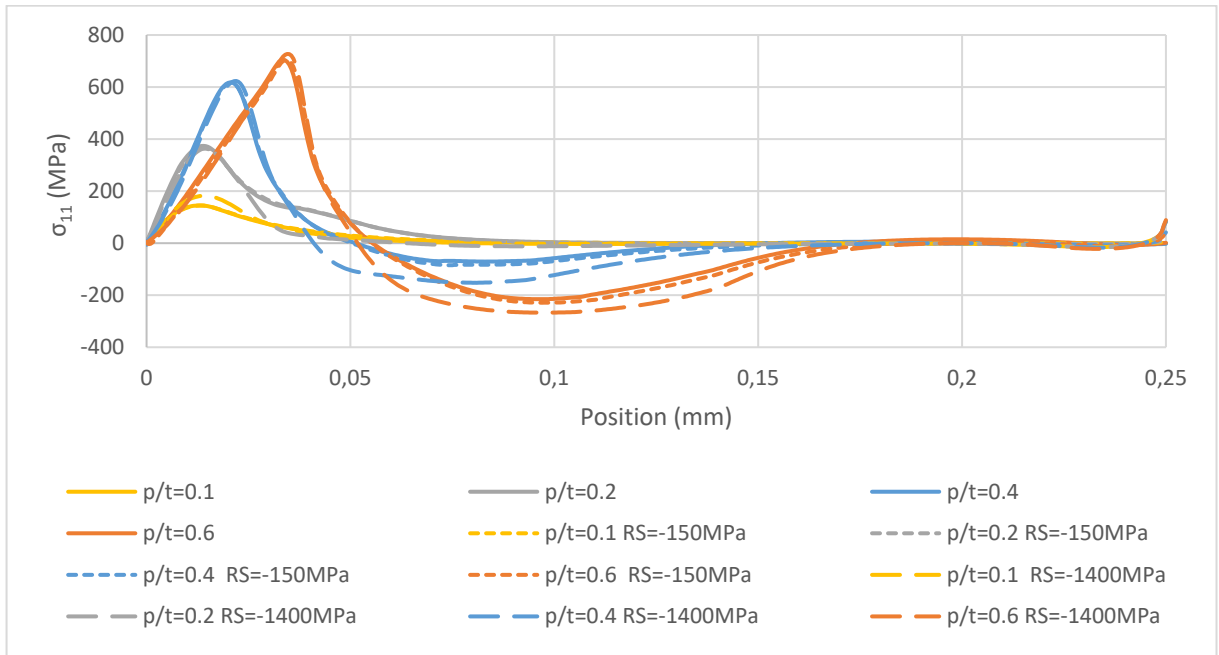


Figure 5.14 : Interfacial profile of the shear stress during the indentation. 4 steps of the loading are plotted. The dashed curves represent the case in which a bi-axial compressive stress of -150 and -1400 MPa are added.

5.3.2.2 Larger residual stresses (-1400 MPa)

A larger residual stress is introduced in the oxide layer (-1400 MPa), that is, much larger than the real state of the oxide at room temperature. The compressive stresses are initially released to -1100 MPa within oxide at the first instant of the simulation. In surface, the σ_{11} stress component is larger (about -1000 MPa) far from the indentation (Figure 5.13 (b)). Below the indenter, the difference with the case without residual stresses is lower due to the plastic deformation induced by the indentation. The shearing component at the interface is quite the same (difference of 20 MPa in Figure 5.14)

Thus, even with an introduction of large residual stresses, cracking and delamination are not affected.

At room temperature, the compressive internal stresses have no influence on the potential fracture of oxide. In the rest of simulations, no internal stresses are considered.

5.4 Modelling the delamination of oxide with CZM elements

5.4.1 Numerical reproduction of the delamination

In the simulation, oxide and steel are still in contact and a tangential frictionless behaviour is specified between the oxide and the steel, thus sliding is possible in the presence of shear stress. Cohesive elements (COHAX4, 4-nodes axisymmetric cohesive elements) are added in the simulation at the interface between oxide and steel with a 1 μm thickness (Figure 5.15). The cohesive elements are tied to the upper part of the steel and the lower part of oxide. The cohesive elements thus undergo the two stresses (normal and shear) present at the interface between the oxide and the steel. The steel and oxide meshes must be coincident at the interface (Figure 5.15). In a preliminary study, not reported here, the influences of the cohesive elements thickness and of the mesh size have been investigated until convergence has been obtained.

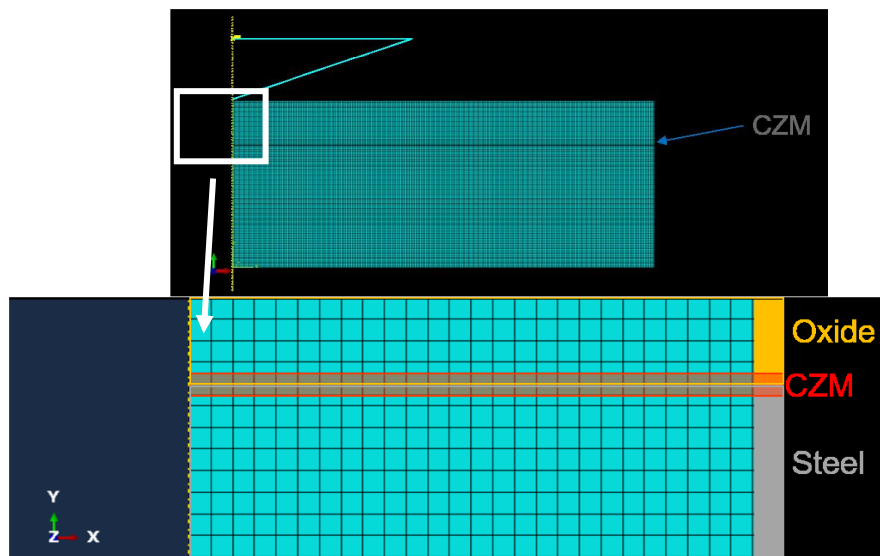


Figure 5.15: Localisation of cohesive elements at the interface between oxide and steel

Here, a complete simulation with a set of CZM parameters is described, with the following parameters:

- 1°) Elastic linear behaviour of cohesive elements: $E=G1=G2=210$ GPa, (the stiffness is then calculated by dividing by the thickness of CZM elements)
- 2°) Initiation criterion: the critical stress with “Maxs damage” option is considered to be the same for all stresses (normal, 1st and 2nd tangential directions). The criterion is equal to 100 MPa.
- 3°) Propagation of the degradation and the damage evolution is considered linear, mode-independent, the interfacial adhesion energy is set to 25 J/m^2 . The same value is taken for pure mode I, and pure mode II.

In order to identify the delaminated area, the scalar stiffness degradation variable SDEG (D of the model, see section 5.2.1) is observed. When $SDEG > 0$, the critical stress is reached and the interface is degrading; where $SDEG = 1$, the interface is fully delaminated. The left end of the crack is called position c_1 and the right end is c_2 . The index i refers to the initiation of cracking and f to the final extension of the crack at the end of indentation.

When $p/t < 0.1$, the shear band is strictly confined inside the oxide (no damage at the interface) (Figure 5.16 (a)). By increasing the penetration, ($\sim p/t = 0.2$), the shear band reaches the interface, σ_{12} is increasing up to the critical stress. Visually, we can observe the sliding of the cohesive elements, confirming that shear is the source of the delamination. This area is always localised below the contact edge. As a reminder, we have no pop-in event on the experimental displacement force curve and the post-mortem cross-sections show no delamination when $p/t \leq 0.2$.

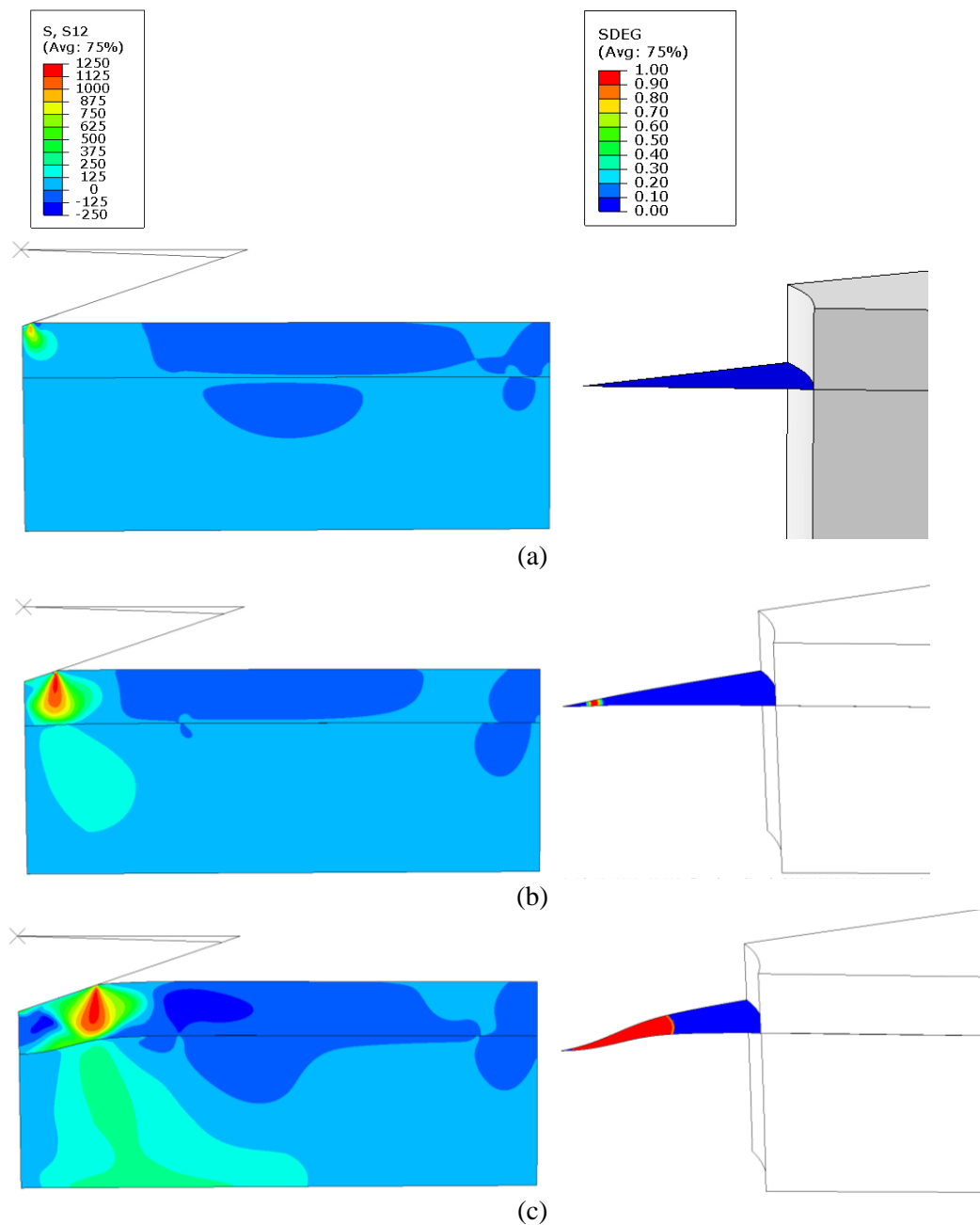


Figure 5.16: Shear stress maps and SDEG value of degraded CZM elements (a) after a penetration of $2,5\mu\text{m}$ $p/t=0.1$ (b) after a penetration of $5.8\mu\text{m}$ when delamination is starting $p/t=0.27$ (c) at the end of loading, depth $15\mu\text{m}$, $p/t = 0.6$. The same color scales are used for all 3 figures.

Once the criterion has been reached, the elements are linearly degraded (SDEG varies from 0 to 1) until the stress is totally relaxed and the delamination starts when $p/t=0.27$ (Figure 5.16(b)). It is interesting to note that the first cohesive element destroyed is at a distance $r = 12\mu\text{m}$ from the symmetry axis, the delaminated area is very narrow ($3\mu\text{m}$). The propagation soon reaches a steady-state speed. The reason for this is that the driving force for crack initiation is the elastic energy stored in the cohesive elements. Once this energy gets released, it may give rise to sudden growth; but here, the stored energy is small due to the weakness of the interface, so that this steady state propagation is predominantly driven by the progress of the indentation process which is performed at a constant rate, and the regular displacement of the shear band. Interfacial crack extends smoothly and the delamination is propagated (new cohesive elements are degraded). Note that the area is extended in both directions, towards and

away from the axis: whereas $c_{1i} = 12 \mu\text{m}$, $c_{1f} = 4 \mu\text{m}$ while c_2 increases from $15 \mu\text{m}$ to $46 \mu\text{m}$ at the end of the loading (Figure 5.16 (c)).

The delaminated areas after loading and unloading are the same. This confirms Rosenfeld's assumption that interfacial crack grows only during loading [158]. This means that this kind of crack does not propagate during unloading, contrary to e.g. lateral cracks in bulk brittle material indentation which are known to form at the end of unloading [163].

It is important to note that outside the contact area, a tensile normal (σ_{22}) component is present (33 MPa) in the Figure 5.17 at the end of the loading: the bending oxide, which is stiffer, tends to move up to limit its curvature (as in Figure 5.4 (b) [168]). This area is localised outside the contact area (distance of $110 \mu\text{m}$). This area is initially appearing for a ratio p/t equal to 0.3 with some MPa in tension, and is increasing to 25 MPa for a ratio $p/t=0.5$. With a still lower critical stress, this normal component could be sufficient to develop a second delaminated area. As a reminder, it could be an explanation of the FIB observation in which the delaminated area extends far beyond the contact area, where the high shear component is not present.

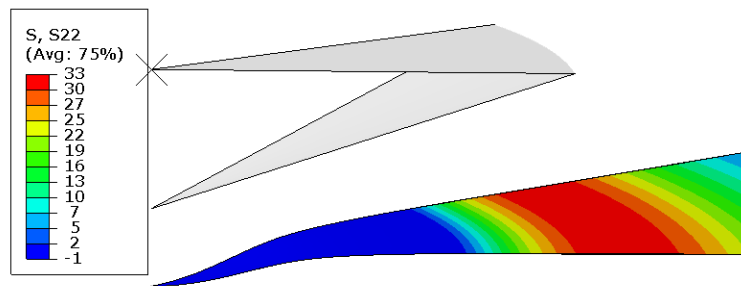


Figure 5.17: Normal stress at the end of the loading $p/t=0.6$ in the CZM elements (only represented in this figure)

A noticeable difference with post-mortem experimental observations has to be noted. With the parameters used here, the delaminated area does not start from the symmetry axis, and it never reaches it completely later on. It is furthermore strictly confined below the indentation. In the experimental work, the delaminated area does start from the axis and its maximum extension $c > 139 \mu\text{m}$ (beyond the FIB section edge) (Figure 5.18).

The mechanism displayed by the simulations with CZM involves a shear band which continuously disconnects oxide from substrate as it scans the interface outwards, following the increase of the indentation radius. The stress is concentrated, so that crack propagation does not extend beyond the shear stress band. Furthermore, at the beginning of indentation, say $p/t < 0.1$ or 0.2 , the plastic strain is strictly confined inside the oxide: all stresses are compressive, the shear band does not exist or does not extend to the interface. The crack first forms at 3.5 N load (indentation depth $11 \mu\text{m}$), when plasticity propagates to the substrate, promoting oxide bending. From then on, the crack tip propagates smoothly, exactly at the same place as the indentation radius and the shear stress band. This suggests that the central part of the interface in fact delaminates by an inward propagation during loading. Moreover, in experiments, crack propagation may have a more sudden character than the one given by the model, thus extending well beyond the shear stress band. Moreover, with a weak interface, one cannot exclude either that a second delamination zone, triggered by the normal stress (33 MPa at the end of the loading), forms beyond the contact zone and connects with the first one described here.

From a more general point of view, remember that CZM is a crack propagation regularization, which bears an intrinsic danger to miss any sudden propagation, e.g. a crack jumping from defect to defect. The choice of the parameters is critical to avoid such dangers. In view of a better understanding, the influence of each CZM parameter is discussed in the next part.

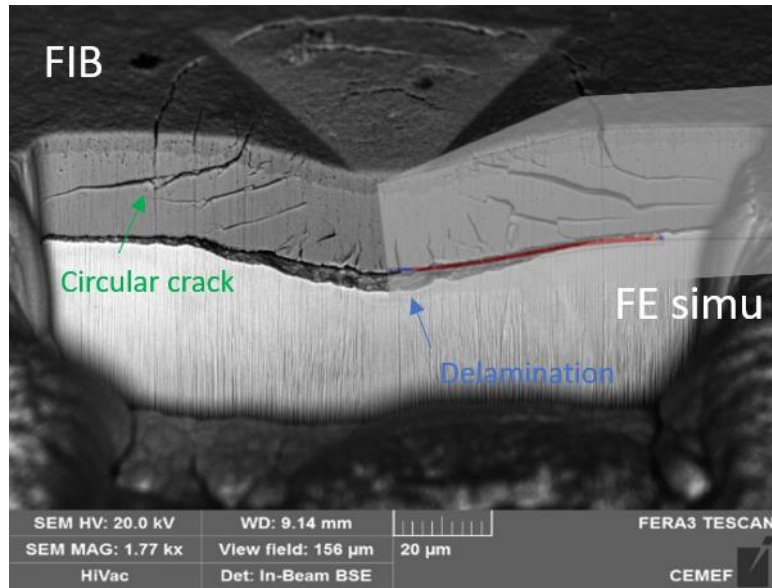


Figure 5.18: Comparison between the experimental test and the corresponding CZM simulation of the delamination of oxide (red elements in the figure)

5.4.2 Influence of CZM parameters

In order to decorrelate the influence of each parameter, in each of the following sub-paragraphs, two of the three CZM parameters (i.e. critical component, interfacial energy and CZM stiffness) are kept fixed and the last one is varied. Note that each parameter is in relation with a different step of the delamination, the choice of the correct parameters considers the initiation of the degradation, and also the final length of the degraded zone.

To select relevant ranges of the CZM parameters, we refer to Noh et al. who used cohesive elements to simulate spallation during a scratch test of iron oxide formed during hot rolling [68]. In their study, cohesive elements parameters were identified by an inverse method and critical stress components were set to 200 MPa, stiffness of cohesive elements 200 GPa/μm, fracture energy 18 J/m².

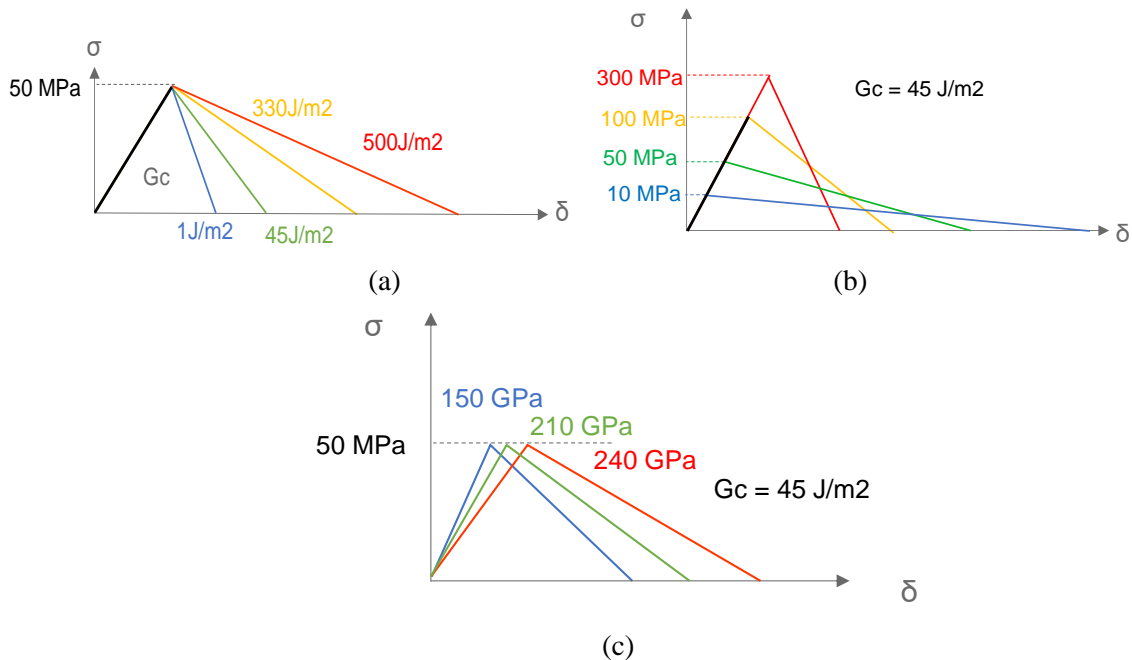


Figure 5.19: Schematic representations of the impact of each CZM parameters on the T-S curves. Variation of (a) the interfacial energy (b) the critical stress (c) the cohesive stiffness.

Hence the (wide) ranges investigated here are:

- 1°) Elastic linear behaviour of cohesive elements: E from 120 to 240 GPa.
- 2°) initiation criterion: the critical t^0 is varied from 10 to 500 MPa.
- 3°) the interfacial energy adhesion G_c is varied from 1 to 500 J/m².

The evolution of each parameter is schematized in Figure 5.19, the representations are not to scale.

5.4.2.1 Interfacial energy adhesion G_c

The critical stress is set to 50 MPa and E=210 GPa.

The experimental work, interpreted using Rosenfeld's model, has given a first evaluation of the interfacial energy G_c strongly dependent on steel grades: 45 and 330 J/m² for HSLA and IF respectively, the former being known as "difficult to descale", contrary to the latter. In this model, the substrate was considered rigid, which is far from our case. Furthermore, experiments showed a large variation of the delamination length, which means a large uncertainty on G_c , just as in the literature (Table 2-7, Table 4-5 and Table 4-6). In the values given by the literature, the energy measured experimentally during interface separation may involve a significant amount of plastic work in the metal during the separation, if the interface is tough. This part of the separation energy should not be counted as interface adhesion energy, since simulation will generate it independently of the adhesion energy. Thus, this interfacial energy may be overestimated.

These are the reasons why such a large range of G_c has been selected.

Firstly, the modification of G_c has no influence on the initiation of the degradation (Figure 5.20), the first elements in which SDEG > 0 appear at the same penetration of the tip at the same position (p/t=0.33). It seems logical because first part of the T-S law is characterised by the critical stress and the stiffness of cohesive elements (which are constant here).

However, the evolution of the degradation (until the delamination) of cohesive elements is directly in relation with G_c . In the Figure 5.20 for each energy, the corresponding level of degradation of cohesive elements is indicated. Let us assume that SDEG close to 1 means delamination ($\geq 0,9$, orange and red in Figure 5.20).

- whatever G_c (except $G_c = 1$ and 5 J/m², see below), the length of the damaged interface (SDEG > 0) is the same, 48-50 μm , 30% larger than the indentation radius, because it just depends on the size of the zone over which the σ_{12} shear stress has reached $t_s^0 = 50$ MPa, which is basically determined by the indentation geometry.
- However, the totally destroyed elements (in red, SDEG = 1) cover a wider area for lower G_c . The estimated crack length (SDEG ≥ 0.9) is zero for $G_c > 300$ J/m² and increases as G_c decreases to reach 47 μm at $G_c = 10$ J/m². This means that the proportion of the area delaminated is equal to 90% of the damaged area with a 10 J/m² energy. By increasing G_c , the delaminated area is lower, because the fracture of the cohesive elements requires more energy.

For low interface fracture energy simulations, as soon as initiation criterion is reached, complete degradation occurs, evolution of D from 0 to 1 is very fast, this means that the first part of the T-S law (elastic until the critical stress) controls delamination, the energy stored in the cohesive elements is instantly restored.

Note that for the very low values ($G_c = 1$ and 5 J/m²), the fractured area is similar to the case of $G_c = 10$ J/m² at the end of the loading stage. However a second area is instantly delaminated, beyond the contact area, during the unloading, because σ_{12} reaches 50 MPa ; this is the reason why the total delaminated length reaches 74 μm . At the end of unloading, the two delaminated areas remain disconnected. This has never been observed experimentally, at least at room temperature. Note that for the other values of G_c , σ_{12} is close to 50 MPa during unloading in the same area, but the SDEG value is low (>0.05).

The main conclusion is that the interfacial adhesion energy has an influence on the level of degradation of cohesive elements, once it has been initiated. It governs the length of the crack, but not the extension of the damaged area.

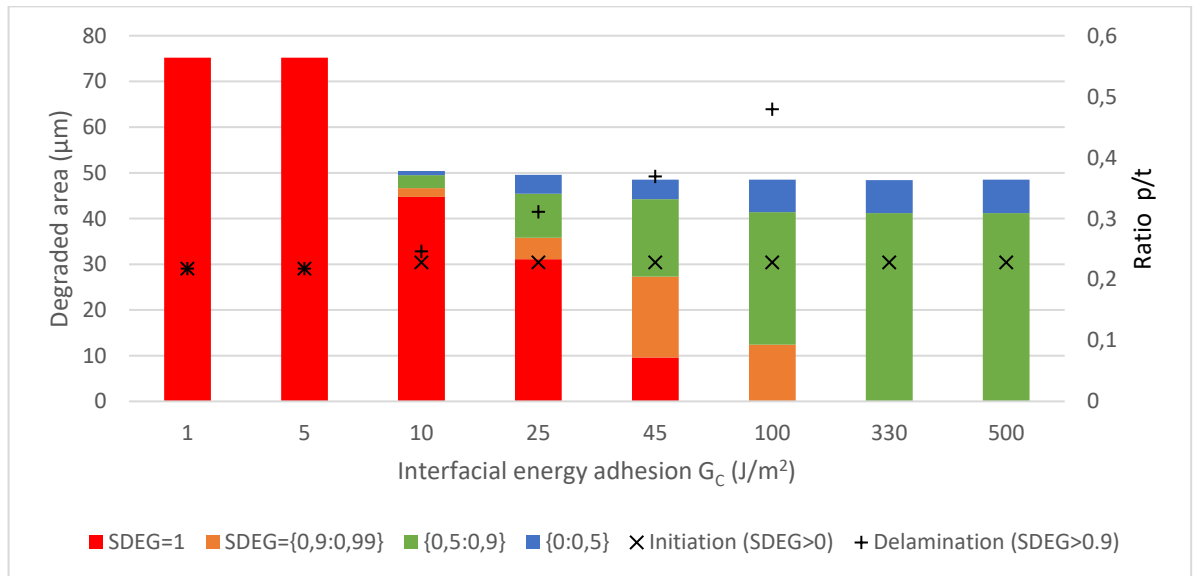


Figure 5.20: Evolution of the state of cohesive elements at the interface depending on the interfacial energy adhesion G_c . Red represents fully delaminated elements ($SDEG=1$), orange quasi-delaminated elements ($0.9 \leq SDEG \leq 0.99$), green quite degraded ($0.5 \leq SDEG \leq 0.9$), and blue little degraded ($0 < SDEG \leq 0.5$). The non-degraded cohesive elements ($SDEG = 0$) are not shown in this figure. The initiation of the degradation ($SDEG > 0$) and the initiation of the delamination ($SDEG > 0.9$) are indicated on the secondary axis. The critical stress is set to 50 MPa and the stiffness to 210 GPa.

5.4.2.2 Critical stress

The interfacial adhesion energy is set to 45 J/m² and the stiffness to 210 GPa. The critical stress t^0 is taken equal for the 3 components (normal and two shear direction).

By increasing the critical stress, the penetration at which the degradation is initiated is delayed (crosses, with scale on the right in Figure 5.21). Indeed, the critical shear stress is reached later at the interface ($p/t=0,15$ for $t^0 = 10$ MPa and $p/t=0,42$ for $t^0 = 200$ MPa). $t^0 = 300$ MPa is higher than any shear or normal stress computed at the interface, so that delamination does not take place, not even any damage.

The critical stress t^0 also has a large influence on the damaged interface length ($SDEG > 0$) and also on the area which is fully delaminated ($SDEG > 0.99$). The latter is maximal with the critical stress of 100 MPa (Figure 5.21). It is explained by the shape of the T-S law. The area below the T-S law curve is constant (45 J/m² in this study), thus with a low critical stress, the deformation of the cohesive elements (partly dictated by the geometry of the indentation) has to be much higher for full damage (Figure 5.19 (b)). At high t^0 , the slope of the damage part of the curve is much steeper, damage starts later but its evolution is faster. With an intermediate t^0 , the maximal displacement of the cohesive elements is reached sooner.

In the case of a low critical stress $t^0 \leq 25$ MPa, a second degraded area is observed beyond the contact area at the end of the loading ($p/t \sim 0,52$), due to σ_{22} as evoked previously (in the part 5.3.1.3). Indeed, the “stress sensitivity” of cohesive elements is very low. This explains the jump in damaged length between 50 and 25 MPa. However, in the cases tested, this normal component never reaches $SDEG \sim 1$, the oxide supposedly remains adherent in this area ($SDEG \leq 0.6$). For the lower $t^0 = 10$ MPa, this area is even larger, but still not delaminated ($SDEG \leq 0.8$).

In the FIB cross-sections, the delaminated area observed is the final resultant of the loading and unloading. Therefore, in the experiment modelled in this paragraph, it was not possible to identify the

moment when the delamination started. However, by combining the observations of other FIB cross-sections (realised with different thicknesses and final ratio p/t), we can say that the first delamination is observed for $p/t \sim 0.2$.

By considering $SDEG > 0.9$ as the delamination criterion (red and orange bar in the Figure 5.21), the crack length is about $40 \mu\text{m}$ from 150 MPa to 10 MPa below the indenter (by not considering the second delaminated area), thus the critical stress has a limited influence for the delamination area below the contact area.

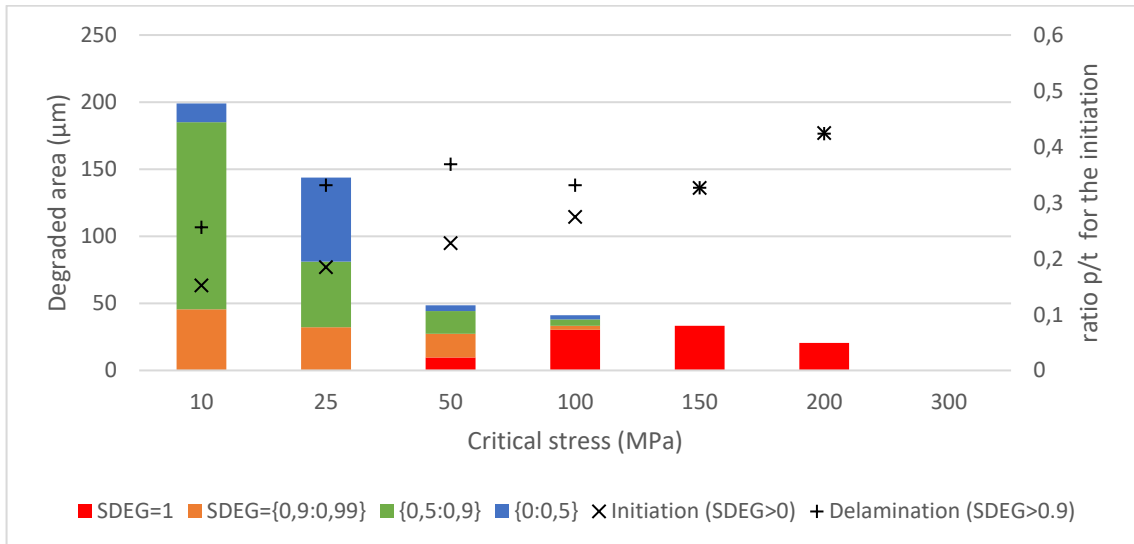


Figure 5.21: Evolution of the state of cohesive elements at the interface depending on the critical stress. red represents fully delaminated elements ($SDEG=1$), orange quasi-delaminated ones ($0.9 \leq SDEG \leq 0.99$), green quite degraded ones ($0.5 \leq SDEG \leq 0.9$), and blue little degraded ones ($0 < SDEG \leq 0.5$). The non-degraded cohesive elements ($SDEG = 0$) are not shown in this figure. The black crosses indicate the ratio p/t for the initiation of degradation (first element with $SDEG > 0$) and the initiation of the delamination ($SDEG > 0.9$). The interfacial energy is set to 45 J/m^2 and the stiffness to 210 GPa .

5.4.2.3 Elastic stiffness of CZM

The interfacial adhesion energy is set to 45 J/m^2 and the critical stress is set to 50 MPa .

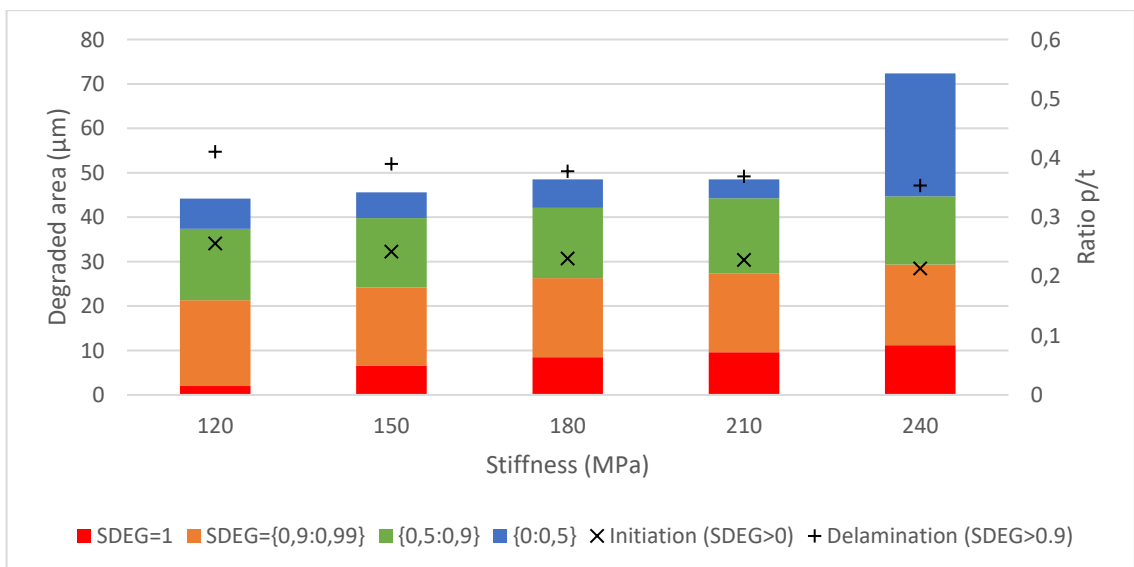


Figure 5.22: Evolution of the state of cohesive elements at the interface depending on the cohesive element stiffness. Red represents fully delaminated elements ($SDEG=1$), orange quasi-delaminated ones ($0.9 \leq SDEG \leq 0.99$), green quite degraded ones ($0.5 \leq SDEG \leq 0.9$), and blue little degraded ones ($0 < SDEG \leq 0.5$). The black crosses indicate the ratio p/t for the initiation of degradation (first element with $SDEG > 0$) and the initiation of the delamination ($SDEG > 0.9$). The interfacial energy is set to 45 J/m^2 and the critical stress is set to 50 MPa .

0.99), green quite degraded ones ($0.5 \leq SDEG \leq 0.9$), and blue little degraded ones ($0 < SDEG \leq 0.5$). The non-degraded cohesive elements ($SDEG = 0$) are not shown in this figure. The black crosses (scale on the right) indicate p/t for the initiation of degradation ($SDEG > 0$) and the initiation of the delamination ($SDEG > 0.9$). The interfacial energy is set to 45 J/m^2 and the critical stress to 50 GPa .

Initially, $E = E_{\text{steel}}$, Young's modulus of steel. By increasing the stiffness of cohesive elements to $E = 240 \text{ GPa}$ ($= E_{\text{oxide}}$), the first degradation occurs at slightly lower penetration, as interface stresses grow faster (Figure 5.22). The area delaminated ($SDEG > 0.9$) is also slightly larger with a higher stiffness.

5.4.2.4 Identification of a set of parameters

This parametric study highlights influence of CZM parameters, pointing more precisely towards the critical stress t^0 for the initiation of the degradation and towards the interfacial adhesion energy G_c for the area in which cohesive elements are completely degraded ($SDEG > 0.9$). The influence of the stiffness is smaller. A summary of the parametric study is made in the Figure 5.23. The tendency indicates that with a lower t^0 and G_c , a larger area is delaminated (as judged by $SDEG > 0.9$). For very low t^0 and G_c , the area is increasing with a second, outmost area delaminated. Numerically, a second delaminated area is observed:

- by decreasing critical stress ($< 30 \text{ MPa}$), a second area generated by the normal component is present far from the indenter at the end of the loading, the only way crack length may significantly exceed indentation radius.
- with a low critical stress ($< 50 \text{ MPa}$) and a low interfacial energy (1 J/m^2) during the unloading, due to the shearing stress component.

In order to choose the correct set of parameters, the model is considering a $26 \mu\text{m}$ oxide, with a final ratio $p/t = 0.6$ and a contact area of $37 \mu\text{m}$. Experimentally, the total delamination length is above $139 \mu\text{m}$, i.e. $70 \mu\text{m}$ on each side. In any case, the delaminated area is composed of a single area from the centre of indentation (no separate area is observed). There is no clear information on the initiation of the delamination, but we can assume that it occurs above $p/t = 0.2$ (Figure 4.22 in Chapter 4), to let the shear band reach the interface. The crack radius is extended well beyond the contact area, the shearing band is not reaching as far, thus it encourages the presence of another mechanism to increase the delamination area.

To choose the correct set of parameters to fit correctly the experimental delamination:

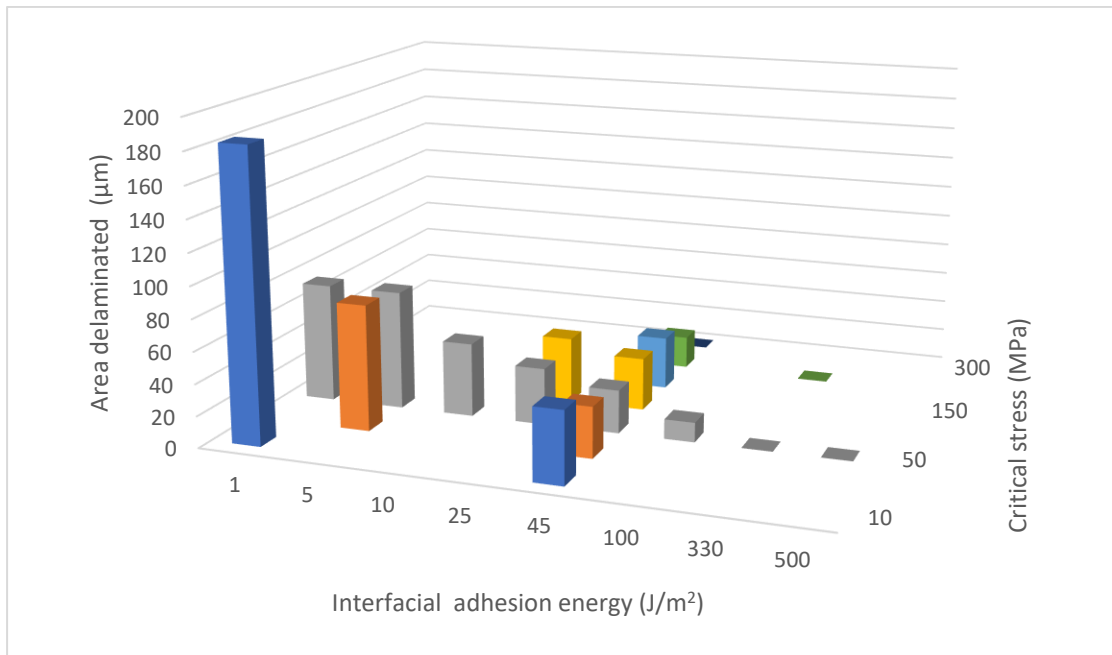
- by considering only the first delaminated area (critical stress above 50 MPa), the length is underestimated. The normal stress at the end of the loading and shearing during the unloading is not reached in this case.
- by considering the potential secondary delamination, (critical stress 25 MPa), it agrees with a delamination at $p/t \sim 0.2$. However, there are two separate area of delamination (and the second zone is offset from to the contact area (extending from $r = 90$ to $120 \mu\text{m}$). The total length fits correctly the experimental data.

As for the size of the crack and the possibility of a double zone, this would argue in favour of $G_c < 10 \text{ J/m}^2$. Note that there is a smaller influence of the interfacial energy adhesion below 5 J/m^2 .

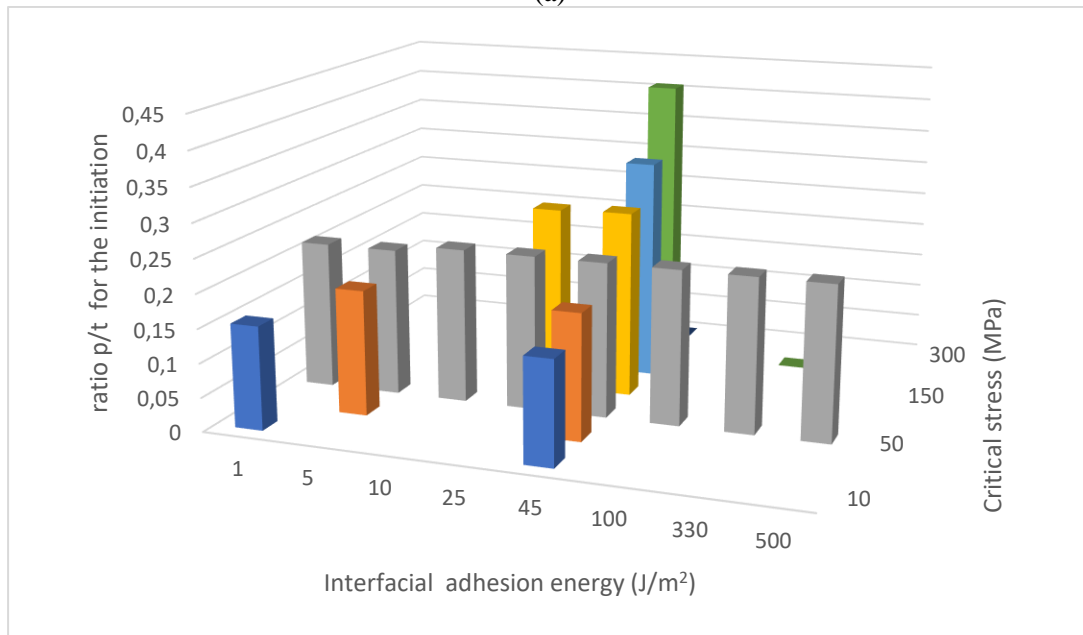
The potential degradation during the FIB cross-section cannot be ruled out. We know that energy involved during the FIB does not create a new delaminated area, (see in Figure 3.6 in which there is no delamination in non-indented area), but there is no information on a possible extension of an existing delaminated area.

The choice of these parameters is crucial to simulate delamination of oxide at the interface. In our case, the correct parameter set for the IF steel seems to be: a critical stress of 25 MPa , with $G_c = 5 \text{ J/m}^2$. This case is described in the following part. The comparison with the Rosenfeld's model

described in chapter 4 indicates that the 45 and 330 J/m² is largely overestimated, probably due to the hypothesis (no deformation of the substrate).



(a)



(b)

Figure 5.23: (a) Delaminated area ($SDEG > 0.9$) (b) the ratio p/t for the initiation as a function of the critical stress and the interfacial adhesion energy

In order to confirm this set of parameters, results of the numerical simulations (in orange) and experiments are compared in Figure 5.24. Each orange point refers to the delaminated area for a penetration p/t in the simulation. The blue points refer to delaminated area measured after a FIB analysis (the blue crosses indicate when no delamination is observed experimentally).

Numerically, the delamination is starting for a ratio p/t of 0.2 (experiments give $p/t \sim 0.20 - 0.22$). For low p/t , the delaminated area is under-estimated. By increasing the penetration depth ($p/t > 0.5$), the second area (developed by the normal traction at the interface) is delaminated and in this configuration joins the first delaminated zone with the shear component for a ratio p/t of 1. For larger

penetration, the delaminated length fits well the experimental data, suggesting the two-steps delamination might occur during the indentation.

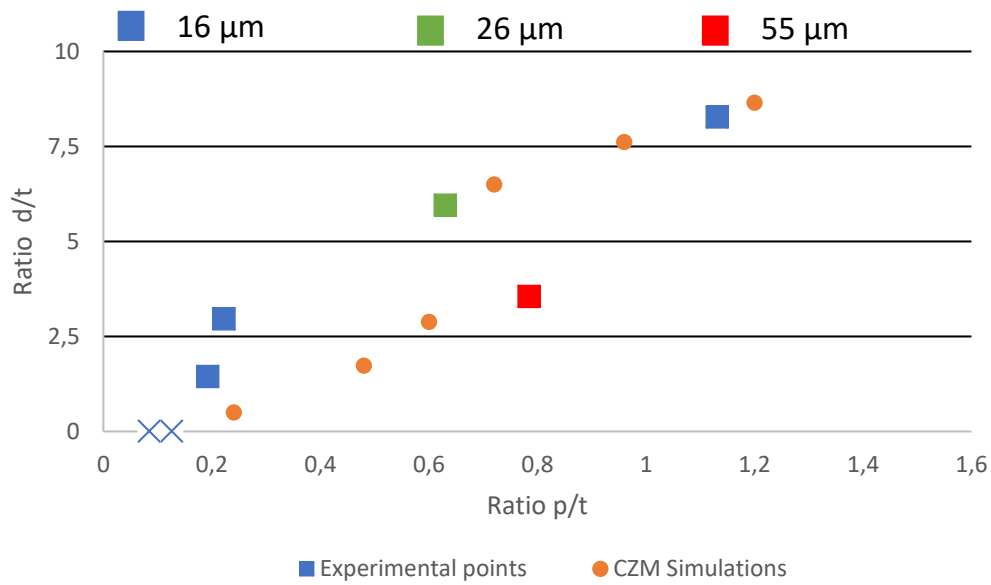


Figure 5.24: Evolution of the delaminated area for the experimental part (in blue) and the CZM simulations (in orange), critical stress 25 MPa, $G_c = 5 \text{ J/m}^2$, elastic modulus 210 GPa. The crosses refer to the FIB cross-sections in which no delamination is observed.

The selected T-S parameters for the cohesive elements reproduce reasonably well the experimental delamination. It is underestimated for low penetration indentations. In the following, the fracture within oxide is studied using an XFEM approach.

5.5 Oxide fracture modelling with XFEM : circular cracks

5.5.1 Description of the model

The same modelled configuration consists of an oxide thickness of 26 μm and $p/t = 0.6$. The boundary conditions described above are used for its simulation. The film/ substrate interface is assumed to be perfectly bonded (i.e., no delamination).

The XFEM-based cohesive segments method is used to simulate crack initiation and propagation along an unknown path, since the crack propagation is not tied to the element boundaries in a mesh. Thus, after analysis of the potential failure locations in surface, two types of simulations are described:

- a single crack initiation generated with a pre-crack (2 μm) inserted directly in the oxide material at a certain distance from the axis. This amounts to consider the presence of a large defect in surface. The oxide area is considered as the crack domain (the enrichment is potentially defined within the whole oxide layer). Thus, a single crack is able to propagate anywhere in the oxide region. A parametric study is done to observe the influence of the parameters: localization of the crack, T-S law parameters.
- multiple spatial cracks. Different XFEM regions are created within oxide to allow multiple crack nucleation and propagation. The length of each zone is set at 10 μm along the radial direction.

The cohesive zone model exhibits a softening behaviour (stiffness degradation), which usually results in serious convergence problems. To improve the convergence performance and stabilise the response during the damage, a small stabilisation parameter called “viscosity coefficient” is used (recommended value, 10^{-5}). Viscous damping regularisation causes the tangent stiffness matrix to be positive definite for sufficiently small-time increments. This coefficient has been checked to be smaller than the time increment step and to not noticeably change the stress distribution [168,184]. Furthermore, simulations at a viscous coefficient of 10^{-5} are stable and converge to quasi-static solutions.

Static et dynamic implicit approach

The XFEM methodology is implemented in a static analysis procedure. Alternatively, you can include an XFEM crack in an implicit dynamic analysis procedure to simulate the fracture and failure in a structure under high-speed impact loading. Both dynamic and static implementations have been tested.

- With the implicit dynamic method, the quasi-static response of the system is calculated using a Hilbert–Hughes–Taylor time integration. The non-linear dynamic equilibrium equations are solved iteratively using Newton’s method. The calculation time is longer in the presence of non-linearity.
- In the static method, the time step is just a measure for incrementing loads. The solver assumes that this is happening extremely slowly. This means that the way the load is applied has no impact on structural behaviour.

In both cases, the equations have to be solved iteratively until the convergence is reached. Similar results have been obtained with the two configurations.

5.5.2 Single crack initiated with a defect in surface (pre-crack)

5.5.2.1 Results

A first case is described here, with the following T-S law parameters:

- the elastic stress evolution is directly in relation with the material law of the oxide ($E=240$ GPa)
- considering the stress level at the surface (Figure 5.9), the criterion « Maxps damage » (see eq. (5-1)) is set initially to 800 MPa.

- the damage evolution is linear and mode-independent with $G_{ox} = 12 \text{ J/m}^2$ ($K_I = 1.7 \text{ MPa}\cdot\sqrt{\text{m}}$).

In this configuration, the crack initiation is set at a distance $R_c = 50 \mu\text{m}$ of the axis. In order to understand the initiation and the further propagation of the crack, the evolution of the maximum principal stress is shown. The influence of each component (σ_{11} and σ_{22} for example) is also detailed as they guide the propagation of the crack.

In the first instant of the propagation, the σ_{11} component in surface is important. This high tensile area in surface is generated for $p/t \geq 0.25$ (cf Figure 5.9 above), when substrate has started to yield significantly, forcing the oxide layer to bend. The σ_{11} stress value is increasing in the XFEM area, near the pre-crack tip (Figure 5.25 (a)). The critical stress (800MPa in this case) is reached at the pre-crack position for $p/t = 0.33$ (i.e. $p^* = 9 \mu\text{m}$, indentation radius $22 \mu\text{m}$, $R_c/a^* = 2.25$).

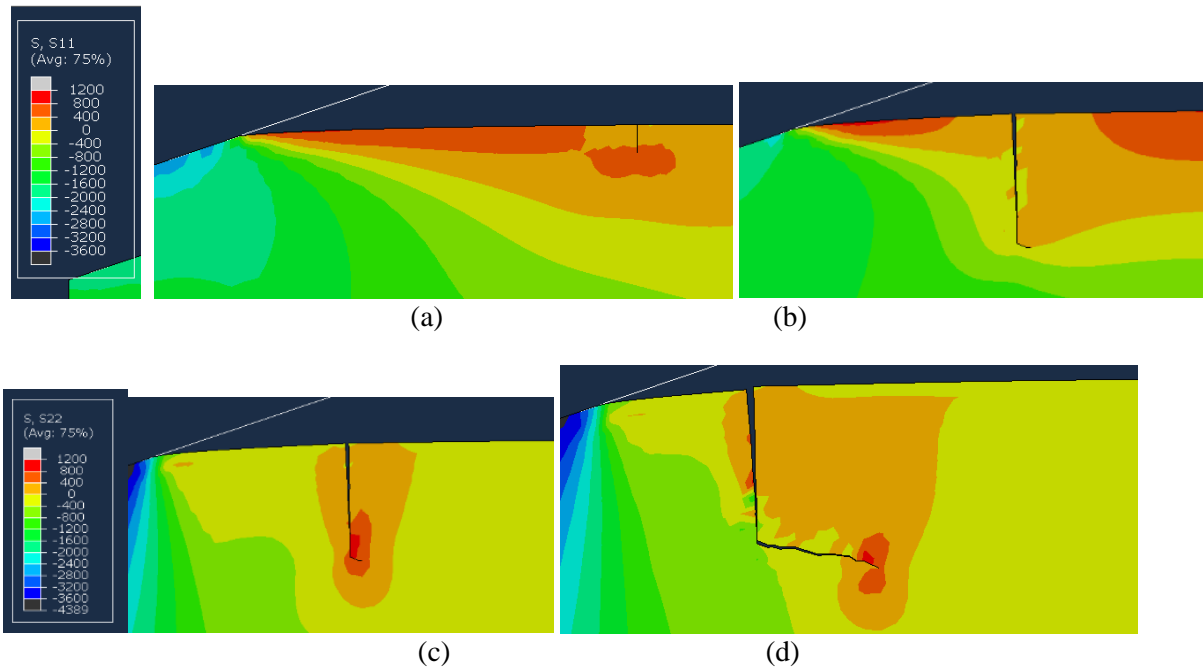


Figure 5.25: Evolution of stress components during the propagation of the crack. Critical stress 800 MPa, fracture energy 12 J/m^2 . (a) σ_{11} at the initiation of the crack (b) σ_{11} at the moment of the deviation (c) σ_{22} at the moment of the deviation (d) σ_{22} at the end of the loading.

The propagation is consistent with the stress field at the tip of the crack, vertical under the influence of tensile σ_{11} (Figure 5.25 (a)). It is continuous until $p/t = 0.5$ ($p^{**} = 13 \mu\text{m}$, $a^{**} = 32 \mu\text{m}$, $R_c/a^{**} = 1.55$). At this moment, the crack tip approaches the compressive part of the bending field, σ_{11} at the crack tip turns compressive (Figure 5.25 (b) and (c)). Thus, the vertical propagation is stopped when crack length is equal to $10 \mu\text{m}$. However, the crack deviates in the horizontal direction outward, and the propagation goes on, driven by the tensile σ_{22} . At the end of the loading, the total length of the crack is about $18 \mu\text{m}$, $10 \mu\text{m}$ in the normal direction and $8 \mu\text{m}$ in the direction parallel to the surface (Figure 5.25 (d)). During the unloading, there is no more propagation of the crack.

A second case is described now with the following T-S parameters:

- the criterion « Maxps damage » is set to 400 MPa.
- the energy damage evolution is linear and mode-independent with $G_{ox} = 12 \text{ J/m}^2$ ($K_I = 1.7 \text{ MPa}\cdot\sqrt{\text{m}}$).

The pre-crack is again at $R_c = 50 \text{ }\mu\text{m}$. In this configuration, the initiation criterion is reached at $p/t=0.3$, a little sooner than in the previous case ($p^* = 7.8 \text{ }\mu\text{m}$, $a^* \sim 18 \text{ }\mu\text{m}$, $R_c/a^* = 2.8$). The vertical propagation continues until $p/t = 0.36$ ($p^{**} = 9.4 \text{ }\mu\text{m}$, $a^{**} \sim 23 \text{ }\mu\text{m}$, $R_c/a^{**} = 2.2$). At this moment, the crack tip approaches the compressive part of the bending field. Thus, the vertical propagation is stopped at a crack length of $8\mu\text{m}$. However, the crack is briefly deviated inwardly, and quickly stopped by the compressive stress field generated by the indentation.

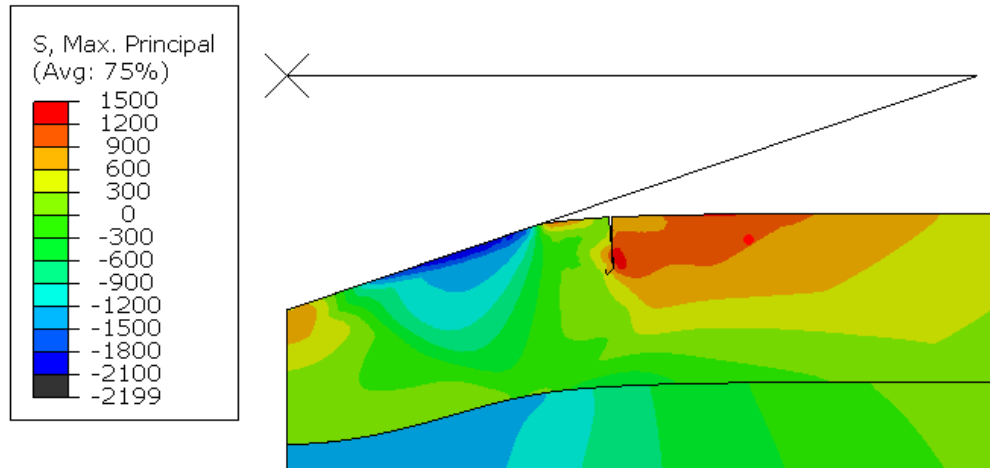


Figure 5.26: Final crack propagation for a critical stress 400 MPa and $G_{ox}=12 \text{ J/m}^2$

5.5.2.2 Pre-crack position

The position chosen for the single pre-crack is modified to observe the evolution of the propagation, from $20 \text{ }\mu\text{m}$ to $100 \text{ }\mu\text{m}$ from the axis. In this case, the T-S parameters are set to 1000 MPa for the critical stress and $G_{ox}=12 \text{ J/m}^2$ for the energy.

In the cases in which the XFEM initiation is closest to the axis ($30\mu\text{m}$ and below), the critical stress is never reached and the pre-crack never propagates. Indeed, the zone in tension which triggers fracture appears for $p/t > 0.2$ only, and the pre-crack is already under the influence of the compressive stress field of the contact (Figure 5.9). By increasing the abscissa of the initial crack, the indentation depth required to initiate the crack increases (orange points in Figure 5.27). The initiation is always normal to the surface. For a larger distance ($\sim 100\mu\text{m}$, three times larger than the final contact area), the critical stress is never reached either, at the maximum $p/t = 0.6$.

For a $40 \text{ }\mu\text{m}$ distance, the crack is initiated but is quickly stopped (length $5 \text{ }\mu\text{m}$) by the contact reaching the crack, making the crack tip stress largely compressive.

For the 50 and $60 \text{ }\mu\text{m}$ position, the crack deviates outward as described in Figure 5.27.

For the 70 and $80\mu\text{m}$ case, the crack propagates towards the indentation axis (Figure 5.27 (b)). A possible explanation for this change is that a crack far from the contact is in a zone where the elastic energy density is relatively low. This energy is larger to the left of the crack (indentation side) than to the right, for which the compressive stress area generated by the indentation and the bending of the oxide is too far. Propagation to the left allows the stresses to be released (to decrease the stored energy where it is the highest): the left lip can be seen to rise, causing the stress release.

Experimentally, no cracks are observed that far from the indenter. Indeed, the tensile stress zone is screened repeatedly by the successive cracks, and a larger indentation depth p would be needed for the tensile stress to reach this position.

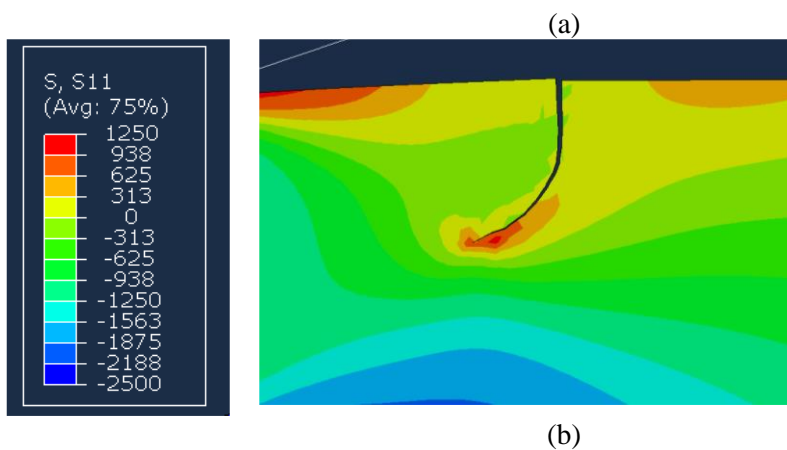
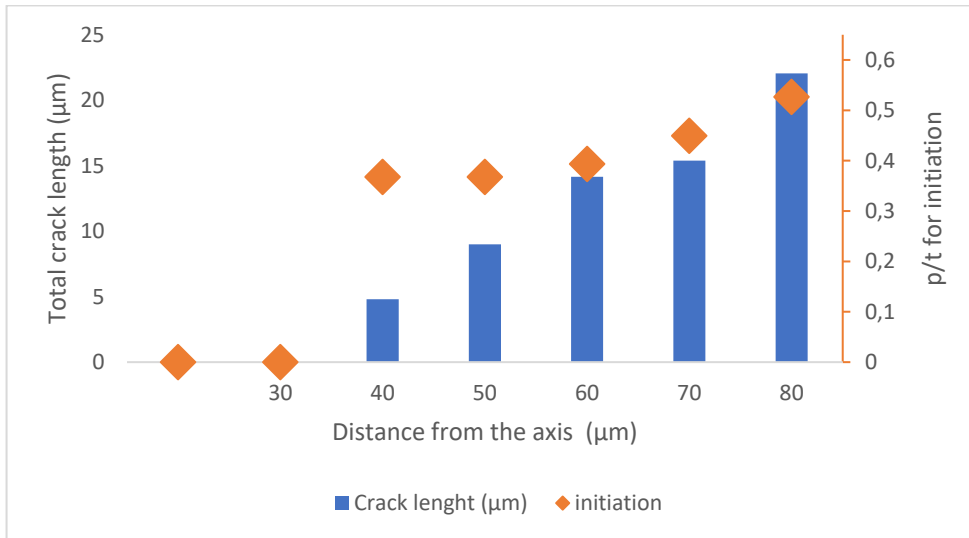


Figure 5.27: (a) Evolution of the crack initiation and the crack length for the position of the crack (critical stress 1000 MPa, $G_{ox} = 12 \text{ J/m}^2$ i.e. $K_{Ic} = 1.7 \text{ MPa} \cdot \sqrt{\text{m}}$) (b) XFEM crack propagation for an initiation site at a distance of 70 μm

The position of the pre-crack has a large influence on the crack path. The further away the crack is, the later it starts, and the more likely it is to move inwards. In the experimental test, no crack are generated beyond 60 μm (in this configuration $p/t=0.6$ and 26 μm oxide thickness)

5.5.1.1 Influence of T-S law parameters

In the T-S law, both the critical stress and the G_{ox} cohesive energy are largely varied:

- from 300 to 1200 MPa
- from 1 to 50 J/m².

In order to decorrelate the influence of each parameter, one of the two parameters is set and the other one is varied. The influence of the T-S law parameters is discussed. The pre-crack is localised at a distance of 50 μm , outside the contact area.

Critical stress

The cohesive energy is set to 12 J/m^2 . Similarly, to the delamination, the critical stress has an influence on crack initiation: by increasing this parameter, the initiation is postponed (Figure 5.28)). The larger the critical stress is, the larger the indentation depth required to form the crack. It seems logical because σ_{11} is increasing as p increases (Figure 5.9). Thus, in the T-S law, an increase in critical stress of coating can effectively prevent the initiation of cracks. However, the crack length before the deviation is independent of the critical stress, (8 to $10 \mu\text{m} \sim t/3$ whatever the stress), because it is dictated by the shape of the bending field. Therefore, p^* , the indentation depth at the beginning of the vertical propagation, appears as the variable to use to identify the critical stress. Considering Figure 5.28 and knowing that fracture initiation is found for $p^*/t \sim 0.3$ or slightly below in the $t = 26 \mu\text{m}$ experiments (Figure 4.19), a critical stress around 400 MPa seems reasonable.

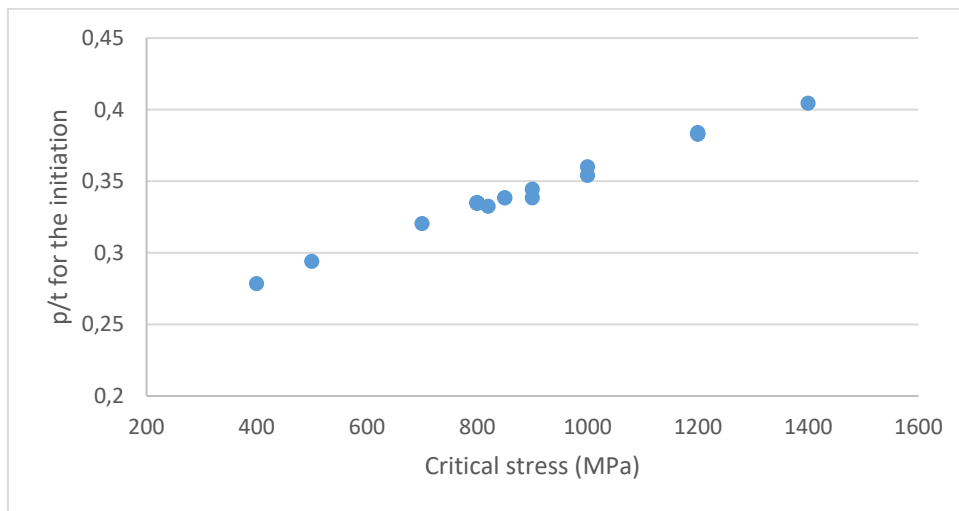


Figure 5.28: Evolution of the ratio p/t for the initiation of the crack with the increasing critical stress ($G_{ox} = 12 \text{ J/m}^2$)

Cohesive energy G_{ox}

By varying the cohesive energy (for a critical stress of 800 MPa), the initiation of cracking is the same, however, the crack length is increasing. First, the vertical crack length seems to be quite independent of the cohesive energy as well (8 to $10 \mu\text{m}$ in all cases). However, after the deviation, the final length at the end of the unloading is higher for lower cohesive energy (Figure 5.29)). Thus, the overall length of cracks decreases as the cohesive energy increases. It can be illustrated by the bilinear T-S law, the total amount of energy needed to propagate the crack is larger, and it tends to slow down the propagation.

Numerically, decreasing G_c makes the computation more difficult, and the artificial viscosity (evoked previously) and the convergence tolerance must be adapted to each simulation.

Even with a large variation of the cohesive energy (by more than an order of magnitude), the crack length does not increase that much, in comparison to the experimental test. With the parameters used in this study (the material law and the corresponding T-S law), the XFEM computation follows the correct path but under-estimates the final length. It should also be kept in mind that the values of the cohesive energy should agree with the literature. For example, a value of 1 J/m^2 corresponds to a toughness of $0.5 \text{ MPa}\cdot\text{m}^{1/2}$ whereas the literature suggests between 1 and $2 \text{ MPa}\cdot\text{m}^{1/2}$ for the three oxide phases (see section 2.5.4). Thus, decreasing the energy too much has no meaning from a “physical” point of view. $G_c \sim 10 \text{ J/m}^2$, below which the crack length stabilises (Figure 5.29) is consistent with both our measurements and the values found in the literature.

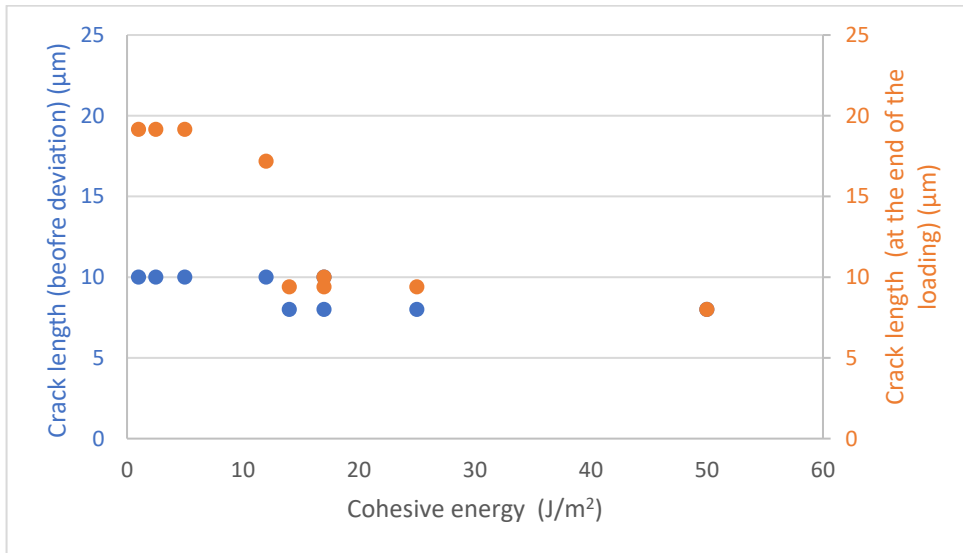


Figure 5.29: Evolution of the crack length with increasing cohesive energy. Blue points refer to the length before the deviation and the orange points to the total length at the end of the loading. In this study, the critical stress is set to 800 MPa.

Another remark about these simulations is that, for the initiation and the vertical propagations, there is no doubt about the crack path. However, when the crack reaches the compressive stress field at mid-thickness, three behaviours may be observed for the crack tip:

- no deviation, the crack propagation is just stopped
- deviation towards the indented area (Figure 5.26). Looking at the stress field, this does not seem consistent, it is probably mesh- and algorithm-dependent. In this case anyway, the propagation is quickly stopped by the compressive stress under the indenter, so that we consider this as a “non-deviating” case.
- deviation away from the indented area (described above and observed experimentally) (Figure 5.25)

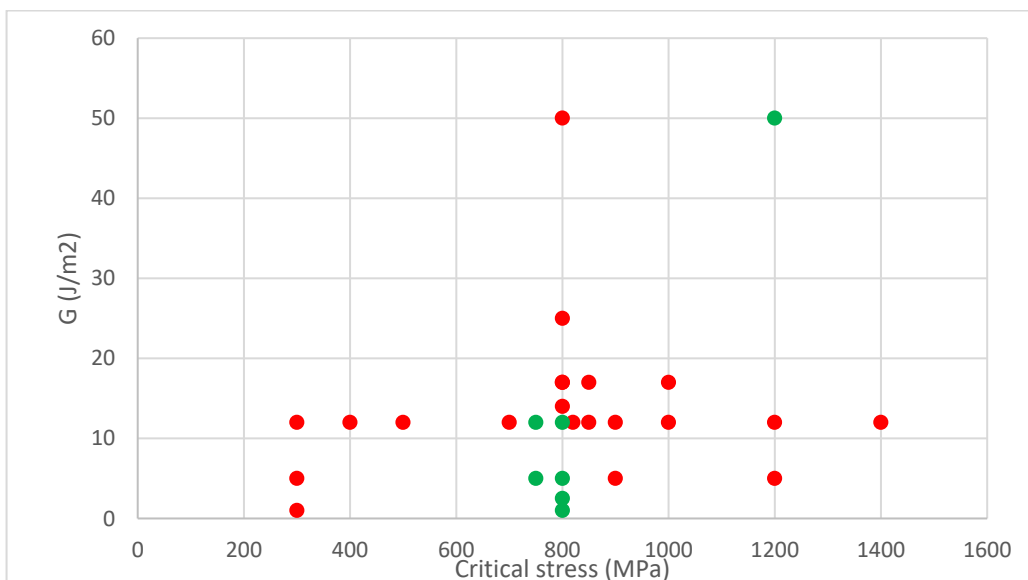


Figure 5.30: Evolution of the propagation after the vertical propagation stage until the compression area. The red points refer to non-deviating cracks and the green points to cracks deviating toward the outside of the indentation. The initiation site is set at a distance of 50µm.

A majority of cracks stop when their tip reaches the neutral surface beyond which the stress is compressive. The Figure 5.30 indicates that there is a set of parameters (for a constant distance of initiation $50\ \mu\text{m}$), in which the deviation is observed: for $R_c = 50\ \mu\text{m}$, $750\text{-}800\ \text{MPa}$ for t^0 and below $12\ \text{J/m}^2$ for cohesive energy. This indicates that the deviation is highly sensitive to the T-S parameters.

The conclusion of the parametric study is that for the case investigated and in the range of values used, higher critical stress tends to delay the occurrence of crack, but has little influence on the crack length (before and after the deviation). The cohesive energy (G) has a larger influence on the crack propagation. Thus, increasing the cohesive strength or energy of the oxide can effectively reduce the probabilities of crack initiation and growth. There is a good prediction of the cracking, even if the crack length remains under-estimated. A correct set of parameters is $400\ \text{MPa} \pm 100$ and $10 \pm 2\ \text{J/m}^2$. A simulation is launched with an initial pre-crack at a distance of $30\ \mu\text{m}$ (closer to the 1st crack observed). The crack is well initiated for a p/t of 0.32 and tends to deviate outward (Figure 5.31)). The final length is $L_f = 8.3\ \mu\text{m}$. It confirms that decreasing R_c to $30\ \mu\text{m}$, the couple of T-S parameters for the vertical initiation and the deviation fits well. The final length is equal to $8.3\ \mu\text{m}$.

Now we have to consider how to simulate multi-cracking as in the experimental work.

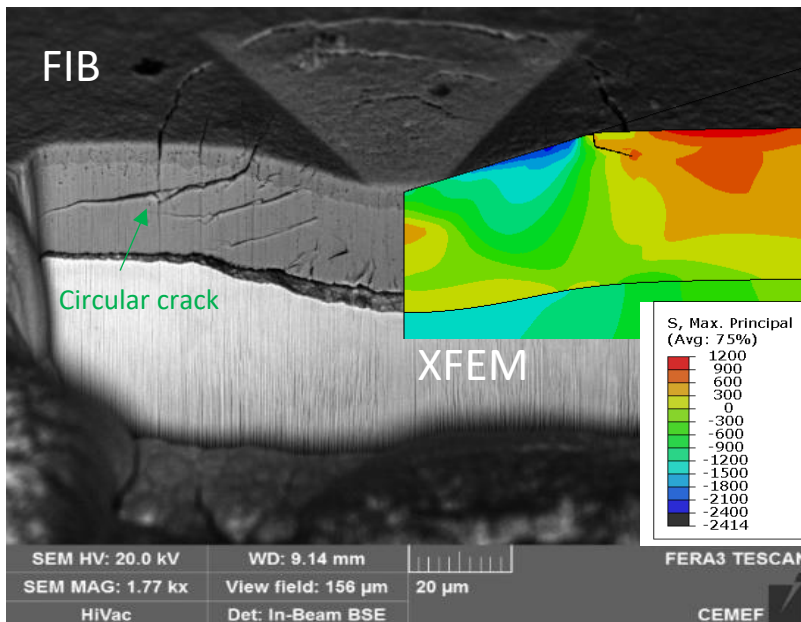


Figure 5.31: Crack propagation of the circular crack a critical stress $400\ \text{MPa}$, fracture energy $12\ \text{J/m}^2$ and a initial pre-crack at a distance of $30\ \mu\text{m}$ of the axis. Comparison between the experimental FIB cross-section (left) and the XFEM simulation (right)

5.5.3 Multiple fracture without pre-crack

In order to reproduce the multiple cracks observed in the test, 11 XFEM regions are created in the oxide around the indenter to allow multiple crack nucleation and propagation.

The size of each region was 10 μm in radial directions through the whole thickness of oxide. In this configuration, there is no particular crack initiation site. The configuration is closer to real indentations in which we saw no large defects near oxide surface.

The elastic stress evolution is directly in relation with the material law of the oxide ($E=240\text{ GPa}$)

- the criterion « Maxps damage » is set to 400 MPa.
- the energy damage evolution is linear and mode-independent with $G_{\text{ox}} = 12\text{ J/m}^2$ ($K_I = 1.7\text{ MPa}\cdot\sqrt{\text{m}}$).

In the Figure 5.32, at four stages of the penetration, fracture behaviour is shown. STATUSXFEM = 1 indicates that the element is completely cracked (analogous to SDEG of the CZM model).

- first, at $p/t = 0.32$ ($a = 20\text{ }\mu\text{m}$), when the tensile stress is localised at the surface, there are several initiation sites simultaneously appear, at $r = 30\text{ }\mu\text{m}$ (crack #1), $40\text{ }\mu\text{m}$ (crack #2) and $51\text{ }\mu\text{m}$ (crack #3).

- then, by increasing the penetration until $p/t=0.39$ ($a = 24\text{ }\mu\text{m}$), cracks #2 and #3 start propagating through the oxide, vertically. A fourth crack is initiated at $r = 60\text{ }\mu\text{m}$.

- for $p/t = 0.51$, $a = 31.5\text{ }\mu\text{m}$ so that crack #1 is below the indenter and in the compressive stress field having no opportunity to grow. It may correspond to tiny cracks confined within the magnetite layer in Figure 5.1. A last crack #5 is initiated at $r = 71\text{ }\mu\text{m}$.

Finally, at the end of the loading, crack #2 has propagated outward, whereas cracks #3 and #4 just grow vertically; crack #5 tends to deviate inward as in Figure 4.25. An additional crack (crack #6) initiates later at a distance of $80\mu\text{m}$, but does not really propagate.

Crack initiation site have appeared at a distance from 30 to $80\text{ }\mu\text{m}$. However, only three cracks are fully developed with at least a complete degradation; they are localised at 40, 51 and $71\text{ }\mu\text{m}$ with crack lengths for a crack length of $12\text{ }\mu\text{m}$, $9\text{ }\mu\text{m}$ and $6\text{ }\mu\text{m}$ respectively. All these locations are outside the final contact area ($37\mu\text{m}$).

Only one crack is deviating outward, as observed experimentally when the contact with the indenter is really close to the crack (end of the loading in this configuration). The failure mechanism is thus clear: cracks form early, reach the neutral line near the edge of the contact and bifurcate outwards. The following cracks, which form a little further, propagate in a straight line and stop on the neutral line. Those that start very far from the contact, and therefore stop on the neutral line when the contact is still far away, eventually return inwards.

The force-displacement indicates some tiny “pop-ins” at the end of the loading (Figure 5.32 (e)), probably corresponding to the deviation of the crack #2. But it does not really depart from the load fluctuations which would be observed in experiments, confirming the difficulty to use the curve to interpret the fracture in our configuration.

The comparison is made in the case with a pre-crack (localization at $50\text{ }\mu\text{m}$ and same T-S law with a critical stress of 400 MPa and $G_{\text{ox}} = 12\text{ J/m}^2$ in Figure 5.26) A difference is observed in the beginning of the propagation, ($p/t=0.3$ with a pre-crack and $p/t 0.39$ for crack #3 in the Figure 5.32). The presence of a large defect in surface accelerates the initiation of the crack. The crack path is however, the same (no deviation in both cases).

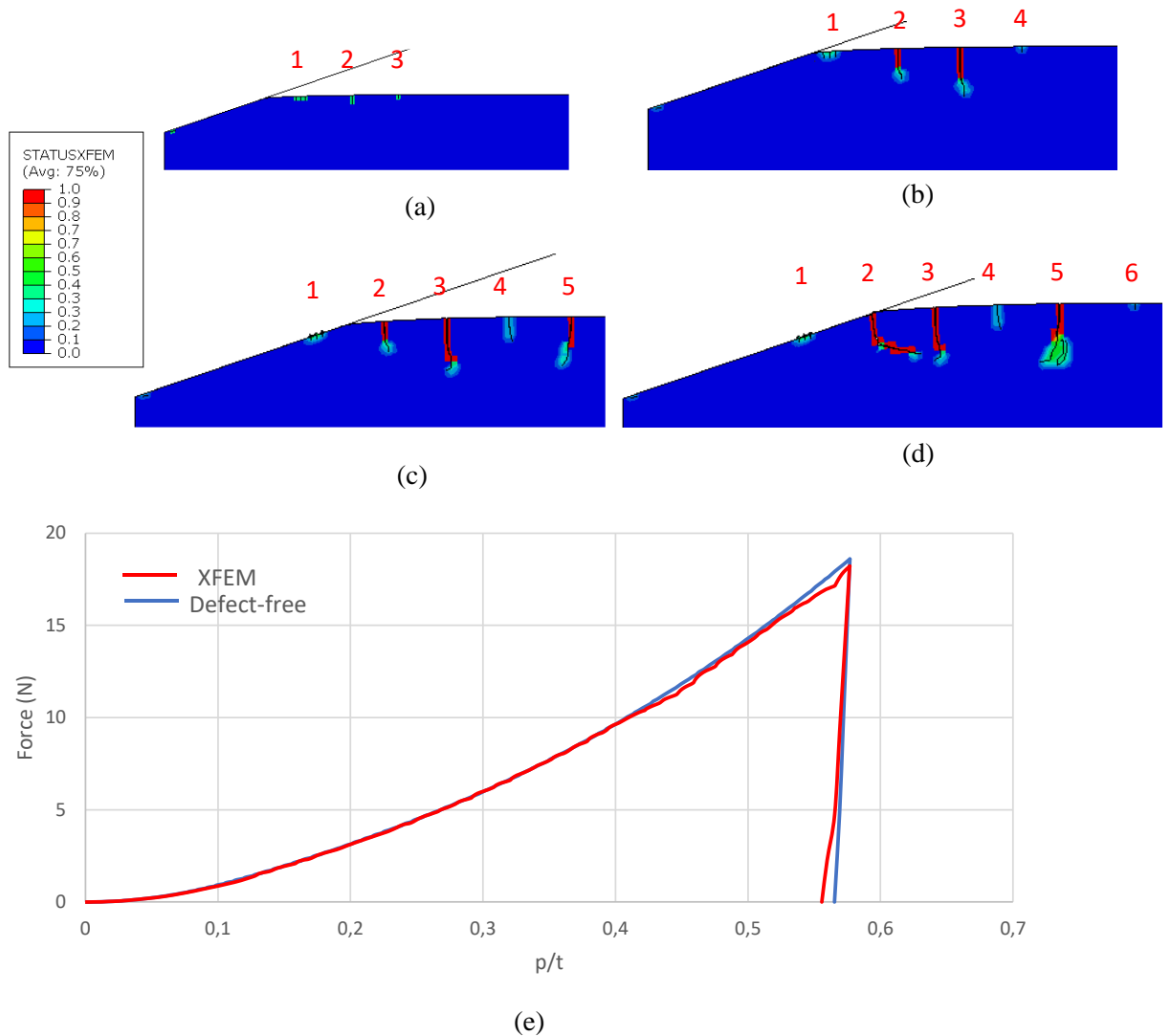


Figure 5.32: Circular crack evolution at 4 moments of the indentation (a) $p/t=0.32$ (b) $p/t=0.39$ (c) $p/t=0.51$ (d) $p/t=0.6$. (T-S law parameters : critical stress 400 MPa, energy 12 J/m² energy) (e) comparison of the force-displacement curve with the XFEM approach and the defect-free simulation

The multi-cracking comparison can be made with another critical stress, 800 MPa (Figure 5.33). The crack location range is reduced (30 to 63 μm) and only two cracks really propagate. There is no clear evidence of the influence of the critical stress on the localization of the crack. In fact, given the thickness of the oxide and the hardness ratio, the tension zone appears on the surface at $p/t \sim 0.25$ ($a = 14\text{-}15\mu\text{m}$), with values immediately or rapidly exceeding 1000 MPa, and the crack opens at $R_c/a \sim 2$, i.e. 30 μm , at the outermost end of the tension zone. This is where values of the order of the critical stress are first reached, for critical stress much lower than 1700 MPa. If the critical stress were, say, 1200 or 1400 MPa, the opening would only occur at the top of the surface stress profile. In this case, there would be an influence of critical stress.

Moreover, the sensitivity to the parameters is not very important, it is linked to the fact that the rupture is essentially governed by the geometry (bending field).

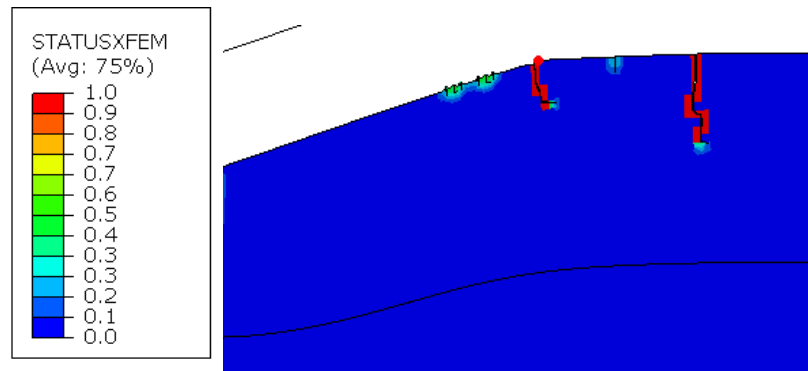


Figure 5.33: Circular crack evolution at the end of the loading for critical stress) 800 MPa ($G_{ox}=12$ J/m²)

The verification of the modelling of the crack formation needs a comparison with the cracks experimentally observed on cross sections. Remember that the FIB/SEM observations are always carried out after the nanoindentation test , and FIB preparation may in itself injure the cut surface, although to a limited extent. Indeed, the numerical cracks resemble those in the FIB/SEM cross sections in Figure 5.31. There are two important observations:

- the localization of the crack is also different, numerically there is no propagated crack that are located in the contact area in the end ($p/t = 0.6$), as is the case for two cracks at 25 and 30 μ m on the experimental side of Figure 5.31. This means that in the real material, some cracks initiate and propagate earlier than in the simulation, although it would be important to establish a criterion to define which experimental cracks are really “circular” (numerical ones are necessarily circular, due to the axis-symmetry assumption). Note that the superficial Magnetite and Hematite phases, that have a lower toughness are not considered here.

- the total length is also lower than in the experimental case.

However, the crack path is well predicted by the XFEM and understandable from the stress field evolution. This propagation is in two steps, first normal to the surface, then deviating as observed in the FIB cross-sections.

Another element to keep in mind is that numerically the oxide material is considered initially from a continuum mechanics point of view, so that the irregularities such a porosity or flaws are not considered, which may influence the cracks propagation.

After the study of the circular crack at the surface, the same methodology is used to model the normal crack at the interface.

5.6 XFEM for “normal” cracks (normal to the interface)

5.6.1 Description of the model

A similar model is used for the simulation of normal cracks; however, the crack initiation site is at the interface. The size of the XFEM pre-crack is $2\ \mu\text{m}$ in vertical direction at 5 to $30\ \mu\text{m}$ from the axis since in the experiments, the cracks are always localised below the final contact area. The whole oxide layer is considered as the XFEM enrichment domain.

The film/ substrate interface is assumed to be perfectly bonded (i.e., no delamination).

In the first case presented below, the initiation site is at $10\ \mu\text{m}$ from the axis and the T-S law parameters are:

- the criterion « Maxps damage » is set to 300 MPa (remember that the tensile stress at the interface at the stage where normal cracks appear reaches 500 MPa, Figure 5.9 (b)).
- the energy damage evolution is linear and mode-independent with $G_{\text{ox}} = 12\ \text{J/m}^2$ (equivalent to $K_I = 1.7\ \text{MPa}\cdot\sqrt{\text{m}}$, consistent with the literature).

5.6.1.1 Results

For the initiation, at the interface, there is a moderately tensile area (σ_{11}) at the beginning of the indentation, for $p/t \approx 0.1$. As soon as the critical stress 300 MPa is reached ($p/t = 0.1$) the crack is initiated (Figure 5.34 (a)). Then it propagates almost normally to the interface, in the bottom-top direction, and tends to deviate towards the axis. As indentation proceeds, the large compressive zone below the indentation reaches the crack tip, and crack propagation is stopped at $p/t = 0.11$ (Figure 5.34 (b)). It explains the small crack length observed experimentally. A good agreement is noted with the experimental test (Figure 5.34d).

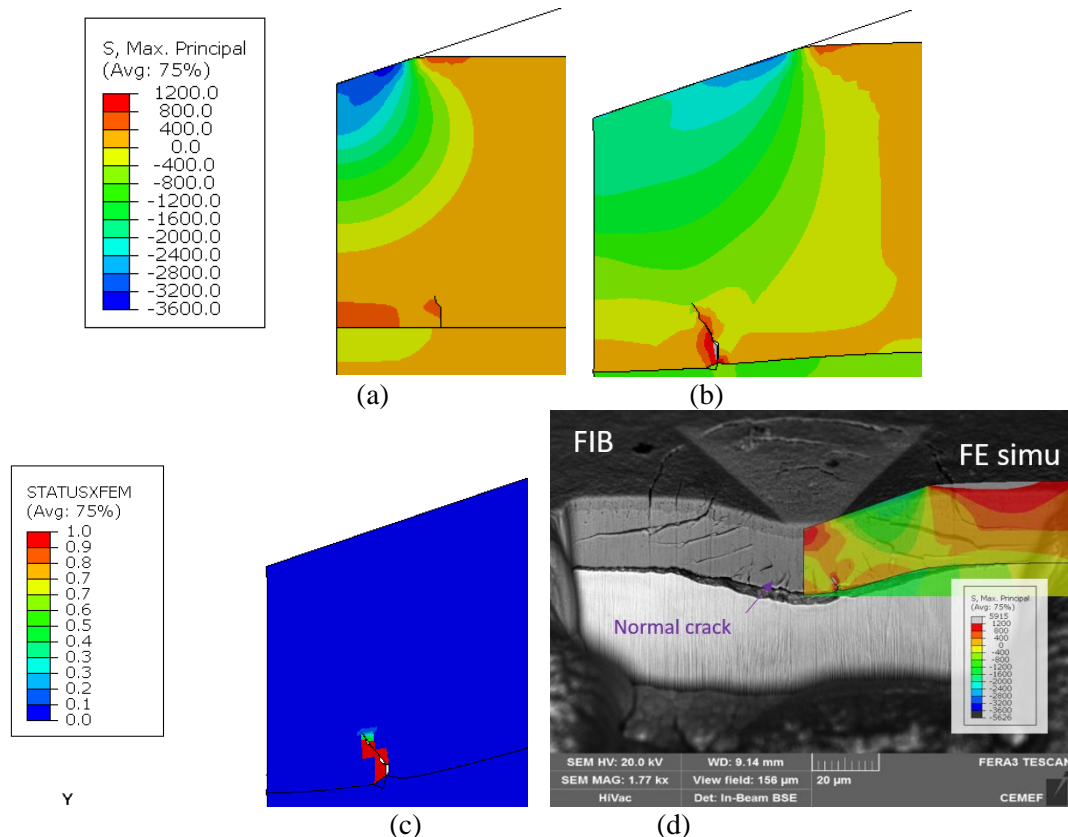


Figure 5.34: Evolution of the crack normal to the interface ; initiation site $10\ \mu\text{m}$ from the axis, critical stress 300 MPa, fracture energy $G_{\text{ox}} 12\ \text{J/m}^2$. (a) maximum principal stress at the initiation ($p/t=0,1$) (b) maximum principal stress at the end of the propagation ($p/t=0,11$) (c) StatusXFEM at the end of the loading (d) Comparison between the experimental FIB cross-section and the XFEM simulation

At $p/t=0.6$, the crack length observed is between 4 and 10 μm (Figure 5.34 (c)). Compared with the circular crack starting from the surface, the normal crack propagation is limited to the beginning of the indentation. In Figure 5.34 (c), the status of the enriched element is described.

5.6.1.2 Influence of pre-crack location

Experimentally, the cracks are always localised below the final contact area. Here, the radial position is varied from 5 to 30 μm (critical stress of 300 MPa and $G_{ox}=12 \text{ J/m}^2$).

Both the initiation penetration and the final crack length are increasing when the initiation site is shifted outward (Figure 5.35 (a)).

For an initiation close to the axis (5 to 15 μm), the same crack path is observed, with a deviation towards the indentation apex and the crack actually stops when reached by the compression zone (Figure 5.34). The increase of the crack length corresponds to a longer propagation as it takes more time for the compressive stress zone to reach the crack tip.

It is clear that the crack propagates quite differently for an initiation site $R_c = 20\mu\text{m}$, the propagation starts at the end of the loading ($p/t = 0.5$) and the crack length is 2.8 μm at the end of the loading ($p/t = 0.6$), i.e. smaller than the previous ones; however in this case, the crack continues to propagate during the unloading (which is not observed for any other condition), resulting in a $\sim 8\mu\text{m}$ long crack in the end. The crack path is also different, due to absence of the compressive area during the unloading (Figure 5.35(b)). Note that the elements are partially cracked only at the crack tip, which makes the status of this outward growing prolongation of the crack dubious.

Finally, for a crack initiation far from the axis (30 μm), no propagation is observed, confirming the experimental localisation of the normal cracks close to the axis. In fact, even at the end of the indentation (contact radius 37 μm), $r = 30 \mu\text{m}$ is at the intrados of the doubly bent oxide layer, not at the extrados. σ_{11} is therefore compressive.

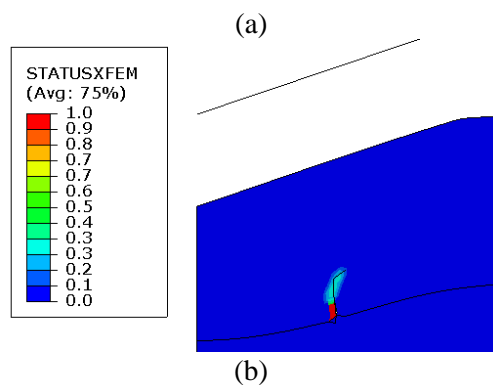
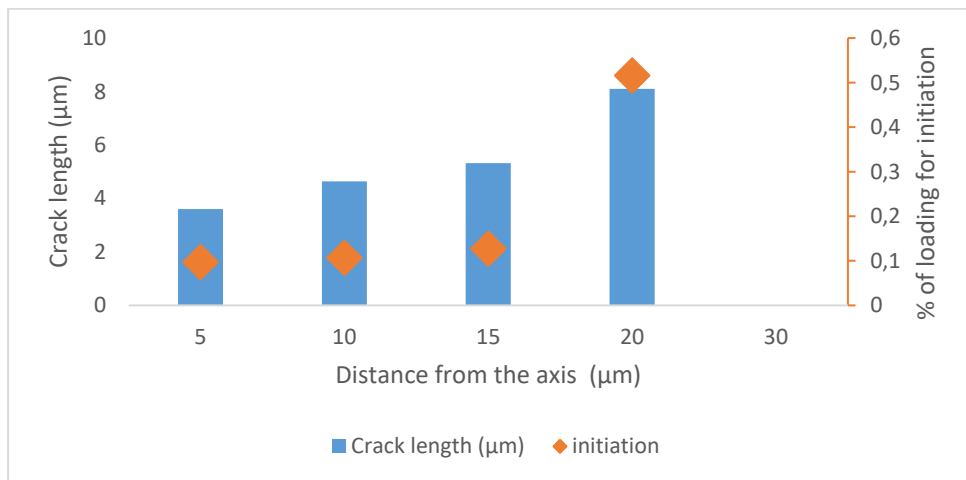


Figure 5.35: (a) Influence of the pre-crack site on the onset of propagation and the crack length (b) crack pathway for a pre-crack at 20 μm from the axis.

5.6.1.3 Influence of T-S law parameters

The T-S parameter range is adapted to the condition of normal cracks:

- critical stress: 150-500 MPa
- G: 1 to 50 J/m².

Critical stress

To study the influence of the critical stress, the energy G is set to 12 J/m². The pre-crack is 10 μm from the axis.

A too high critical stress ($t^0 = 450$ MPa and above) is never reached and the pre-crack does not propagate (Figure 5.36)).

For lower critical stresses, t^0 has a small impact on the onset of propagation, but in all cases, the cracks are initiated when the ratio $p/t \sim 0.1$ (between $p/t = 0.09$ and 0.11). When the crack starts earlier, its final length seems to be higher, because it has more time before it meets the compressive contact zone.

For stresses below 200 MPa, simulations did not converge until $p/t = 0.6$, probably due a too fast crack propagation. Therefore, the final length is not available, a lower bound is represented.

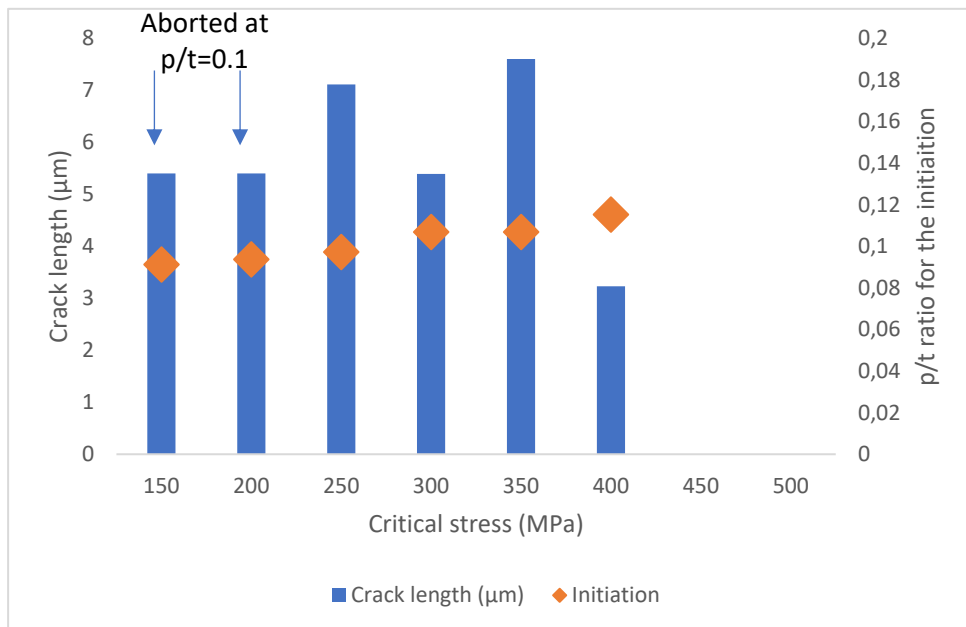


Figure 5.36: Influence of the critical stress on the onset of propagation and on the crack length. $G_{ox} = 12$ J/m² and the crack site is at 10 μm from the axis.

Cohesive energy G_{ox}

The cohesive energy G is largely varied from 1 to 50 J/m² while the critical stress is set to 300 MPa. It has no influence for the initiation of the crack ($p/t = 0.1$ for all simulations). By reducing the energy, the final crack length is slightly increasing (Figure 5.37). It can be explained by the “slowest” propagation rate when the energy to fracture is higher. This influence is however small, increasing the energy by a factor of 50 gives, representing only a 40% of increase of the crack length.

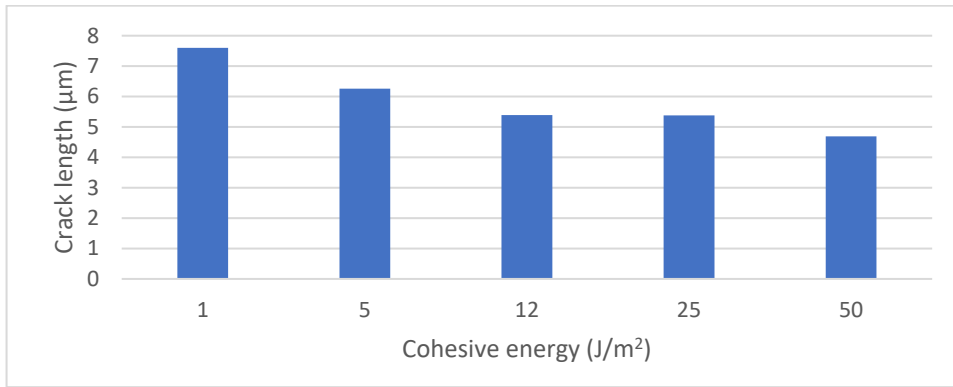


Figure 5.37: Influence of the fracture energy on the crack length (Critical stress is set to 300MPa and the crack site is at 10µm of the axis).

We may conclude that normal cracks are mainly governed by the global stress field resulting from the indentation and interface geometry. Propagation results from the pre-crack being at an extrados of the bending oxide layer and stops as soon as the growing crack meets the compressive, sub-contact zone. From the graphs above, given that normal cracks are found experimentally, we can affirm that $t^0 \leq 400$ MPa; the crack lengths obtained let us assume that $300 < t^0 < 400$ MPa. As for G_{ox} , its influence is too small to determine it, normal cracks are not a good observable for this purpose.

5.6.2 Conclusion on the room temperature indentation

The normal and circular cracks and delamination have been well reproduced qualitatively with the XFEM methodology. CZM and XFEM confirm the order of appearance of the diverse cracks:

- normal cracks which initiate and propagate only for $p/t \sim 0.1$, when an extrados forms on the doubly bending interface after the end of the validity of the “1/10th rule”
- delamination, starting a few µm from the axis at $p/t \sim 0.2$ when the shear band due to the local shear force reaches the interface, and propagating all along with the growth of the indentation radius,
- circular, from $p/t \sim 0.3$ when significant plate bending forms a large tensile zone at the surface, and propagating until the compressive contact zone reaches it,
- and finally, corner cracks (not modelled in this work)

These bounds are of course given for the conditions investigated here, namely $H_{V_{oxide}} / H_{V_{steel}} = 3$. This ratio probably has a significant influence on the way the oxide bends over the deforming steel, its radii of curvature, therefore on the p/t range in which the different fracture mechanisms occur.

The interaction between delamination and the other cracks has not been considered. Normal cracks seem to form and stop before delamination starts, however, the normal crack tends to redistribute stresses and may impact delamination. Delamination and circular cracks are triggered by different components of the stress field and seem to live their lives separately. But more work is needed, since literature claims an interaction: according to Shu et al. [170], the interfacial delamination hastened the cracking at the bottom surface of the film because of the enhancement of the film stretching. Indeed, normal cracks are like defects of the interface and may explain e.g. why the later-growing experimental delamination always includes the axis, contrary to the simulations without crack interaction.

5.7 Transposition to high temperature

In order to determine fracture parameters usable for the simulation of the descaling, the high temperature indentations are also computed with the same methodology. In this approach, the previous model is adapted to reproduce the high temperature tests. The results of section 4.5.2 indicate that during high temperature indentation, the interfacial delamination is quite difficult to interpret because of the oxide buckling/blistering. Thus, this study is focused on the circular crack visible from the surface. In Figure 5.38 for instance, only one crack is observed and localised at a distance of 17 μm from the centre of the indentation for a 600°C Berkovich indentation on IF_700_4.5 sample.

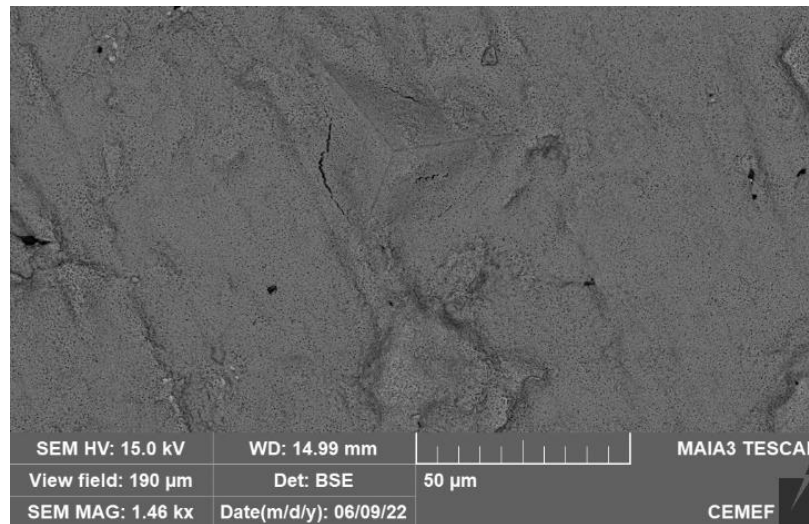


Figure 5.38: Berkovich indentation at 600°C on the IF_700_4.5 ($p/t=1.4$, indentation speed 0.25 $\mu\text{m/s}$).

5.7.1 Description of the model for high temperature indentation

Different tests are simulated at high temperature to evaluate the properties of the thin film. For each temperature, both the indenter and the sample are at the same temperature to make the simulation isothermal – as in the experiments. The geometry of the tip is the same (Berkovich and Vickers tips have the same equivalent angle, 70.3°). The oxide is perfectly bonded to the oxide (ie. no delamination). It must be borne in mind that the oxide thickness is much lower (4.5 – 7 μm) than in the case investigated at room temperature (26 μm). On the contrary, the penetration / thickness ratio p/t is larger (Table 5-2).

Table 5-2: Experimental indentations reproduced numerically

Grade	Thickness (μm)	Temperature ($^{\circ}\text{C}$)	Final ratio p/t	Speed ($\mu\text{m/s}$)	Crack
IF	4.5	600	1.4	0.25	Yes (17 μm from centre) (Figure 5.38)
HSLA	7	700	1.55	0.25	No
HSLA	7	700	1.55	30	Yes (28 μm from cent)
IF	4.5	800	1.4	0.25	No
IF	4.5	800	1.4	3	No

The material law is extracted from the study of Picqué [4]. A visco-elasto-plastic behaviour is considered for both oxide and steel are given as a visco-elasto-plastic behaviour. Relaxation effects detailed in the DRX study of chapter 3 plead for this at temperatures of 600°C and above. Furthermore, tests described in section 4.5.2 have shown a strong dependence of indentation load on indentation speed (Figure 4.34 (a)).

Assuming isotropic elasticity and in agreement with the literature [98,99], the Young’s moduli of oxide and steel are decreasing with increasing temperature and are given in Table 5-3. In the absence of more precise data, Poisson’s coefficients are taken as 0.3.

The visco-plastic part is defined with the identification of two parameters, the consistency K, the strain hardening coefficient n and the strain rate sensitivity coefficient m, as follows:

$$\sigma = K(T)\varepsilon^{n(T)}\dot{\varepsilon}^{m(T)} \quad (5-5)$$

Coefficient K is multiplied by 3 for the oxide, because the ratio of hardness used at room temperature is still valid in the 600-800°C range [75] (Figure 4.30). m and n are assumed to be the same for oxide and steel, a strong hypothesis made necessary by the absence of reliable data for the oxide.

All the parameters used are described in the Table 5-3.

Table 5-3: Summary of all the material parameters used for high temperature indentation simulations

Temperature (°C)	Material	Young’s Modulus (GPa)	Poisson ratio	K (MPa)	n	m
600	Steel	175	0.3	307	0.152	0.1
	Oxide	175	0.3	921	0.152	0.1
700	Steel	145	0.3	213	0.159	0.1
	Oxide	164	0.3	639	0.159	0.1
800	Steel	125	0.3	124	0.139	0.1
	Oxide	153	0.3	372	0.139	0.1

For each configuration, a first “perfect” (defect-free) simulation is launched, followed by a XFEM simulation for surface cracks in the cases where cracks have been observed experimentally. For each temperature, a parametric study is made to evaluate the T-S law parameters. The same procedure as before is used, varying the critical stress, then the fracture energy. In this study, no initiation sites are introduced (no surface defect) as the previous part indicates that the presence of a pre-crack (a defect), tends to anticipate the initiation.

5.7.1.1 Circular crack - Indentation at 600°C (IF_650_4.5)

The “perfect” case is useful to determine the stress variation during the indentation (Figure 5.39). At the surface, for $p/t \geq 0.3$, a tensile area (σ_{11}) is observed, similar to the results described in the previous part, although the values are of course much lower than at 20°C: the circular cracks can be generated, provided that the critical stress for propagation is reached. The other stress components also show the same pattern as at 20°C, especially the shear stress σ_{12} , which means potential delamination and normal cracks at the interface. The latter are investigated after.

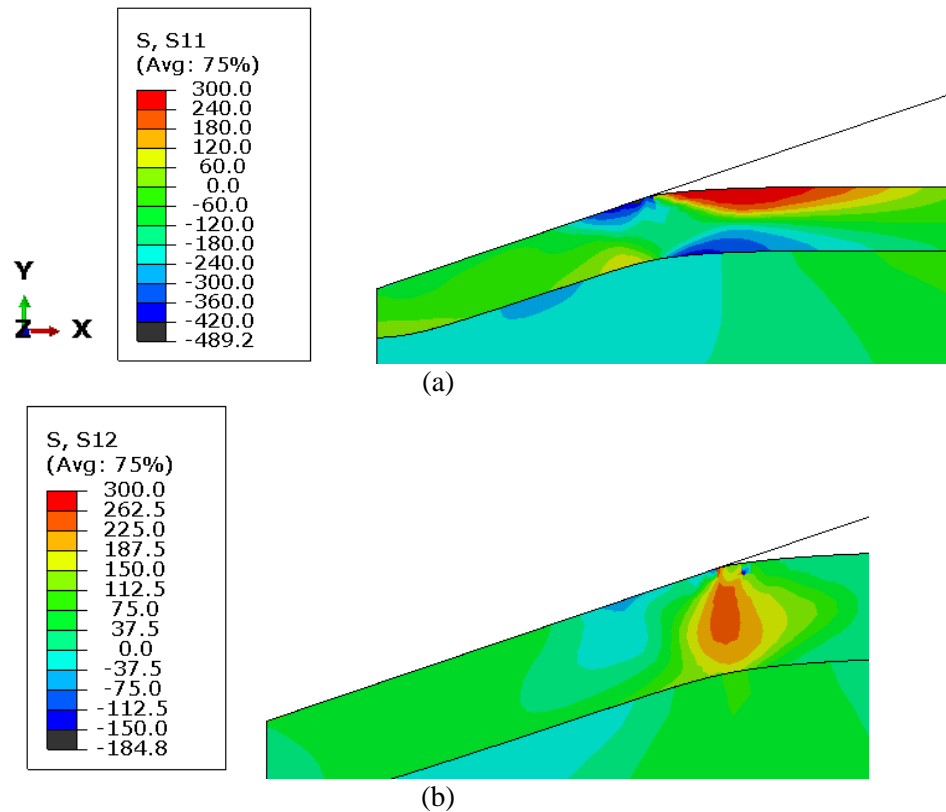


Figure 5.39: Stress evolution during the indentation at 600°C (final $p/t = 1.5$) (a) σ_{11} (b) σ_{12}

In a second stage, fracture modelling by XFEM is introduced. At 600°C, the T-S parameters are varied from 200 to 350 MPa for the critical stress and 1 to 50 J/m² for the energy.

For the small oxide thickness simulated here, the crack is initiated at a distance of 21 μm for a ratio p/t of 1,5, the crack is not deviating, and is limited to the subsurface (length below 1 μm) (Figure 5.40). There is no influence of the cohesive energy on initiation of the crack and the final crack length, the same crack length is observed whatever the fracture energy used. Thus, we tentatively select $G_{\text{ox}} = 12 \text{ J/m}^2$ by analogy with room temperature values.

The critical stress has a large impact on the circular cracking, being directly related to the initiation, increasing the delays to fracture. Considering a critical stress of 350 MPa, no cracks appearing the XFEM model.. At 300 MPa, a crack propagates by a fraction of a μm . The localisation is near the edge of the contact area ($a = 19 \mu\text{m}$), in good agreement with experiment ($R_{\text{c_exp}} = 17 \mu\text{m}$ versus 21 μm in the simulation). In the corresponding experiments, cracks are observed in half of the experiments. This means that the critical stress is in the 300 MPa range.

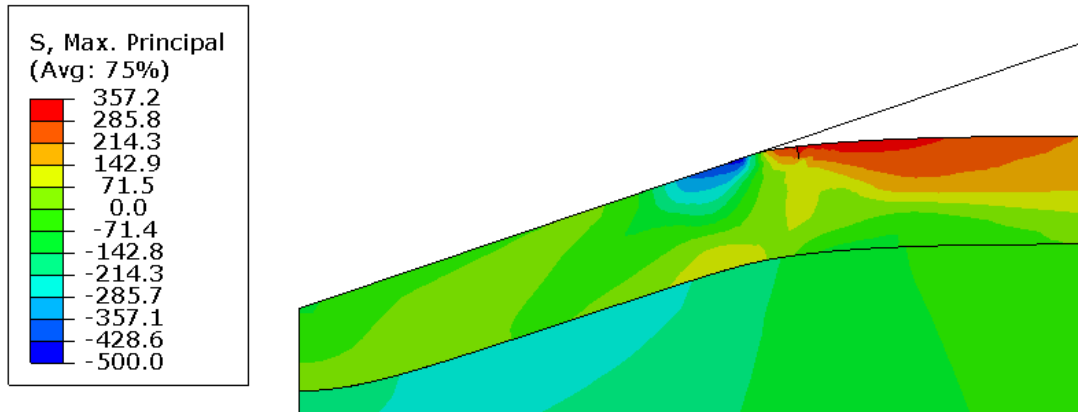


Figure 5.40: The XFEM crack at the end of the loading at 600°C on a 4µm oxide thickness. Critical stress 300 MPa, Fracture energy 12 J/m². ; $p^*/t = 1,5$, $a^* = 19, \mu\text{m}$, $R_c = 21 \mu\text{m}$

5.7.1.2 Indentation at 700°C (HSLA_700_7)

The same procedure is used for the higher temperatures. In the experiments at 700°C, for a speed of 0.25 µm/s, no circular cracks are visible from the surface (in this case with 7 µm of oxide). This means that in the simulations, the critical stress must be selected such that it is not reached. In other words, we can only determine a lower bound of the critical stress. The simulation without fracture gives a maximum σ_{11} of 210 MPa at the end of the loading.

By increasing the displacement rate by a factor of 120 (30µm/s), a circular crack is present in the experiment at a distance of 28 µm from the centre of indentation (Figure 4.34). At higher speed, the stress values are increasing due to the strain rate dependence. For example, the maximum stress in the corresponding fracture-less simulation is $\sigma_{11} = 320$ MPa.

We can conclude that the critical stress at 700°C is between 210 and 320 MPa.

In order to confirm this hypothesis, XFEM areas are added with a critical stress of 300 MPa and $G_{ox}=12$ J/m² in agreement with the previous results. A numerical crack is generated at a distance of 24 µm from the axisymmetric axis (close to the experimental 28µm) (Figure 5.41). The crack does not grow because it is soon reached by the compressive stress field of the indentation. If the critical stress is increased to 350 MPa, the simulation predicts no crack, in agreement with the results of the fracture-less simulations.

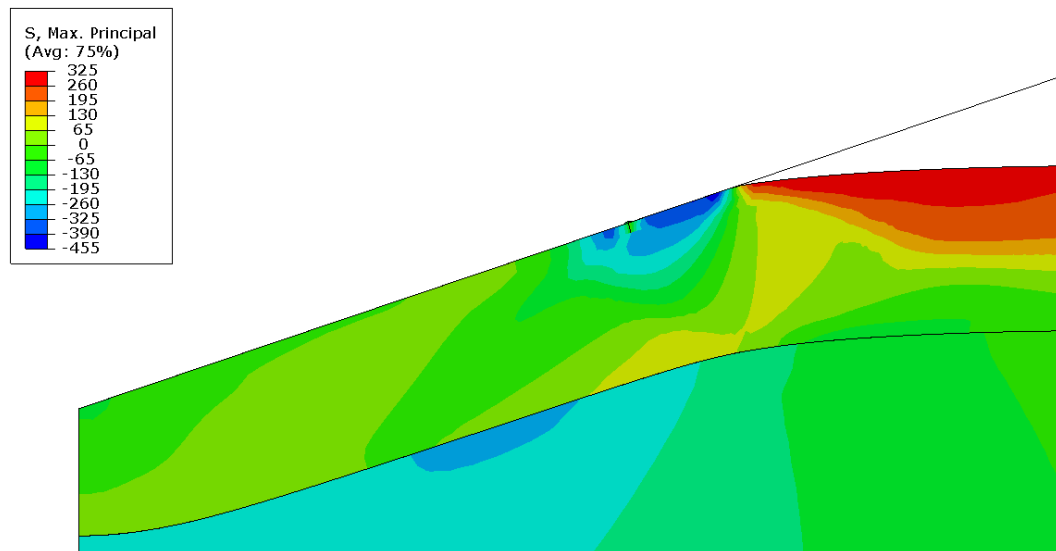


Figure 5.41: Circular crack generated during the indentation of HSLA_700_7 at 700°C at the end of the loading : $t = 7 \mu\text{m}$, $p = 10 \mu\text{m}$, $a_{final} = 28 \mu\text{m}$, critical stress 300 MPa, Fracture energy 12 J/m²; $p^*/t = 1$, $a^* = 19,5 \mu\text{m}$, $R_c = 24 \mu\text{m}$

5.7.1.3 Indentation at 800°C (IF_650_4.5)

At 800°C, considering the two speeds used (0.25 $\mu\text{m/s}$ and 3 $\mu\text{m/s}$), no cracks have been observed in the experiments for the 4.5 μm oxide thickness. This means that the critical stress at this temperature should not be reached numerically, i.e. that the critical stress is above 170 MPa (the maximum stress for the 3 $\mu\text{m/s}$ displacement rate in a fracture-less simulation, Figure 5.42).

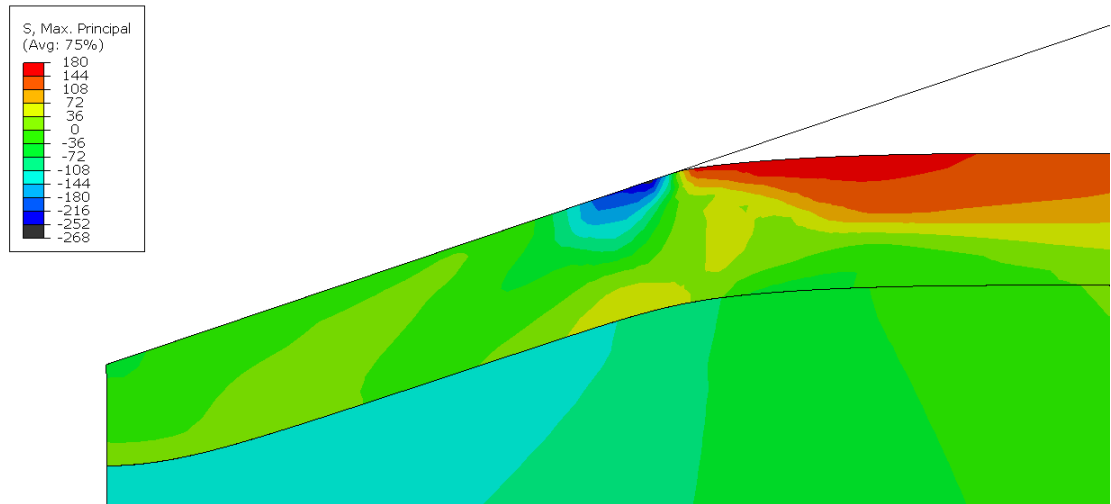


Figure 5.42: Maximum principal stress map at the end of the loading for an indentation at 800°C
Fracture-less simulation, displacement rate 3 $\mu\text{m/s}$. $t = 4.5\mu\text{m}$, $p = 7\mu\text{m}$, $a_{\text{final}} = 19\mu\text{m}$

5.7.1.4 Impact of temperature on fracture parameters

The critical stresses evaluated for each temperature are summarised in the Table 5-4. In the Figure 5.43, the maximum stress component reached in the simulation is indicated. The red bar represents simulations where cracks are observed (the critical stress is below these values), the green bar corresponds to the configurations in which no crack is observed (the critical stress is larger). The strain rate study allows a better estimation of the critical stress – assuming the latter is rate-independent.. The critical stress tends to decrease with the temperature, however the ratio t^0/H is increasing.

Table 5-4: Critical stress for circular cracks evaluated

Temperature (°C)	Critical stress t^0 (MPa)	Ratio t^0/H
20°C	~400	0.06
600°C	$t^0 \leq 300$	≤ 0.3
700°C	$210 \leq t^0 \leq 310$	$0.42 \leq t^0/H \leq 0.64$
800°C	≥ 170	≥ 0.52

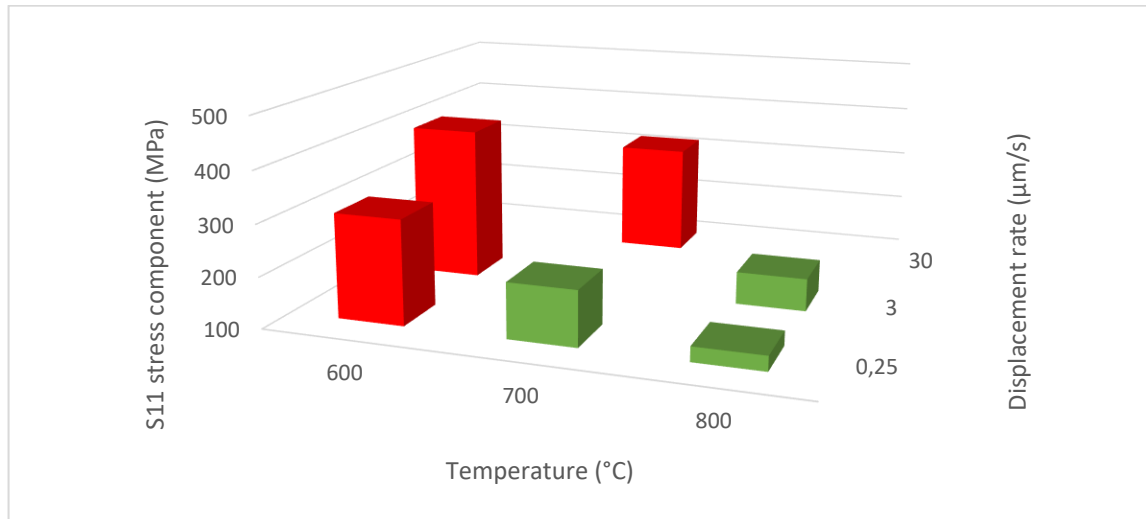


Figure 5.43: Influence of the temperature and the displacement rate on the maximum stress component (MPa). Green bars refer to indentation in which no crack has been observed, red bars to indentation in which cracks are noticed

The fracture behaviour and the critical stress of oxide is determined at high temperature. Given the limited number of tests carried out, only ranges are evaluated.

5.7.2 Delamination for adhesion

Concerning the interface, no large and clear delamination is observed at high temperature. We can consider that the critical shear stress (responsible for the delamination at room temperature) is not reached at the interface. From the defect-free simulation (without CZM elements at the interface), the shear band is reaching the interface with a value of 180 MPa at 600°C and 100 MPa at 800°C, which proved experimentally incapable to trigger delamination under the contact. We might therefore conclude that $t^0 > 180$ MPa at 600°C and $t^0 > 100$ MPa at 800°C. However, these values are much higher than the 25 MPa calculated at room temperature.

However, a curious decohesion at the edge of indentation has been noticed (see Figure 4.38). The computed stress field in this area shows a positive normal component during the unloading ($\sim +50$ MPa at 600°C) (Figure 5.44). This normal stress being much lower than the shear stresses, could it be the reason for a delamination? In the simulation, the same t^0 is selected for mode I and mode II. Only an interface with “normal” properties lower than the shear properties could explain this partial delamination. This could be an explanation. However, small decohesions identical to the one observed on the edge of this indentation have also been widely observed far from the indentation on this same sample, which means poor adhesion of the oxide after 2 thermal cycles before indentation. This indentation has perhaps been performed on an already delaminated or pre-damaged area. More observations on better quality samples would be necessary to investigate this peculiar phenomenon.

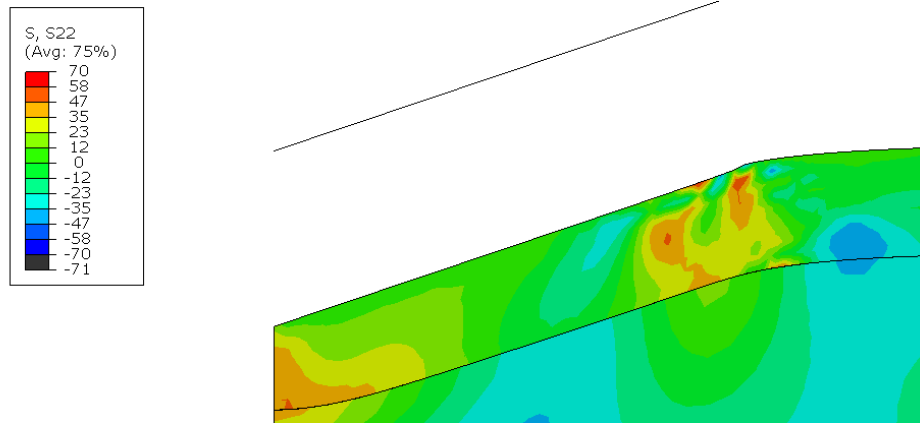


Figure 5.44: σ_{22} stress component at the end of the unloading (600°C , penetration of $7\mu\text{m}$, oxide thickness $4.5\mu\text{m}$)

The delamination of oxide is still not understood at high temperatures. The delamination observed during the indentation at room temperature (initiated by the shear component) is not reproduced at high temperature. Therefore, only lower bounds of interface shear resistance can be assumed. Furthermore, uncontrolled oxide buckling has been observed in experiments, due to the thermal stresses generated during re-heating. It prevents further analysis, requesting different experimental protocols.

5.8 Conclusion

This chapter presents numerical simulations that are conducted to understand the experimental data. Indentations discussed in Chapter 4: are successfully modelled for different conditions including oxide thickness, temperature, and tip penetration. After investigating various configurations such as 3D, indenter geometry, and the influence of residual stresses, the model was simplified to a 2D axisymmetric indentation on a single-phase, stress-free oxide to reduce computation time.

The chapter is composed of three types of simulations:

- Crack-free simulation with a perfectly bonded oxide. The stress field during loading is analysed to explain the localization of cracks within the oxide and the chronology of fracture. The first stage involved normal cracks in the oxide initiated from the interface, followed by delamination at the interface, and finally circular cracks on the surface.

- Cohesive Zone Model simulations. Cohesive elements are implemented at the interface to allow oxide delamination. The high shearing stress component generated during indentation may be a first cause of delamination axial stresses being compressive on the interface. Due to the unique characteristics of the early stage of indentation on such thick layers (26 μm), delamination occurred only after a certain penetration depth, causing the centre of the contact to initially remain intact. Thus, a crack forms at a distance from the centreline and propagates inward and outward along the loading. To explain cases with a very wide delaminated area, well beyond the indentation edge, we propose the following scenario: a second delamination area is formed due to the tensile normal stress generated at the interface, far outside the contact area, at a deeper penetration. This second area joins the first delamination - if the indentation is deep enough.. In terms of CZM parameters, both the critical stress and the interfacial energy to initiate delamination are found to be the main parameters that influence the localization of the delaminated area. Values of 25 MPa for the critical stress and $G_c = 5 \text{ J/m}^2$ for the critical energy release rate allow approaching experimental measurements.

- An XFEM methodology with a Traction-Separation law has been implemented to reproduce the two-cracking behaviour observed in the experiments. The circular cracks on the surface are propagated in two stages, first normal to the surface and then deviating outward from the indentation. The initiation of the cracks is influenced by the critical stress (when $p/t \sim 0.3$), while the cohesive energy mainly impacts their propagation after deviation. However, the final crack length is underestimated compared to the experimental results. The potential for fracture simulation is confirmed by the creation of multiple XFEM regions near the indenter.

The normal cracks at the interface are generated at the early stage of indentation ($p/t \sim 0.1$) and propagated until reaching the superficial compressive stress. A good correlation was observed between the experimental tests and the model for the crack length and path. Values of $400 \pm 100 \text{ MPa}$ for the critical stress and $12 \pm 2 \text{ J/m}^2$ for the critical energy release rate ($K_{Ic} \sim 1.7 \text{ MPa}\cdot\sqrt{\text{m}}$) allow approaching experimental measurements.

The whole methodology is first developed for the room temperature indentation, and then is adapted to high temperature conditions, and the T-S parameters are identified to reproduce the high-temperature tests. The critical stress to fracture the oxide is found to decrease with increasing temperature. No clear interface delamination has been evidenced at high temperatures, so that only a lower bound of interface toughness parameters can be given. The same can be said of oxide bulk fracture at 700°C and 800°C since no crack has been found on which to fit the critical stress and energy release rate. At 600°C, the few cracks observed and simulated and the large dispersion of results give only a blurred view on these parameters. All the data extracted from this chapter are summarised in Table 5-5.

This double (experimental and numerical) methodology would benefit from in-situ monitoring of fracture propagation during experiments, such as by using acoustic emission signals or measuring superficial micro-displacements. The lack of information on the loading-displacement curves hinders precise identification of the development time of each crack family, and the corresponding p/t . Finally, it seems difficult to achieve high precision on critical stress and interfacial energy adhesion G_c and K_{Ic} because the observables (p^*/t , crack length and position) depend primarily on the geometry of the indentation and the stress field, and therefore on the hardness ratio.

Another point of interest would be to investigate the possible interactions between different crack types. For instance, do cracks perpendicular to the interface start because of delamination, or do they appear first and facilitate delamination? The model can also be made more complex to better represent the reality of the oxide, by considering the three oxide phases and their corresponding properties.

Table 5-5: Summary of the data extracted in this chapter

Temperature	Adhesive strength (MPa)	Adhesive energy G_c (J/m^2)	Fracture strength (MPa)	Fracture energy (G_{ox}) (J/m^2)	Fracture strength (GPa)	Fracture toughness Energy release rate for cohesive failure (G_c) (J/m^2)
	Interfacial properties (delamination)		Oxide properties in surface (circular crack)		Oxide properties at the interface (normal crack)	
RT	25	5 J/m^2	400	12	300 < t^0 < 400	12
600°C	-	-	< 300	12		
700°C	-	-	210 < t^0 < 310	12		
800°C	-	-	>170	12		

Résumé

Ce chapitre présente les simulations numériques réalisées pour comprendre les données expérimentales. Les indentations abordées au chapitre 4 sont modélisées avec succès pour différentes conditions, notamment l'épaisseur de l'oxyde, la température et la pénétration de la pointe.

Le chapitre est composé de trois types de simulations :

- des simulations sans fissure avec un oxyde parfaitement adhérent. Le champ de contrainte pendant le chargement est analysé pour comprendre la localisation des fissures dans l'oxyde et la chronologie de la fissuration. La première étape implique des fissures normales dans l'oxyde initiées à partir de l'interface, suivies par une délamination à l'interface, et enfin des fissures circulaires à la surface.

- des simulations impliquant une zone cohésive (CZM). Des éléments cohésifs sont insérés à l'interface pour permettre la délamination de l'oxyde. La forte composante de contrainte de cisaillement générée pendant l'indentation est une première cause de délamination, les contraintes axiales étant compressives sur l'interface. La délamination ne se produit qu'après une certaine profondeur de pénétration, ce qui fait que le centre de l'indentation est resté intact dans un premier temps. Puis, une fissure se forme à une certaine distance du centre de l'indentation, et se propage vers l'intérieur et vers l'extérieur le temps du déchargement. Pour expliquer les cas où la zone délaminée est très large, bien au-delà du bord de l'indentation, nous proposons le scénario suivant : une deuxième zone de délamination se forme en raison de la contrainte normale de traction générée à l'interface, bien en dehors de la zone de contact, à une pénétration plus profonde. Cette seconde zone rejoint la première délamination - si l'indentation est suffisamment profonde. En ce qui concerne les paramètres CZM, la contrainte critique et l'énergie interfaciale pour initier la délamination sont les principaux paramètres qui influencent la localisation de la zone délaminée. Les propriétés de l'interface sont faibles.

- des simulations utilisant une méthodologie XFEM a été mise en œuvre pour reproduire la fissuration au sein de l'oxyde. Les fissures circulaires en surface se propagent en deux temps, d'abord perpendiculairement à la surface, puis en s'écartant vers l'extérieur de l'indentation. L'initiation des fissures est influencée par la contrainte critique, tandis que l'énergie de cohésion a principalement un impact sur leur propagation après déviation. Cependant, la longueur finale des fissures est sous-estimée par rapport aux résultats expérimentaux. Dans un deuxième temps, les multi-fissurations expérimentales sont confirmés par la création de multiples fissures numériques. Les fissures normales à l'interface sont générées au début de l'indentation ($p/t \sim 0,1$) et se propagent jusqu'à atteindre la contrainte de compression induite par la pointe. Une bonne corrélation a été observée entre les essais expérimentaux et le modèle pour la longueur et la trajectoire des fissures. Des valeurs de 400 ± 100 MPa pour la contrainte critique et de 12 ± 2 J/m² pour le taux de libération d'énergie ($K_{IIC} \sim 1,7$ MPa. \sqrt{m}) permettent d'approcher les mesures expérimentales.

L'ensemble de la méthodologie est d'abord développé pour l'indentation à température ambiante, puis adapté aux conditions de haute température, et les paramètres T-S sont identifiés pour reproduire les essais à haute température. On constate que la contrainte critique de rupture de l'oxyde diminue avec l'augmentation de la température. Aucune délamination claire de l'interface n'a été mise en évidence à haute température, de sorte que seule une limite inférieure des paramètres interfaciales ce peut être donnée. Il en va de même pour la rupture de l'oxyde à 700°C et 800°C, car aucune fissure n'a été trouvée sur laquelle adapter la contrainte critique et le taux de libération d'énergie. A 600°C, les quelques fissures observées et simulées et la grande dispersion des résultats ne donnent qu'une première approximation de ces paramètres.

Conclusion

The objective of this study was to improve understanding of the behaviour of oxide at high temperature to fill a knowledge gap in descaling. The descaling defects have several origins, which depend on many parameters such as temperature, scale thickness, chemical composition... Most of them are interconnected and impede other aspects of the rolling process, so that they cannot be freely adjusted. During the descaling operation, the oxide scale suffers high levels of stresses, mainly coming from the temperature gradient existing in the scale layer when the water jets impact the strip surface. These stresses are responsible for fracture followed by spallation of the scale fragments. Thus, the descalability of a steel grade will be characterised by the capacity of the scale layer to fracture and to detach, all or in part but as homogeneously as possible, from the steel substrate. These phenomena are directly dependent on the process conditions but above all on the thermomechanical behaviour of the oxide scale, on its internal structure and on its adherence to the metal.

The final goal is to build a capacity to model numerically the descaling with proper oxide parameters, to observe which parameters influence the efficiency of the descaling, and to reproduce the oxide layer damage. A correct fracture data set is needed to reproduce in a coherent manner the industrial process.

First, an extensive bibliographic study has been performed to describe the descaling. It is a complex process that involves the fluid mechanics for the water jets, the oxide properties and the rolling conditions. This study is then focused on the global behaviour of oxide. Unfortunately, data found in the literature appeared to be unsuited to the extremely complex conditions applied by descaling. Among the questions was the applicability to descaling of oxide layers a few tens μm in thickness, of Wüstite properties (hardness, toughness) measured by diverse techniques on massive samples. In particular, the well-known ductile-brittle transition at intermediate temperature, close to the Wüstite decomposition temperature (570°C), is of primary importance for descaling. Another question was the interface fracture behaviour at high temperatures, its dependence on steel grade composition and its impact on “descalability” as felt by the HSM operators.

A mixed experimental – numerical methodology has been implemented to understand the thermo-mechanical behaviour of oxide.

The X-Ray diffraction has been used to evaluate both the phase changes and the internal stress evolution within oxide during thermal cycles, which clearly may impact descaling. The in-situ control of oxidation has highlighted the fast relaxation of growth or thermal stresses by plastic deformation at temperatures above 700°C , slow relaxation in the $600\text{--}700^\circ\text{C}$ temperature range, partial relaxation only below 600°C . This points to a slow transition between a visco-plastic behaviour at high temperature (“plastic oxide”, “lubricating oxide”) to elastic-plastic or brittle at low temperature. These oxide properties have been determined up to 810°C , i.e. in the range of temperature which we consider critical for descaling because of both high enough thermo-elastic stresses and sufficient brittleness.

Indentation has been chosen to characterise oxide and its interface in terms of fracture mechanics properties. Indeed, literature has shown that it allows the two fracture mechanisms to be addressed, within oxide and at the interface, which is its advantage for a complete description of oxide behaviour. A fairly wide campaign of micro-indentations has been carried out at room temperature, to set up the methods and protocols through a dialogue between experiments and numerical simulation ; CZM and XFEM were selected as crack prediction tools for the interface and bulk oxide respectively. Two steel grades have been compared, an Interstitial-Free (IF) and a High Strength Low Alloy (HSLA) steel. The experimental study, coupled with Focused Ion Beam (FIB) cross-sections, shows several families of cracks, all consistent with a well-known deformation mechanism for hard-on-soft indentation: jump of the plastic yielding into the steel substrate when the “ $1/10^{\text{th}}$ rule” is broken, fracture in mode I at the extrados of the bending oxide plate. The interfacial delamination is close to mode II, shear induced by the flow of steel under a 3 times harder oxide. Based on the experiment – simulation dialogue, realistic

Conclusion

values of initiation fracture stress (400 ± 100 MPa) and critical elastic strain energy release rate (10 ± 2 J/m²) have been identified. The rather large uncertainty ranges are due to the limited sensitivity of the observables (crack position, shape, length) to these two parameters of the XFEM model ; but part of it may result from the well-known variability of Wüstite properties. Nevertheless, these values are consistent with the known ones for bulk oxide. Furthermore, IF and HSLA show very similar behaviour for bulk fracture, but the latter has a more brittle interface. We can therefore conclude that the oxide bulk properties remain valid for the oxide layers formed on steels at temperatures 650-700°C in dry air. The more brittle interface of HSLA is also in line with the poor descalability reported by mill operators, if we admit that it will lead to very uneven descaling, formation of blisters and double-oxide layer rolling, embedding fragments.

The characterisation has been completed by a more limited set of micro-indentations at 600°C, 700°C and 800°C. The behaviour of oxide scale is also evaluated as a function of indentation speed for the same two steel grades, IF and HSLA. In accordance with industrial observations, HSLA presents a poor adhesion responsible for intensive blistering, due to alloying elements such as Mn. On both grades, the oxide is changing from a systematically brittle behaviour at room temperature to a more ductile one at 700°C and 800°C. 600°C gives an intermediate behaviour with random cracking, exacerbated when higher indentation speed is selected. A ductility map has been drawn in the temperature-speed diagram. It points to a graded brittle-ductile transition, just as we found a graded transition between stress relaxation at 700°C and no stress relaxation below 600°C. It is important to remind that these gradual evolutions are observed in a single oxide phase, Wüstite.

No clear interface delamination has been evidenced at high temperatures, so that only a lower bound of interface toughness parameters can be given. The same can be said of oxide bulk fracture at 700°C and 800°C since no crack has been found on which to fit the critical stress and energy release rate. At 600°C, the few cracks observed and simulated and the large dispersion of results give only a blurred view on these parameters.

Practical consequences can be proposed based on these characteristics at the temperatures involved during the descaling operations in the HSM. For the low carbon steels studied in this study, some conditions have to be respected for a good descaling:

- cool the oxide below or at least inside the transition ductile-brittle transition temperature range (600-700°C)
- generate thermal stresses above the critical stress to fracture oxide (which is tentatively estimated between 210 and 310 Mpa at 700°C) ; this requires a large temperature gradient, the stress generator, which in turn requires very fast cooling.
- rapid cooling is indeed necessary to avoid the relaxation of stress and enlarge the brittleness range (transition from an elasto-visco-plastic to elasto-plastic behaviour above 700°C), but this is guaranteed by the nature of the process.

Therefore, to optimise the descaling, an idea could be bring the temperature down into the brittle regime in surface at the entry of the finishing mill (e.g. by reducing the speed of the steel slabs), then to enhance heat transfer for faster cooling (increase pressure, water flow).

As a reminder, in the descaling study realised by Zhang et al. [9], the oxide surface is cooled down to 700°C and the interface to 800°C, the corresponding stress calculated is respectively 150 MPa (100 MPa) (see Figure 1.23). In the light of critical stresses evaluated here, it could be insufficient in practice and explain that cracks do not penetrate down to the interface, and the residual oxide part.

Indeed, there is still oxide after the descaling. This suggests that the supposedly ductile scale is not cooled enough and remains adherent, so that cracking is limited to the superficial oxide. This is probably why the complete delamination is not observed, and this is also what we see during high temperature indentation. Based on our results, we can assume that surface cracking (vertical propagation) is probably limited to the thickness in which the ductile-brittle transition has taken place, then cracks deviate to spall the fractured part of the oxide. There is also a stress gradient within the oxide, which generates shearing stress. These potential mechanisms have to be confirmed by the future descaling simulations.

For each part of the manuscript, we propose the following perspectives

The methodology described in this manuscript mainly for IF steel, secondarily for HSLA, should be applied to other grades of interest, in particular difficult-to-descale ones, Si grades for example that generate liquid phases at the interface above 1177°C. But protocols should be improved or complemented in different ways.

In the present study, the range of temperature has been limited to 560°C - 810°C in order to identify the two transitions, brittle to ductile and elasto-visco-plastic to elasto-plastic. We think it is the relevant temperature range into which oxide should be cooled during descaling. But austenite/ferrite transformation has not been considered. At 912°C (a temperature which depends on alloying elements), the volumetric change of steel tends to generate stresses in the oxide, tensile on cooling due to the sudden expansion of the ferrite. Indeed, some studies indicate that oxide fractures at this temperature in spite of its viscoplastic character, as observed during cooling from 1000°C to 900°C [4]. This has to be considered in real descaling since the transfer bar temperature is generally above 900°C at the entry of the descaling box. At the other end of the range, below 560°, Wüstite is no more stable and is transformed into Ferrite and Magnetite. The complex, long time evolution between 570°C and ~300°C is important for the behaviour of the oxide not so much during secondary descaling as during strip cooling in coils. It could be addressed by similar approaches.

All the described that are long (stabilisation of temperature, control of indentation parameters, time of analysis in XRD), much longer than the real descaling process, and we know now that strain rate is important in the behaviour of oxide. future tests should be conducted at shorter time scales:

- higher indentation speed (high strain rate) closer to descaling to evaluate more precisely the ductile brittle transition. It is now possible using the “Quenching furnace” described in Appendix D.
- the in-situ X-Ray diffractions made in the laboratory imply long times of analysis (25 minutes for a complete stress evaluation). These times have brought some relaxation capacity to light, but at high temperature, it is not enough. For future work, the synchrotron should be better adapted to analyse stress relaxation with measurement acquisition of stress within seconds [130] and a larger penetration depth.

Laboratory scale oxidation (in a separate furnace or reproduced in-situ) may also be different from secondary scale that have been deformed in the roughing mill. The history of oxide (thickness, porosity, temperature of oxidation) influences its behaviour. In terms of structure and compactness, we think the oxide investigated here was satisfactory, as shown by the mechanical properties identified, but the control of the thickness should be improved and the thickness range studied enlarged, as real oxide scales from the roughing mill are rather 80-100 µm thick, so that e.g. Hematite may not be negligible.

A crucial point in our approach is the simulation-based determination of critical crack initiation stresses from the experimental indentation tests. In the present study, due to the absence of a clear event (pop-in) on the force-displacement curve, determining the onset of fracture has necessitated multiple tests at increasing penetration p/t for each oxide thickness, and the identification of the p/t ratio at which the first cracks were detected. Certainty on the latter requires FIB cuts which cannot be done for each indentation, all the more as we feel that even more indentations would have been necessary for a better precision. This critical stress determination could be done more easily and more precisely if fracture could be continuously monitored, e.g. by Acoustic Emission. The technique is available at room temperature and has been used in with success in 4-point hot bending tests [4]. It is probably less simple during in-situ high temperature indentation.

Finally, the experiment-simulation dialogue proved essential and fruitful for the purpose of this work. Thanks to the simulations, the different fracture mechanisms have been well understood and reproduced, one by one independently. The next step should be to combine the fracture mechanism and the potential delamination. Particularly at the interface, the “normal” crack pattern and delamination may interfere with the redistribution of stresses induced at the crack tip. Also, in the present work, a single, uniform Wüstite scale has been considered, based on observation of cracked samples where Magnetite seems to play a role more in crack initiation (critical stress), whereas propagation (energy release rate) is in Wüstite. However, the internal structure is in fact much more complex: it can be composed of several oxide types organised in a multilayered system, voids (porosities) may be present and the steel/oxide interface, rarely flat, show a certain degree of roughness. Notion of adherence is also

Conclusion

not straightforward (and even less its quantification) but this property is a determinant factor regarding the descalability of a steel grade. These local effects should be considered in the descaling simulations to come. They would of course be even more important in studies of primary descaling, due to the much more defective internal structure.

Résumé

L'objectif de cette étude était d'améliorer la compréhension du comportement de l'oxyde à haute température afin de combler une lacune dans les connaissances sur le décalaminage. Les défauts de décalaminage ont plusieurs origines, qui dépendent de nombreux paramètres tels que la température, l'épaisseur de la calamine, la composition chimique... La plupart d'entre eux sont interconnectés et entravent d'autres aspects du processus de laminage, de sorte qu'ils ne peuvent pas être réglés indépendamment. Au cours du décalaminage, la calamine subit des contraintes importantes, principalement dues au gradient de température existant dans la couche de calamine lorsque les jets d'eau impactent la surface de la bande. Ainsi, la capacité à être décalaminée d'une nuance d'acier sera caractérisée par la capacité de la couche de calamine à se fissurer et à se détacher, en tout ou en partie mais de façon la plus homogène possible. Ces phénomènes dépendent directement des conditions du procédé mais surtout du comportement thermomécanique de la calamine, de sa structure interne et de son adhérence au métal.

La finalité est de construire un modèle numérique du décalaminage avec des paramètres d'oxyde appropriés, d'observer quels paramètres influencent l'efficacité du décalaminage et de reproduire les fissurations de la couche d'oxyde. Un ensemble de données adaptée sur les oxydes est nécessaire pour reproduire de manière cohérente le processus industriel.

Tout d'abord, une étude bibliographique approfondie a été réalisée pour décrire le décalaminage. Il s'agit d'un processus complexe qui implique la mécanique des fluides pour les jets d'eau, les propriétés de l'oxyde et les conditions de laminage. Cette étude se concentre ensuite sur le comportement global de l'oxyde. Malheureusement, les données trouvées dans la littérature semblent inadaptées aux conditions complexes du décalaminage. Parmi les questions posées, on peut citer le comportement lors du décalaminage de couches d'oxyde de quelques dizaines de μm d'épaisseur, des propriétés de la Wüstite (dureté, ténacité) mesurées par diverses techniques sur des échantillons massifs. En particulier, la transition ductile-fragile bien connue à une température intermédiaire, proche de la température de décomposition de la Wüstite (570°C), est d'une importance primordiale pour le décalaminage. Une autre question concerne le comportement de la rupture de l'interface à haute température, sa dépendance vis-à-vis de la composition de la nuance d'acier et son impact sur le décalaminage telle qu'elle est indiquée par les opérateurs du laminoir

Une méthodologie mixte expérimentale et numérique a été mise en œuvre pour comprendre le comportement thermomécanique de l'oxyde.

La diffraction des rayons X a été utilisée pour évaluer les changements de phase et l'évolution des contraintes internes dans l'oxyde au cours des cycles thermiques, ce qui peut clairement avoir un impact sur le décalaminage. Le contrôle in situ de l'oxydation a mis en évidence la relaxation rapide des contraintes de croissance ou thermiques par déformation plastique à des températures supérieures à 700°C , une relaxation lente dans la plage de température $600\text{-}700^\circ\text{C}$, une relaxation partielle seulement en dessous de 600°C . Cela indique une transition lente entre un comportement viscoplastique à haute température ("oxyde plastique", "oxyde lubrifiant") et un comportement élastique-plastique ou cassant à basse température. Ces propriétés de l'oxyde ont été déterminées jusqu'à 810°C , c'est-à-dire dans la plage de température que nous considérons comme critique pour le décalaminage en raison de contraintes thermo-élastiques suffisamment élevées et d'une fragilité suffisante.

L'indentation a été choisie pour caractériser l'oxyde et son interface en termes de propriétés mécaniques de rupture. En effet, la littérature a montré qu'elle permet d'aborder les deux mécanismes de rupture, au sein de l'oxyde et à l'interface, ce qui constitue son avantage pour une description complète du comportement de l'oxyde. Une campagne assez large de microindentations a été menée à température ambiante, afin de mettre en place les méthodes et les protocoles par un dialogue entre les expériences et la simulation numérique ; les méthodes CZM et XFEM ont été choisies comme outils de prédiction des fissures pour l'interface et l'oxyde, respectivement. Deux nuances d'acier ont été comparées, un acier (IF) et un acier faiblement allié à haute résistance (HSLA). L'étude expérimentale, couplée à des coupes transversales par Sonde Ionique Focalisée (FIB), montre plusieurs familles de

Conclusion

fissures, toutes cohérentes avec un mécanisme de déformation bien connu pour l'indentation couche dure sur substrat mou: déformation plastique dans le substrat d'acier lorsque la "règle du 1/10e" est dépassée, fissuration en mode I à l'extrados de la plaque d'oxyde en flexion. La délamination interfaciale est proche du mode II, cisaillement induit par l'écoulement de l'acier sous un oxyde 3 fois plus dur.

Sur la base du dialogue expérience-simulation, des valeurs réalistes de la contrainte critique d'initiation de la fissure au sein de l'oxyde (400 ± 100 MPa) et du taux critique de libération de l'énergie de déformation élastique (10 ± 2 J/m²) ont été identifiées. Les plages d'incertitude assez larges sont dues à la sensibilité limitée des observables (position, forme, longueur de la fissure) à ces deux paramètres du modèle XFEM ; mais une partie peut résulter de la variabilité bien connue des propriétés de la Wüstite. Néanmoins, ces valeurs sont cohérentes avec celles connues pour l'oxyde. En outre, IF et HSLA présentent un comportement très similaire pour la rupture, mais ce dernier a une interface plus fragile. Nous pouvons donc conclure que les propriétés de l'oxyde restent valables pour les couches d'oxyde formées sur les aciers à des températures de 650-700°C en atmosphère sèche. L'interface plus fragile du HSLA est également en accord avec la mauvaise décalaminabilité signalée par les exploitants de laminoirs, si l'on admet qu'elle conduira à un décalaminage très irrégulier, à la formation de cloques et à un laminage de la double couche d'oxyde, incrustants ainsi des fragments.

La caractérisation a été complétée par une série plus limitée de micro-indentations à 600°C, 700°C et 800°C. Le comportement de la couche d'oxyde est évalué pour les deux mêmes nuances d'acier, IF et HSLA. Conformément aux observations industrielles, l'acier HSLA présente une mauvaise adhérence responsable d'un cloquage intensif, dû à des éléments d'alliage tels que le Mn. Sur les deux nuances, l'oxyde passe d'un comportement fragile à température ambiante à un comportement plus ductile à 700°C et 800°C. 600°C donne un comportement intermédiaire avec une fissuration aléatoire, exacerbée lorsqu'une vitesse d'indentation plus élevée est choisie. Une carte de ductilité a été dessinée dans le diagramme température-vitesse. Elle indique une transition fragile-ductile graduelle, tout comme nous avons trouvé une transition graduelle entre la relaxation des contraintes à 700°C et l'absence de relaxation des contraintes en dessous de 600°C. Il est important de rappeler que ces évolutions graduelles sont observées dans une seule phase d'oxyde, la Wüstite.

Aucune délamination claire de l'interface n'a été mise en évidence à des températures élevées, de sorte que seule une limite inférieure des propriétés de l'interface peut être donnée. Il en va de même pour la rupture de l'oxyde à 700°C et 800°C, car aucune fissure n'a été observée pour adapter la contrainte critique et le taux de libération d'énergie. A 600°C, les quelques fissures observées et simulées et la grande dispersion des résultats ne donnent qu'une approximation de ces paramètres.

A l'issue de ces travaux, des indications pratiques peuvent être proposées aux températures impliquées lors des opérations de décalaminage dans le HSM. Pour les aciers à faible teneur en carbone étudiés dans cette étude, certaines conditions doivent être respectées pour obtenir un bon décalaminage :

- refroidir l'oxyde en dessous la plage de température de transition ductile-fragile (600-700°C)
- générer des contraintes thermiques supérieures à la contrainte critique de rupture de l'oxyde (estimée entre 210 et 310 Mpa à 700°C) ; cela nécessite un gradient de température important, à l'origine de contraintes, qui à son tour nécessite un refroidissement très rapide.
- un refroidissement rapide est en effet nécessaire pour éviter la relaxation des contraintes et élargir la plage de fragilité (transition d'un comportement élasto-visco-plastique à élasto-plastique au-dessus de 700°C), mais cela est garanti par la nature rapide du décalaminage.

Par conséquent, pour optimiser le décalaminage, une idée pourrait être diminuer la température pour atteindre le régime fragile en surface à l'entrée du laminoir de finition (par exemple en réduisant la vitesse des brames d'acier), puis d'améliorer le transfert de chaleur pour un refroidissement plus rapide (augmentation de la pression, du débit d'eau).

Pour rappel, dans l'étude de décalaminage réalisée par Zhang et al [9], la surface d'oxyde est refroidie à 700°C et l'interface à 800°C, la contrainte correspondante calculée est respectivement de 150 MPa (et 100 MPa). Au vu des contraintes critiques évaluées ici, cela pourrait être insuffisant en pratique et expliquer que les fissures ne pénètrent pas jusqu'à l'interface, et donc la partie résiduelle de l'oxyde. En effet, il reste de l'oxyde après le décalaminage. Cela suggère que la calamine supposée ductile n'est pas suffisamment refroidie et reste adhérente, de sorte que la fissuration se limite à l'oxyde en surface. Sur la base de nos résultats, nous pouvons supposer que la fissuration superficielle

(propagation verticale) est probablement limitée à l'épaisseur dans laquelle la transition ductile-fragile a eu lieu, puis les fissures dévient pour écailler la partie fracturée de l'oxyde. Il existe également un gradient de contrainte à l'intérieur de l'oxyde, qui génère une contrainte de cisaillement. Ces mécanismes potentiels doivent être confirmés par les futures simulations de décalaminage.

Pour chaque chapitre du manuscrit, nous proposons les perspectives suivantes

La méthodologie décrite dans ce manuscrit, principalement pour l'acier IF, puis pour HSLA, devrait être appliquée à d'autres nuances critiques, en particulier celles qui sont difficiles à évaluer, les nuances contenant du Si par exemple qui génèrent des phases liquides à l'interface au-dessus de 1177°C. Les essais devraient être améliorés ou complétés de différentes manières.

Dans cette étude, la plage de température a été limitée de 560°C à 810°C afin d'identifier les deux transitions, fragile à ductile et élasto-visco-plastique à élasto-plastique. Nous pensons qu'il s'agit de la plage de température pertinente dans laquelle l'oxyde doit être refroidi pendant le décalaminage. La transformation austénite/ferrite n'a pas été prise en compte. A 912°C (température qui dépend des éléments d'alliage), la variation volumétrique de l'acier tend à générer des contraintes dans l'oxyde, en traction lors du refroidissement du fait de l'expansion brutale de la ferrite. En effet, certaines études indiquent que l'oxyde se rompt à cette température malgré son caractère viscoplastique, comme cela a été observé lors du refroidissement de 1000°C à 900°C [4]. Il faut en tenir compte dans le décalaminage réel, car la température de la barre de transfert est généralement supérieure à 900°C à l'entrée de la boîte de décalaminage. À l'autre extrémité de la gamme de température, en dessous de 560°, la Wüstite n'est plus stable et se transforme en Ferrite et en Magnétite. L'évolution complexe et longue entre 570°C et ~300°C est importante pour le comportement de l'oxyde, non pas tant pendant le décalaminage secondaire que pendant le refroidissement de la bande dans les bobines. Elle pourrait être abordée par des approches similaires.

Tous les essais décrits sont longs (stabilisation de la température, contrôle des paramètres d'indentation, temps d'analyse en XRD), beaucoup plus longs que le processus de décalaminage réel, et nous savons maintenant que la vitesse de déformation est importante pour le comportement de l'oxyde:

- vitesse d'indentation plus élevée (vitesse de déformation élevée) plus près du décalaminage pour évaluer plus précisément la transition ductile-fragile. C'est maintenant possible en utilisant le "Quenching Furnace" décrit dans l'annexe D.

- les diffractions de rayons X in situ réalisées en laboratoire impliquent des temps d'analyse longs (25 minutes pour une évaluation complète des contraintes). Ces temps ont permis de mettre en évidence une certaine capacité de relaxation, mais à haute température, elle n'est pas suffisante. Pour les travaux futurs, le synchrotron devrait être mieux adapté à l'analyse de la relaxation de contrainte avec une acquisition de mesure de contrainte en secondes [130] et une plus grande profondeur de pénétration.

L'oxydation en laboratoire (pré-oxydation ou reproduite in situ) peut également être différente de celle de la calamine secondaire qui a été déformée dans le laminoir. L'historique de l'oxyde (épaisseur, porosité, température d'oxydation) influence sur son comportement. En termes de structure et de compacité, nous pensons que l'oxyde étudié ici était satisfaisant, comme le montrent les propriétés mécaniques identifiées, mais le contrôle de l'épaisseur devrait être amélioré et la gamme d'épaisseur étudiée élargie, car les couches d'oxyde réelles provenant du broyeur d'ébauche ont plutôt une épaisseur de 80-100 µm, de sorte que l'Hématite, par exemple, peut ne pas être négligeable.

Un point crucial de notre approche est la détermination par simulation des contraintes critiques d'initiation des fissures à partir des essais d'indentation expérimentaux. Dans cette étude, en raison de l'absence de variation (pop-in) sur la courbe force-déplacement, la détermination du début de la fissuration a nécessité des essais multiples à des taux de pénétration p/t croissants pour chaque épaisseur d'oxyde, et l'identification du rapport p/t auquel les premières fissures ont été détectées. La certitude sur ce dernier point nécessite des coupes FIB qui ne peuvent être pas effectuées pour chaque empreinte, d'autant plus que nous pensons qu'un nombre plus important d'empreintes aurait été nécessaire pour une meilleure précision. Cette détermination de la contrainte critique pourrait être

Conclusion

effectuée plus facilement et plus précisément si la fissuration pouvait être analysée en continu, par exemple par Emission Acoustique. Cette technique est possible à température ambiante et a été utilisée avec succès dans des essais de flexion à chaud en 4 points [4]. Elle est probablement moins simple lors de l'indentation in situ à haute température.

Enfin, le dialogue expérience-simulation s'est avéré essentiel et fructueux dans le cadre de ce travail. Grâce aux simulations, les différents mécanismes de rupture ont été bien compris et reproduits, un par un, indépendamment les uns des autres. L'étape suivante devrait consister à combiner le mécanisme de rupture et la délamination potentielle. En particulier à l'interface, la configuration "normale" de la fissure et le délamination peuvent interférer avec la redistribution des contraintes induites à la pointe de la fissure. De plus, dans ce travail, une seule couche de Wüstite uniforme a été considérée, sur la base d'observations d'échantillons fissurés où la Magnétite semble jouer un rôle plus important dans l'initiation de la fissure (contrainte critique), alors que la propagation (taux de libération d'énergie) se fait dans la Wüstite. Cependant, la structure interne est en fait beaucoup plus complexe : elle peut être composée de plusieurs types d'oxydes organisés en un système multicouche, de la porosité peut être présente et l'interface acier/oxyde, rarement uniforme, présente un certain degré de rugosité. La notion d'adhérence n'est pas non plus évidente (et encore moins son évaluation) mais cette propriété est un facteur déterminant du décalaminage d'une nuance d'acier. Ces effets locaux devraient être pris en compte dans les simulations de décalaminage à venir. Ils seraient bien sûr encore plus importants dans les études de décalaminage primaire, en raison de la structure interne plus défectueuse.

Appendices

Appendix A.

Stress in the different oxide phases

In this appendix, a more detailed literature review is done. First, the Table 0-1 summarises all the studies that analysed iron and steel oxide phases by X-Ray Diffraction. Secondly, three High-Temperature X-Ray diffraction stress analyses are described.

Table 0-1: Summary of phase analysis on iron and steel oxide (in bold, HTXRD analysis)

Grade	Oxidation conditions	Anticathode	Measurement Temp (°C)	Phase	Ref
High Strength Steel	600°C dry air	Cu	RT	W, M, H	[78]
Low carbon steel (540L)	900°C	Cu	RT	W, M, H	[119]
Hot-rolled carbon steels containing 0.04–0.18 wt.% C	Finishing rolling: 1020/860°C and coiling: 540–650°	Cu	RT	M, H	[85]
Continuous casting slabs	coiled finishing temperature 880°C)	Cu	RT	W, M, H	[120]
Micro-alloys steel	Oxidation 900–1200°C	Cu	RT	M, H	[121]
Low carbon steel	Oxide powder	Cu	RT	W, M, H	[122]
Iron plate	800°C for 24 hours	Cu	RT	W, M, H	[110]
Low carbon steel	Oxidation at 750°C	Cu	HT (900/700/550)	W, M phase transformation	[59]
Low carbon steel	Oxidation 1200/1140 °C	Cu	RT	W, M, H	[123]
Pure iron plate	Oxidation 700°C for 1.5 to 55 hours	Cu	HT (25/900)	W, M	[124]
Mild steel	Oxidation at 800, 900 and 1000°C	Cu	RT	W, M, H	[125]
Low carbon steel	Oxidation 850°C for 10s	Cu	RT	W, M, H	[86]
Powder		Cu	RT	H	[118]
Hot rolled low carbon	Oxidation at finishing temperature 760 and	Co	HT (760/200)	W, M,	[128]
High Strength steel (30)	Oxidation 900°C	Co	RT	H	[129]
Low carbon steel	800°C/1200°C	Co	RT	W, M, H	[80]

Pure iron	700°C	Co	HT (700 to 380)	W, H	[130]
Iron ARMCO	Oxidation at 260 and 500°C	Co	RT	M, H	[127]
Pure iron	Oxidation for 30 hours at 800°C	Cr	HT (800°C to RT)	W	[126]
Ultra High strength steel	Oxidation 900°C/1000°C	-	HT (1000 to 650)	W, M, H	[16]
1% Si Steel	Oxidation at 900°C 15 seconds	Synchrotron	HT (900 to RT)	W, M, H	[56]
Iron	Oxidation 650°C (10 hours)	Synchrotron	HT (650)	W, M, H	[131]

Juricic et al. study the isothermal oxidation of iron at 650°C for 10 hours. HTXRD is used with a synchrotron source to show the time-evolution of growth stresses in Magnetite and Wüstite, (Figure 0.1 (a)) [131]. This study emphasises growth stresses, since temperature is fixed. In addition, these in-situ measurements are compared to the residual stresses at room temperature (Figure 0.3 (b)), which points to the effects of thermal stresses. The penetration depth of X-Ray is about 45µm. The thickness of oxide at the end of the cycle is 150 µm for Wüstite, 8 µm for Magnetite and 1µm for Hematite (after 1 hour the thickness of oxide is 50µm). This means that only the superficial part of Wüstite is analysed during the test. The time of analysis for a stress measurement is 30 minutes.

In the isothermal measurement, Wüstite is in tension during two periods, 2.5-3.5 hours and 7-8 hours and in compression for the rest of the time. In the same period, Magnetite is in compression. During the test, the stress in Wüstite is observed to follow a trend, which is opposite to that encountered in Magnetite. The stress situation within this upper region of the Wüstite layer is influenced by the growth of Magnetite on it. According to the authors, during the isothermal cycle, the source of stresses are multiple :

- volumetric strain caused by differences in atomic volume between the first-formed grains of Magnetite and Wüstite. Indeed, the anionic volume ratio (AVR) is equal to 0.94 (defined at the Magnetite/Wüstite interface as $VO(Fe_3O_4)/VO(FeO)$, where VO represents the volume of the corresponding oxide per oxygen atom). It predicts that Magnetite, which has a smaller atomic volume, is subjected to tensile stresses, whereas Wüstite undergoes compressive stresses.
- within Wüstite, the gradient of stoichiometry across the thickness decreases towards its outer interface with Magnetite. It tends to reduce the volume with increasing distance to the iron substrate
- the micro-cracking in Wüstite (not observed in Magnetite) is relieving the stress, and it allows the inward migration of oxygen molecules. Oxygen can then rapidly react with iron, closing the micro channels within the Wüstite layer by inner oxide formation, thus causing compressive stresses
- the pore formation both in Magnetite and Wüstite is also a source of relaxation.
- creep occurs in Magnetite at 650 °C. The long-term creep further increases porosity at grain boundaries and causes intergranular failure. This allows inward oxygen migration and internal oxide formation. This causes increasing compressive stresses after 6 h of oxidation.
- however, the creep of Wüstite is hampered by its long columnar grains oriented perpendicular to the growth stresses.
- Magnetite is also influenced by the growth of Hematite, as Hematite has a greater atomic volume than Magnetite. This rapidly leads to high compressive stresses in Hematite during the early oxidation stages, but also supports the formation of tensile stresses in Magnetite at its interface with Hematite.

Due to the long-time analysis, it is not possible to accurately identify the sources, the measured value is therefore the sum of all components over time.

After cooling, the thermal stresses superpose to the stress state existing at higher temperature. Magnetite changes from compression to tension and stresses are still compressive within Hematite and Wüstite. It is what is expected from the CTE coefficients (see Figure 3.27). However, the values are

lower due to the micro-cracking which is likely to occur on cooling, relieving the internal stress in Hematite and Wüstite. This study emphasizes the fact that analysing the final state of the oxide is not enough to understand the behaviour of oxide at high temperature.

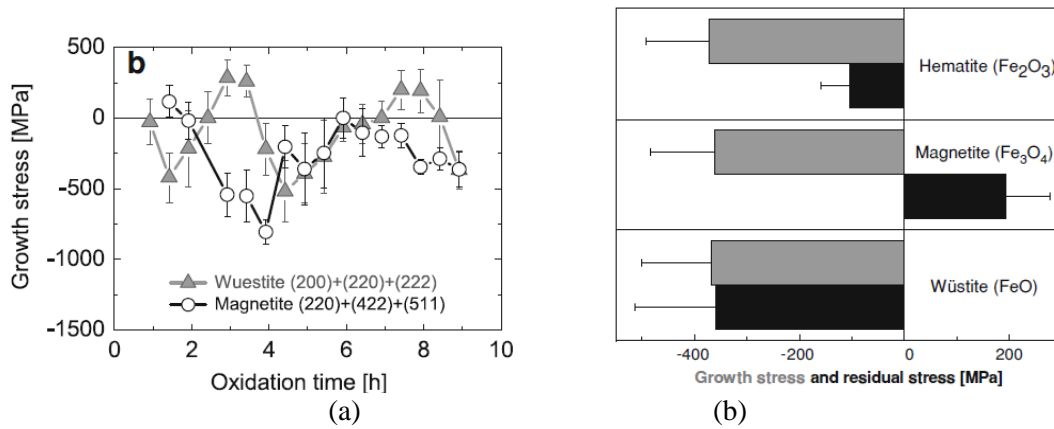


Figure 0.1: (a) time evolution of average internal stresses in Wüstite and Magnetite during isothermal oxidation at 650°C (b) comparison between growth stress values at 650°C for 10 hours (grey bars) and the residual stresses after cooling (black) [131]

Buscail et al. oxidize pure iron at 800°C for 30 hours (with an oxygen partial pressure $p(O_2) = 2.10^{-3}$ Pa ensuring slow oxidation) [126]. After 2 hours of oxidation, the thickness is equal to 5 μm . A kinetics test shows a linear regime (80 μm after 80 hours). Analysis is made with chromium radiation based on the {311} planes ($2\theta = 124^\circ$) of FeO. Thus, the entire Wüstite thickness is not analysed (penetration depth with Chromium is about 12 μm). The first 5 hours are the heating stage, only Fe peaks are visible, residual stress is relieved (by plastic deformation). It remains zero until time = +5 hours, i.e. 10 hours after the start of the experiment. The oxidation starts immediately but FeO is not sufficiently crystallised to be detected by XRD before 5 h. After $t = +5$ hours, the FeO peak is finally detected and stress is measured each hour (Figure 0.2). Stress is compressive during the whole process and maximal (-400 MPa) at $t = +5$ hours, i.e. initial growth, then it decreases in ca. 3 hours to -150 MPa. This compressive stress is attributed to the lateral growth of Wüstite. We have to keep in mind that after 10 hours of oxidation, only the surface of Wüstite is analysed. In this study, full relaxation is not observed in this study in comparison to Sasaki et al.

During cooling, this value is increasing, reaching -240 MPa at room temperature (explained by the thermal stresses). The authors observe Magnetite on the specimen at room temperature, because in-situ quenching is not possible and thus the decomposition of Wüstite into Magnetite has happened during the slow cooling process. The residual stress at 20°C can be modified by this phase transition.

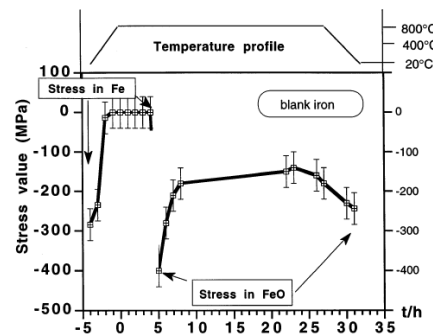


Figure 0.2 : In-situ stress value versus time for pure Fe specimen oxidized for 30 hours at 800°C under $p(O_2) = 2.10^{-3}$ Pa [126]

In Hayashi et al. [130], the stress behaviour of pure Fe during isothermal oxidation at 700°C and isothermal transformation at 500° and 380°C is measured by in situ high-temperature X-ray diffraction with the $\sin^2\psi$ method [130]. A rotating anticathode tube with a Co $K\alpha$ radiation and 2D detector is used. The phase analysis (Figure 0.3 (a)) shows that at 700°C, Wüstite is the main phase,

followed by the formation of a small amount of Magnetite. During cooling, at 500°C (below the Wüstite stability range), Wüstite is decomposed in two steps as described in the equation (2-3).

The stress in the oxide scale is analysed with the Fe_3O_4 {008} reflection ($2\theta = 117^\circ$) (Figure 0.3 (b)). Ψ angle is varied from 0 to 24° for 10s of recording. A tensile growth stress is generated during the isothermal oxidation at 700°C. It is attributed to the volume changes at the $\text{Fe}_2\text{O}_3/\text{Fe}_3\text{O}_4$ and $\text{Fe}_3\text{O}_4/\text{FeO}$ interfaces. During the heat treatment at 500°C, the tensile stress is due to the outer Fe_3O_4 growth that implies volume reduction. Finally, at lower temperature (380°C), the stress within Fe_3O_4 decreases and transitions to compression with the occurrence of the eutectoid reaction.

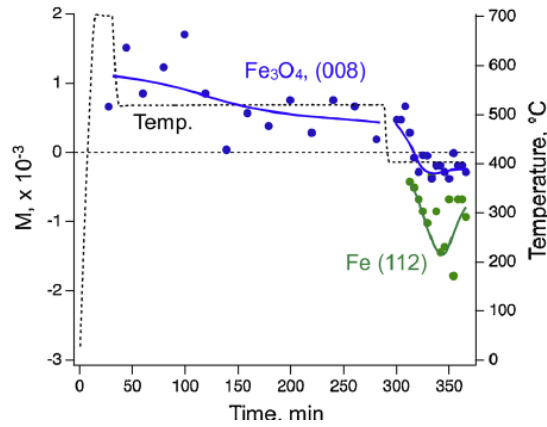


Figure 0.3: In situ stress measurement during isothermal oxidation at 700°C and isothermal transformation at 500°C and 380°C, . M is the slope of the $\sin^2\psi$ within Magnetite (blue) and Fe (green)

Appendix B.

Stress gradient within each oxide layer

For the stress analysis at room temperature detailed in section 3.5.3.2, there is no clear dependence on the thickness (Figure 3.25). For a same anticathode, the penetration depth is the same even if the thickness of oxide is increasing. For thicker samples (above 15 μm), only the superficial $\sim 12\ \mu\text{m}$ of the oxide is analysed.

In order to evaluate the evolution of stresses through the scale thickness, analysis can be made with different anticathodes. Indeed, the volume analysed is larger with Mn for example. For the 55 μm oxide thickness sample, by increasing the penetration depth from 12 μm to 20 μm (Cr to Mn source), the measured compressive stress in Wüstite changed from -130 to -150 MPa.

Similarly, by decreasing, the penetration depth with the Copper anticathode from 12 μm to 6 μm , the stress measurement changed from -105 to -90 MPa in Magnetite (the whole Magnetite is analysed with the 12 μm penetration, it is not the case for the 6 μm penetration). Globally, the residual stresses seem to be more compressive near the interface with the steel, but they gradually change towards the interface. It can be explained by the abrupt changes of thermal expansion at the existing interface as in [131]. As described previously, the compressive stress is higher in the Wüstite than in the Magnetite. The gradient of stress is visualised in the Figure 0.4. Nevertheless, this study has to be followed to confirm this stress evolution.

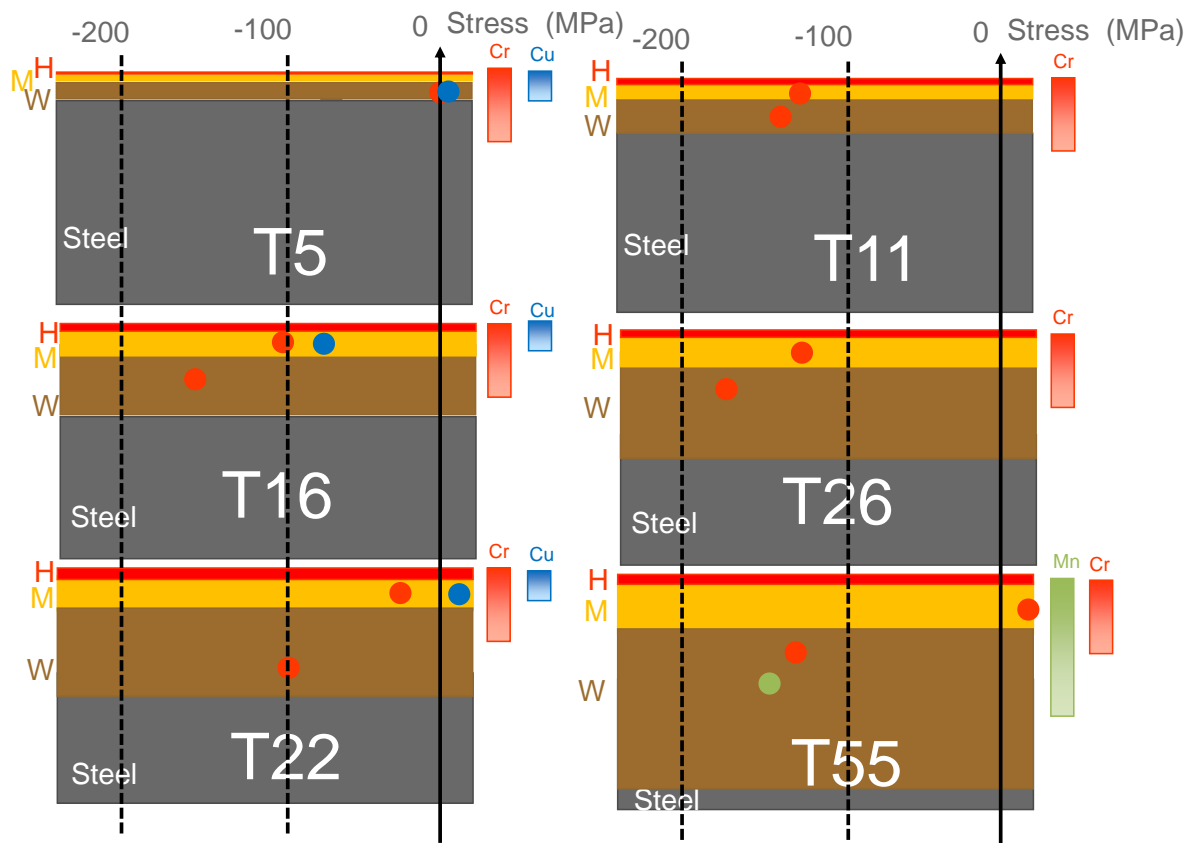


Figure 0.4: Schematic representation of the spatial variations of stress for all samples (T5 refers to 5 μm of oxide). The different points correspond to the measured stress (horizontal scale). The penetration depth of X-Rays for each anticathode is represented by the color bars on the right.

In the literature, a gradient is also observed for a two-phase oxide (Hematite and Magnetite) scale obtained after heating-up for 6.5 min until 650°C, holding for 1 s and cooling down to room temperature. The thickness is below 5µm and is analysed by grazing-incidence XRD (3 nm to 5 µm analysed penetration) [131]. Here, the compression in Magnetite is moving from -200 MPa to 0 within 2.5 µm. Stresses gradually change into tensile stresses towards the interface with Hematite and the free surface, respectively Figure 0.5. The gradient is explained by the authors by the abrupt changes in thermal expansion occurring at the inner scale interfaces.

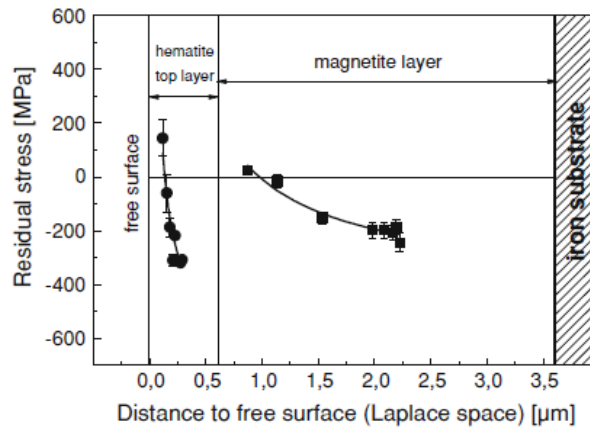


Figure 0.5: Residual stress gradients in Hematite and Magnetite after oxidation at 650°C for 1s [131]

According to Mitchell et al., a stress gradient is also found in an adherent Hematite layer after oxidation between 400 and 700°C [185]. The largest stress is at the oxide-substrate interface and the minimum stress is zero at the surface. In this study, these stresses can be relaxed by the decohesion of Hematite in surface.

Appendix C.

Quenching furnace for in-situ indentation

Description of the equipment

At still higher temperature, a last equipment is used, in fact a “quenching furnace” recently developed at ArcelorMittal Lab (Figure 0.6) checked here for its capacity to perform in-situ oxidation + indentation experiments. The main advantage of the equipment is (i) the high indentation speed and (ii) the indentation is made directly after the oxidation (only one thermal cycle in comparison to the Alemmis set-up with its first oxidizing cycle and its re-heating to make the indentation at high temperature).

The set-up is composed of the furnace, the indenter part (upper part) and the sample (lower part). The sample and the tip are on the same axis, mounted on the hydraulic cylinder (Figure 0.6). During the test, the sample placed on an alumina block is moving up until it contacts the tip of the indenter. Then, the sample+indenter is moved up until it contacts the spring scale and the desired force is reached (minimum force 50N, maximum force 2000) ; then it is maintained under load for 10 seconds. The displacement rate of the cylinder is between 0.1mm/s to 10mm/s.

The geometry of the tip is described in the Figure 0.6, a 45° cone terminated by a spherical cap of radius 1mm. The material chosen is Alumina which is inert up to very high temperature with a correct hardness (Table 4-7).

Dimensions of the samples are 25mm x 25mm x 25mm. The face to oxidize is beforehand ground with a 800 grit paper. An oxide layer (predominantly FeO) is built on both faces. For high temperature indentation, the core of the Carbolyte Gero furnace heats the sample and the tip by convection in an inert atmosphere (argon). A low speed of heating/cooling is needed to avoid the fracture of the ceramic parts (1°C every 10 seconds). After a temperature stabilisation, the oxidative gas is introduced (21% of O₂) for a given time of oxidation. To stop the growth of oxide, the indentation area is flushed again with inert argon gas. The temperature on the sample is controlled by a thermocouple. Time, temperature and load are continuously recorded during the test (every two seconds). The main advantage of the equipment is that the indentation is made directly after the oxidation (without cooling that generates thermal stresses and potential fracture). However, due to the coaxiality of tip and sample, only one indentation is made for a thermal cycle which lasts 10 hours. No in-situ observations are possible. Under these conditions, just a few feasibility tests have been carried out.

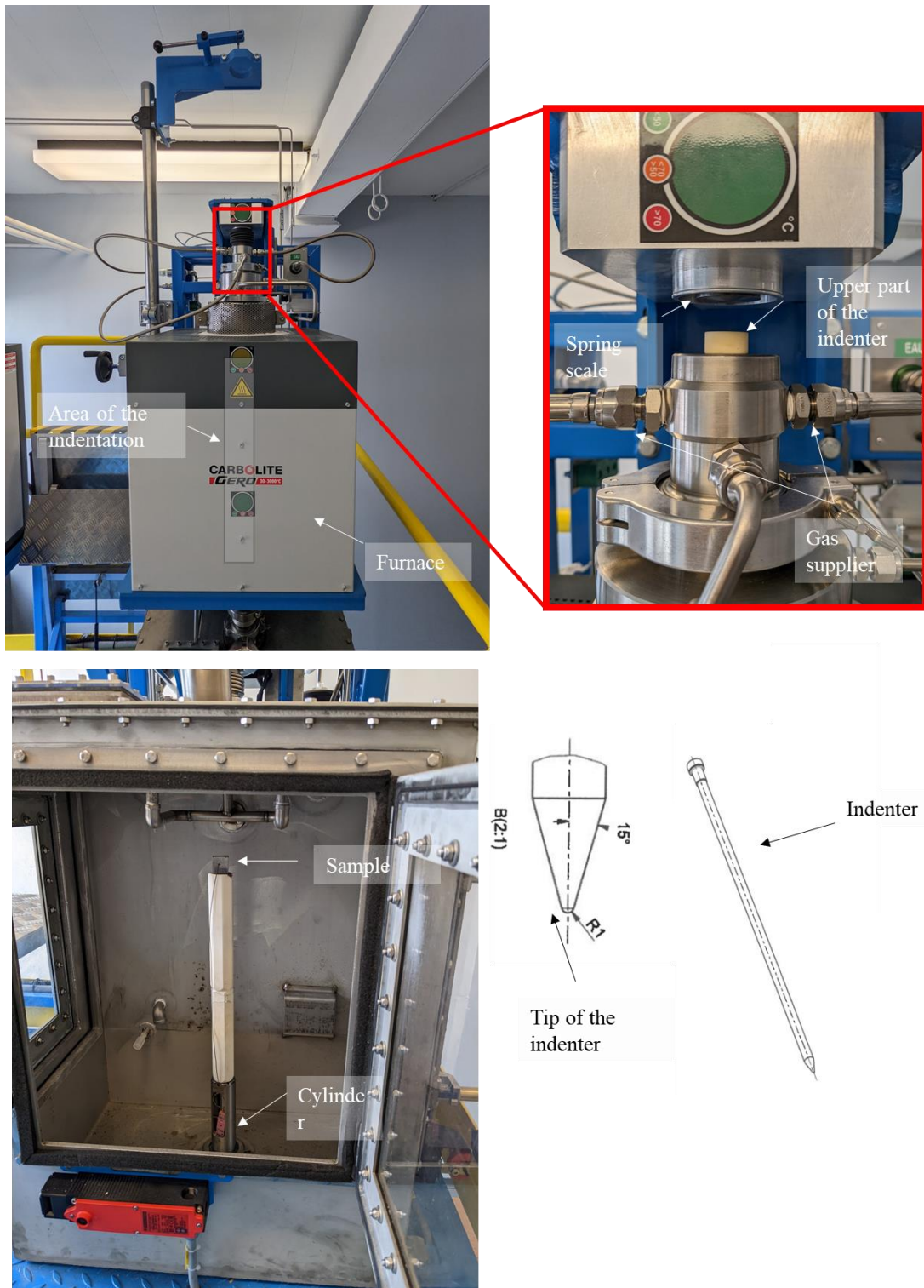


Figure 0.6: “ Quenching furnace” set-up. The upper part is dedicated to the indenter, the lower part to the sample. The furnace is heating both the sample and the tip. The Alumina tip is conical with a final 1mm radius. The atmosphere is controlled during the test with gas supply

Methodology

Tests are made at several temperatures (from 750°C to 920°C) with 50 and 250N loads. At 920°C, the ferrite-to-austenite transition occurs and the dilatation causes fracture before the indentation [53], this temperature is therefore not considered. The loading and unloading are done at the same speed, between 100 $\mu\text{m/s}$ and 300 $\mu\text{m/s}$. Each test protocol has been repeated minimum 2 times. SEM observations are made post-mortem.

Appendices

After the fast cooling, the main phase is Wüstite. The thickness is evaluated with a FIB cross-section as $90\mu\text{m}$. Only large loads are available, so that the thickness had to be increased in comparison to the previous tests.

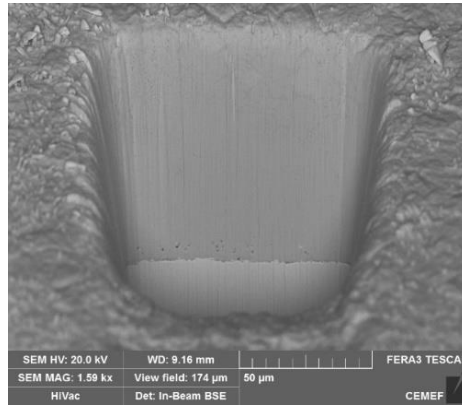


Figure 0.7: FIB cross-section of a sample oxidized within the quenching furnace at 800°C for 7 minutes

Ductile behaviour at higher temperature

After the cooling, the visual observations (Figure 0.8) show no cracks at 800°C and 700°C (whatever the speed used). It confirms the ductile behaviour and the plastic deformation of Wüstite at high temperature, in spite of the still much higher speed compared with the HTM800 equipment. This result has been appended to the Alemnis HTM800 tests in Figure 4.39.

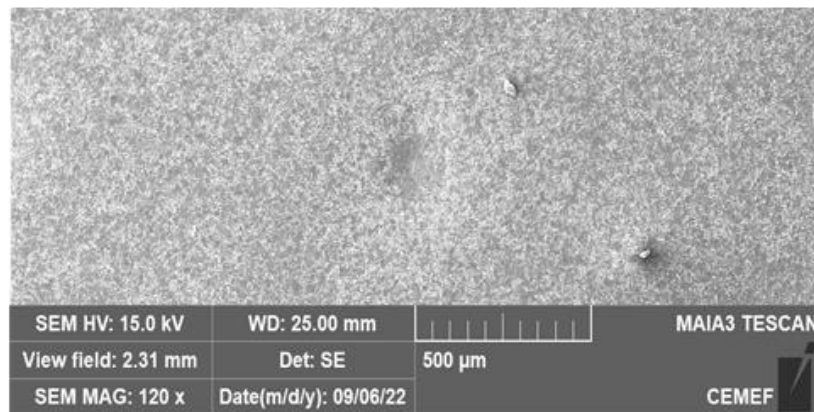


Figure 0.8: SEM observation of the indentation at 800°C with a 50N loading

Adhesion

The same method for the FIB cross-section is applied to observe the interface. Figure 0.9 shows the test at 800°C with a 50N loading at $100\mu\text{m/s}$. The estimation of the ratio p/t is about 0.8 and neither normal cracks nor delamination are present. This is an important result which shows that the oxide remains adherent during the test at 800°C . There is also an irregularity in the oxide thickness below the indentation. This is just a first, isolated observation, more cross-sections (and indentations) are needed to confirm that the oxide is still attached after the indentation, and to quantify the adhesion of oxide.

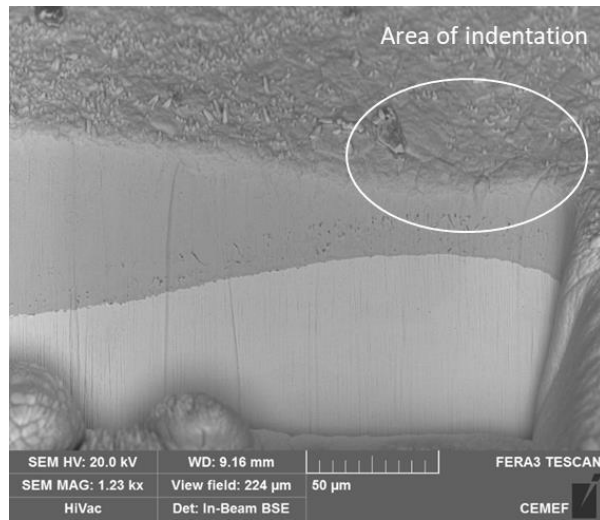


Figure 0.9: FIB cross-section after a 50N indentation at 800°C at 100 $\mu\text{m/s}$

Appendix D. Preliminary 3D study

In this part, 3D simulations are compared with 2D axisymmetric to validate the latter, much less costly approach. This study was made at the beginning of the study using Forge software and different conditions, e.g. the material law of oxide and steel is adapted to a temperature of 600°C, the thickness of oxide is equal to 90µm, the substrate thickness is 810 µm.

First, a pyramidal Vickers indenter, then a 3D cone-shaped tip are modelled to observe the influence of the precise indenter geometry. The comparison is finally made with the axis-symmetric simulation with the same parameters.

In the Forge® software, the boundary conditions are set with rigid support, the sample side and bottom surface are attached (surface nodes are blocked with a contact with a physical object). This is equivalent to the conditions imposed in Abaqus®.

The pyramidal geometry of the Vickers indenter is designed to avoid the influence of friction (thanks to a large angle between faces). After a preliminary study, a Tresca-limited Coulomb's law is used :

$$\tau < \text{Min}\left(\mu\sigma_n, \bar{m}\frac{\sigma_0}{\sqrt{3}}\right) \rightarrow \text{sticking} \quad \text{and} \quad \tau = \text{Min}\left(\mu\sigma_n, \bar{m}\frac{\sigma_0}{\sqrt{3}}\right) \rightarrow \text{sliding} \quad (0-1)$$

with τ the shear stress, μ the coulomb coefficient, \bar{m} the Tresca coefficient, σ_n the normal stress. In this study, the coefficients are set to $\mu = 0,1$ and $\bar{m} = 0,6$.

All the supports and the ambient air are at the same temperature of 600°C, the exchange is considered as adiabatic for the support pieces, and the exchange between the indenter and the specimen is medium, the heat transfer coefficient is set to 10 000 W/(m²K). Such conditions have been selected for the model to be isothermal, just as the experiment is.

In all the simulation, some parameters are set:

- The loading and unloading rates are 5 µm/s.
- The indentation depth is through the totality of the scale, $p = t = 90$ µm, after which unloading is performed.
- A multi-material mode is configured, the interface between the oxide scale and the steel is fixed. No delamination is possible in this configuration.

Vickers tip

The Vickers tip is a pyramid with 136° between the opposite faces. Two symmetry planes are assumed.

At the end of the loading, the maximum deformation is along the diagonal of the imprint (Figure 0.10) but around it, the strain field is homogeneous. Plasticity ($\epsilon^{pl} > 10^{-3}$ e.g.) is confined in a sphere with radius ~2 times the indentation diagonal.

For the 1st principal stress component, the maximum of the compression is located near the corner, a high-tension zone is present (120 MPa) and is slightly impacted by the corner (a little less tensile). The maximum is reached in the middle of the face, at a radius at which the experimental cracks are localised. The only possibility to initiate cracks is near the intender with the highly bi-axial tensile zone described in 5.3 paragraph.

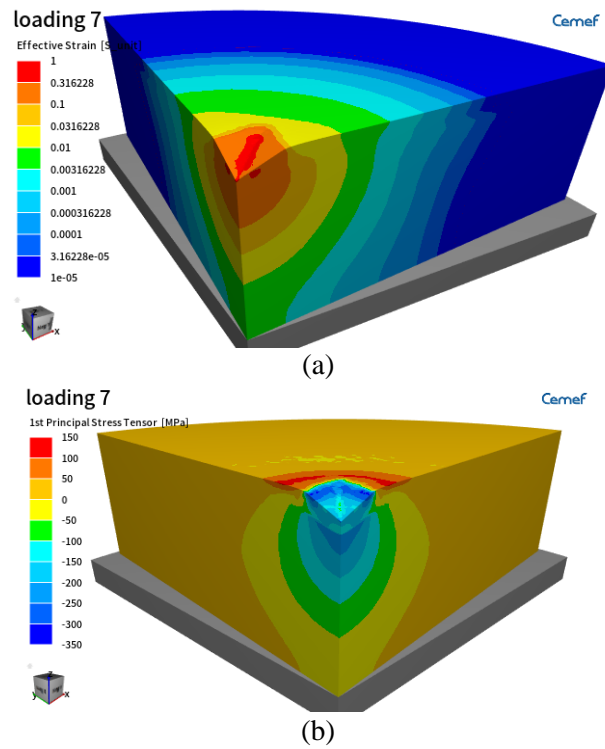


Figure 0.10: (a) strain field (b) 1st principal stress at the end of indentation with the 3D Vickers tip using Forge®. Oxide thickness $t = 90\mu\text{m}$, penetration $p = 90\mu\text{m}$, $T = 600^\circ\text{C}$.

Cone geometry

The geometry of the tip in this 3D simulation is now a cone, the total included angle is 140° , i.e. the standard Vickers-equivalent cone. It is obtained by a 360° degrees rotation of the 2D triangle and a quarter of the cone only is simulated to reduce calculation time. Compared with the 3D Vickers indentation simulation above (Figure 0.10), the singularity of the corner is eliminated, the rest of the field is similar.

The same stress profile is observed in both cases, 2D and 3D. In the Figure 0.11, the 1st principal stress tensor of 2D and 3D cone simulations are compared. For the loading, the high tensile zone is present in both cases, and the maximum value is quite the same, the maximum of compression at the tip of the indenter is also the same. At the right side boundary, in both cases, the stress is low, which means this artificial boundary does not disturb the results (our sample is large enough). The profile of the stress is quite the same, validating the results of chapter 5, established in 2D.

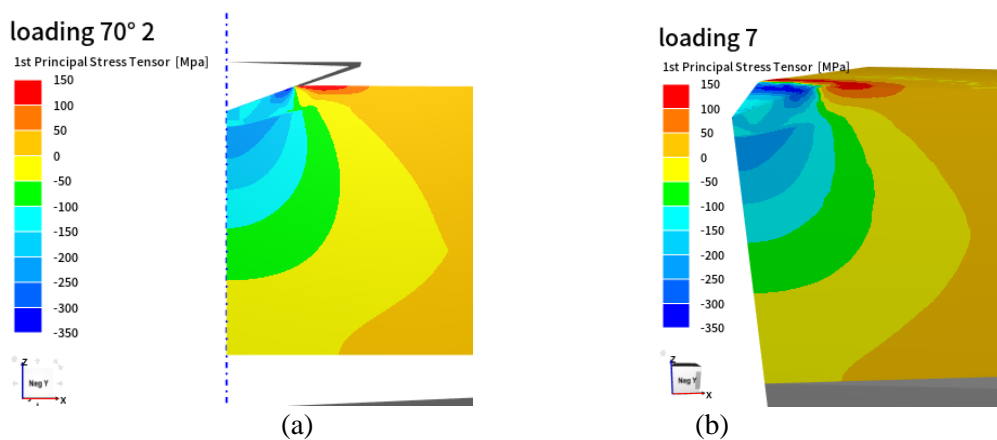


Figure 0.11: 1st principal stress at the end of loading indentation with the cone tip using Forge®. Oxide thickness $t = 90\mu\text{m}$, indentation depth $p = 90\mu\text{m}$, $T = 600^\circ\text{C}$. (a) 2D simulation (b) 3D simulation

Appendices

Bibliography

- [1] ArcelorMittal, *Making Steel | ArcelorMittal*, <https://corporate.arcelormittal.com/about/making-steel>.
- [2] ArcelorMittal Luxembourg, *Nouveau Suivi de Production Pour l'aciérie de Belval*, <https://luxembourg.arcelormittal.com/5/18/288/language/FR>.
- [3] M. Krzyzanowski, J. H. Beynon, and D. C. J. Farrugia, *Oxide Scale Behavior in High Temperature Metal Processing* (John Wiley & Sons, 2010).
- [4] B. PICQUÉ, *Experimental Study and Numerical Simulation of Iron Oxide Scales Mechanical Behavior in Hot Rolling*, PhD Dissertation, ENSMP, (2004).
- [5] M. Picard, *Hot Oxidation of Carbon Steels*, Internal Report, ArcelorMittal (2017) - confidential
- [6] H. E. Evans, *Spallation Models and Their Relevance to Steam-Grown Oxides*, *Materials at High Temperatures* **22**, 155 (2005).
- [7] M. Krzyzanowski, J. H. Beynon, and C. M. Sellars, *Analysis of Secondary Oxide-Scale Failure at Entry into the Roll Gap*, *Metallurgical and Materials Transactions B* **31**, 1483 (2000).
- [8] M. Schütze, *Mechanical Properties of Oxide Scales*, *Oxidation of Metals* **44**, 29 (1995).
- [9] M. Zhang, B. Liu, C. Grenier, P. Montmitonnet, M. Picard, and J.-L. Borean, *Oxide Fracture Mechanisms in Descaling of Steel Strips on the Hot Strip Mill*, *AIP Conference Proceedings* **1353**, 333 (2011).
- [10] Q. Dong, J. Zhang, and H. Liu, *The Effects of High-Speed Steel Roll and Lubrication on Work Roll Wear and Fatigue During Electrical Steel Strip Hot Rolling*, *Journal of Failure Analysis and Prevention* **20**, 432 (2020).
- [11] N. Mickler, B. Goncalves, V. Leblanc, V. Lanteri, and C. Le Felic, *Décalaminage Secondaire Des Aciers Bas Carbone Efficacité, Impact Thermique et Décontrainte Process*, Internal Report, ArcelorMittal No. THEMEF/01/R/78, (2001) - confidential
- [12] J. Frick, *Improved Energy Efficiency and Surface Quality in High Pressure Descaling*, in Proc. European Oxide Scale Conference OXI2022, London, (2022).
- [13] P. O. of the E. Union, *Innovative High Temperature and Mechanical Descaling (HIDES)*, <http://op.europa.eu/en/publication-detail/-/publication/24628475-9c4a-4110-8321-f3c5f01a5b3e>.
- [14] V. V. Basabe and J. A. Szpunar, *Effect of O₂ in Heating Atmosphere on Hydraulic Descaling in Hot Rolling of Low Carbon Steel*, *ISIJ International* **48**, 467 (2008).
- [15] J. Horsky, M. Raudensky, and L. Vavrecka, *Experimental Study of Hydraulic Descaling*, in Proc. 5th International Conference on Heat Transfer, Fluid Mechanics and Thermodynamics, (2007).
- [16] W. M. Melfo, S. Melzer, and P. H. Bolt, *In situ determination of oxides forming on steels containing Mn and Si at finishing mill hot rolling conditions*, in Proc. European Oxide Scale Conference OXI2014, London (2014), pp. 79–82.
- [17] J. W. Choi and J. W. Choi, *Convective Heat Transfer Coefficient for High Pressure Water Jet*, *ISIJ International* **42**, 283 (2002).
- [18] J. Horský, M. Raudenský, and M. Pohanka, *Influence of parameters of hydraulic descaling on temperature losses and surface quality of rolled material*, in Proc. Metal Forming 2004, (2004), pp. 367–370.
- [19] F. Matsuno, *Blistering and Hydraulic Removal of Scale Films of Rimmed Steel at High Temperature*, *Transactions ISIJ* **20**, 413 (1980).
- [20] D. Farrugia, A. Richardson, and Y. J. Lan, *Advancement in Understanding of Descalability during High Pressure Descaling*, *Key Engineering Materials* **622–623**, 29 (2014).
- [21] L. Robb, *Effect of Spray Height, Lead Angle and Offset Angle on Impact*, in Proc. AISTech2005 – The Iron & Steel Technology Conference and Exposition, (2005).
- [22] W. Melfo, H. Bolt, M. Rijnders, D. Staalman, C. B. Castro, D. Crowther, and B. Jana, *Experimental Study on Primary Scale Formation and Descalability on Steels Containing Ni and Ni+Si*, *ISIJ International* **53**, 866 (2013).

Bibliography

- [23] T. Asai, T. Soshiroda, and M. Miyahara, *Influence of Ni Impurity in Steel on the Removability of Primary Scale in Hydraulic Descaling*, ISIJ International **37**, 272 (1997).
- [24] T. Kizu, Y. Nagataki, T. Inazumi, and Y. Hosoya, *Effects of Chemical Composition and Oxidation Temperature on the Adhesion of Scale in Plain Carbon Steels.*, ISIJ International **41**, 1494 (2001).
- [25] R. Osei, S. Lekakh, and R. O'Malley, *Effect of Cu Additions on Scale Structure and Descaling Efficiency of Low C Steel Reheated in a Combustion Gas Atmosphere*, Oxidation of Metals **98**, 363 (2022).
- [26] J. Robertson and M. I. Manning, *Limits to Adherence of Oxide Scales*, Materials Science and Technology **6**, 81 (1990).
- [27] M. Raudensky, A. Horak, J. Horsky, M. Pohanka, and P. Kotrbacek, *Hydraulic descaling improvement, findings of jet structure on water hammer effect*, in *ATS International Steelmaking Conference*, Vol. 104 (EDP Sciences, ATS International Steelmaking Conference, 2007), pp. 84–90.
- [28] N. Barbooth, *Corrosion sèche des métaux et alliages*, Techniques de l'Ingénieur **M170**, (1979).
- [29] V. Lanteri, *Défauts d'incrustation Calamine Secondaire Au Train à Bandes Synthèse Des Mécanismes et Perspectives*, No. RC 98.42, IRSID, 1998 - confidential.
- [30] C. Wagner, *Theoretical Analysis of the Diffusion Processes Determining the Oxidation Rate of Alloys*, Journal of The Electrochemical Society **99**, 369 (1952).
- [31] J. Païdassi, *Sur la cinétique de l'oxydation du fer dans l'air dans l'intervalle 700–1250°C*, Acta Metallurgica **6**, 184 (1958).
- [32] F. Koch and J. B. Cohen, *The Defect Structure of Fe_{1-x}O*, Acta Crystallographica Section B **25**, 275 (1969).
- [33] G. S. Parkinson, *Iron Oxide Surfaces*, Surface Science Reports **71**, 272 (2016).
- [34] K. E. Sickafus, J. M. Wills, and N. W. Grimes, *Structure of Spinel*, Journal of the American Ceramic Society **82**, 3279 (1999).
- [35] L. Pauling and S. B. Hendricks, *The Crystal Structures of Hematite and Corundum*, Journal of the American Chemical Society **47**, 781 (1925).
- [36] V. V. Basabe and J. A. Szpunar, *Growth Rate and Phase Composition of Oxide Scales during Hot Rolling of Low Carbon Steel*, ISIJ International **44**, 1554 (2004).
- [37] L. Broussard, *Disproportionation of Wüstite*, The Journal of Physical Chemistry **73**, 1848 (1969).
- [38] B. Schmid, N. Aas, Ø. Grong, and R. Ødegård, *High-Temperature Oxidation of Iron and the Decay of Wüstite Studied with in Situ ESEM*, Oxidation of Metals **57**, 115 (2002).
- [39] R. Y. Chen and W. Y. D. Yuen, *A Study of the Scale Structure of Hot-Rolled Steel Strip by Simulated Coiling and Cooling*, Oxidation of Metals **53**, 539 (2000).
- [40] S. Liu, D. Tang, H. B. Wu, and Z. X. Cai, *Isothermal Transformation of Wüstite for Low Carbon Micro-Alloyed Steel*, Advanced Materials Research **683**, 457 (2013).
- [41] H. J. T. Ellingham, *Reducibility of Oxides and Sulphides in Metallurgical Processes*, Journal of the Society of Chemical Industry **63**, 125 (1944).
- [42] J. Eliasson, T. Siwecki, and B. Hutchinson, *Processing of Copper-Containing Steel via Strip Casting - a Laboratory Evaluation*, Steel Research International **77**, 409 (2006).
- [43] T. Nilsonthi, *Caractérisation Physico-chimique et adhérence de couches d'oxydes thermiques sur des aciers recyclés.*, PhD Dissertation, Université de Grenoble, (2013).
- [44] A. Harashima, Y. Kondo, and S. Hayashi, *Time Change in Scale Microstructure of Fe-5 Mass%Ni Alloy at 1200°C*, ISIJ International **60**, 352 (2020).
- [45] H. D. Alvarenga, T. V. De Putte, N. Van Steenberge, J. Sietsma, and H. Terryn, *Influence of Carbide Morphology and Microstructure on the Kinetics of Superficial Decarburization of C-Mn Steels*, Metallurgical and Materials Transactions A **46**, 123 (2015).
- [46] J. Baud, J. C. Charbonnier, and J. Métivier, *Etude de La Dureté Des Solutions Solides FeO.MnO*, IRSID, (1973).
- [47] E. Ahtoy, *Effect of Alloying Elements (Si, Al, P, B) on Low Carbon Steel Oxidation in Low Process at High Temperatures : Mechanisms and Modelling.*, PhD Dissertation, Grenoble, (2010).
- [48] S. J. Bull, *Modeling of Residual Stress in Oxide Scales*, Oxidation of Metals **49**, 1 (1998).
- [49] H. E. Evans, *Stress Effects in High Temperature Oxidation of Metals*, International Materials Reviews **40**, 1 (1995).

- [50] N. B. Pilling and R. E. Bedworth, *Mechanism of Metallic Oxidation at High Temperature*, Journal of the Institute of Metals **29**, 529 (1923).
- [51] B. Panicaud, J. L. Grosseau-Poussard, and J. F. Dinhut, *On the Growth Strain Origin and Stress Evolution Prediction during Oxidation of Metals*, Applied Surface Science **252**, 5700 (2006).
- [52] B. Pieraggi and R. A. Rapp, *Stress Generation and Vacancy Annihilation during Scale Growth Limited by Cation-Vacancy Diffusion*, Acta Metallurgica **36**, 1281 (1988).
- [53] S. Taniguchi and D. L. Carpenter, *Stresses Developed during Oxidation of Iron at Relatively High Temperatures*, Transactions ISIJ **18**, 530 (1978).
- [54] F. N. Rhines and J. S. Wolf, *The Role of Oxide Microstructure and Growth Stresses in the High-Temperature Scaling of Nickel*, Metallurgical Transactions **1**, 1701 (1970).
- [55] W. K. Appleby and R. F. Tylecote, *Stresses during the Gaseous Oxidation of Metals*, Corrosion Science **70**, 325 (1970).
- [56] K. Sasaki, K. Hayashi, M. Takeda, S. Nakakubo, Y. Yamada, A. Kitahara, R. Wada, and I. Saeki, *Effect of Argon-Purged Cooling on Generating Residual Stress in Oxide Scale Formed on Si-Containing Steels Examined by In Situ X-Ray Diffraction and Finite Element Analysis*, Materials Transactions **61**, 136 (2020).
- [57] M. Takeda, T. Onishi, S. Nakakubo, and S. Fujimoto, *Physical Properties of Iron-Oxide Scales on Si-Containing Steels at High Temperature*, Materials Transactions **50**, 2242 (2009).
- [58] P. K. Foster and A. J. E. Welch, *Metal-Oxide Solid Solutions. Part 1.—Lattice-Constant and Phase Relationships in Ferrous Oxide (Wustite) and in Solid Solutions of Ferrous Oxide and Manganous Oxide*, Transactions of the Faraday Society **52**, 1626 (1956).
- [59] H. Tanei and Y. Kondo, *Strain Development in Oxide Scale during Phase Transformation of FeO*, ISIJ International **57**, 506 (2017).
- [60] H. E. Evans and M. P. Taylor, *Creep Relaxation and the Spallation of Oxide Layers*, Surface and Coatings Technology **94–95**, 27 (1997).
- [61] J. D. Mackenzie and C. E. Birchenall, *Plastic Flow of Iron Oxides And the Oxidation of Iron*, Corrosion **13**, 17 (1957).
- [62] M. Krzyzanowski and J. H. Beynon, *Modelling the Behaviour of Oxide Scale in Hot Rolling*, ISIJ International **46**, 1533 (2006).
- [63] M. Krzyzanowski and J. H. Beynon, *Finite Element Model of Steel Oxide Failure during Tensile Testing under Hot Rolling Conditions*, Materials Science and Technology **15**, 1191 (1999).
- [64] M. Krzyzanowski and J. H. Beynon, *Effect of oxide scale failure in hot steel rolling on subsequent hydraulic descaling: numerical simulation*, in Proc. 3rd International Conference on Hydraulic Descaling, (2000), pp. 77–86.
- [65] P. Hancock and J. R. Nicholls, *Application of Fracture Mechanics to Failure of Surface Oxide Scales*, Materials Science and Technology **4**, 398 (1988).
- [66] M. M. Nagl, S. R. J. Saunders, W. T. Evans, and D. J. Hall, *The Tensile Failure of Nickel Oxide Scales at Ambient and at Growth Temperature*, Corrosion Science **35**, 965 (1993).
- [67] M. Krzyzanowski and J. H. Beynon, *Modelling the Boundary Conditions for Thermo-Mechanical Processing - Oxide Scale Behaviour and Composition Effects*, Modelling and Simulation in Materials Science and Engineering **8**, 927 (2000).
- [68] W. Noh, J.-M. Lee, D.-J. Kim, J.-H. Song, and M.-G. Lee, *Effects of the Residual Stress, Interfacial Roughness and Scale Thickness on the Spallation of Oxide Scale Grown on Hot Rolled Steel Sheet*, Materials Science and Engineering: A **739**, 301 (2019).
- [69] H. E. Evans and R. C. Lobb, *Conditions for the Initiation of Oxide-Scale Cracking and Spallation*, Corrosion Science **24**, 209 (1984).
- [70] Y. Kondo, H. Tanei, N. Suzuki, K. Ushioda, and M. Maeda, *Blistering Behavior during Oxide Scale Formation on Steel Surface*, ISIJ International **51**, 1696 (2011).
- [71] Y. Kondo, H. Tanei, K. Ushioda, and M. Maeda, *Role of Hematite Formation on Blister Generation during High Temperature Oxidation of Steel*, ISIJ International **52**, 2254 (2012).
- [72] G. Cao, X. Gao, S. Pan, W. Shan, H. Wang, and Z. Liu, *In-Situ Observation of Cracking and Healing Behavior of High-Carbon Steel during Oxide Scale Growth*, ISIJ International **61**, 2284 (2021).
- [73] M. Krzyzanowski, W. Yang, C. M. Sellars, and J. H. Beynon, *Analysis of Mechanical Descaling: And Modelling Approach Experimental*, Materials Science and Technology **19**, 109 (2003).

Bibliography

- [74] S. Taniguchi, T. Furukawa, and T. Shibata, *Failure of Scales Formed on Cu-Containing Low Carbon Steels during Cooling*, ISIJ International **37**, 263 (1997).
- [75] G. Vagnard, *Etude de La Plasticité Du Protoxyde de Fer et l'oxyde Cuivreux*, Mémoires et Etudes Scientifiques de La Revue de Métallurgie **61**, 768 (1964).
- [76] Ph. Charpentier, P. Rabbe, and J. Manenc, *Mise en évidence de la plasticité de la magnetite mesure de la dureté en fonction de la température*, Materials Research Bulletin **3**, 69 (1968).
- [77] T. Amano, M. Okazaki, Y. Takezawa, A. Shiino, M. Takeda, T. Onishi, K. Seto, A. Ohkubo, and T. Shishido, *Hardness of Oxide Scales on Fe-Si Alloys at Room- and High-Temperatures*, Materials Science Forum **522–523**, 469 (2006).
- [78] G. Y. Deng, A. K. Tieu, L. H. Su, H. T. Zhu, M. Reid, Q. Zhu, and C. Kong, *Microstructural Study and Residual Stress Measurement of a Hot Rolling Work Roll Material during Isothermal Oxidation*, The International Journal of Advanced Manufacturing Technology **102**, 2107 (2019).
- [79] J. Lee, W. Noh, D.-J. Kim, and M.-G. Lee, *Spallation Analysis of Oxide Scale on Low Carbon Steel*, Materials Science and Engineering: A **676**, 385 (2016).
- [80] O. A. Zambrano, J. J. Coronado, and S. A. Rodríguez, *Mechanical Properties and Phases Determination of Low Carbon Steel Oxide Scales Formed at 1200°C in Air*, Surface and Coatings Technology **282**, 155 (2015).
- [81] Y. Hidaka, T. Anraku, and N. Otsuka, *Deformation of Iron Oxides upon Tensile Tests at 600–1250°C*, Oxidation of Metals **59**, 97 (2003).
- [82] D. Chicot, F. Roudet, A. Zaoui, G. Louis, and V. Lépingle, *Influence of Visco-Elasto-Plastic Properties of Magnetite on the Elastic Modulus: Multicyclic Indentation and Theoretical Studies*, Materials Chemistry and Physics **119**, 75 (2010).
- [83] M. J. Monteiro, S. R. J. Saunders, and F. C. Rizzo, *The Effect of Water Vapour on the Oxidation of High Speed Steel, Kinetics and Scale Adhesion*, Oxidation of Metals **75**, 57 (2011).
- [84] H. Rojacz, F. Birkelbach, L. Widder, and M. Varga, *Scale Adhesion, Scratch and Fracture Behaviour of Different Oxides Formed on Iron Based Alloys at 700°C*, Wear **380–381**, 126 (2017).
- [85] S. Chandra-ambhorn, T. Phadungwong, and K. Sirivedin, *Effects of Carbon and Coiling Temperature on the Adhesion of Thermal Oxide Scales to Hot-Rolled Carbon Steels*, Corrosion Science **115**, 30 (2017).
- [86] S. Chandra-ambhorn and N. Klubvihok, *Quantification of Adherence of Thermal Oxide Scale on Low Carbon Steel Using Tensile Test*, Oxidation of Metals **85**, 103 (2016).
- [87] S. Chandra-Ambhorn, K. Ngamkham, and N. Jirathanakul, *Effects of Process Parameters on Mechanical Adhesion of Thermal Oxide Scales on Hot-Rolled Low Carbon Steels*, Oxidation of Metals **80**, 61 (2013).
- [88] T. Nilsonthi, S. Chandra-ambhorn, Y. Wouters, and A. Galerie, *Adhesion of Thermal Oxide Scales on Hot-Rolled Conventional and Recycled Steels*, Oxidation of Metals **79**, 325 (2013).
- [89] J. Mougin, M. Dupeux, L. Antoni, and A. Galerie, *Adhesion of Thermal Oxide Scales Grown on Ferritic Stainless Steels Measured Using the Inverted Blister Test*, Materials Science & Engineering A **1–2**, 44 (2003).
- [90] L. Suárez, Y. Houbaert, X. V. Eynde, and R. Colás, *High Temperature Deformation of Oxide Scale*, Corrosion Science **51**, 309 (2009).
- [91] D. Filatov, O. Pawelski, and W. Rasp, *Hot-Rolling Experiments on Deformation Behaviour of Oxide Scale*, Steel Research International **75**, 20 (2004).
- [92] Y. H. Li and C. M. Sellars, *Evaluation of interfacial heat transfer and friction conditions and their effects on hot forming processes* ., in Vol. 33 37th Mechanical Working and Steel Processing Conference, (1996), pp. 385–393.
- [93] X. Sun, W. N. Liu, E. Stephens, and M. A. Khaleel, *Determination of Interfacial Adhesion Strength between Oxide Scale and Substrate for Metallic SOFC Interconnects*, Journal of Power Sources **176**, 167 (2008).
- [94] M. Graf and R. Kawalla, *Scale Development on Steel during Hot Strip Rolling*, in Proc. 9th International Rolling Conference, (2013), pp. 43–49.
- [95] H. Berns, *Microstructural Properties of Wear-Resistant Alloys*, Wear **181–183**, 271 (1995).
- [96] W. C. Oliver and G. M. Pharr, *Measurement of Hardness and Elastic Modulus by Instrumented Indentation: Advances in Understanding and Refinements to Methodology*, Journal of Materials Research **19**, 18 (2004).

- [97] M. F. Doerner, *A Method for Interpreting the Data from Depth-Sensing Indentation Instruments*, Journal of Materials Research **1**, 601 (1986).
- [98] J. D. Fletcher, Y. H. Li, J. H. Beynon, and C. M. Sellars, *The Influence of Surface Conditions in Hot Forming Determined by Ring Upsetting: A Numerical and Experimental Investigation*, Proceedings of the Institution of Mechanical Engineers, Part J: Journal of Engineering Tribology **212**, 453 (1998).
- [99] R. Morrel, *Handbook of Properties of Technical and Engineering Ceramics* (HSMO, London, 1987).
- [100] J. H. Westbrook, *Temperature Dependence of Hardness of Some Common Oxides*, Image de Couverture Pour Revue Internationale Des Hautes Températures et Des Réfractaires **3**, (1966).
- [101] D. Chicot, J. Mendoza, A. Zaoui, G. Louis, V. Lepingue, F. Roudet, and J. Lesage, *Mechanical Properties of Magnetite (Fe_3O_4), Hematite ($\alpha-Fe_2O_3$) and Goethite ($\alpha-FeO\cdot OH$) by Instrumented Indentation and Molecular Dynamics Analysis*, Materials Chemistry and Physics **129**, 862 (2011).
- [102] AFNOR, *NF EN ISO 15732 - Céramiques Techniques - Méthode d'essai de Ténacité à La Rupture Des Céramiques Monolithiques à Température Ambiante Sur Éprouvette Préfissurée Sur Une Seule Face (Méthode SEPB)*, (2005).
- [103] G. R. Anstis, P. Chantikul, B. R. Lawn, and D. B. Marshall, *A Critical Evaluation of Indentation Techniques for Measuring Fracture Toughness: I, Direct Crack Measurements*, Journal of the American Ceramic Society **64**, 533 (1981).
- [104] M. D. Drory and J. W. Hutchinson, *Measurement of the Adhesion of a Brittle Film on a Ductile Substrate by Indentation*, Proceedings of the Royal Society of London. Series A: Mathematical, Physical and Engineering Sciences **452**, 2319 (1996).
- [105] A. Vasinonta and J. L. Beuth, *Measurement of Interfacial Toughness in Thermal Barrier Coating Systems by Indentation*, Engineering Fracture Mechanics **68**, 843 (2001).
- [106] E. Ahtoy, M. Picard, G. Leprince, A. Galerie, Y. Wouters, X. Wang, and A. Atkinson, *Time and Temperature Dependence of the Adhesion of Oxide Scales Formed on Phosphorus-Containing Steels during Short Term Oxidation*, Materials Chemistry and Physics **148**, 1157 (2014).
- [107] AFNOR, *NF EN ISO 20502- Fine Ceramics (Advanced Ceramics, Advanced Technical Ceramics) — Determination of Adhesion of Ceramic Coatings by Scratch Testing*, (2016).
- [108] S. Suresh and A. E. Giannakopoulos, *A New Method for Estimating Residual Stresses by Instrumented Sharp Indentation*, Acta Materialia **46**, 5755 (1998).
- [109] P. Gravereau, *Introduction à la pratique de la diffraction des rayons X par les poudres.*, (2011).
- [110] M. Marcius, M. Ristic, M. Ivanda, and S. Music, *Formation of Iron Oxides by Surface Oxidation of Iron Plate*, Croatica Chemica Acta **85**, 117 (2012).
- [111] Z.-H. Xu and X. Li, *Influence of Equi-Biaxial Residual Stress on Unloading Behaviour of Nanoindentation*, Acta Materialia **53**, 1913 (2005).
- [112] AFNOR, *NF EN 15305 Non-Destructive Testing - Test Method for Residual Stress Analysis by x-Ray Diffraction*, (2009).
- [113] K. Kitamura, Y. Nishiyama, Y. Higashida, N. Otsuka, T. Doi, Y. Hidaka, and Y. Masaki, *Dynamics of Oxide Films Using In-Situ Analysis for Surface Properties of Steel Products*, NIPPON STEEL & SUMITOMO METAL TECHNICAL REPORT No. 114, Nippon Steel, (2017).
- [114] G. Hilson, K. R. Hallam, and P. E. J. Flewitt, *The Measurement of Stresses within Oxides Produced on Austenitic and Ferritic Steels Using Raman Spectroscopy*, Materials Science Forum **524–525**, 957 (2006).
- [115] J. Mougín, N. Rosman, G. Lucazeau, and A. Galerie, *In Situ Raman Monitoring of Chromium Oxide Scale Growth for Stress Determination*, Journal of Raman Spectroscopy **32**, 739 (2001).
- [116] K. Kitamura, Y. Nishiyama, S. Fujimoto and N. Otsuka, *Stress and Adhesion of Protective Oxide Scales on Stainless Steels and RE Effects*, ISIJ International **59**, 9, 1642 (2019),
- [117] C. Mennicke, D. R. Clarke, and M. Rühle, *Stress Relaxation in Thermally Grown Alumina Scales on Heating and Cooling FeCrAl and FeCrAlY Alloys*, Oxidation of Metals **55**, 551 (2001).
- [118] P. Pourghahramani, *Mechanical Activation of Hematite Using Different Grinding Methods with Special Focus on Structural Changes and Reactivity*, PhD Dissertation, Luleå University, (2007).

Bibliography

- [119] G. Cao, Z. Li, J. Tang, X. Sun, and Z. Liu, *Oxidation Kinetics and Spallation Model of Oxide Scale during Cooling Process of Low Carbon Microalloyed Steel*, *High Temperature Materials and Processes* **36**, 927 (2017).
- [120] N. Na Kalasin, S. Yenchum, and T. Nilsonthi, *Adhesion Behaviour of Scales on Hot-Rolled Steel Strips Produced from Continuous Casting Slabs*, *Materials Today: Proceedings* **5**, 9359 (2018).
- [121] S. Liu, D. Tang, H. Wu, and L. Wang, *Oxide Scales Characterization of Micro-Alloyed Steel at High Temperature*, *Journal of Materials Processing Technology* **213**, 1068 (2013).
- [122] V. V. Basabe, *Scale Formation and Descaling in Hot Rolling of Low Carbon Steel*, PhD Dissertation, McGill University, (2009).
- [123] S. Taniguchi, K. Yamamoto, D. Megumi, and T. Shibata, *Characteristics of Scale/Substrate Interface Area of Si-Containing Low-Carbon Steels at High Temperatures*, *Materials Science and Engineering: A* **308**, 250 (2001).
- [124] M. Li, R. Endo, M. Akoshima, and M. Susa, *Temperature Dependence of Thermal Diffusivity and Conductivity of FeO Scale Produced on Iron by Thermal Oxidation*, *ISIJ International* **57**, 2097 (2017).
- [125] W. Sun, *A Study on the Characteristics of Oxide Scale in Hot Rolling of Steel*, University of Wollongong Thesis Collection 1954-2016 (2005).
- [126] H. Buscail, M. F. Stroosnijder, Y. P. Jacob, and E. Sciora, *Influence of Yttrium Implantation on Growth Stresses Developed in FeO Scales Formed on Pure Iron at 800°C.*, *Materials Science and Engineering: A* **262**, 184 (1999).
- [127] N. Bertrand, C. Desgranges, D. Poquillon, M. C. Lafont, and D. Monceau, *Iron Oxidation at Low Temperature (260–500 °C) in Air and the Effect of Water Vapor*, *Oxidation of Metals* **73**, 139 (2010).
- [128] P. H. Bolt, *Understanding the Properties of Oxide Scales on Hot Rolled Steel Strip*, *Steel Research International* **75**, 399 (2004).
- [129] T. K. Rout, J. Go, A. V. Gaikwad, and S. Melzer, *High Temperature Oxidation of Advanced High Strength Steel: HT-XRD Method for Quantitative Evaluation*, *Materials Science Forum* **696**, 107 (2011).
- [130] S. Hayashi, Y. Yamanouchi, K. Hayashi, Y. Hidaka, and M. Sato, *Stress Measurement in the Iron Oxide Scale Formed on Pure Fe during Isothermal Transformation by in Situ High-Temperature X-Ray Diffraction*, *Corrosion Science* **187**, 109482 (2021).
- [131] C. Juricic, H. Pinto, D. Cardinali, M. Klaus, C. Genzel, and A. R. Pyzalla, *Evolution of Microstructure and Internal Stresses in Multi-Phase Oxide Scales Grown on (110) Surfaces of Iron Single Crystals at 650 °C*, *Oxidation of Metals* **73**, 115 (2010).
- [132] Y. M. Mos, A. C. Vermeulen, C. J. N. Buisman, and J. Weijma, *X-Ray Diffraction of Iron Containing Samples: The Importance of a Suitable Configuration*, *Geomicrobiology Journal* **35**, 511 (2018).
- [133] J. Liu, R. E. Saw, and Y.-H. Kiang, *Calculation of Effective Penetration Depth in X-Ray Diffraction for Pharmaceutical Solids*, *Journal of Pharmaceutical Sciences* **99**, 3807 (2010).
- [134] R. L. Higginson, B. Roebuck, and E. J. Palmiere, *Texture Development in Oxide Scales on Steel Substrates*, *Scripta Materialia* **47**, 337 (2002).
- [135] V. V. Basabe and J. A. Szpunar, *Texture of Oxide Scales during Hot Rolling of Low Carbon Steel*, *Materials Science Forum* **495–497**, 339 (2005).
- [136] R. L. Higginson and G. D. West, *The Study of Texture Development of High Temperature Oxide Scales on Steel Substrates Using Electron Backscatter Diffraction*, *Materials Science Forum* **495–497**, 399 (2005).
- [137] H. Buscail, J. P. Larpin, J. J. Heizmann, and C. Laruelle, *Wustite Texture and Microstructure Modification by Ceria Surface Addition during Low Pressure Oxidation of Pure Iron at High Temperatures*, *Revue de Métallurgie* **92**, 5 (1995).
- [138] G. V. Samsonov, *The Oxide Handbook*, Springer Science & Business Media, (1973).
- [139] S. Fischer, E. Houtman, and H. R. Maier, *Influence of PSI- and OMEGA-Tilting on X-Ray Stress Analysis*, *Materials Science Forum* **79–82**, 153 (1991).
- [140] K. L. Johnson, *The Correlation of Indentation Experiments*, *Journal of the Mechanics and Physics of Solids* **18**, 115 (1970).
- [141] C. M. Perrot, *Elastic-Plastic Indentation: Hardness and Fracture*, *Wear* **45**, 293 (1977).

- [142] B. R. Lawn and E. R. Fuller, *Equilibrium Penny-like Cracks in Indentation Fracture*, Journal of Materials Science **10**, 2016 (1975).
- [143] B. R. Lawn, A. G. Evans, and D. B. Marshall, *Elastic/Plastic Indentation Damage in Ceramics: The Median/Radial Crack System*, Journal of the American Ceramic Society **63**, 574 (1980).
- [144] S. M. Smith and R. O. Scattergood, *Crack-Shape Effects for Indentation Fracture Toughness Measurements*, Journal of the American Ceramic Society **75**, 305 (1992).
- [145] X. Chen, J. W. Hutchinson, and A. G. Evans, *The Mechanics of Indentation-Induced Lateral Cracking*, Journal of the American Ceramic Society **88**, 1233 (2005).
- [146] B. Lawn and R. Wilshaw, *Indentation Fracture: Principles and Applications*, Journal of Materials Science **10**, 1049 (1975).
- [147] D. Chicot, A. Pertuz, F. Roudet, M. H. Staia, and J. Lesage, *New Developments for Fracture Toughness Determination by Vickers Indentation*, Materials Science and Technology **20**, 877 (2004).
- [148] B. R. Lawn, *Indentation of Ceramics with Spheres: A Century After Hertz*, Journal of the American Ceramic Society **81**, 1977 (1998).
- [149] S. K. Lee, S. Wuttiphon, and B. R. Lawn, *Role of Microstructure in Hertzian Contact Damage in Silicon Nitride: I, Mechanical Characterization*, Journal of the American Ceramic Society **80**, 2367 (1997).
- [150] A. G. Evans and E. A. Charles, *Fracture Toughness Determinations by Indentation*, Journal of the American Ceramic Society **59**, 371 (1976).
- [151] R. F. Cook and G. M. Pharr, *Direct Observation and Analysis of Indentation Cracking in Glasses and Ceramics*, Journal of the American Ceramic Society **73**, 787 (1990).
- [152] A. Lee, B. M. Clemens, and W. D. Nix, *Stress Induced Delamination Methods for the Study of Adhesion of Pt Thin Films to Si*, Acta Materialia **52**, 2081 (2004).
- [153] Y.-W. Rhee, H.-W. Kim, Y. Deng, and B. R. Lawn, *Contact-Induced Damage in Ceramic Coatings on Compliant Substrates: Fracture Mechanics and Design*, Journal of the American Ceramic Society **84**, 1066 (2001).
- [154] H. Chai and B. R. Lawn, *Fracture Mode Transitions in Brittle Coatings on Compliant Substrates as a Function of Thickness*, Journal of Materials Research **19**, 1752 (2004).
- [155] S. V. Hainsworth, M. McGurk, and T. Page, *The Effect of Coating Cracking on the Indentation Response of Thin Hard-Coated Systems*, Surface and Coatings Technology **102**, 97 (1998).
- [156] D. B. Marshall and A. G. Evans, *Measurement of Adherence of Residually Stressed Thin Films by Indentation. I. Mechanics of Interface Delamination*, Journal of Applied Physics **56**, 2632 (1984).
- [157] Y. Xiao, W. Shi, Q. Wan, and J. Luo, *Evaluation of Failure Properties of a DLC/Steel System Using Combined Nanoindentation and Finite Element Approach*, Diamond and Related Materials **93**, 159 (2019).
- [158] L. G. Rosenfeld, J. E. Ritter, T. J. Lardner, and M. R. Lin, *Use of the Microindentation Technique for Determining Interfacial Fracture Energy*, Journal of Applied Physics **67**, 3291 (1990).
- [159] X. Li and B. Bhushan, *Measurement of Fracture Toughness of Ultra-Thin Amorphous Carbon Films*, Thin Solid Films **315**, 214 (1998).
- [160] J. M. Wheeler, D. E. J. Armstrong, W. Heinz, and R. Schwaiger, *High Temperature Nanoindentation: The State of the Art and Future Challenges*, Current Opinion in Solid State and Materials Science **19**, 354 (2015).
- [161] W. C. Oliver and G. M. Pharr, *An Improved Technique for Determining Hardness and Elastic Modulus Using Load and Displacement Sensing Indentation Experiments*, Journal of Materials Research **7**, 1564 (1992).
- [162] T. Pachler, R. M. Souza, and A. P. Tschiptschin, *Finite Element Analysis of Peak Stresses Developed during Indentation of Ceramic Coated Steels*, Surface and Coatings Technology **202**, 1098 (2007).
- [163] D. B. Marshall, B. R. Lawn, and A. G. Evans, *Elastic/Plastic Indentation Damage in Ceramics: The Lateral Crack System*, Journal of the American Ceramic Society **65**, 561 (1982).
- [164] J. Mougou, T. Le Bihan, and G. Lucazeau, *High-Pressure Study of Cr₂O₃ Obtained by High-Temperature Oxidation by X-Ray Diffraction and Raman Spectroscopy*, Journal of Physics and Chemistry of Solids **62**, 553 (2001).

Bibliography

- [165] N. M. Everitt, M. I. Davies, and J. F. Smith, *High Temperature Nanoindentation – the Importance of Isothermal Contact*, Philosophical Magazine **91**, 1221 (2011).
- [166] S. Korte, R. J. Stearn, J. M. Wheeler, and W. J. Clegg, *High Temperature Microcompression and Nanoindentation in Vacuum*, Journal of Materials Research **27**, 167 (2012).
- [167] J. M. Wheeler and J. Michler, *Invited Article: Indenter Materials for High Temperature Nanoindentation*, Review of Scientific Instruments **84**, 101301 (2013).
- [168] Y. Xiao, W. Shi, and J. Luo, *Indentation for Evaluating Cracking and Delamination of Thin Coatings Using Finite Element Analysis*, Vacuum **122**, 17 (2015).
- [169] E. Weppelmann and M. V. Swain, *Investigation of the Stresses and Stress Intensity Factors Responsible for Fracture of Thin Protective Films during Ultra-Micro Indentation Tests with Spherical Indenters*, Thin Solid Films **286**, 111 (1996).
- [170] K. Shu, C. Zhang, D. Zheng, S. Cui, P. Hou, and L. Gu, *Analysis on the Cracking of Thin Hard Films Considering the Effects of Interfacial Delamination*, Surface and Coatings Technology **402**, 126284 (2020).
- [171] M. Rusinowicz et al., *Failure of a Brittle Layer on a Ductile Substrate: Nanoindentation Experiments and FEM Simulations*, Journal of the Mechanics and Physics of Solids **163**, 104859 (2022).
- [172] A. Abdul-Baqi and E. Van der Giessen, *Indentation-Induced Interface Delamination of a Strong Film on a Ductile Substrate*, Thin Solid Films **381**, 143 (2001).
- [173] A. Abdul-Baqi and E. Van der Giessen, *Numerical Analysis of Indentation-Induced Cracking of Brittle Coatings on Ductile Substrates*, International Journal of Solids and Structures **39**, 1427 (2002).
- [174] N. K. Fukumasu and R. M. Souza, *Numerical Evaluation of Cohesive and Adhesive Failure Modes during the Indentation of Coated Systems with Compliant Substrates*, Surface and Coatings Technology **260**, 266 (2014).
- [175] A. G. Evans and J. W. Hutchinson, *On the Mechanics of Delamination and Spalling in Compressed Films*, International Journal of Solids and Structures **20**, 455 (1984).
- [176] K. Park and G. H. Paulino, *Cohesive Zone Models: A Critical Review of Traction-Separation Relationships across Fracture Surfaces*, Applied Mechanics Reviews **64**, 061002 (2011).
- [177] D. S. Dugdale, *Yielding of Steel Sheets Containing Slits*, Journal of the Mechanics and Physics of Solids **8**, 100 (1960).
- [178] G. I. Barenblatt, *The Mathematical Theory of Equilibrium Cracks in Brittle Fracture*, in *Advances in Applied Mechanics*, Vol. 7 (Elsevier, 1962), pp. 55–129.
- [179] J. H. Lee, Y. F. Gao, K. E. Johanns, and G. M. Pharr, *Cohesive Interface Simulations of Indentation Cracking as a Fracture Toughness Measurement Method for Brittle Materials*, Acta Materialia **60**, 5448 (2012).
- [180] J. M. Melenk and I. Babuška, *The Partition of Unity Finite Element Method: Basic Theory and Applications*, Computer Methods in Applied Mechanics and Engineering **139**, 289 (1996).
- [181] N. Moës and T. Belytschko, *X-FEM, de nouvelles frontières pour les éléments finis*, Revue Européenne des Éléments Finis **11**, 305 (2002).
- [182] D. Tabor, *The Hardness of Metals* Oxford University Press, (1951).
- [183] Y.-H. Lee and D. Kwon, *Estimation of Biaxial Surface Stress by Instrumented Indentation with Sharp Indenters*, Acta Materialia **52**, 1555 (2004).
- [184] W. Zhu, L. Yang, J. W. Guo, Y. C. Zhou, and C. Lu, *Determination of Interfacial Adhesion Energies of Thermal Barrier Coatings by Compression Test Combined with a Cohesive Zone Finite Element Model*, International Journal of Plasticity **64**, 76 (2015).
- [185] T. E. Mitchell, D. A. Voss, and E. P. Butler, *The Observation of Stress Effects during the High Temperature Oxidation of Iron*, Journal of Materials Science **17**, 1825 (1982).

RÉSUMÉ

Lors du laminage à chaud, une couche d'oxyde, la calamine, se forme à la surface des brames d'acier, responsable de défauts de surface. Le décalaminage, en envoyant de l'eau à haute pression à la surface de l'acier, permet de limiter l'épaisseur de l'oxyde, et donc d'améliorer la qualité de surface. L'objectif de cette étude est d'améliorer la compréhension des phénomènes mis en jeu lors du décalaminage secondaire à l'entrée du finisseur. Plusieurs nuances d'acier à faible teneur en carbone, caractérisées par des différences de décalaminage, sont choisies en vue d'analyser leurs disparités sur le plan industriel. Le comportement de la calamine est évalué par diffraction des rayons X à haute température de manière in situ, ce qui permet de reproduire un refroidissement contrôlé. Cette analyse comprend à la fois l'analyse des phases et des contraintes afin d'observer les transitions dans le comportement de l'oxyde, notamment la relaxation des contraintes internes au-delà de 700°C. Les propriétés mécaniques de l'oxyde sont évaluées par des essais d'indentation à température ambiante et à haute température. À faible température (<600°C), plusieurs familles de fissures se forment en indentations, compatibles avec un modèle de flexion d'une plaque dure (l'oxyde) sur un substrat mou (le métal) : fissures circulaires, délamination. À plus haute température, l'oxyde devient ductile. En parallèle, des simulations numériques par éléments finis (FEM) du processus d'indentation sont réalisées à l'aide du logiciel Abaqus® afin de mieux comprendre le mécanisme de fissuration et de délamination de l'oxyde. Ces simulations visent également à extraire les propriétés de fissuration de l'oxyde et de son interface. Ces données vont par la suite être utilisées pour une future modélisation complète du décalaminage hydraulique.

MOTS CLÉS

Calamine, Décalaminage, Laminage à chaud, Diffraction des Rayons X, Indentation, Simulation numérique

ABSTRACT

During the hot rolling process, a thin layer of oxide scale forms on the surface of steel slabs, leading to surface defects. Descaling, by applying high-pressure water to the steel surface, helps limit the thickness of the oxide and improve surface quality. This study aims to enhance the understanding of the phenomena involved in secondary descaling. Several low-carbon steel grades, characterised by differences in descaling, have been selected to analyse their discrepancies in industrial configurations. The behaviour of the oxide scale is evaluated through in situ high-temperature X-ray diffraction, enabling control over oxidation. This analysis includes both phase and stress evaluations to observe transitions in the behaviour of the oxide, particularly the relaxation of internal stresses above 700°C. Mechanical properties of the oxide are determined through indentation tests conducted at both room temperature and elevated temperatures. At lower temperatures (<600°C), indentation-induced cracks manifest in different patterns, consistent with a model of a hard film (the oxide) bending on a soft substrate (the metal), such as circular cracks and delamination. As the temperature increases, the oxide becomes ductile. Concurrently, numerical finite element simulations (FEM) of the indentation process are conducted to elucidate the mechanisms of fracture within the oxide layer. These simulations aim to extract essential fracture properties of the oxide layer and its interface. The acquired data will be used to develop a comprehensive model for hydraulic descaling.

KEYWORDS

Oxide scale, Descaling, Hot rolling, X-Ray diffraction, Indentation, Numerical simulation